University of Nevada, Reno

# Development of Magnetorheological Elastomer System for Adaptive Vibration Isolation

A dissertation submitted in partial fulfillment of the requirements for the degree of Doctor of Philosophy in Civil and Environmental Engineering

by

Siddaiah Yarra

Dr. Gokhan Pekcan/Dissertation Advisor

Dr. Gordaninejad Faramarz/Co-Advisor

December, 2018

THE GRADUATE SCHOOL

We recommend that the dissertation
prepared under our supervision by

**SIDDAIAH YARRA**

Entitled

**Development of Magnetorheological Elastomer System for Adaptive Vibration Isolation**

be accepted in partial fulfillment of the
requirements for the degree of

DOCTOR OF PHILOSOPHY

Gokhan Pekcan, Ph. D., Advisor

Faramarz Gordaninejad, Ph. D., Co-advisor

Ahmad Itani, Ph. D., Committee Member

Ian G. Buckle, Ph. D., Committee Member

Hanif Livani, Ph. D., Graduate School Representative

David W. Zeh, Ph. D., Dean, Graduate School
December, 2018

# ABSTRACT

This main objective of this study was focused on a proof-of-concept study of the performance of an adaptive bearing (AB) system under traffic and wind loadings, featuring magnetorheological elastomers (MREs). MREs were utilized to generate adaptability (variable stiffness) to the AB system. The investigations of this project were fundamental and developmental studies ranging from material synthesis, material characterization, theoretical studies, design and fabrication of the AB system, and large-scale component testing and evaluation. In addition, since no fabrication and testing systems were available in the market, testing and fabrication units were developed to facilitate the manufacturing of small and large-size MRE specimen, and a double-lap shear test unit to characterize MRE samples based on the ASTM standards.

Project started with an extensive literature survey to identify feasible material compositions that were reported to have achieved high magnetorheological (MR) effect under different loading conditions. Carbonyl iron, medium (Tap silicone and Natural rubber), and additives (Carbon black and Carbon nanofibers) mixed MRE's were fabricated under applied magnetic field of 1.2 Tesla. Scanning electron Microscope (SEM) pictures of the MREs showed the chain-like structure within MREs. A small-scale shear and compression test setup was manufactured for the characterization of MREs. Quasi-static and sinusoidal cyclic experiments were performed to investigate the magnetic field-dependent change on MREs properties under simultaneous shear and compression loads.

In second phase of the project, bridge load requirements were established under traffic and wind loads. A large-scale shear and compression test setup was designed and manufactured to study the performance of the AB system under combined and compression loads. Component

tests were successfully performed on two quarter-scale prototype bearings, measuring the changes in the stiffness of the adaptive bearing under the applied magnetic field, strain level, loading frequency, and compression load.

Finally, a seven-parameter viscoelastic model was developed and adapted to simulate the response of natural rubber – based MREs and concluded it can capture the behavior sufficiently accurate.

Results demonstrated that plastic silicone MREs show high MR effect at lower strains and MR effect diminishes for large strains whereas natural rubber based MREs show uniform MR effect for strains up to 150%. Also, carbon black improves the base passive stiffness and carbon nanofiber improves MR effect due to magnetically permeable characteristics. Storage modulus, loss modulus, effective stiffness, and effective damping showed increasing trend with increased applied magnetic field. However, MR effect was reduced with increased frequency. Experimental results demonstrated that the effective stiffness of adaptive bearing increases with increased applied magnetic field.

DEDICATED

To

***My parents, Nageswara Rao and Venkata Narasamma***

*For their unwavering faith, unconditional support and love throughout my academic career.*

***My wife, Sai Ramya***

*For her eternal friendship, love, care, patience, faith, and understanding throughout my Ph. D.*

***My In-laws, Bose Babu and Narmada***

*Indebted for allowing their daughter to sunshine in my life while doing my Ph.D.*

***My mentors, Sameer and Akhila***

*For enlightening my thinking to pursue my dream.*

***Prashant***

*Who had traveled more often to Reno to help unconditionally.*

*My educators and untold others who have helped, inspired and prayed for me.*

# Acknowledgements

Funding for the study was provided by the Federal Highway Administration under the contract number DTFH61-13-C-00020. I would like to express my gratitude to Dynamic Isolation Systems, Inc. for allowing modification and use their bearing test setup, to Scougal Rubber Corporation for their assistance with material testing and with the fabrication of the adaptive bearings, and to Advanced Materials and Devices for their help with material testing.

I would like to sincerely thank my advisors, Dr. Gokhan Pekcan, Dr. Gordaninejad Faramarz, and Dr. Ahmad Itani for their guidance, patience, and for giving me the opportunity to participate in a multidisciplinary research project. Dr. Pekcan have taught me so many little details that matter the most in academic field while conducting research. He is professional when it comes to getting things done in right way, caring and understanding while going through difficult times, flexible to new ideas. Dr. Faramarz have taught me how to balance professional and personal life to achieve more.

Committee members Ian G. Buckle and Hanif Livani are thankfully acknowledged for their time and their insightful remarks and suggestions. In addition, I would like to thank the outstanding faculty and staff of the Department of Civil and Environmental Engineering, the Office of International Students and Scholars, the Graduate School, and the Graduate Student Association at the University of Nevada, Reno for their contribution to my academic career.

I also acknowledge Mr. Tony Berendsen, Development Technician of the Mechanical Engineering Department, for his assistance with the fabrication; Mr. Chad Lyttle, Development Technician of the University of Nevada, Reno Center for Civil Engineering Earthquake Research, for his assistance with performing experiments; and Dr. Patrick Laplace, Research

Associate Professor and Manager of the Large Scale Structures and Earthquake Engineering Laboratory, for his assistance with instrumentation of the adaptive bearing experiments at the University of Nevada, Reno. I wish to thank Mr. Troy Martin, Structures Division of the Nevada Department of Transportation (NDOT), for his valuable feedback and participation during the component testing of the adaptive bearings.

Thanks are due to Dr. Majid Behrooz, Dr. Ali Mehrsoroush, Dr. Mostafa Tazarv, Dr. Amarjeet Saini, Dr. Suiwen Wu, Dr. Sevki Cesmeci, Dr. Reihaneh Sarraf Shirazi, Ecem Ozsahin, Dr. Alireza Mohebbi, Dr. Denis Istrati for their encouragement and help during various stages of the experimental testing. Also, thanks to undergrad student assistants Nathan Pinuleas, David Mar, and Blake Muzinich.

# Table of Contents

**ABSTRACT……i**

**Acknowledgements ..... iv**

Chapter 1. Introduction ..... 1

1.1. Background ..... 1

1.2. Literature Review ..... 1

1.2.1. Material characterization ..... 1

1.2.2. MRE – based devices ..... 2

1.2.3. Modeling ..... 3

1.3. Objective and scope ..... 5

1.4. Organization of document ..... 6

1.5. References ..... 7

Chapter 2. Performance of natural rubber and silicon-based magnetorheological elastomers under large-strain combined axial and shear loading ..... 12

2.1. Introduction ..... 13

2.2. MRE specimens fabrication process ..... 17

2.3. Experimental setup ..... 20

2.4. Experimental results and discussion ..... 21

2.4.1. Monotonic experiments ..... 21

2.4.2. Sinusoidal cyclic experiments ..... 25

2.5. Summary and conclusions ..... 37

2.6. Acknowledgements ..... 38

2.7. References ..... 38

Chapter 3. Performance of a large-scale magnetorheological elastomer-based vibration isolator for highway bridges ..... 43

3.1. Introduction ..... 43

3.2. System requirements for the design of bearings ..... 47

3.3. Design and fabrication of the bearings ..... 49

3.3.1. Fabrication of MREs, steel shims and preparation of stacks ..... 50

3.3.2. Fabrication of electromagnets for bearing ..... 51

3.4. Experimental evaluation of the scaled bridge bearings ..... 54

3.4.1. Double-lap shear and compression experimental setup ..... 54

3.4.2. Instrumentation and data processing ..... 55

3.4.3. Experimental results and discussion ..... 56
3.5. Conclusions ..... 65
3.6. Acknowledgements ..... 66
3.7. References ..... 66
Chapter 4. Modeling of natural rubber-based isotropic magnetorheological elastomers subjected to combined loading ..... 71
4.1. Introduction ..... 71
4.2. Experimental study of natural rubber-based MREs ..... 74
4.2.1. Material fabrication ..... 74
4.2.2. Experimental setup and testing ..... 75
4.2.3. Summary of experimental observations ..... 76
4.3. Material modelling of natural rubber-based MRE ..... 77
4.3.1. Identification of viscoelastic model parameters ..... 79
4.4. Experimental versus model-predicted response ..... 82
4.4.1. Shear load only ..... 82
4.4.2. Combined compressive and shear load ..... 85
4.5. Concluding remarks ..... 88
4.6. Acknowledgements ..... 89
4.7. References ..... 90
Chapter 5. Summary, Conclusions and Recommendations for future research ..... 95
5.1. Summary ..... 95
5.2. Conclusions ..... 95
5.3. Recommendations for future research ..... 98
Appendix A. Conference papers ..... 99
A.1 Characterization of carbon black-filled natural rubber and silicone magnetorheological elastomers under pure shear loading ..... 99
A.1.1 Introduction ..... 99
A.1.2 Fabrication of natural rubber and silicone MREs ..... 101
A.1.3 MRE microstructure analysis ..... 103
A.1.4 Experimental setup ..... 104
A.1.5 Conclusions ..... 111
A.1.6 Acknowledgments ..... 112
A.1.7 References ..... 112

A.2 A large-scale adaptive magnetorheological elastomer-based bridge bearing ..... 114
A.2.1 Introduction ..... 114
A.2.2 MRE – based bearing design and fabrication ..... 116
A.2.3 Experimental study ..... 118
A.2.4 Results and discussion ..... 119
A.2.5 Conclusions ..... 122
A.2.6 Acknowledgements ..... 123
A.2.7 References ..... 124
A.3 A self-sensing magnetorheological elastomer-based adaptive bridge bearing with a wireless data monitoring system ..... 127
A.3.1 INTRODUCTION ..... 127
A.3.2 WIRELESS SENSING SYSTEM DESIGN ..... 129
A.3.3 MRE Characterization ..... 132
A.3.4 ADAPTIVE BRIDGE BEARING DESIGN ..... 136
A.3.5 SUMMARY AND CONCLUSIONS ..... 139
A.3.6 ACKNOWLEDGEMENT ..... 139
A.3.7 REFERENCES ..... 139
Appendix B. Experiments documentation ..... 142
B.1 Quasi –Static (Monotonic) Test Results of Silicone-based MRE Samples ..... 142
B.2 Quasi –Static Test Results of Natural rubber-based MRE Samples ..... 145
B.3 Cyclic Tests Results Summary for Natural rubber-based MRE Sample ..... 147
B.4 Test Protocol ..... 148
B.5 Test setup Assembly ..... 149
B.6 Test Protocol ..... 151
B.7 Test Results ..... 168
Appendix C. Viscoelastic Material Modeling ..... 177
Appendix D. MRE-Based Sensor and Wireless Sensing System ..... 184
D.1 MRE-Based Sensor ..... 184
D.2 Wireless Sensing System ..... 187

# Chapter 1. Introduction

## 1.1. Background

Approximately 45% of the nation's inventory of 590,000 bridges is rapidly approaching the end of its intended design life (National Bridge Inventory, 2011). Bridges are commonly subjected to wind and traffic loads. The continuous deterioration due to various loading conditions has become a major concern to FHWA, DOTs, bridge owners and engineers. Continuous structural health monitoring along with vibration suppression systems for bridges has been recognized as means to increase the service life of bridges and ensure their safety. The vibration suppression systems can be passive, active, or semi-active. Passive conventional bearings with elastomeric layers have been installed in a variety of highway bridges to accommodate translations and rotations. The performance of these passive systems can be tailored to specific stiffness and damping; however, they cannot be tuned in real-time for different operating conditions. A semi-active variable stiffness system may overcome such a limitation. Semi-active vibration absorption systems have the advantage of tunability while they require less power compared to active systems. Semi-active vibration absorption systems can change the stiffness of an isolated bridge and hence avoided resonant frequencies or reduce the vibration when used with a controller.

## 1.2. Literature Review

### 1.2.1. Material characterization

Different materials and technologies are suggested for semi-active systems, such as MREs which are magnetically controllable elastomers. A MRE is composed of micron-size magnetically permeable particles, elastomeric medium, and additives such as carbon black and carbon nanofiber. MRE exhibits magnetoviscoelastic behavior and upon application of an external

magnetic field, the force between the particles increases that results in an increased stiffness, damping, and hysteresis of MREs; however, damping change is smaller compared to stiffness change (Behrooz et al., 2013a). When MREs are cured within a strong magnetic field, chain-like structures of particles are created that result in a higher stiffness change when MRE is subjected to the magnetic field. Characterization experiments of mechanical properties showed that the moduli of MRE samples can be significantly increased by applying a magnetic field (Gong et al., 2007). The optimum particle concentration for increasing the shear modulus is 27% by volume (Davis, 1999). It is shown that MR effect is stronger for softer elastomer matrix and the storage modulus can be increased up to 800% (Gong et al., 2007), if the off-state shear modulus is on the order of kilo Pascals. Also, MR effect ($\Delta G/G_0\%$) increases at higher loading frequencies (Jung et al., 2009) and a compressive force reduces the MR effect of a MRE subjected to shear deformation (Dong et al., 2012). (Stepanov et al., 2007) showed that the MR effect is higher for a MRE subjected to small strains.

### 1.2.2. MRE – based devices

Researchers have been testing MRE based devices due to its enarmous potential of changing its stiffness under external stimuli. A MRE-based vibration isolation system utilizes changes in shear modulus (G) or stiffness (K) of MRE under an applied magnetic field. MREs have a very fast response time that is 7 ms under impact loading (Fu et al., 2013) or about 60 ms under large strains (Nguyen and Ramanujan, 2010). MRE vibration absorbers have shown promising performances in a vehicles' engine mounts (Ginder et al., 2000), vehicle transmission system (Hoang et al., 2011), vehicle seat suspension (Du et al., 2011), and adaptive tuned vibration absorbers (Deng et al., 2006; Deng and Gong, 2008).

Due to MRE's fast response and proportionality of the change in stiffness of an isolation system to that of MRE layers, it may be possible to control the response of a supported structural by controlling the stiffness of MRE layers and prevent or attenuate resonant vibrations. (Li et al., 2013) demonstrated the design of a MRE base isolator by replacing traditional rubber layers in a bearing with MRE layers and achieved a 30% increase in effective stiffness. (Behrooz et al., 2013a) presented a variable stiffness and damping isolator for seismic base isolation of buildings and modeled its behavior using a phenomenological model with springs, viscous dampers, and a hysteretic Bouc-Wen element. (Behrooz et al., 2013b) used the current-dependent relations of the MRE base isolator with a control algorithm to control its performance. A design for a MRE base isolator was presented by (Yang et al., 2014) that incorporates a permanent magnet and can achieve both positive and negative stiffness changes based on the direction of the applied magnetic field. (Tu et al., 2014) investigated the field-dependent shear modulus of a MRE isolator. (Xing et al., 2015) designed and tested the performance of a bridge bearing using MRE layers and implemented a field-dependent model to consider the dependency of the stiffness and damping of the isolator on the applied magnetic field.

### 1.2.3. Modeling

Modeling efforts of magnetorheological elastomer materials and devices made of elastomers have been increased. However, not much data and modeling are available to accurately predict long-term durability and performance of MRE's. Therefore, there is a need to develop models which can predict performance of desired MRE based devices during the design and evaluation stages. In recent years, many models have been developed and evaluated against experimental data. Models have been categorized based on particle interaction based, magneto-elastic response

based, magneto-viscoelastic response based, or models including the effects of environmental conditions and fatigue (Cantera et al., 2017).

(Norouzi et al., 2017) proposed a generalized Maxwell viscoelastic model by placing two Maxwell elements and a spring in parallel to capture the dynamic behavior of isotropic MRE's under combined tensile – compressive loadings and concluded it can portray the behavior well. (Wang and Gordaninejad, 2009) developed a three-parameter model with two elements, the friction damping force as a function of applied magnetic field and displacement and a stiffness element as a function of displacement and captured the MR-fluid elastomer mount behavior well. A four-parameter viscoelastic model to portray MRE behavior under harmonic loading, consists of a standard solid model and a spring parallel to the standard solid model representing field dependency of modulus. The model predicted versus experimentally recorded responses are compared and concluded it can predict effectively (Li et al., 2010). (Chen and Jerrams, 2011) discussed a model considers the influences of viscoelasticity of the polymer composite, magnetic-field induced mechanical properties, and internal slippage between the matrix and iron particles. A standard liner solid model, variable stiffness spring, and a spring-Coulomb friction were arranged in parallel to model three components respectively. (Eem et al., 2012) presented a model by combining a Maxwell element and a Ramberg-Osgood model in parallel to study behavior of MRE under shear deformation and concluded it can capture dynamic behavior over a wide range of operating conditions. A magnetoviscoelasticity parametric model by a spring element, a fractional derivative dashpot element, a nonlinear spring element and analogous dashpot element in parallel was developed to describe the behavior of MRE device and concluded it can capture response effectively (Zhu et al., 2012). To capture the MRE based base isolator, (Yu et al., 2015) proposed a model by placing LuGre fricition element parallel to

Kelvin-Voigt element and showed the proposed model is capable of forecasting MRE base isolator behavior effectively. (Behrooz et al., 2013a) modeled and captured MRE isolator response by combining standard solid linear model, Bouc-Wen element, a field-dependent spring and a damping coefficient in parallel.

## 1.3. Objective and scope

The goal of the project was to design, develop, test and evaluate the performance of an adaptive bridge bearing system using magnetorheological elastomer (MRE). The proposed adaptive bearing (AB) encompasses a semi-active bearing system. The adaptive bridge bearing includes MRE layers that can be tuned to desired stiffness with an external magnetic field. Such a system has the potential to offer the structural vibration suppression. In first part of the project, an extensive literature survey was conducted followed by material characterization. Before finalizing bearing dimensions and loading protocols, different designs for the AB system were investigated. An innovative design of variable stiffness bearings employing MREs was finalized and two bearings were manufactured. The passive rubber layers of conventional bearings are replaced with layers MREs, which provide controllable stiffness while retaining the fail-safe characteristic of the traditional isolators. The applied magnetic field, produced by the built-in electromagnet, changes the stiffness of MREs and the adaptive bearing. The performance of the AB system was examined in a double lap shear and compression test setup.

The objectives of this study were to:

1. Literature survey to identify feasible material composition to achieve high magnetorheological (MR) effects under large strains.

2. Characterize the mechanical properties of MREs (TAP Silicone based, and Natural Rubber based) using a newly designed and built combined double-lap shear and compression test setup.
3. Identify bridge load requirements under traffic and wind loads.
4. Design a bearing system, similar to a conventional bridge bearing system, utilizing MREs and considering all materials, geometrical and bridge system requirements.
5. Develop a large-scale double-lap shear and compression test setup for characterization of the adaptive bearings.
6. Experimentally examine the performance of the AB system using the large-scale combined double-lap shear and compression test setup.
7. Modeling of natural rubber -based magnetorheological elastomers under combined loading.

## 1.4. Organization of document

The report organization is as follows: after introduction in Chapter 1, Chapter 2 is a stand-alone published journal paper, describes the characterization of mechanical properties of natural rubber and plastic silicone based MRE materials. Chapter 3 is a published journal paper explains the magnetic field analysis of the bearing. The fabrication process of the bearing and the double lap shear and compression test setup and the results of the double lap shear and compression experiments to investigate the performance of the AB system. Chapter 4 describes the analytical study of magnetorheological elastomers under combined loading. Chapter 5 describing a summary, conclusions, and recommendations for future research. The paper in Chapter 2 and Chapter 3 were published in 2018 and the paper in Chapter 4 have been submitted for review.

Two appendices are included after Chapter 5. Appendix A includes three published conference papers. Appendix B provides the experimental and analytical investigations discussed in Chapter 2-4. Appendix C discusses viscoelastic material modeling. Finally, Appendix D includes MRE-based sensor and wireless sensing system.

## 1.5. References

ASCE (2010) Minimum Design Loads for Buildings and Other Structures, ASCE 7-10 ed. American Society of Civil Engineers.

AmiriHormozaki, E., Pekcan G., and Itani, A. (2013). "Analytical Fragility Curves for Horizontally Curved Steel Girder Highway Bridges," Center for Civil Engineering Earthquake Research, Report No. CCEER-13-03, University of Nevada, Reno, February 2013

Behrooz M, Wang X and Gordaninejad F (2013a) Modeling of a new magnetorheological elastomer-based isolator. In: *Proc. SPIE*, San Diego, Ca, p. 86880Z–86880Z. Available from: http://dx.doi.org/10.1117/12.2009946 (accessed 2 May 2013).

Behrooz M, Wang X and Gordaninejad F (2013b) Seismic control of base isolated structures using novel magnetorheological elastomeric bearings. In: *Proc. ASME*, Snowbird, UT, p. V001T03A027-V001T03A027.

Behrooz M, Sutrisno J, Zhang L, et al. (2015) Behavior of magnetorheological elastomers with coated particles. *Smart Materials and Structures* 24(3): 35026. Available from: http://iopscience.iop.org/0964-1726/24/3/035026 (accessed 19 February 2015).

Ceylan H, Gopalakrishnan K, Taylor P, et al. (2011) A Feasibility Study on Embedded Micro-Electromechanical Sensors and Systems (MEMS) for Monitoring Highway Structures. Available from: https://works.bepress.com/halil_ceylan/52/ (accessed 28 November 2016).

Chen L, Gong XL and Li WH (2008) Effect of carbon black on the mechanical performances of magnetorheological elastomers. *Polymer Testing* 27(3): 340–345. Available from: http://www.sciencedirect.com/science/article/pii/S0142941807001845 (accessed 26 February 2015).

Chen L and Jerrams S (2011) A rheological model of the dynamic behavior of magnetorheological elastomers. *Journal of Applied Physics*, *110*(1), p.013513.

Davis LC (1999) Model of magnetorheological elastomers. *Journal of Applied Physics* 85(6): 3348. Available from: http://adsabs.harvard.edu/abs/1999JAP....85.3348D (accessed 26 November 2012).

Deng H and Gong X (2008) Application of magnetorheological elastomer to vibration absorber. *Communications in Nonlinear Science and Numerical Simulation* 13(9): 1938–1947. Available from: http://www.sciencedirect.com/science/article/pii/S1007570407000524 (accessed 17 August 2012).

Deng H, Gong X and Wang L (2006) Development of an adaptive tuned vibration absorber with magnetorheological elastomer. *Smart Materials and Structures* 15(5): N111–N116. Available from: http://iopscience.iop.org/0964-1726/15/5/N02.

Dong X, Ma N, Qi M, et al. (2012) The pressure-dependent MR effect of magnetorheological elastomers. *Smart Materials and Structures* 21(7): 75014. Available from: http://iopscience.iop.org/0964-1726/21/7/075014 (accessed 22 August 2013).

Du H, Li W and Zhang N (2011) Semi-active variable stiffness vibration control of vehicle seat suspension using an MR elastomer isolator. *Smart Materials and Structures* 20(10): 105003. Available from: http://iopscience.iop.org/0964-1726/20/10/105003.

Eem SH, Jung HJ and Koo JH (2012) Modeling of magneto-rheological elastomers for harmonic shear deformation. *IEEE transactions on magnetics*, *48*(11), pp.3080-3083.

Fu J, Zheng X, Yu M, et al. (2013) A new magnetorheological elastomer isolator in shear - Compression mixed mode. In: *2013 IEEE/ASME International Conference on Advanced Intelligent Mechatronics (AIM)*, pp. 1702–1706.

Ginder JM, Nichols ME, Elie LD, et al. (1999) Magnetorheological elastomers: properties and applications. *Proceedings of SPIE* 3675(1): 131–138. Available from: http://spiedigitallibrary.org/proceedings/resource/2/psisdg/3675/1/131_1?isAuthorized=no.

Ginder JM, Nichols ME, Elie LD, et al. (2000) Controllable-stiffness components based on magnetorheological elastomers. *Proceedings of SPIE* 3985(1): 418–425. Available from: http://spiedigitallibrary.org/proceedings/resource/2/psisdg/3985/1/418_1?isAuthorized=no.

Gong XL, Chen L and Li JF (2007) Study of Utilizable Magnetorheological Elastomers. *International Journal of Modern Physics B* 21: 4875–4882. Available from: http://adsabs.harvard.edu/abs/2007IJMPB..21.4875G (accessed 17 August 2012).

Hoang N, Zhang N and Du H (2011) An adaptive tunable vibration absorber using a new magnetorheological elastomer for vehicular powertrain transient vibration reduction. *Smart Materials and Structures* 20(1): 15019. Available from: http://stacks.iop.org/09641726/20/i=1/a=015019?key=crossref.71451c14fc991cce2bbdd22311c833de (accessed 19 April 2013).

Jolly MR, Carlson JD, Muñoz BC, et al. (1996) The Magnetoviscoelastic Response of Elastomer Composites Consisting of Ferrous Particles Embedded in a Polymer Matrix. *Journal of Intelligent Material Systems and Structures* 7(6): 613–622. Available from: http://jim.sagepub.com/content/7/6/613 (accessed 26 February 2015).

Jung H-J, Lee S-J, Jang D-D, et al. (2009) Dynamic Characterization of Magneto-Rheological Elastomers in Shear Mode. *IEEE Transactions on Magnetics* 45(10): 3930–3933.

Kchit N, Lancon P and Bossis G (2009) Thermoresistance and giant magnetoresistance of magnetorheological elastomers. *Journal of Physics D: Applied Physics* 42(10): 105506. Available from: http://stacks.iop.org/0022-3727/42/i=10/a=105506 (accessed 3 March 2016).

Li WH, Zhou Y and Tian TF (2010) Viscoelastic properties of MR elastomers under harmonic loading. *Rheologica acta*, *49*(7), pp.733-740.

Li Y, Li J, Li W, et al. (2013) Development and characterization of a magnetorheological elastomer based adaptive seismic isolator. *Smart Materials and Structures* 22(3): 35005. Available from: http://iopscience.iop.org/0964-1726/22/3/035005 (accessed 22 August 2013).

Liao G, Gong X and Xuan S (2013) Influence of shear deformation on the normal force of magnetorheological elastomer. *Materials Letters* 106: 270–272. Available from: http://www.sciencedirect.com/science/article/pii/S0167577X13006836 (accessed 27 August 2015).

Norouzi M, Gilani M, Alehashem SM and Vatandoost H (2017) Dynamic Characterization and Modeling of Isotropic Magnetorheological Elastomers Under Tensile-Compressive Loadings. *IEEE TRANSACTIONS ON MAGNETICS MAG*, *53*(9), pp.1-12.

Nguyen VQ and Ramanujan RV (2010) Novel Coiling Behavior in Magnet-Polymer Composites. *Macromolecular Chemistry and Physics* 211(6): 618–626. Available from: http://onlinelibrary.wiley.com/doi/10.1002/macp.200900478/abstract (accessed 27 November 2016).

Schubert G and Harrison P (2015) Large-strain behaviour of Magneto-Rheological Elastomers tested under uniaxial compression and tension, and pure shear deformations. *Polymer Testing* 42: 122–134. Available from: http://www.sciencedirect.com/science/article/pii/S0142941815000124 (accessed 3 August 2015).

Shen Y, Golnaraghi MF and Heppler GR (2004) Experimental Research and Modeling of Magnetorheological Elastomers. *Journal of Intelligent Material Systems and Structures* 15(1): 27–35. Available from: http://jim.sagepub.com/content/15/1/27 (accessed 26 November 2012).

Stepanov GV, Abramchuk SS, Grishin DA, et al. (2007) Effect of a homogeneous magnetic field on the viscoelastic behavior of magnetic elastomers. *Polymer* 48(2): 488–495. Available from: http://linkinghub.elsevier.com/retrieve/pii/S0032386106012912 (accessed 19 April 2013).

Tu JW, Tu B, Mei ST, et al. (2014) Research on new type MRE isolator and its mechanical model. *Materials Research Innovations* 18(S2): S2-552. Available from: http://www.maneyonline.com/doi/abs/10.1179/1432891714Z.000000000479 (accessed 30 July 2015).

Wang X, Gordaninejad F, Calgar M, et al. (2008) Electrical properties of magneto-rheological elastomers. In: ASME Conference on Smart Materials, Adaptive Structures and Intelligent Systems, SMASIS2008, October 28, 2008 - October 30, 2008, Proceedings of the ASME Conference on Smart Materials, Adaptive Structures and Intelligent Systems, SMASIS2008, American Society of Mechanical Engineers, pp. 869–874.

Wang X and Gordaninejad F (2009) A new magnetorheological fluid–elastomer mount: phenomenological modeling and experimental study. Smart Materials and Structures, 18(9), p.095045.

Xing Z-W, Yu M, Fu J, et al. (2015) A laminated magnetorheological elastomer bearing prototype for seismic mitigation of bridge superstructures. *Journal of Intelligent Material Systems and Structures*: 1045389X15577654. Available from: http://jim.sagepub.com/content/early/2015/03/19/1045389X15577654 (accessed 3 August 2015).

Yang J, Sun SS, Du H, et al. (2014) A novel magnetorheological elastomer isolator with negative changing stiffness for vibration reduction. *Smart Materials and Structures* 23(10): 105023. Available from: http://iopscience.iop.org/0964-1726/23/10/105023 (accessed 18 August 2015).

Yu Y, Li Y and Li J (2015) Forecasting hysteresis behaviours of magnetorheological elastomer base isolator utilizing a hybrid model based on support vector regression and improved particle swarm optimization. *Smart Materials and Structures*, *24*(3), p.035025.

Zhu JT, Xu ZD and Guo YQ (2012) Magneto viscoelasticity parametric model of an MR elastomer vibration mitigation device. *Smart Materials and Structures*, *21*(7), p.075034.

# Chapter 2. Performance of natural rubber and silicon-based magnetorheological elastomers under large-strain combined axial and shear loading

Note. This chapter is a stand-alone paper published in Journal of Intelligent Materials Systems and Structures.

Yarra, S., Gordaninejad, F., Behrooz, M., & Pekcan, G. (2018). Performance of natural rubber and silicone-based magnetorheological elastomers under large-strain combined axial and shear loading. Journal of Intelligent Material Systems and Structures.
https://doi.org/10.1177/1045389X18808393

## ABSTRACT

This study presents an experimental investigation on large-strain behavior of natural rubber and silicone-based magnetorheological elastomers (MREs) within a larger scope of structural vibration mitigation due to wind, traffic and seismic events. MRE samples with different weight percentages of iron particles, additives and elastomer matrix were fabricated. The microstructures of specimens were examined, and their mechanical properties were investigated by a unique electromagnetic double-lap shear experimental setup capable of applying simultaneous compression and shear loads. The experimental results demonstrated that the isotropic natural rubber-based MREs exhibit about 30%, magnetorheological (MR) effect under large strains while they achieve a higher MR effect under the combined axial and shear loading. The MR effect was 92% and 33% for 10% and 100% shear strains when 100psi axial stress was applied. A natural rubber-based MRE was further investigated applying dynamic cyclic load with and without compression load for different strains, frequencies and magnetic field intensities. It was observed that for higher frequency, MR effect was reduced. MR effects were 73% and 29% for 0.1Hz and 10Hz frequencies, respectively, under 100psi axial stress at 150% shear strain. The result of this study suggests that isotropic natural rubber-based MREs may be suitable for high-demand-force applications, and in paarticular in civil structures.

**KEYWORDS:** Magnetorheological elastomers, natural rubber, carbon black, shear and compression loading

## 2.1. Introduction

Conventional (passive) elastomers, such as natural rubber, have been utilized in structures, vehicles and other machineries to mitigate shock and vibration. Passive elastomeric layers have limitations in accomodating a wide range of operating conditions. Magnetorheological elastomers (MREs) are a class of materials whose monotonic (shear modulus) and dynamic (storage and loss moduli) properties can be tuned by an external magnetic field. For fabrication of MREs, magnetically permeable particles are mixed with an elastomeric matrix. When the mixture is cured under a magnetic field, iron particles form chains. On the other hand, when the mixture is cured without a magnetic field, iron particles randomly scatter in elastomer and result in an isotropic MRE. Polyurethane-based anisotropic MRE showed 20% better MR effect than anisotropic natural rubber MRE (Shen et al., 2004). Gong et al. (2005) investigated the relation between microstructure and mechanical properties of isotropic magnetorheological elastomers and concluded that the isotropic MRE with 70%wt. iron particle showed 51% MR effect. Chen et al. (2007) reported 133% MR effect for the 80%wt. anisotropic natural rubber MRE.

Lokander and Stenberg (2003) demonstrated that natural rubber based isotropic MR material with irregularly shaped iron particles has a better MR effect than with carbonyl iron. However, MR effect was reduced with a high-viscous matrix than the softer matrix due to less well-dispersed iron particles. The shear modulus of anisotropic MRE increases with increasing strain rate, magnetic field intensity, and pre-compressed loading (Jung et al., 2009; Behrooz et al., 2016). The increase in modulus is significant, if the applied stress is parallel to the particle alignment (Ruddy et al., 2012). A theoretical model based on effective permeability rule and the

consideration of normal pressure concluded that the shear modulus of MREs increases with increased normal pressure, and the influence of normal pressure is more significant at higher levels of the magnetic field (Dong et al., 2013). Schumann et al. (2017) analyzed magnetic field effect on the particle movement and concluded that magnetic field does have significant effect on rotation and translation of the particles. The addition of carbon black into the matrix enhances the passive shear modulus of isotropic and anisotropic MREs (Chen et al., 2008; Nayak et al., 2015). Hang at el. (2017) proved that carbon nanotubes can enhance field-dependent conductivity by at least two orders of magnitude. In a previous work by the authors Yarra et al. (2017), isotropic natural rubber MREs showed better MR effect than anisotropic silicone based MRE at large strains. The stiffness of anisotropic MREs increases with increased frequency (Behrooz et al., 2016). Stepanov at el. (2007) demonstrated an increase in shear modulus and in loss modulus from three different experimental techniques such as elongation, quasi-static, and dynamic shear tests. Wen et al. (2017) demonstrated that storage modulus of isotropic and anisotropic MRE's made of hard magnetic particles can increase with increasing magnetic field and decrease with increasing magnetic field of opposite orientation. Also, asymmetric storage modulus curves were observed if the magnetizing field was higher than the test magnetic field.

Depending on the application of magnetic field during fabrication of MREs, different iron particle dispersion and different directional mechanical properties can be achieved. Isotropic and anisotropic MREs have been utilized in vibration absorption applications, such as vehicular powertrains (Hoang et al., 2010) and vehicle seat suspension (Du et al., 2011). Popp et al. (2010) built a MRE-based vibration absorber and demonstrated capabilities in reducing vibrations. Deng et al. (2006) proved that resonance frequency of MRE-based adaptive tuned vibration absorber can be controlled by electrical currents. Also, MREs were used in

controllable stiffness and damping devices to evaluate feasibility of adapting in civil engineering applications. MRE-based isolator was tested under shear and compression loading and experimental results showed 175% increase in stiffness, and 216% in damping at 40Hz when the current was increased from 0A to 1.5A (Fu et al., 2013a, 2017b; Yang et al., 2014a, 2015b). Yancheng et al. (2013) designed, developed, and tested a MRE based seismic isolator and concluded that the stiffness and damping can alter up to 37% and 45%, respectively. Li and Li, (2007) designed and tested MRE based isolator and showed an increase of 16 times in lateral stiffness at 8% strain and 0.1 Hz. The optimal design of MRE bearings depends upon particle volume fraction (Shiwei et al., 2016). Lujie et al. (2017) showed MRE isolator can be used for vibration suppression of bridge monitoring equipment. Authors have presented a large-scale MRE bridge bearing that showed reduced MR effect of 12% to 5% for strain amplitudes of 20% to 50% (Yarra et al., 2017).

Since there have been multiple studies on properties of MRE mainly in a low strain regime, summary of mechanical properties from previous works is carried out to better compare with the current large strain results. Based on the data presented in Table 1 and to the best of the authors' knowledge, the research to date on magnetorheological elastomers has been mainly focused on small strain regimes, loading and scaled geometry which is not reliable as MRE materials' behavior is nonlinear in nature for higher strains. Also, methods of testing that most of results presented in Table 1 are obtained does not replicate the method used to test isolation bearings for structures. Therefore, large strains study of MREs is essential in the understanding of structural vibration isolation using MRE isolator since large strains (up to 150%) are possible in structural events. In this study, test setup was designed such that both shear strain and compression force can be applied and controlled individually or at the same time on ASTM

standard size MRE samples. Electromagnets with extended trapezoidal prism shape were fabricated and used to apply uniform magneticfield focused to surface area of MRE samples. MR effects were studied experimentally using double lap shear and compression method described in ASTM D5992 for natural rubber and platinum silicone MRE samples for large strains.

**Table 1.** A Summary of MR Effect under Different Loading Conditions.

| Reference [number] | IP | Area of sample | thickness | Loading conditions | | | $G_{off}$ | $G_{on}$ | $\Delta G/G_0$ | Work Type[c,d] |
|---|---|---|---|---|---|---|---|---|---|---|
| | (%) | ($in^2$) | (in) | Freq. (Hz) | Strain (%) | B (Tesla) | (psi) | (psi) | (%) | |
| (Jolly et al., 1996) | 30v | 0.23 | 0.04 | 2 | 1 | 0.85 | 261 | 342 | 31 | E |
| (Jolly et al., 1996) | 30v | 0.23 | 0.04 | 2 | 10 | 0.85 | 261 | 290 | 11 | E |
| (Ginder et al., 1999) | 27v | na | na | 2 | 10 | 1 | 319 | 435 | 36 | E |
| (Ginder et al., 1999) | 40v | na | na | 2 | 3 | 1 | 435 | 566 | 30 | E |
| (Ginder et al., 1999) | 40v | na | na | 2 | 6 | 1 | 391 | 471 | 21 | E |
| (Ginder et al., 1999) | 40v | na | na | 2 | 12 | 1 | 290 | 341 | 17 | E |
| (Davis, 1999) | 27v | na | na | na | 14 | >1 | 109 | 145 | 33 | FEM |
| (Davis, 1999) | 27v | na | na | na | 19 | >1 | 87 | 115 | 32 | FEM |
| (Shen et al., 2004) | 25v | na | na | 1[a] | 11.5 | 0.4 | 64 | 82 | 27 | E |
| (Deng et al., 2006) | 70w | na | na | 10 | na | 0.9 | 87 | 197 | 126 | E |
| (Deng et al., 2006) | 70w | na | na | 20 | na | 0.9 | 93 | 210 | 127 | E |
| (Deng et al., 2006) | 70w | na | na | 30 | na | 0.9 | 96 | 218 | 126 | E |
| (Gong et al., 2007) | 80w | na | na | 5 | 2 | 1 | 49 | 484 | 882 | E |
| (Chen et al., 2008) | 33v | 0.16 | 0.12 | 1 | 0.30 | 0.8 | 152 | 286 | 88 | E |
| (Chen et al., 2008) | 33v | 0.16 | 0.12 | 1 | 0.30 | 0.8 | 255 | 498 | 95 | E |
| (Chen et al., 2008) | 33v | 0.16 | 0.12 | 1 | 0.30 | 0.8 | 561 | 1146 | 104 | E |
| (Jung et al., 2009) | 30v | 0.38 | 1.50 | 0.1 | 7.80 | 0.5 | 223 | 325 | 46 | E |
| (Liao et al., 2013) | 80w | 0.12 | 0.04 | 0.06[a] | 10 | 1.1 | 10 | 50 | 390 | E |
| (Behrooz et al., 2015) | 50w | 0.44 | 0.50 | 0.10 | 17.50 | 0.2 | 52 | 61 | 16 | E |
| (Schubert et al., 2015) | 20w | 2.32 | 1.00 | 50[a] | 45 | 0.3 | 297 | 467 | 57 | E |
| (Li and Li, 2015) | 70w | 17.53 | 0.98 | 0.10 | 8 | 3[b] | 1 | 20 | 1,629 | E |
| (Li and Li, 2015) | 70w | 17.53 | 0.98 | 0.10 | 32 | 3[b] | 1 | 12 | 881 | E |
| (Li and Li, 2015) | 70w | 17.53 | 0.98 | 4 | 8 | 3[b] | 2 | 21 | 848 | E |
| (Li and Li, 2015) | 70w | 17.53 | 0.98 | 4 | 32 | 3[b] | 2 | 13 | 530 | E |
| (Yang et al., 2015) | 70w | 17.53 | 0.16 | na | na | 1.5[b] | 6 | 28 | 330 | E |
| (Behrooz et al., 2016) | 80w | 0.99 | 0.20 | 0.10 | 10 | 0.8 | 58 | 88 | 53 | E |
| (Behrooz et al., 2016) | 80w | 0.99 | 0.20 | 0.10 | 50 | 0.8 | 32 | 45 | 39 | E |
| (Behrooz et al., 2016) | 80w | 0.99 | 0.20 | 0.100 | 30 | 0.8 | 43 | 56 | 32 | E |
| (Behrooz et al., 2016) | 80w | 0.99 | 0.20 | 5 | 30 | 0.8 | 49 | 67 | 39 | E |
| (Chen et al., 2016) | 5v | 1.10 | 1.18 | 0.2 | 6.67 | 3[b] | 46 | 86 | 87 | E |
| (Chen et al., 2016) | 11v | 1.10 | 1.18 | 1 | 6.67 | 3[b] | 49 | 92 | 88 | E |
| (Chen et al., 2016) | 15v | 1.10 | 1.18 | 2 | 6.67 | 3[b] | 61 | 120 | 95 | E |
| (S Yarra et al., 2017) | 80w | 7.07 | 1.25 | 0.10 | 20 | 19.5 | 592 | 665 | 12 | E |
| (S Yarra et al., 2017) | 80w | 7.07 | 1.25 | 0.10 | 50 | 19.5 | 513 | 540 | 5 | E |
| (S Yarra et al., 2017) | 80w | 1.00 | 0.20 | 0.10 | 30 | 0.7 | 137 | 152 | 11 | E |
| (S Yarra et al., 2017) | 76w | 1.00 | 0.20 | 0.10 | 30 | 0.7 | 33.3 | 50.2 | 51 | E |

[a] mm/min; [b] Amp; [c] E=Experimental; [d] FEM=FEM analysis; na=Not available; IP=Iron particles

## 2.2. MRE specimens fabrication process

Isotropic and anisotropic standard size (ASTM, 2011) MREs with silicone and natural rubber matrices, different weight percentages of carbonyl iron particles, and additives were fabricated. Elastomer matrix used in the mixture to fabricate anisotropic MRE samples were TAP platinum silicone is a bi-component comprised of silicone side A base and silicone side B catalyst with a weight ratio of 1:1 should be mixed to catalyze the polymer and Carbonyl iron particles with an average size of 5 micron (Sigma-Aldrich company). In addition, carbon nanofibers, type PR-19-XT-PS (Pyrograf Products, Inc.) contain less than 14,000 ppm of iron and average diameter of nanofiber is 150 nanometers (0.15 micron) was included in the mixture to further enhance the magneticfield by linking iron particles together as an additive, carbon black, type SR303 (SidRichardson carbon and energy co.) was used as an additive to increase base passive shear modulus.

In this study, maximum weight percentage of additives were used to achieve highest mechanical and magnetic properties, possible for current samples. Maximum weight percentage of carbon nanofiber (CNF's) and carbon black (CB) was determined by mixing different weight percentage of CNF's and CB into the base mixture and observing molding capability of the mixture. The different weight percentage of these composites are mixed in a beaker and then placed into a mold designed to produce ASTM (2011) standard size (1.6 in x 0.625 in x 0.2 in) MRE samples. To remove any air bubbles, the mold was kept in a vacuum chamber until the pressure reaches to -70 kpa. Lastly, the mold was placed into the electromagnet and cured under 1.2 Tesla magnetic field.

Isotropic natural rubber, type TSR 20 MRE slabs (10 in x 10 in x 0.5 in) comprised of different weight percentage of carbonyl iron particles, and carbon black were fabricated using

rubber mills. The natural rubber based MRE slabs were cut to ASTM standard size to compare with anisotropic silicone based MRE material properties. Figure 1 (a) shows natural rubber based MRE with carbonyl iron particles and carbon black. Figure 1 (b) and Figure 1 (c) shows silicone-based MREs with added iron particles, carbon black (Figure 1 (b)), and carbon nanofiber (Figure 1 (c)). Reduction in elongation was observed due to carbonyl iron particles and carbon black presence in natural rubber based MRE. Silicone-based MRE fabricated with carbon nanofiber showed smooth surface than made with carbon black. The material compositions of different tested MRE samples are summarized in Table 2.

(a) (b) (c)

**Figure 1.** ASTM standard size MRE samples fabricated with: (a) Natural rubber, carbon black; (b) TAP silicone, carbon black; (c) TAP silicone, carbon nanofiber.

**Table 2.** The Composition of Different MRE Samples.

| Test ID | Polarized particles | Additives | | Matrix | | |
|---|---|---|---|---|---|---|
| | | | | TAP Platinum Silicone | | Natural Rubber |
| | Iron Particle (g) | Carbon Black (g) | Carbon Nanofiber (g) | Side A - Base (g) | Side B - Catalyst (g) | TSR20 (g) |
| MRE-S-3 | 80.0 | 2.0 | 0.0 | 9.00 | 9.00 | 0.0 |
| MRE-S-4 | 80.0 | 1.0 | 0.2 | 9.40 | 9.40 | 0.0 |
| MRE-S-5 | 80.0 | 0.0 | 0.3 | 9.85 | 9.85 | 0.0 |
| MRE-S-6 | 75.0 | 0.0 | 1.0 | 12.00 | 12.00 | 0.0 |
| NR-S-1 | 80.0 | 0.0 | 0.0 | 0.0 | 0.0 | 20.00 |
| NR-S-4 | 77.6 | 3.0 | 0.0 | 0.0 | 0.0 | 19.40 |

A scanning Electron Microscope (SEM) (Hitachi S-4700) was used to understand the microstructure of silicone and natural rubber based MREs. The MRE samples were cut into small pieces by submerging in liquid nitrogen to achieve smooth sectional surface. Subsequently, the surface of the MRE sample was coated with a thin layer of platinum by a turbo sputter coater for SEM microstructure analysis. Figure 2(a) represents silicone MRE with 50%wt. iron particles and 5%wt. carbon black. As can be seen in Figure 2(a), iron particles were arranged in chain-like forms because MRE was cured under magnetic field. Figure 2(b) shows isotropic microstructure of natural rubber based MRE sample that was cured without a magnetic field. This sample included 80%wt. iron particles and 5%wt. carbon black.

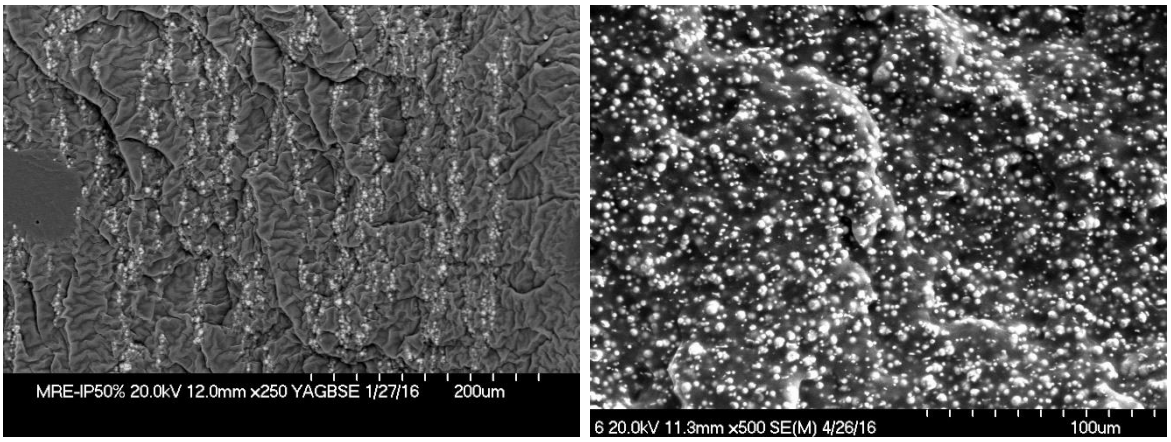


(a) (b)

**Figure 2.** Microstructure of MREs with different matrix and fabricated at different curing conditions (a) Silicone MRE cured under magnetic field (b) Natural rubber MRE cured with no applied magnetic field.

## 2.3. Experimental setup

A unique double–lap shear and compression test setup was designed and fabricated as shown in Figure 3. The test setup was used to conduct monotonic and sinusoidal cyclic experiments to characterize quasi-static (shear modulus) and dynamic (storage and loss moduli) properties of MRE samples. The test setup was designed such that the electromagnets generate a closed loop magnetic field with a strength of 0.6 Tesla at 4 amp using TDK -Lambda GEN 300-5 power supplies through the thickness of MRE samples, and was verified by ANSYS Maxwell FEA simulation. Rubber pads were used on both sides of electromagnets to apply uniform compression load over an entire surface area of MRE samples. The test setup shown in Figure 3 was used to apply a shear load, compression load, and magnetic field on the ASTM (2011) standard size MRE samples. The actuator was used to apply shear strain and inbuilt load cell and displacement transducer of the MTS testing machine were used to measure the shear force and associated strain amplitude in the MRE samples during the tests. Pre-compression handle was used to apply compression force and measured using external load cell as shown in Figure 3.

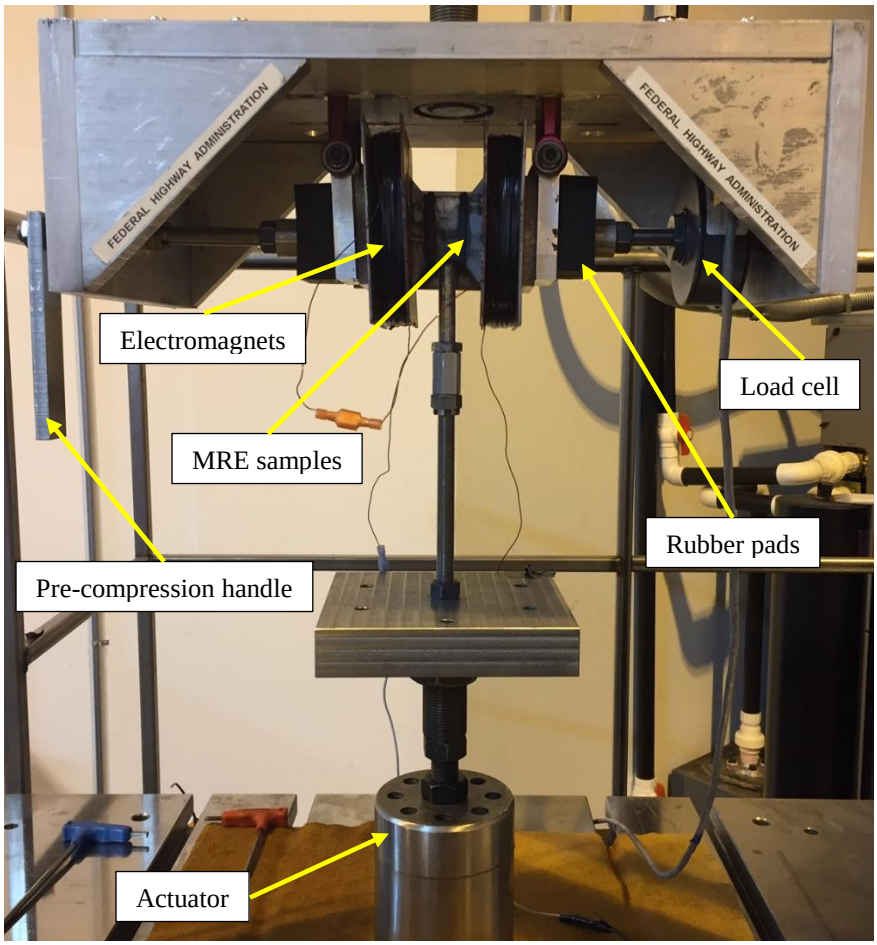


**Figure 3.** Double-lap shear and compression experimental setup.

## 2.4. Experimental results and discussion

### 2.4.1. Monotonic experiments

The main objective of monotonic experiments was to identify quasi-static material properties such as shear modulus of silicone-based and natural rubber-based MREs. Experimentally observed shear force-displacement response for the silicone and natural rubber-based samples due to monotonically applied forces are shown in Figures 4 and 5.

Specimens were subjected to monotonically increasing shear strains (10%, 30%, 50%, 75%, and 100%) with applied magnetic field intensities of 0, 0.3, 0.5, and 0.6 Tesla. Each test was repeated five times to ensure repeatability and average results are presented. Based on the

experimentally recorded response data, the MR effect (*i.e.*, change in apparent shear modulus with respect to passive mode shear modulus) is quantified by Eq. (1):

$$\%MR\ effect = \frac{G_{on} - G_{off}}{G_{off}} * 100 \quad (1)$$

where $G_{off}$ is shear modulus obtained with no applied magnetic field, and $G_{on}$ is shear modulus obtained under a magnetic field. As can be seen in Figures 4 and 5, silicone (MRE-S-5) and natural rubber (NR-S-4) based MRE samples show various levels of MR effect due to applied magnetic field under pure shear. It was observed that the MR effect can be characteristically different for cases when iron particles are distributed isotopically or anisotropically within the elastomeric compound. The MR effect reduces significantly at large strains (Table 1) for silicone-based anisotropic MRE samples due to increasing distance between iron particles, which are initially aligned in chain-like formations. Furthermore, as these chain-like formations are subjected to shear deformations, the apparent magnetic field intensity diminishes (Table 1). However, silicone MREs can be recommended for lower strain application due to high MR effect. Also, it can be observed from Table 1that the base passive shear modulus for MRE-S-5 is lower than the MRE-S-4 sample due to the absence of carbon black in MRE-S-5 sample. MRE-S-5 shows higher MR effect (Table 1) compared to MRE-S-4 sample, due to the higher weight percentage of carbon nanofiber presence in MRE-S-5 sample. Therefore, it may be concluded that carbon black and carbon nanofibers served their purpose as intended. Carbon black was used to improve base passive shear modulus and carbon nanofiber was used to link iron particles together and to improve magnetic permeability of magnetorheological materials (Luo et al., 2015). Less iron content (75g) in MRE-S-6 leads to reduced MR effect than MRE-S-5 which

has 80g even though MRE-S-6 has 1g carbon nanofiber compared to 0.3g in MRE-S-5. The, iron content influences MR effect more than carbon nanofiber.

In case of natural rubber-based isotropic MRE sample (NR-S-4), it was observed that the MR effect for shear modulus was very stable (Table 4). The MR effect for 0.1Hz frequency remained nearly constant (approximately 30%) for all strain amplitudes and with no axial force. The constant MR effect on shear modulus is attributed to the nominally isotropic material composition. The random distribution of iron particles allows the formation of alternative and desirable magnetic field paths irrespective of the deformation field within the material.

Figure 6 shows the MR effect of natural rubber based MRE (NR-S-4) under combined loading. Natural rubber MRE (NR-S-4) demonstrated a better MR effect under axial force, however, the MR effect reduced with increasing strains. It was observed that at 10% and 100% strain with 100 psi axial stress, the MR effects were 92% and 33% (Table 5) respectively. This observation is attributed to the fact that axial force reduces the spacing between iron particles, thus increases forces, thereby enhancing the magnetic field. At constant axial force, increased strain pulls iron particles away from each other thus causes reduced MR effects shown in Table 5. However, at 75% strain the observed MR effect was 26% which is less than the MR effect (33%) at 100%. Test conditions, such as, temperature of the room, wait time to run the test, timing to switch on power supplies to create magnetic field, distribution of iron particles while fabricating natural rubber based isotropic MRE's and arrangement of iron particles due to applied magnetic field are possible reasons. The effective shear modulus values for all tested samples are summarized in Table 3 through Table 5.

**Table 3.** Effective Shear Modulus Values of Different Silicone MREs under Pure Shear.

| Effective shear modulus (psi) | | | | | | | | | | | | |
|---|---|---|---|---|---|---|---|---|---|---|---|---|
| | MRE-S-3 | | | MRE-S-4 | | | MRE-S-5 | | | MRE-S-6 | | |
| Shear strain | 10% | 30% | 50% | 10% | 30% | 50% | 10% | 30% | 50% | 10% | 30% | 50% |
| $G_{off}$ | 74.5 | 79.2 | 85.0 | 86.8 | 84.2 | 91.2 | 79.6 | 62.8 | 68.0 | 72.2 | 78.0 | 78.6 |
| $G_{on}$ | 94.1 | 86.1 | 86.3 | 98.9 | 91.5 | 93.6 | 104.3 | 78.4 | 76.1 | 96.0 | 89.2 | 83.4 |
| %MR effect | 26 | 9 | 1 | 14 | 9 | 3 | 31 | 25 | 12 | 33 | 14 | 6 |

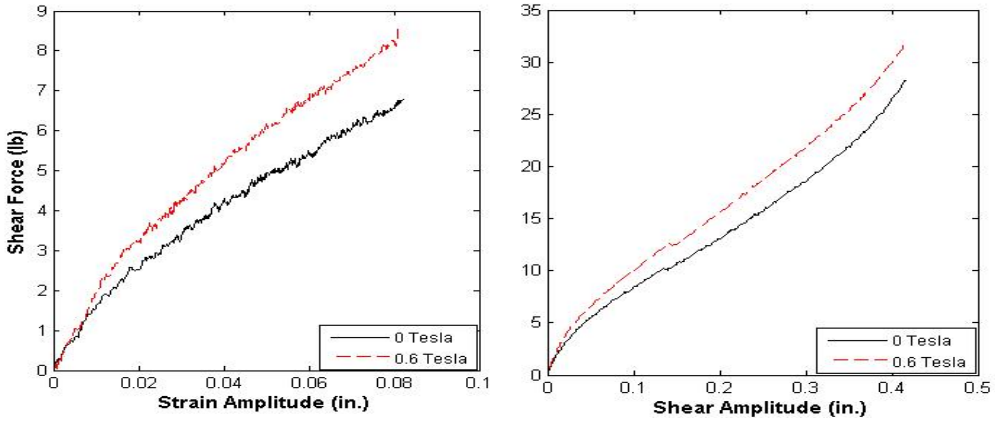


(a) 10% Shear strain (b) 50% Shear strain

**Figure 4.** Monotonic force–displacement curves for silicone based MRE (MRE-S-5) under pure shear.

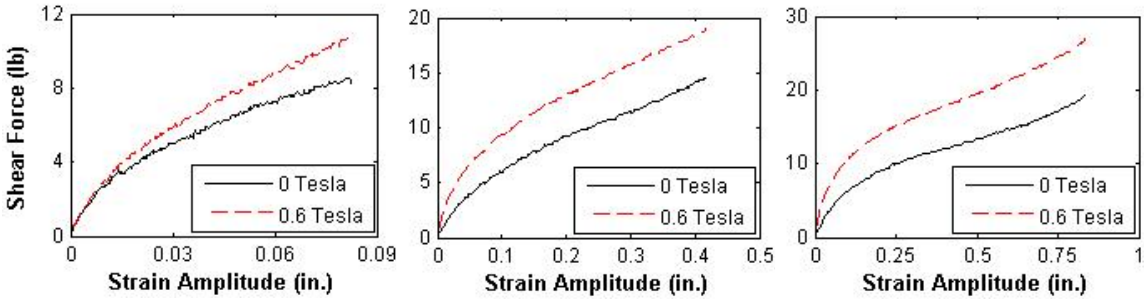


(a) 10% Shear strain (b) 50% Shear strain (c) 100% Shear strain

**Figure 5.** Monotonic force-displacement curves for natural rubber based MRE (NR-S-4) under pure shear.

**Table 4.** Effective Shear Modulus for Different Natural Rubber MREs under Pure Shear.

| Effective shear modulus (psi) | | | | | | | | | | | |
|---|---|---|---|---|---|---|---|---|---|---|---|
| | NR-S-1 | | | | | NR-S-4 | | | | | |
| Shear strain | 10% | 30% | 50% | 75% | 100% | 10% | 30% | 50% | 75% | 100% | 150% |
| $G_{off}$ | 202.2 | 60.9 | 40.0 | 33.6 | 25.5 | 100.1 | 50.7 | 34.7 | 27.0 | 23.1 | 22.0 |
| $G_{on}$ | 217.2 | 69.9 | 51.8 | 41.5 | 32.5 | 132.1 | 64.4 | 43.7 | 35.0 | 30.5 | 29.4 |
| %MR effect | 7 | 15 | 29 | 23 | 28 | 32 | 27 | 26 | 30 | 32 | 33 |

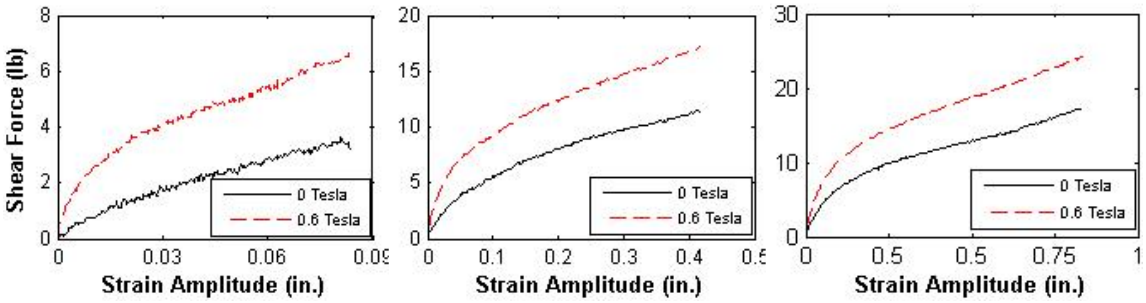


(a) 10% Shear strain (b) 50% Shear strain (c) 100% Shear strain

**Figure 6.** Monotonic force-displacement curves for natural rubber based MRE (NR-S-4) under combined loading, 100psi axial stress.

**Table 5.** Effective Shear Modulus Values of NR-S-4 under Combined Compressive and Shear loading.

| Effective Shear Modulus (psi) | | | | | |
|---|---|---|---|---|---|
| | NR-S-4 | | | | |
| Shear strain | 10% | 30% | 50% | 75% | 100% |
| $G_{off}$ | 40.9 | 31.8 | 27.4 | 26.3 | 20.9 |
| $G_{on}$ | 78.7 | 50.6 | 39.5 | 33.1 | 27.7 |
| %MR effect | 92 | 59 | 44 | 26 | 33 |

### 2.4.2. Sinusoidal cyclic experiments

Monotonic test results demonstrated that the NR-S-4 was the best candidate for further investigation. A series of sinusoidal cyclic experiments were conducted to study viscoelastic

properties and effective stiffness of NR-S-4 sample under varying strain amplitudes (10%, 30%, 50%, 75%, 100%, 125%, and 150%), test frequencies (0.1 Hz, 0.5Hz, 1Hz, 3Hz, 5Hz, 7Hz, and 10Hz), and magnetic field intensities of 0, 0.3, 0.5, and 0.6 Tesla. The loading and unloading cycles were repeated until the load-displacements curve stabilized. The storage and loss moduli were obtained by using Eqs. (2) and (3), respectively. The effective stiffness was determined from the second cycle of force-displacement hysteresis by equation 17.8-1 of ASCE-7-16 (2016) shown in Eq. (4). The effective damping was determined from the force-displacement loop by using equation 17.8-2 of ASCE-7-16 (2016) shown in Equation (5), below:

$$G' = \tau/\gamma \cos\delta \tag{2}$$

$$G'' = \tau/\gamma \sin\delta \tag{3}$$

$$k_{eff} = \frac{|F^+| + |F^-|}{|\Delta^+| + |\Delta^-|} \tag{4}$$

$$\beta_{eff} = \frac{2}{\pi}\left[\frac{E_{loop}}{k_{eff}(|\Delta^+| + |\Delta^-|)^2}\right] \tag{5}$$

where δ is the phase lag measured from the shear stress and shear strain responses. $F^+$ and $F^-$ are the positive and negative forces, at $\Delta^+$ and $\Delta^-$, respectively. $E_{loop}$ is the energy dissipated per cycle, $k_{eff}$ is the effective stiffness, and $\Delta^+$ and $\Delta^-$ in Eq. (5) are peak displacements in force-displacement hysteresis curve.

The effect of frequency on storage and loss moduli of NR-S-4 is shown in Figure 7. Both moduli increase with increasing test frequency, on the other hand, MR effect reduces with increasing frequencies. As can be seen in Figure 8, the NR-S-4 sample shows an increase in magnetic field results in increase in storage and loss moduli for any given strain amplitude.

Unlike silicone MREs, the natural rubber-based MREs shows a uniform MR effect with increasing strain amplitudes. For storage modulus, NR-S-4 sample achieved approximately 41%, 47%, 56%, 74%, and 55% MR effect at 10%, 30% 50% 100% and 125% strain amplitudes, respectively. For the loss modulus, experimentally determined MR effects were 60%, 52%, 50%, 57%, and 50% at 10%, 30%, 50%, 100%, and 125% strain amplitudes, respectively, which implies a constant damping capacity for all strain amplitudes.

Figure 9 and Figure 10, show the shear force-deformation response for different strain amplitudes (10%, and 125%), test frequencies (0.1 Hz, 3 Hz, 7Hz, and 10Hz) and applied magnetic fields. Accordingly, the effective stiffness and effective damping values show increasing trend with increasing magnetic field intensity. Effective stiffness increases with increased loading rate. However, effective damping values show decreasing trend with increased loading rate. Table 6 summarizes the effective stiffness and damping values with the corresponding MR effect. The MR effect of effective stiffness show decreasing trend with increased frequency. Also, it was observed that the effective damping for small strains show increasing trend while it shows nearly unaffected for large strains. The MR effect on effective stiffness at different strains depend on the formation of magnetic paths and magnetic intensity of those paths due to randomly distributed iron particles.

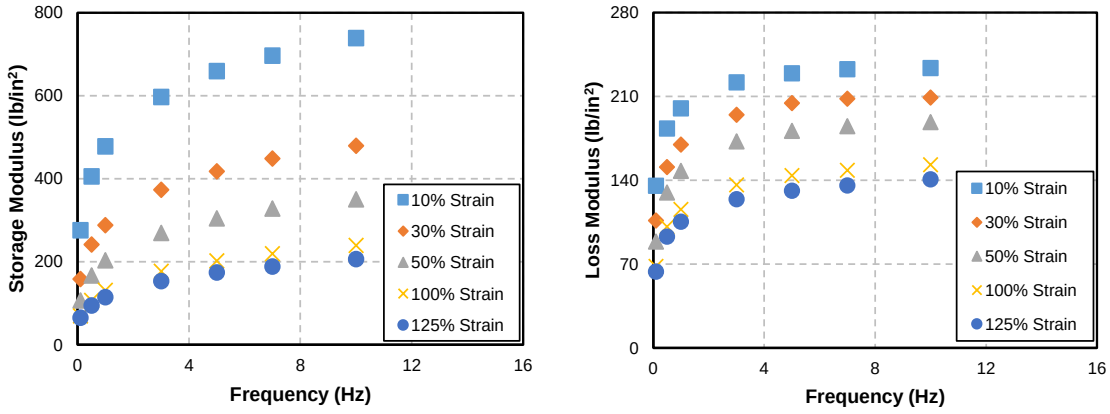


(a) (b)

**Figure 7.** Effect of frequency on the rheological properties of NR-S-4 at zero magnetic fields: (a) Storage modulus, and (b) Loss modulus.

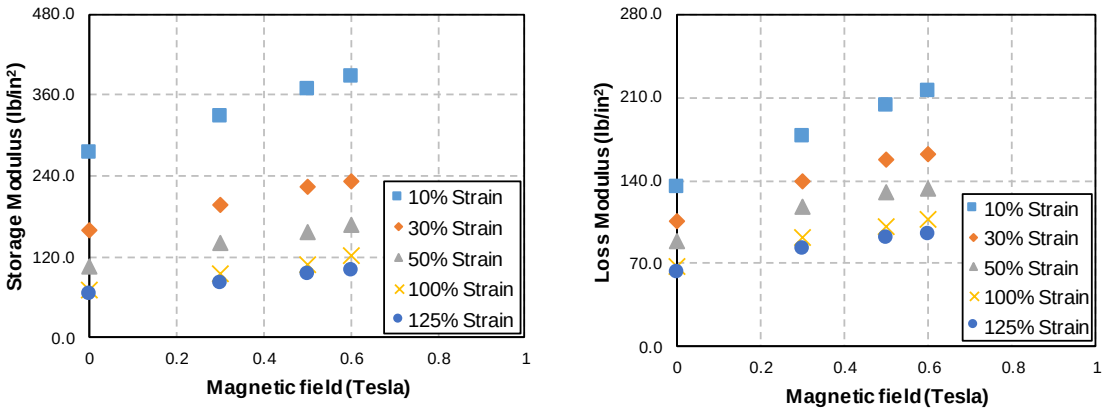


(a) (b)

**Figure 8.** Effect of magnetic field on the rheological properties of NR-S-4 at 0.1 Hz: (a) Storage modulus, and (b) Loss modulus.

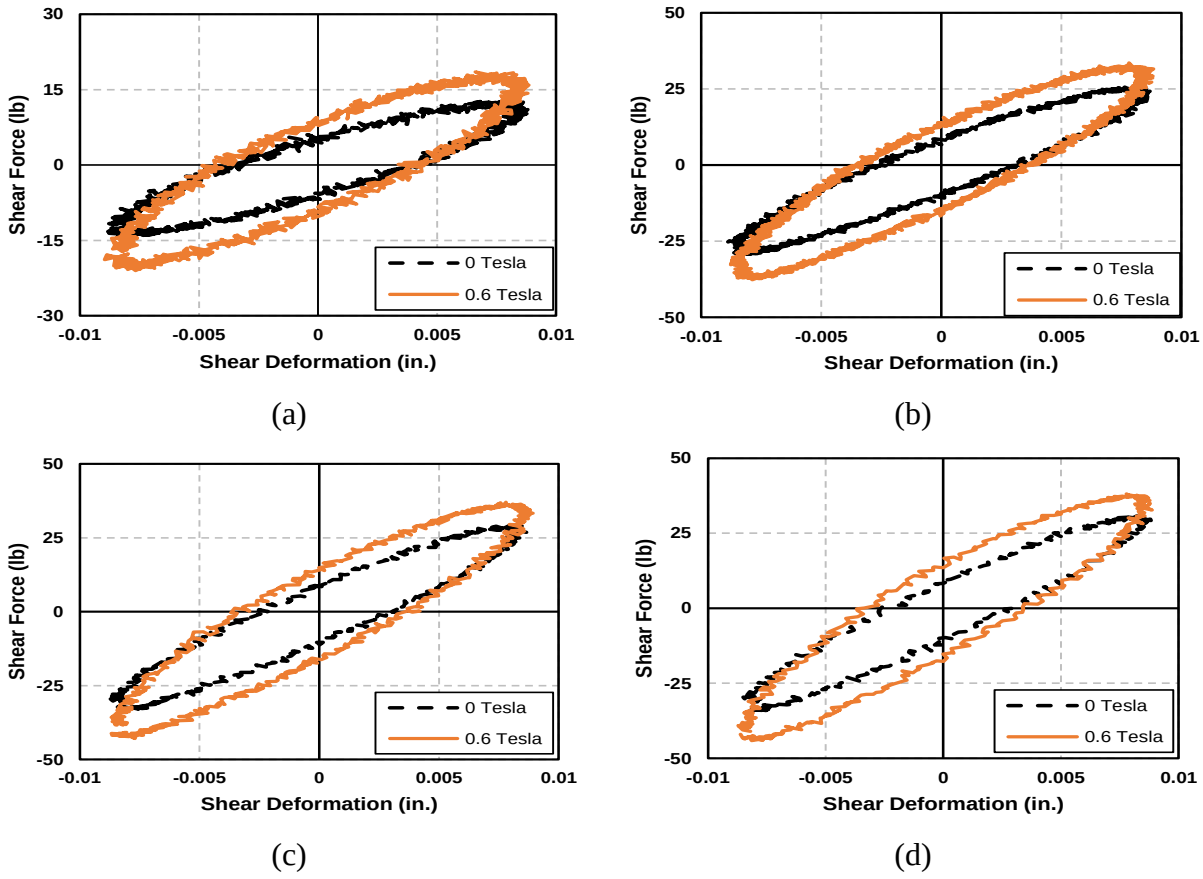


**Figure 9.** Force versus displacement hysteresis of NR-S-4 at 10% shear strain for different frequencies: (a) 0.1 Hz; (b) 3 Hz; (c) 7 Hz; (d) 10 Hz.

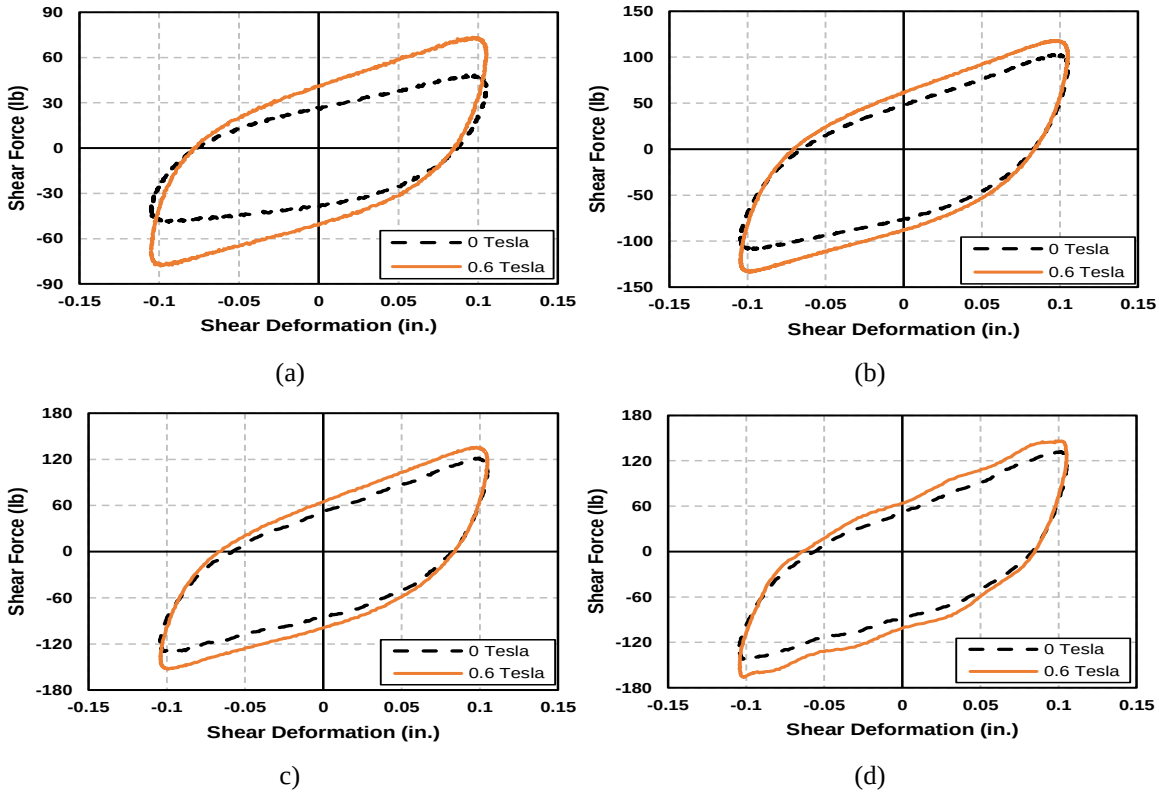


**Figure 10.** Force versus displacement hysteresis of NR-S-4 at 125% shear strain for different frequencies: (a) 0.1 Hz; (b) 3 Hz; (c) 7 Hz; (d) 10 Hz.

**Table 6.** Summary of Effective Stiffness and Damping Values and their Corresponding MR effect of NR-S-4.

| Effective stiffness (kip/in) | | | | | | Effective damping | | | |
|---|---|---|---|---|---|---|---|---|---|
| Frequency, Hz | 0.1 | 3 | 7 | 10 | | 0.1 | 3 | 7 | 10 |
| 10% Shear Strain | | | | | | | | | |
| $K_{off}$ | 1,795 | 3,587 | 3,822 | 4,166 | $\beta_{eff\ -\ off}$ | 0.12 | 0.09 | 0.07 | 0.07 |
| $K_{on}$ | 2,772 | 4,544 | 5,159 | 5,167 | $\beta_{eff\ -\ on}$ | 0.14 | 0.12 | 0.10 | 0.11 |
| % MR effect | 54 | 27 | 35 | 24 | | 17 | 33 | 43 | 57 |
| 30% Shear strain | | | | | | | | | |
| $K_{off}$ | 1,119 | 2,277 | 2,703 | 2,895 | $\beta_{eff\ -\ off}$ | 0.17 | 0.14 | 0.12 | 0.11 |
| $K_{on}$ | 1,654 | 2,807 | 3,039 | 3,271 | $\beta_{eff\ -\ on}$ | 0.18 | 0.15 | 0.15 | 0.14 |
| % MR effect | 48 | 23 | 12 | 13 | | 6 | 7 | 25 | 27 |
| 50% Shear Strain | | | | | | | | | |
| $K_{off}$ | 899 | 1,775 | 2,030 | 2,161 | $\beta_{eff\ -\ off}$ | 0.19 | 0.17 | 0.16 | 0.15 |
| $K_{on}$ | 1,236 | 2,129 | 2,352 | 2,543 | $\beta_{eff\ -\ on}$ | 0.20 | 0.18 | 0.17 | 0.16 |
| % MR effect | 37 | 20 | 16 | 18 | | 5 | 6 | 6 | 7 |
| 75% Shear Strain | | | | | | | | | |
| $K_{off}$ | 892 | 1,609 | 1,833 | 1,922 | $\beta_{eff\ -\ off}$ | 0.21 | 0.17 | 0.16 | 0.16 |
| $K_{on}$ | 1,004 | 1,555 | 1,753 | 1,956 | $\beta_{eff\ -\ on}$ | 0.21 | 0.21 | 0.20 | 0.19 |
| %MR effect | 13 | 3 | 4 | 2 | | 0 | 24 | 25 | 19 |
| 100% Shear Strain | | | | | | | | | |
| $K_{off}$ | 561 | 1,210 | 1,438 | 1,530 | $\beta_{eff\ -\ off}$ | 0.22 | 0.21 | 0.19 | 0.19 |
| $K_{on}$ | 932 | 1,498 | 1,664 | 1,735 | $\beta_{eff\ -\ on}$ | 0.25 | 0.22 | 0.20 | 0.20 |
| % MR effect | 66 | 24 | 16 | 13 | | 14 | 5 | 5 | 5 |
| 125% Shear Strain | | | | | | | | | |
| $K_{off}$ | 510 | 1,083 | 1,253 | 1,362 | $\beta_{eff\ -\ off}$ | 0.24 | 0.22 | 0.21 | 0.20 |
| $K_{on}$ | 775 | 1,289 | 1,461 | 1,540 | $\beta_{eff\ -\ on}$ | 0.26 | 0.23 | 0.22 | 0.22 |
| % MR effect | 52 | 19 | 17 | 13 | | 8 | 5 | 5 | 10 |

To evaluate the effect of compressive stress on the behavior of natural rubber MRE (NR-S-4), a constant compression force of 100lb (100psi) was applied and the tests were repeated for all

strain amplitudes, frequencies, and magnetic fields described previously. Figure 11 shows the effect of frequency on storage and loss moduli under combined loads. As can be seen, both moduli increase with increased frequency. The effect of magnetic field on storage and loss moduli is shown in Figure 12. Increased magnetic field yields increased storage and loss moduli for any given strain amplitude under a compression stress of 100psi. Storage and loss moduli of natural rubber MRE (NR-S-4) sample showed nearly constant MR effect (65% and 55% for storage and loss, respectively) over a wide range of strain amplitudes from 10% to 150%.

Figure 13 and 14, show the cyclic shear force-deformation relationship for 10% and 150% strain amplitudes, and different frequencies (0.1 Hz, 3 Hz, 7Hz, and 10Hz) with varying magnetic field intensities (0 and 0.6 Tesla). The effective stiffness increases with increasing magnetic field intensity for any test frequency and strain amplitude. Also, it was observed that the effective stiffness shows increasing trend with increased frequency at any given strain. The MR effect was 29% for the frequency of 10 Hz and strain amplitude of 150%. As shown in Table 7, the MR effect of effective damping shows increasing trend with increasing frequency at 10% strain. However effective damping, Eq. (5), MR effect was insignificant for large strains (Table 7). Summary of effective stiffness and damping values with their corresponding MR effect are presented in table 7. The MR effect of effective stiffness reduces with increased frequency. In addition to desirable magnetic field paths due to uniformly dispersed iron particles, the compression force brings iron particles closer to each other and improves the strength of the magnetic field that results improved MR effect.

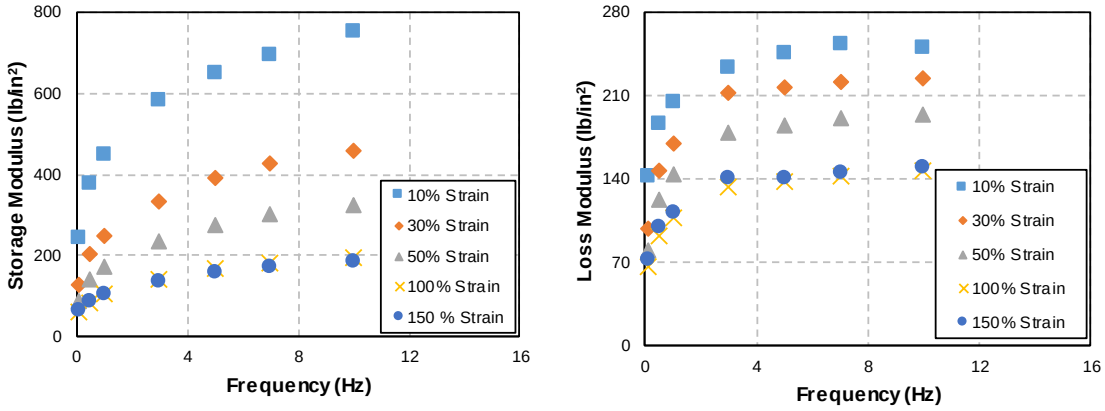


(a) (b)

**Figure 11.** Effect of frequency on the rheological properties of NR-S-4 at zero magnetic field and compressive pressure of 100psi: (a) Storage modulus, and (b) Loss modulus.

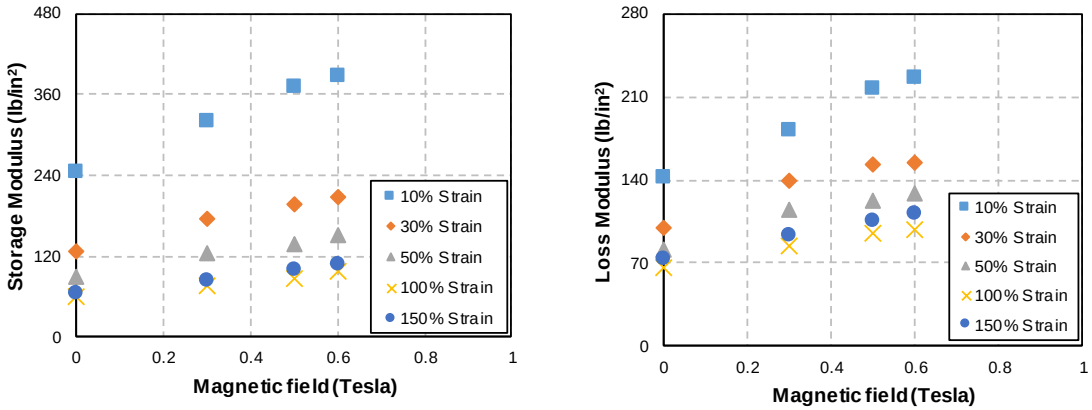


(a) (b)

**Figure 12.** Effect of magnetic field on the rheological properties of NR-S-4 at 0.1 Hz and compressive pressure of 100psi: (a) Storage modulus, and (b) Loss modulus.

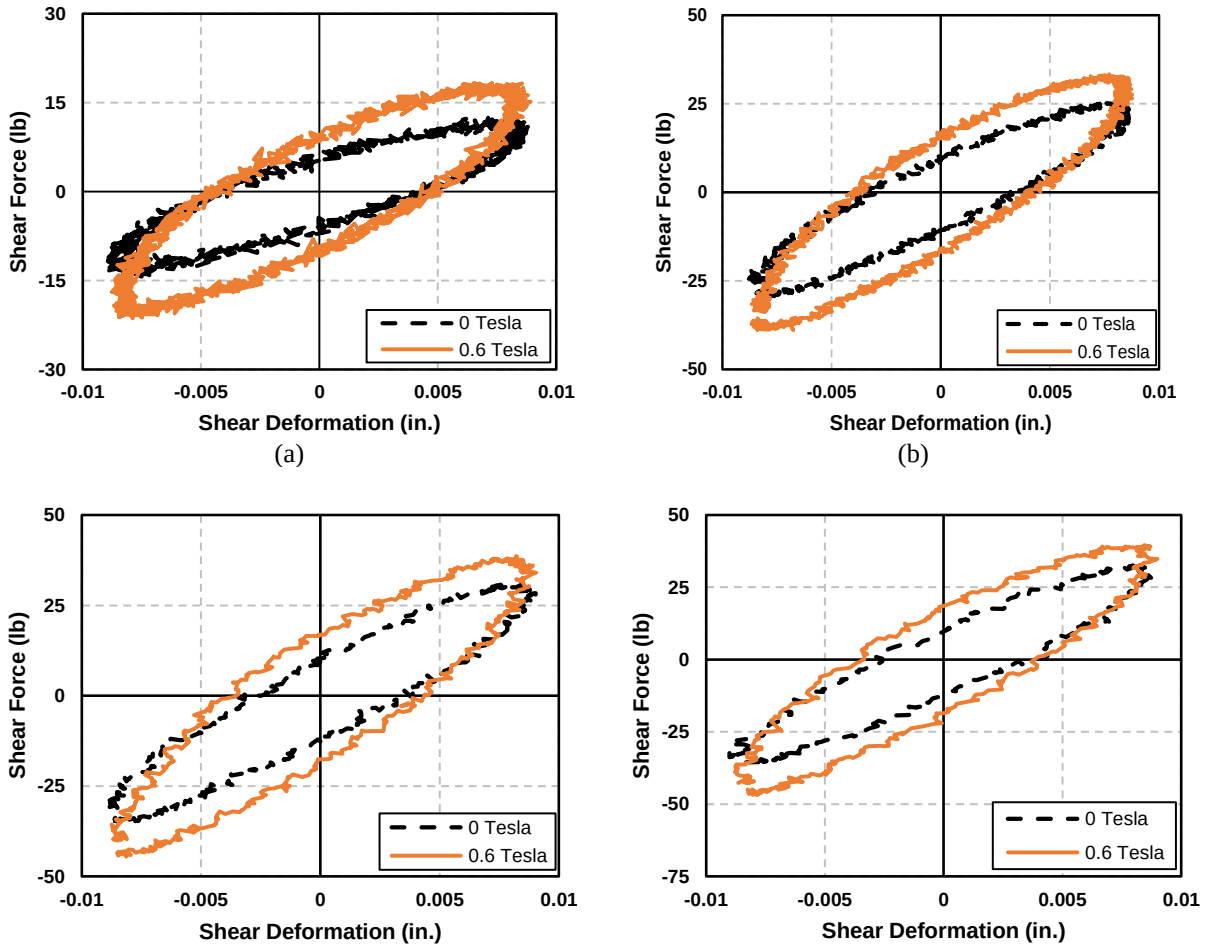


**Figure 13.** Force versus displacement hysteresis of NR-S-4 at 10% shear strain and compressive pressure of 100psi for different frequencies: (a) 0.1 Hz; (b) 3 Hz; (c) 7 Hz; (d) 10 Hz.

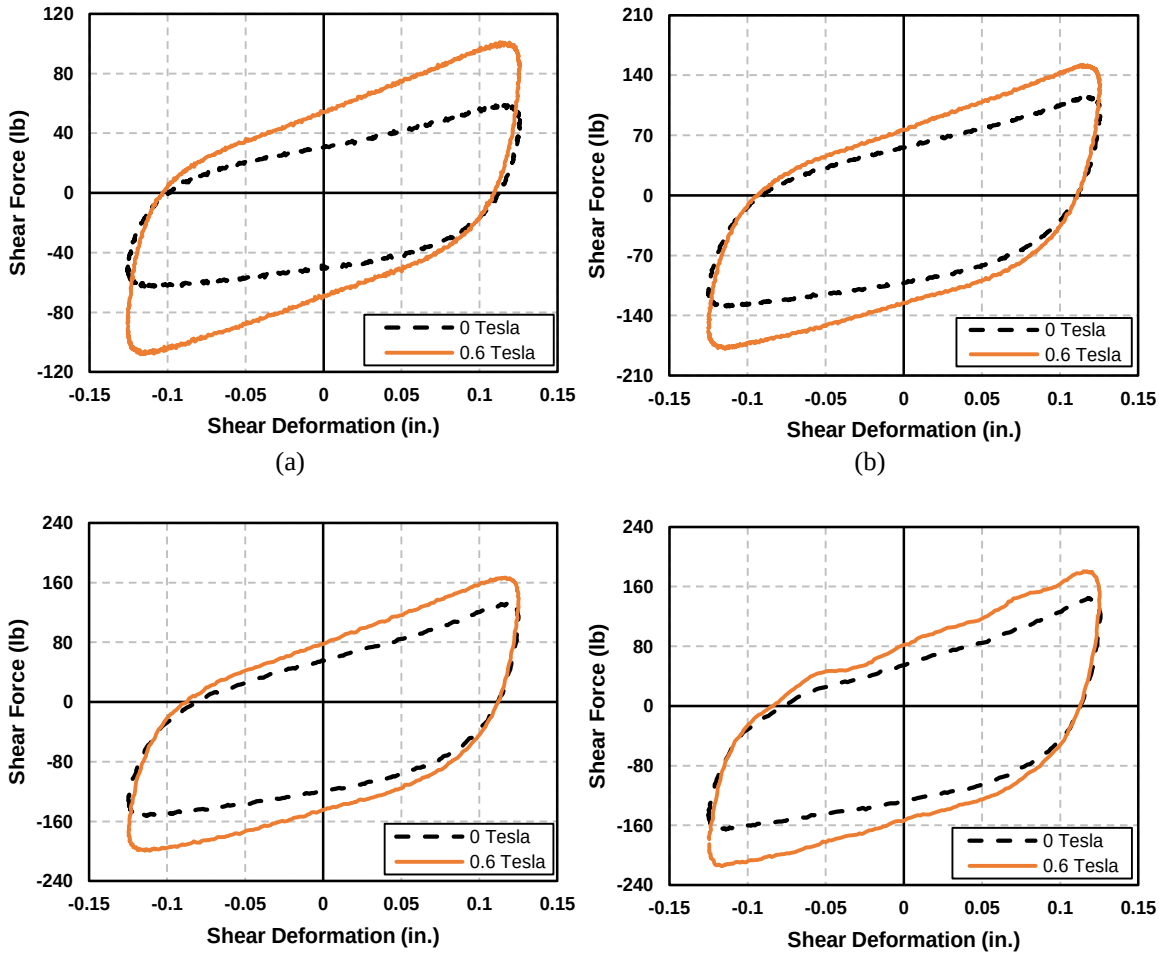


**Figure 14.** Force versus displacement hysteresis of NR-S-4 at 150% shear strain and compressive pressure of 100psi for different frequencies: (a) 0.1 Hz; (b) 3 Hz; (c) 7 Hz; (d) 10 Hz.

**Table 7.** Summary of Effective Stiffness and Damping Values and their Corresponding MR effect of NR-S-4.

| Compression force (p=100lb) | | | | | | | | | |
|---|---|---|---|---|---|---|---|---|---|
| Effective stiffness (kip/in.) | | | | | | Effective damping | | | |
| Frequency, Hz | 0.1 | 3 | 7 | 10 | | 0.1 | 3 | 7 | 10 |
| 10% Shear Strain | | | | | | | | | |
| $K_{off}$ | 1,832 | 3,750 | 4,070 | 4,086 | $\beta_{eff\ -\ off}$ | 0.17 | 0.10 | 0.09 | 0.08 |
| $K_{on}$ | 2,613 | 4,487 | 5,087 | 5,295 | $\beta_{eff\ -\ on}$ | 0.17 | 0.13 | 0.13 | 0.13 |
| % MR effect | 43 | 20 | 25 | 30 | | 0 | 30 | 44 | 63 |
| 30% Shear strain | | | | | | | | | |
| $K_{off}$ | 1,007 | 2,261 | 2,728 | 2,903 | $\beta_{eff\ -\ off}$ | 0.19 | 0.16 | 0.15 | 0.14 |
| $K_{on}$ | 1,539 | 2,793 | 3,189 | 3,281 | $\beta_{eff\ -\ on}$ | 0.20 | 0.17 | 0.16 | 0.17 |
| % MR effect | 53 | 24 | 17 | 13 | | 5 | 6 | 7 | 21 |
| 50% Shear Strain | | | | | | | | | |
| $K_{off}$ | 780 | 1,646 | 2,054 | 2,046 | $\beta_{eff\ -\ off}$ | 0.22 | 0.20 | 0.18 | 0.19 |
| $K_{on}$ | 1,115 | 2,053 | 2,390 | 2,482 | $\beta_{eff\ -\ on}$ | 0.22 | 0.21 | 0.19 | 0.19 |
| % MR effect | 43 | 25 | 16 | 21 | | 0 | 5 | 6 | 0 |
| 75% Shear Strain | | | | | | | | | |
| $K_{off}$ | 597 | 1,369 | 1,614 | 1,673 | $\beta_{eff\ -\ off}$ | 0.24 | 0.22 | 0.21 | 0.21 |
| $K_{on}$ | 910 | 1,619 | 1,844 | 1,899 | $\beta_{eff\ -\ on}$ | 0.26 | 0.23 | 0.22 | 0.23 |
| %MR effect | 52 | 17 | 14 | 14 | | 8 | 5 | 5 | 10 |
| 100% Shear Strain | | | | | | | | | |
| $K_{off}$ | 488 | 1,105 | 1,323 | 1,379 | $\beta_{eff\ -\ off}$ | 0.26 | 0.24 | 0.22 | 0.23 |
| $K_{on}$ | 779 | 1,365 | 1,547 | 1,685 | $\beta_{eff\ -\ on}$ | 0.27 | 0.25 | 0.24 | 0.23 |
| % MR effect | 60 | 24 | 17 | 22 | | 4 | 4 | 9 | 0 |
| 150% Shear Strain | | | | | | | | | |
| $K_{off}$ | 524 | 1,053 | 1,230 | 1,313 | $\beta_{eff\ -\ off}$ | 0.37 | 0.36 | 0.35 | 0.35 |
| $K_{on}$ | 909 | 1,456 | 1,585 | 1,692 | $\beta_{eff\ -\ on}$ | 0.41 | 0.37 | 0.35 | 0.36 |
| % MR effect | 73 | 38 | 29 | 29 | | 10 | 3 | 0 | 3 |

## 2.5. Summary and conclusions

Different anisotropic silicone-based and isotropic natural rubber-based MREs were fabricated. Monotonic and cyclic experiments were conducted to investigate the static and dynamic properties of MREs. Monotonic experimental results demonstrated that silicone-based MREs are a good choice for lower strain applications due to high MR effect. However, the MR effect reduces with increasing shear deformations due to the increased distance between iron particles that reduces magnetic field flow intensity. Carbon nanofiber improved the performance of silicone-based anisotropic MRE (MRE-S-5) and showed 31% and 12% MR effect at 10% and 50% shear strains, respectively. This is attributed to the magnetic permeability of carbon nanofibers, which resulted in higher MR effects.

Natural rubber-based MREs demonstrated constant MR effect (around 30%) at all strain levels due to random dispersion of distributed iron particles that allows the formation of alternative magnetic field paths irrespective of the deformation. For natural rubber MRE (NR-S-4) at 10% and 100% strain with 100 psi axial stress, the achieved MR effects were 92% and 33% (Table 5) compared to 32% and 32% (Table 4) under no axial stress, respectively. This observation is attributed to the fact that axial force, hence axial deformation, reduces the spacing between iron particles, thereby enhancing the magnetic field.

Further, sinusoidal cyclic experiments of NR-S-4 for both cases: (i) without compression, and (ii) with compression for any given strain and/or frequency, the effective stiffness and damping showed increasing trend with increased magnetic field intensity. The MR effect on the effective stiffness reduced with increased frequency. The MR effect on the effective damping for NR-S-4 sample was 57% at 10% shear strain and 10 Hz test frequency. Also, it was observed that the MR effect on the effective damping varied from 2 to 13% for all other shear strains

(30%, 50%, 75%, 100%, and 125%) and applied frequencies (0.1 Hz, 3 Hz, 7Hz, and 10 Hz) without compression load (Table 6). However, 63% MR effect was observed at 10% strain at 10Hz test frequency under a uniform compression stress of 100psi. For all other strains and frequencies, MR effect on the effective damping was varied between 3 to 21%.

## 2.6. Acknowledgements

This project was funded by the Federal Highway Administration under the contract number DTFH61-13-C-00020. The authors would like to express their gratitude to Advanced Materials and Devices, Inc., and to Scougal Rubber Corporation for helping with this effort. The authors also acknowledge employees of Advanced Materials and Devices, Dr. Barkan Kavlicoglu and Mr. Kyle Willens. The authors also wish to thank Mr. Pete Etcheverry of Scougal Rubber Corporation. Finally, the authors would like to thank undergraduate assistants Mr. David Mar and Mr. Nathan Pinuelas.

## 2.7. References

American Society of Civil Engineers (2016) Minimum design loads for buildings and other structures. ISBN: 9780784414248.

ASTM (2011) Standard Guide for Dynamic Testing of Vulcanized Rubber and Rubber-Like Materials Using Vibratory Methods, ASTM International, http://dx.doi.org/10.1520/D5992-96R11.

Behrooz M, Wang X and Gordaninejad F (2013) Modeling of a new magnetorheological elastomer-based isolator. In Proc. SPIE (Vol. 8688, p. 86880Z).

Behrooz M, Sutrisno J, Zhang L, et al. (2015) Behavior of magnetorheological elastomers with coated particles. Smart Materials and Structures, 24(3), p.035026.

Behrooz M, Yarra S, Marc D, et al. (2016) A self-sensing magnetorheological elastomer-based adaptive bridge bearing with a wireless data monitoring system. In Proc. of SPIE Vol (Vol. 9803, pp. 98030D-1).

Chen L, Gong XL, Jiang WQ, et al. (2007) Investigation on magnetorheological elastomers based on natural rubber. Journal of Materials Science. 42(14), 5483-9.

Chen L, Gong XL and Li WH (2008) Effect of carbon black on the mechanical performances of magnetorheological elastomers. Polymer Testing, 27(3), pp.340-345.

Chen S, Wang X, Zhang Z, et al. (2016) Optimal design of laminated-MRE bearings with multi-scale model. Smart Materials and Structures, 25(10), p.105037.

Davis LC (1999) Model of magnetorheological elastomers. Journal of Applied Physics, 85(6), pp.3348-3351.

Deng HX, Gong XL and Wang LH (2006) Development of an adaptive tuned vibration absorber with magnetorheological elastomer. Smart materials and structures, 15(5), p. N111.

Dong X, Ma N, Ou J, et al. (2013) Predicating magnetorheological effect of magnetorheological elastomers under normal pressure. In *Journal of Physics: Conference Series*, (Vol. 412, No. 1, p. 012035).

Du H, Li W and Zhang N (2011) Semi-active variable stiffness vibration control of vehicle seat suspension using an MR elastomer isolator. Smart materials and structures, 20(10):105003.

Fu J, Zheng X, Yu M, et al. (2013) A new magnetorheological elastomer isolator in shear-Compression mixed mode. In Advanced Intelligent Mechatronics (AIM), 2013 IEEE/ASME International Conference on (pp. 1702-1706).

Fu J, Li P, Liao G, et al. (2017) Development and Dynamic Characterization of a Mixed Mode Magnetorheological Elastomer Isolator. *IEEE Transactions on Magnetics*, *53*(1), pp.1-4.

Ginder JM, Nichols ME, Elie LD, et al. (1999) Magnetorheological elastomers: properties and applications. In Smart Structures and Materials, Vol. 3675, pp. 131-139

Ginder JM, Nichols ME, Elie LD, et al. (2000) Controllable-stiffness components based on magnetorheological elastomers. In Proceedings-SPIE the International Society for Optical Engineering (pp. 418-425).

Gong XL, Zhang XZ and Zhang PQ (2005) Fabrication and characterization of isotropic magnetorheological elastomers. Polymer testing, 24(5):669-76.

Gong XL, Chen L and Li JF (2007) Study of utilizable magnetorheological elastomers. International Journal of Modern Physics B, 21(28n29), pp.4875-4882.

Hang Qu, Miao Yu, Jie Fu, et al. (2017) Enhanced field-dependent conductivity of magnetorheological gels with low-doped carbon nanotubes. Smart Materials and Structures, 26(10), p.105026

Hoang N, Zhang N and Du H (2010) An adaptive tunable vibration absorber using a new magnetorheological elastomer for vehicular powertrain transient vibration reduction. Smart Materials and Structures, 20(1), p.015019.

Jolly MR, Carlson JD, Muñoz BC, et al. (1996) The magneto viscoelastic response of elastomer composites consisting of ferrous particles embedded in a polymer matrix. Journal of Intelligent Material Systems and Structures, 7(6), pp.613-622.

Jung HJ, Lee SJ, Jang DD, et al. (2009) Dynamic characterization of magneto-rheological elastomers in shear mode. IEEE transactions on magnetics, 45(10), pp.3930-3933.

Liao G, Gong X and Xuan S (2013) Influence of shear deformation on the normal force of magnetorheological elastomer. Materials Letters, 106, pp.270-272.

Li Y and Li J (2014) Base isolator with variable stiffness and damping: design, experimental testing and modelling. In ST Smith (ed.), 23rd Australasian Conference on the Mechanics of Structures and Materials (ACMSM23), vol. II, pp. 913-918. ISBN: 9780994152008.

Li Y, Li J, Li W, et al. (2013) Development and characterization of a magnetorheological elastomer based adaptive seismic isolator. Smart Materials and Structures, 22(3), p.035005.

Lokander M and Stenberg B (2003) Performance of isotropic magnetorheological rubber materials. *Polymer Testing*, *22*(3), pp.245-251.

Lujie Z, Miao Y, Jie F, et al. (2017) A miniature MRE isolator for lateral vibration suppression of bridge monitoring equipment: design and verification. Smart Materials and Structures, 26(4), p.047001.

Luo C, Fu Q and Pan C (2015) Strong magnetic field-assisted growth of carbon nanofibers and its microstructural transformation mechanism. Scientific reports, 5, p.9062.

Nayak B, Dwivedy SK and Murthy KS (2015) Fabrication and characterization of magnetorheological elastomer with carbon black. *Journal of Intelligent Material Systems and Structures*, *26*(7), pp.830-839.

Popp KM, Kröger M, Li WH, et al. (2010) MRE properties under shear and squeeze modes and applications. *Journal of Intelligent Material Systems and Structures*, *21*(15), pp.1471-1477.

Ruddy C, Ahearne E and Byrne G (2012) A review of magnetorheological elastomers: properties and applications. Advanced Manufacturing Science (AMS) Research. http://www. ucd. ie/mecheng/ams/news_items/Cillian% 20Ruddy. pdf Accessed, 20.

Schubert G and Harrison P (2015) Large-strain behaviour of magneto-rheological elastomers tested under uniaxial compression and tension, and pure shear deformations. Polymer Testing, 42, pp.122-134.

Schumann M, Borin D Y, Huang S, et al. (2017) A characterization of the magnetically induced movement of NdFeB-particles in magnetorheological elastomers. Smart Materials and Structures, 26(9), p.095018.

Shen Y, Golnaraghi MF and Heppler GR (2004) Experimental research and modeling of magnetorheological elastomers. Journal of Intelligent Material Systems and Structures, 15(1), pp.27-35.

Stepanov GV, Abramchuk SS, Grishin DA, et al. (2007) Effect of a homogeneous magnetic field on the viscoelastic behavior of magnetic elastomers. Polymer, 48(2), pp.488-495.

Tu JW, Tu B, Mei ST, et al. (2014) Research on new type MRE isolator and its mechanical model. Materials Research Innovations, 18(sup2), pp. S2-552.

Wen Q, Wang Y, and Gong X (2017) The magnetic field dependent dynamic properties of magnetorheological elastomers based on hard magnetic particles. Smart Materials and Structures, 26(7), p.075012.

Xing ZW, Yu M, Fu J, et al. (2015) A laminated magnetorheological elastomer bearing prototype for seismic mitigation of bridge superstructures. Journal of Intelligent Material Systems and Structures, 26(14), pp.1818-1825.

Yang CY, Fu J, Yu M, et al. (2015) A new magnetorheological elastomer isolator in shear–compression mixed mode. Journal of Intelligent Material Systems and Structures, 26(10), pp.1290-1300.

Yang J, Sun SS, Du H, et al. (2014) A novel magnetorheological elastomer isolator with negative changing stiffness for vibration reduction. Smart materials and structures, 23(10), p.105023.

Yarra S, Behrooz M, Pekcan G, et al. (2017) A large-scale adaptive magnetorheological elastomer-based bridge bearing. In SPIE Smart Structures and Materials+ Nondestructive Evaluation and Health Monitoring (pp. 1016425-1016425).

Yarra S, Pekcan G, Behrooz M, et al. (2017) Characterization of Carbon Black-Filled Natural Rubber and Silicone Magnetorheological Elastomers under pure shear loading. In 8th ECCOMAS Thematic Conference on Smart Structures and Materials 2017 June 6 (pg. 860-870).

# Chapter 3. Performance of a large-scale magnetorheological elastomer-based vibration isolator for highway bridges

Note. This chapter is a stand-alone paper published in Journal of Intelligent Materials Systems and Structures.

Yarra, S., Gordaninejad, F., Behrooz, M., Pekcan, G., Itani, A. M., & Publicover, N. (2018). Performance of a large-scale magnetorheological elastomer–based vibration isolator for highway bridges. Journal of Intelligent Material Systems and Structures. https://doi.org/10.1177/1045389X18799493

## ABSTRACT

This study presents an experimental investigation on magnetorheological (MR) effect of a new magnetorheological elastomer (MRE)-based adaptive bridge isolation bearing system. Two identical MRE-based adaptive bridge bearings (isolators) were designed and fabricated. Electromagnets were incorporated to create a closed-loop magnetic path in the MRE layers. A double-lap shear and compression test setup was utilized to characterize the mechanical properties of the system subjected to scaled structural cyclic forces and strains. Experimental results demonstrated that the effective stiffness of adaptive bridge bearings increase with increased applied magnetic field and a compressive force resulted in larger apparent shear stiffness. Also, increasing loading frequency resulted in larger apparent shear stiffness and lower MR effect and similarly; however, a compressive force resulted in smaller MR effects.

KEYWORDS: Magnetorheological elastomer (MRE), adaptive bridge bearing isolator, vibration control, MR effect

## 3.1. Introduction

Various mechanical systems may be susceptible to high frequency vibration, which can result in metal fatigue. Similarly, vibration sensitive equipment such as medical and electronic equipment may malfunction due to short duration as well as sustained vibration, even low intensities. Furthermore, structural systems may be subjected to adverse ambient conditions due to wind,

traffic and rare events such as earthquakes, which impose various levels of deformation and acceleration demands. Vibration isolation is recognized as an effective means to mitigate shock and vibration induced damage in mechanical and structural systems. Over the last 80 years, the concept of isolation has evolved, and large number of research culminated in categorically three sets of strategies and devices/systems. These systems may be passive, semi-active or active; while passive devices are well established and most commonly used in various applications, research on the latter two continues to develop alternatives that are more versatile than their passive counterparts. Passive devices can be designed to accommodate various vibration-induced translation and rotational deformation demand. However, they cannot be tuned in real time for different loading and operating conditions. Semi active vibration isolation systems may overcome such limitations since their apparent properties can be tuned while they consume significantly less power than active systems.

There is a variety of materials and technologies suggested for semi-active vibration isolation, such as magnetorheological elastomers (MREs). MREs are composed of micron-size magnetically permeable particles, elastomeric medium, and can have other additives such as carbon black and carbon nanofibers. They exhibit a magneto-viscoelastic behavior and upon application of an external magnetic field, the force between the particles increases which results in an increased stiffness and damping. However, damping change is typically smaller compared to stiffness change (Behrooz et al., 2016). When MREs are subjected to a variable magnetic field, changes in stiffness can be realized in relation to the field intensity. In general, material tests conducted on MREs with various compositions showed that the moduli of MRE samples can be significantly increased by applying a magnetic field (Gong et al., 2007) and the optimum particle concentration for increasing the shear modulus is approximately 27% by volume (Davis,

1999). In addition to the applied magnetic field, the MR effect (percentage of increase in stiffness due to the applied magnetic field) is sensitive to loading conditions such as loading frequency, shear strain level, and applied compressive force. For example, simultaneous application of compressive force can result in reduced (around 50%) MR effect in shear mode (Dong et al., 2012). Furthermore, Stepanov et al. (2007) showed that the MR effect is higher when samples were subjected to small strains. Nonetheless, experimentally observed fast response times (7 ms under impact loading (Fu et al., 2013) and 60 ms under large strains (Nguyen and Ramanujan, 2010)) makes the MREs potential candidates for use in vibration isolation applications in over a wide range of frequencies. MRE vibration isolators have been studied in vehicles' engine mounts (Ginder et al., 2000), vehicle transmission system (Hoand et al., 2010), vehicle seat suspension (Du et al., 2011), and adaptive tuned vibration absorbers (Deng et al., 2006; Deng and Gong, 2008; Liu et al., 2017). Recently, MREs have been proposed for use in structural vibration isolation applications. Li et al. (2013) demonstrated the design of a MRE-based isolator by replacing traditional rubber layers in a bearing with MRE layers and achieved a 30% increase in effective stiffness. Behrooz et al. (2013) presented a variable stiffness and damping isolator for seismic base isolation of buildings and modeled its behavior using a phenomenological model with springs, viscous dampers, and a hysteretic Bouc-Wen element. Behrooz et al. (2013) used the current-dependent relations of the MRE-base isolator with a control algorithm to control the performance of the isolator and reduce vibrations in a scaled model of a building. A design methodology was presented for a MRE base isolator by Yang et al. (2014) that incorporates a permanent magnet and can achieve both positive and negative stiffness changes based on the direction of the applied magnetic field. Tu et al. (2014) investigated the field-dependent shear modulus of a MRE isolator and concluded that shear

modulus increases 40% before reaching magnetic saturation. Xing et al. (2015) designed and tested the performance of a bridge bearing using MRE layers and implemented a field-dependent model to consider the dependency of the stiffness and damping of the isolator on the applied magnetic field.

Both isotropic and anisotropic MREs were studied experimentally and analytically for different applications and loading conditions to evaluate their feasibility. These studies concluded that mechanical properties of magnetorheological elastomers are influenced by volume of iron particles, curing conditions, magnetic field intensity. Chen et al. (2016) theoretically and experimentally determined that the optimal design of MRE isolator depends upon the particle volume fraction particle distribution. The reported maximum and minimum MR effect in past research were varied between 1,629% (Li and Li, 2014) and 5% (Yarra et al., 2017) which depends on magnetic field intensity, thickness of sample, iron particle shape and size, viscosity of matrix and additives. Zhao et al. (2017) designed a miniature MRE isolator for lateral vibration suppression of bridge monitoring equipment and showed a maximum increase of 114% in effective stiffness through experimental results when current was increased from 0 A to 3 A. Wahab et al. (2016) developed a natural rubber (1 mm thick) based MRE isolator and tested to evaluate compression force and concluded an increase of 14.5% during static and an increase of 7% for dynamic experiments (5Hz). MREs with carbon black content showed enhanced off-state shear modulus (Chen et al., 2008; Yarra et al., 2017). However, studies related to MREs use in civil engineering applications, such as bridges and buildings, with combined shear and compression loads calculated from following standard codes were slim to none.

This study presents an experimental investigation on a new MRE-based adaptive isolation bearing particularly for highway bridges. The prototype geometry and properties of the bearings were selected based on a comprehensive analytical investigation of typical steel-reinforced elastomeric bearings with comparable passive characteristics. A geometric scale factor of four was selected based on the test setup and equipment limitations. Two bearings which were designed and fabricated for this study incorporated eight electromagnets per bearing. Electromagnets were designed to generate a closed loop magnetic field and optimized to produce an average magnetic field of 1.3 Tesla through four MRE stacks. Each stack consisted of alternating layers of MRE material and steel shims. TAP platinum silicone (Side A base and Side B catalyst with 1:1 ratio) and carbonyl iron particles were used to fabricate MRE layers. Electromagnets, steel shims, sole plate, and masonry plate were fabricated using steel 1018 due to its high magnetic permeability. A specially designed double-lap shear test setup was used to evaluate the performance of the bearings under different applied current, shear strain levels, loading frequency, and compression loads.

## 3.2. System requirements for the design of bearings

To establish realistic force and deformation demands on the MRE-based bearings, steel-reinforced elastomeric bearings with similar passive characteristics were considered first. The baseline passive (off-state) properties were determined after a comprehensive analytical evaluation of 24 steel plate-girder benchmark bridge configurations. The bridges vary in span length, bridge width, and girder spacing as shown in Figure 1. A complete statistical analysis of geometric properties of steel girder bridges across the United States was presented by Amiri Hormozaki (2013). It was found that most of the common steel plate-girder bridges have one of the following geometric configurations including three different average span lengths (80ft,

130ft, and 170ft), four different bridge widths (34ft, 58ft, 82ft, and 106ft), which represent 2-lane to 8 lane bridges, and two different girder spacing (10.5ft and 12ft). Each geometric configuration of reinforced elastomeric bearings was analyzed for three different shear moduli (100 psi, 175psi, and 250psi) to quantify the effect of stiffness changes on the various response quantities.

The steel-reinforced elastomeric bearings for all the benchmark bridges were designed in accordance with AASHTO LRFD Bridge Design Specifications (AASHTO, 2012). Based on the service limit criteria in AASHTO provisions (AASHTO, 2012), permanent and transient loads are considered. For this purpose, the analytical models of the bridges were developed using CSiBridge software (2015). The software has the capability of analyzing bridges under different types of loading.

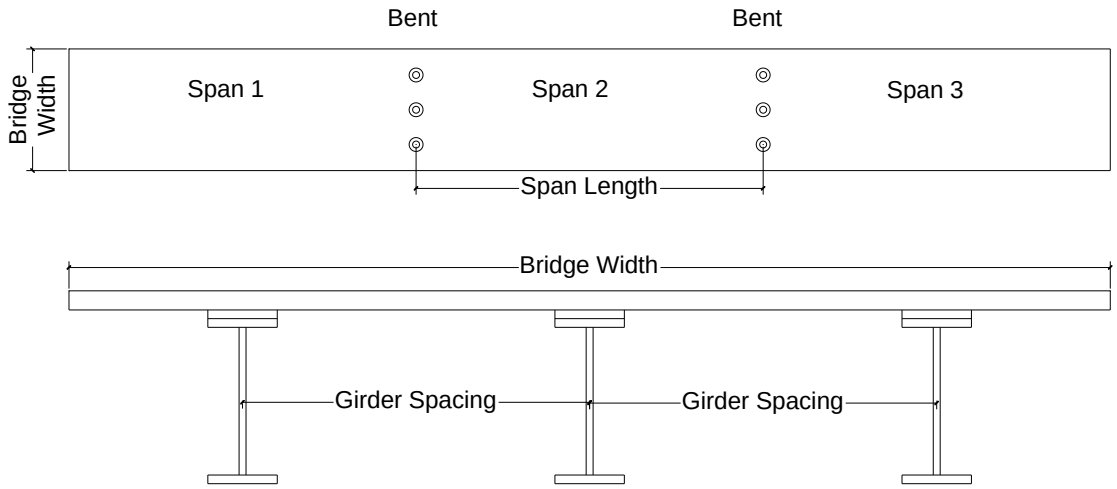


**Figure 1.** Parameters considered in geometric properties of the bridge.

The diameter of the bearing and elastomer height were considered as the main design parameters. These two parameters are selected in a way that the bearing design would be applicable for three different shear moduli in each benchmark bridges. The total rubber

thickness is determined to ensure shear strain due service load conditions remain under 50%, hence it is controlled by the minimum anticipated shear modulus (softer bearing will result in smaller shear stiffness, hence larger deformations). On the other hand, the surface area of the rubber was determined to ensure the sufficiently high axial stiffness to limit the axial strain below 4.5% under gravity loading as well as the smallest possible diameter as per AASHTO LRFD, therefore it was governed by the largest shear modulus.

Finally, the prototype bearing diameter (24") and elastomer height (5") with an average shear modulus of elasticity, G, of 175 psi were established based on the deformation and forced demands on the bearings. These prototype dimensions, with a geometric scale factor of 4, were adopted in view of the test setup and equipment limitations as well as other requirements, e.g., electromagnetic field design. The test protocol for the component tests were determined to satisfy the minimum requirements of AASHTO (AASHTO, 2012). Accordingly, maximum anticipated forces were 23 kip (in compression) and 5 kip (in shear).

## 3.3. Design and fabrication of the bearings

The bearings were designed such that they resemble traditional passive isolation bearings commonly used in highway bridges. Overall dimensions, rubber area, shear stiffness and deformation demand were determined from an extensive analytical study of different bridges around the United States. For the analytical study, AASHTO M251 (AASHTO, 2016) which is referenced in Section 14 of AASHTO LRFD Bridge Design Specs (AASHTO, 2012) and Section 18 of AASHTO LRFD Bridge Construction Specs (AASHTO, 2015), were considered as the basis for the laminated bridge bearing design and properties. A geometric scale factor of 4 was adopted for the bearings that were experimentally evaluated in this study. The MRE-based bearings feature four stacks of alternating MRE and steel shim layers, eight coils, sole plate and

masonry plate. Each stack consisted of 3-in diameter of ten 1/8-in thick MRE and nine 1/8-in steel shim layers. Figure 2 shows the overall dimensions and geometry.

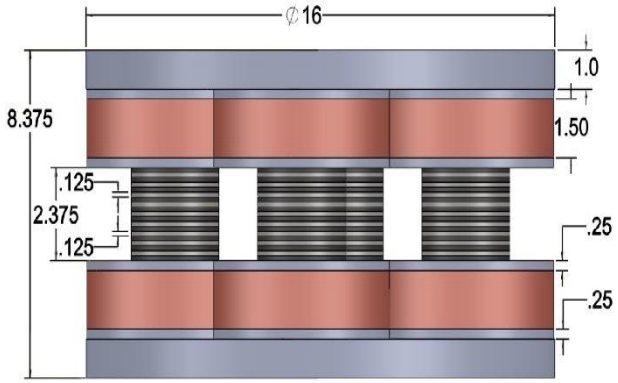


**Figure 2.** Overall dimensions of the bearing
(All dimensions are in inches).

### 3.3.1. Fabrication of MREs, steel shims and preparation of stacks

The MRE material consisted of 35.3%vol. (80%wt.) spherical shape iron particles (Grade-R-2410; Provided by ISP Technologies Inc.), 3.7%vol. (2%wt.) SR303 carbon black (Provided by Sid Richardson), and 30.5vol. (9%wt.) base A and 30.5vol. (9%wt.) base B of Taps Platinum Silicone. The average diameter ranging from 5 to 8 microns of iron particles were used for MR effect. SR303 was used as an additive to improve base passive stiffness of MRE material. The mixture was prepared by using the above composition, poured into a pre-fabricated mold designed to produce 1/8-in thickness and 3-in diameter MRE then the mold was placed into a vacuum chamber and suctioned to -70 kPa to remove air bubbles. Then, the mold was placed in a vise and squeezed until the desired thickness of MRE was produced. Finally, the mold was placed into the electromagnets consisted of two coils wrapped with superior Essex 19 Heavy AWG magnet wire, with each coil ranging from 13-17 ohms and capable of producing 1.2 Tesla of magnetic field and cured for 4 hours at room temperature. Two power supplies (Sorensen

SGA 400-25) were used to apply a constant 5 amp which generates the desired magnetic field. Figure 3 shows the electromagnet system used for fabrication of MRE layers.

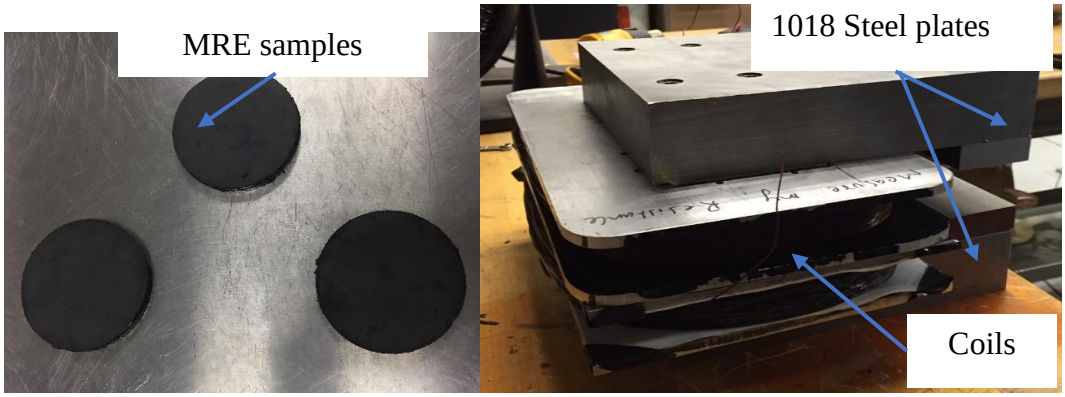


**Figure 3.** Electromagnet system used for MRE fabrication.

Steel shims (1/8-in thickness and 3-in diameter) were made from high magnetic permeability steel 1018. Steel shims were sand blasted for better bonding. Extensive testing was performed to determine the bonding strength of three commonly used adhesives used for bonding silicone and rubber materials to steel. The three adhesives were Loctite 380 Instant Adhesive, Titebond Construction Adhesive, and Dow Corning 832 RTV Sealant. Finally, MRE and steel layers were connected using an adhesive (Dow Corning 832 Multi-Surface Adhesive Sealant), which also included iron particles with a 1:1 ratio to ensure better magnetic conductivity through the adhesive.

### 3.3.2. Fabrication of electromagnets for bearing

The coils used to induce the magnetic field in MREs of the bearing were made from 2.25-in length and 6-in diameter 1018 steel rod. CNC mill was used for precision and to fabricate 3-in diameter and 1.5-in long electromagnet cores with 6-in diameter and ¼-in thickness plates at top and bottom. Fabricated coils can be seen in Figure 4. Coils were double insulated with non-magnet conductive CP high-temperature red varnish insulation spray and Teflon liners as they

were wound using Superior Essex 15 heavy AWG Ultra shield plus magnet wire to achieve desired magnetic field. Each electromagnet was built to have same number of windings which was 515, sub-sequent to the fabrication and winding of each electromagnet, measured resistance of each electromagnet was 2.5Ω. Therefore, all electromagnets were considered as identical thus bearings. The coils were designed to carry 19.5 amperage. The detailing and the material properties of the electromagnets result in capacities of several folds larger than the capacity of the elastomer stacks that ensures safe load path from the top and bottom plates to the MRE stacks. A photo of one of the fabricated bearing is shown in Figure 5.

**Figure 4.** Electromagnets for bearing.

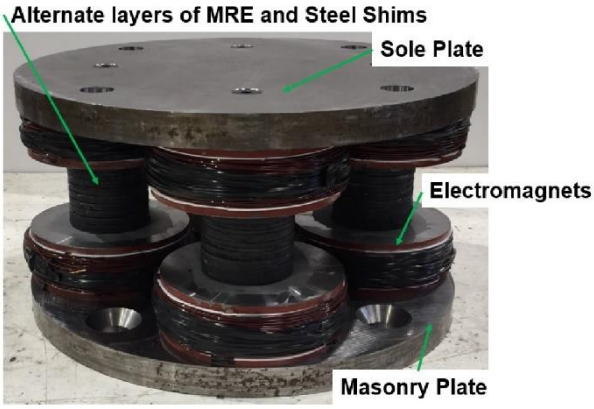


**Figure 5.** Fully assembled scaled bridge bearing.

To ensure sufficient magnetic field for the activation of the MRE layers, three-dimensional magnetic field analyses were performed by modeling the bearings shown in Figure 5 using ANSOFT/Maxwell3D FEA software package (2016). A direct current (DC) of 10,000 amp-turns was applied through insulated copper wire gage 15 with a resistance of 2.5 Ω. Figure 6 shows the analytically predicted magnetic field distribution along the height of each stack (total of 8 stacks for two bearings) with an average of 1.3 Tesla. The alternating magnetic field is due to higher magnetic permeability in the steel shims than MREs. Similarly, the maximum

magnetic field of over 1.6 T is achieved in the steel top and bottom load bearing plates. However, after designed matrix was completed, the middle and outer most MRE layers were cut with a blade, size as probe of a gaussmeter and measured the magnetic field at the same applied amperage for experimental tests. This procedure was not an ideal as gap between probe and hole might filled with some air, thus reducing the magnetic field and the experimentally measured magnetic fields at 1/16 inch and 1-1/16 inch were 0.5 to 0.7 Tesla, respectively. The difference between the analytically predicted and experimentally measured field intensities was attributed to less than ideal physical bonding between elastomer and steel shim layers which analytical model does not account. In addition, the magnetic permeability of the MRE material used in the analytical models was estimated based on previously published research (Kashima, 2012), hence, it was deemed as one of the factors that contributed to this discrepancy. In conclusion, reduction in experimentally measured magnetic field was due to magnetic permeability, saturation limits of materials used, and method used to measure the magnetic field.

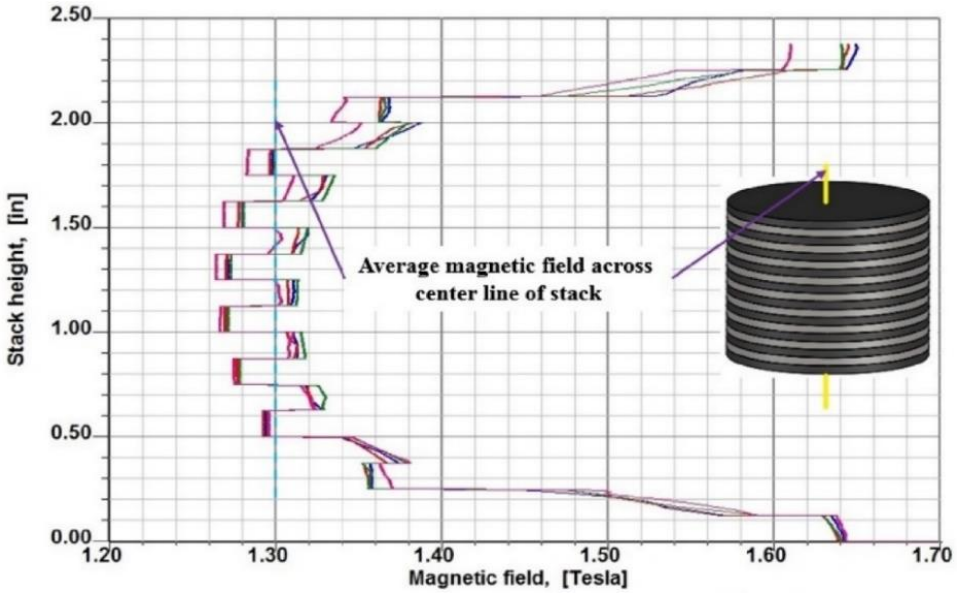


**Figure 6.** Analytically predicted magnetic field distribution across the stack height.

## 3.4. Experimental evaluation of the scaled bridge bearings

### 3.4.1. Double-lap shear and compression experimental setup

The component tests were conducted at the Large-Scale Structures Laboratory at the University of Nevada, Reno. The main objective of the component tests was to characterize the mechanical properties of the bearings such as axial (compressive) and shear stiffness as well as energy dissipation characteristics under various magnetic field intensities. A double-lap shear and compression test setup was designed and fabricated for this purpose as shown in Figure 7. The setup was used for the application and control of shear and axial force and strains on the bearing system. The shear strain was applied and controlled using a hydraulic actuator (type MTS 244.22) and axial force was applied and controlled by a hydraulic cylinder (Manufactured by William S Pine). Hydraulic actuator (MTS 244.22) has stroke length of 20-in and with force rating of 22 kip in compression and in tension. Hydraulic cylinder has stroke length of 12-in and with force rating of 360 kip. Two power supplies (Sorensen SGA 400-25) were used to apply a varying amperage (0-amp, 7-amp, 14 -amp, and 19.5-amp) which generates the desired magnetic field. As shown in the Figure 7, aluminum plates were used to prevent magnetic field passing through entire test setup and to magnetically isolate the bearings, thereby preserving the high levels of the magnetic field in the MRE layers.

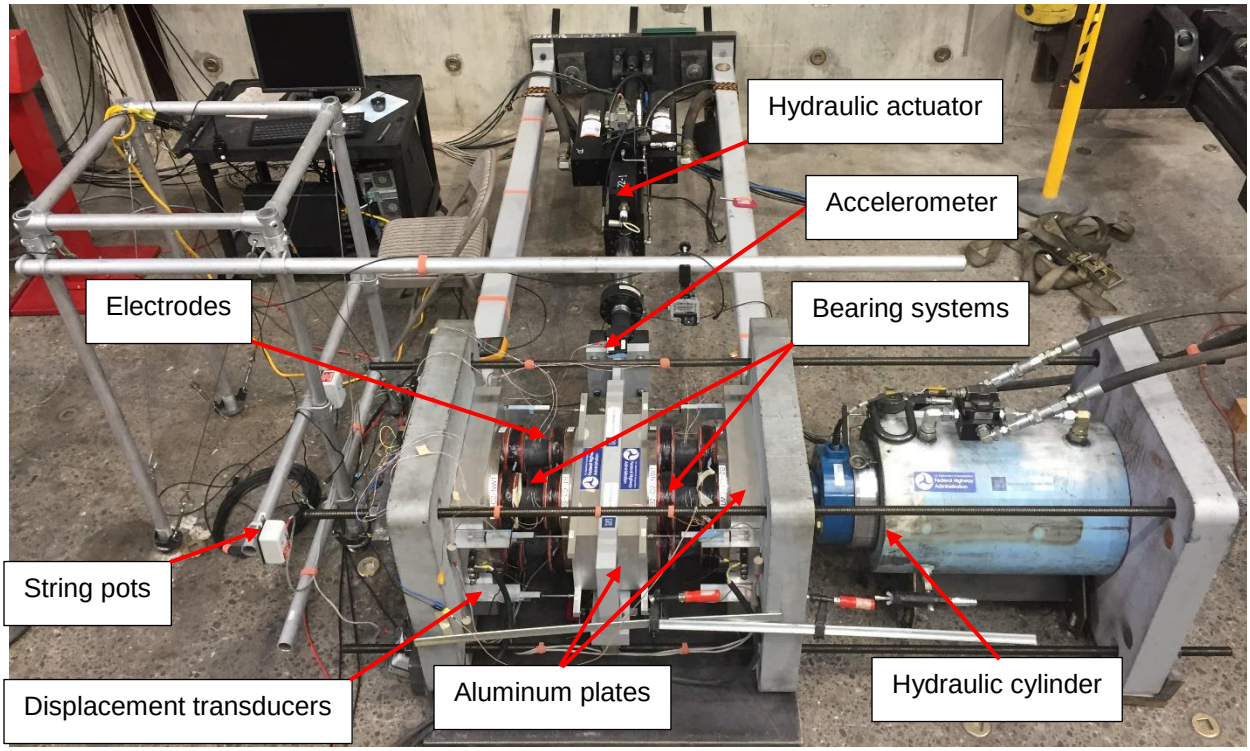


**Figure 7.** Experimental test setup for the MRE adaptive bearing system.

### 3.4.2. Instrumentation and data processing

A total of eight displacement transducers (four per bearing; Novotechnik TR75) were installed to measure axial deformation and potential rotation of bearings when they were subjected to combined shear and compression loading. Three string pots (UniMeasure PA40) were used to capture the out of plane deformations that may result due to imperfections in the test setup. In addition, two thermocouples were installed to measure the temperature of the MRE layers before and after each test. Finally, one accelerometer was used to measure absolute acceleration at the actuator head. The accelerometer was a three-axis Analog Devices Model ADXL326 MEM with nominal measurement ranges of ± 16g. Each sensor was connected to National Instrument data acquisition system, conditioned and low-pass filtered with a cut-off frequency of 80Hz. And sampled at 48Hz.

After each test, preliminary inspection and processing of recorded data was performed to ensure fidelity. The measured acceleration response was used to apply the necessary correction to measured bearing forces due to induced inertia forces, particularly during the high frequency tests. Further post-processing of effective stiffness and damping were carried out using a custom-developed software in MATLAB (2014).

### 3.4.3. Experimental results and discussion

The experimental program was developed to apply six constant strain cycles and the following test parameters were considered: (1) shear strains (5%, 10%, 15%, 20%, and 50%); (2) axial load (0, 2.5kip, 5kip, and 10kip with corresponding normal stress on each stack as 0 lb/in$^2$, 88 lb/in$^2$, 177 lb/in$^2$, and 353 lb/in$^2$); (3) Sinusoidal loading frequency (0.1Hz, 0.5Hz, 1Hz, and 4Hz), and (4) magnetic field intensities that correspond to 0, 7, 14, and 19.5 amps of applied current to the electromagnets. Effective stiffness was calculated using the procedure recommended by US codes ASCE 7-16 and AASHTO (2015). The effective shear stiffness is defined as shown in Figure 8 and determined using Equation (1) (ASCE, 2016), as follows:

$$k_{eff} = \frac{|F^+| + |F^-|}{|\Delta^+| + |\Delta^-|} \quad (1)$$

where $F^+$ and $F^-$ are the positive and negative forces, at $\Delta^+$ and $\Delta^-$, respectively. The component tests were used to evaluate the effect of various magnetic field intensities on the effective stiffness calculated from the force-displacement curves. The MR effect is defined as the change in the properties of MRE under the magnetic field and quantified as the ratio of absolute change in effective stiffness due to a given magnetic field intensity to zero field effective stiffness ($k_{o,\,eff}$) and determined using Equation (2).

$$\%MR\ effect = \frac{k_{MR,eff} - k_{0,eff}}{k_{0,eff}} \quad (2)$$

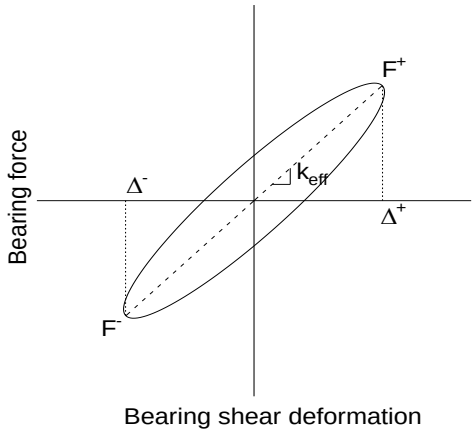


**Figure 8.** Definition of effective shear stiffness.

### 3.4.3.1. Response under shear-only loading

Experiments were carried out for different strains, frequencies, and magnetic fields using hydraulic actuator and by setting hydraulic cylinder at zero position as pre- load condition. The percent change in effective shear stiffness is determined relative to the 0.1 Hz tests as summarized in Table 1. For a given strain level with varying frequencies, the increase in effective shear stiffness varies between 13% to 66%. While the increase is insignificant for frequencies up to 1 Hz, up to 66% increase in effective stiffness was observed corresponding to 4 Hz and 20% shear strain. The effective shear stiffnesses are summarized in Table 1. Figure 9 shows a sample shear force-displacement hysteresis. The overall behavior of MRE follows the stress-strain relationship of rubber-like materials which show a higher initial effective stiffness. Also, due to viscoelastic behavior of MREs, a higher stiffness is observed at higher loading frequencies.

**Table 1.** Effect of Loading Frequency on the Effective Shear Stiffness.

| Effective stiffness (kip/in.) | | | |
|---|---|---|---|
| Loading frequency (Hz) | Strain (%) | | |
| | 5 | 10 | 20 |
| 0.1 | 4.10 | 3.70 | 3.47 |
| 0.5 | 4.13 | 3.67 | 3.52 |
| 1.0 | 4.20 | 3.68 | 3.57 |
| 4.0 | 4.62 | 4.99 | 5.76 |
| Frequency effect (%) | 13 | 35 | 66 |

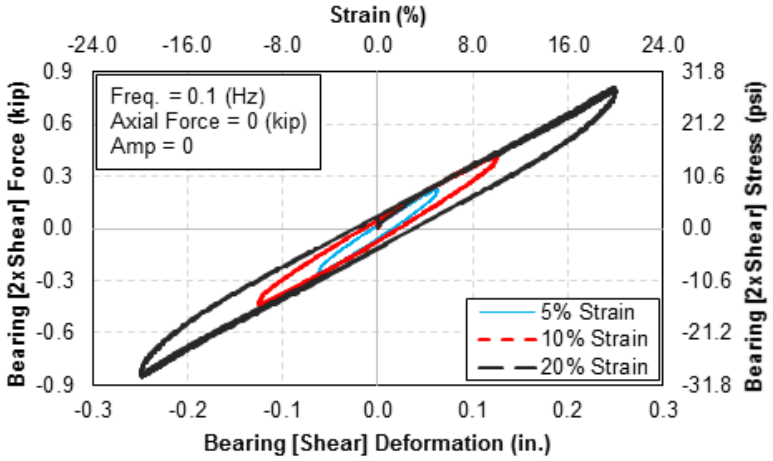


**Figure 9.** Shear force-displacement response of the bearing with f = 0.1 Hz, P = 0, Amp = 0.

Figure 10 shows an example of shear force-deformation response for loading frequency of 0.1 Hz and applied strain of 50% with different magnetic field intensities corresponding to 0 Amp and 19.5 Amp. For a given test frequency, an increase in effective stiffness due to increasing magnetic field was observed. For example, Figure 11(a) shows that for the quasi-static tests (0.1 Hz) at 20%-shear strain and 19.5 Amp input current, the increase in stiffness is approximately 12%. However, for a given magnetic field intensity, the increase in effective

stiffness reduces with increasing strain amplitude. In summary, the percent increase in effective stiffness reduces from 18% at 5% strain to 5% at 50% strain since a larger force is applied at higher strains and the ratio of generated magnetic force to mechanical force decreases. It can also be seen in the Figure 11(comparison between Figure 11(a) and 11(b)) that the MR effect is reduced with increasing frequencies. This is due to higher forces being applied at higher frequencies and a reduced ratio of magnetic force to mechanical force. Figure 11(b) shows that the maximum increase in effective shear stiffness is approximately 14% at 5% strain for test frequency of 4 Hz. Effective shear stiffness with zero axial force and varying frequencies and strains are summarized in Table 2.

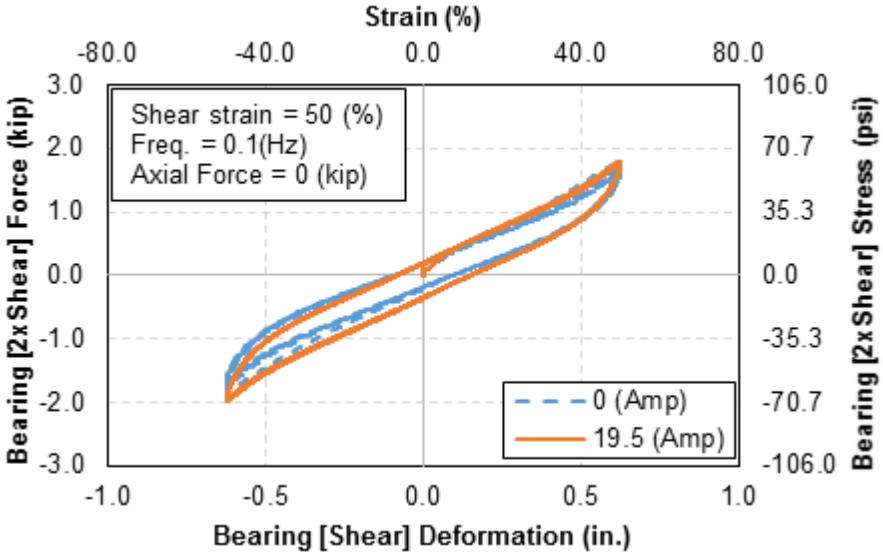


**Figure 10.** Force-displacement response at 0.1 Hz with varying input electrical subjected to 50% Strain.

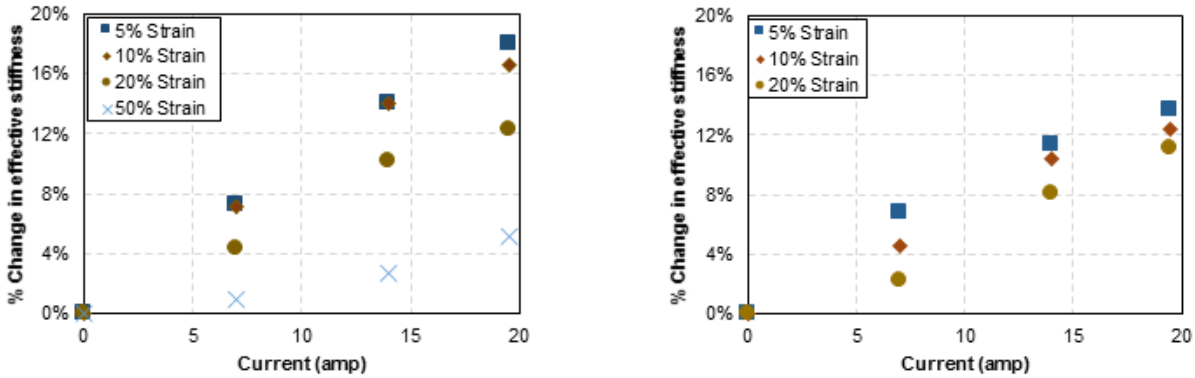


**Figure 11.** Effect of magnetic field on the effective shear stiffness with no axial force and loading frequency of: (a) f = 0.1 Hz, and (b) f = 4 Hz loading frequency.

### 3.4.3.2. Combined shear and compression loading

The test setup was used to apply simultaneous shear strains and axial forces. Hydraulic cylinder was used to hold a constant axial force and applied different strains, frequencies, and magnetic fields using hydraulic actuator. As shown in Figure 12(a) and (b), for a given strain amplitude, the effective shear stiffness of the bearing increases with increasing compression force. It can also be observed that the effective shear stiffness increases for larger magnetic field intensities for any given compression force and strain. Table 2 summarizes the effect of axial force on shear force-deformation properties of the bearing. Figure 13(a) shows that under quasi-static shear deformation and an axial force of 5 kip, effective shear stiffness enhancement due to magnetic field is 23% at low strain level (5%), but reduces to 9% at higher strain amplitude of 20%. The corresponding enhancement in the effective stiffness with 10.0 kips of axial force decreases from 22% to 4% when the strain level increases from 5 to 20%. Therefore, it is reaffirmed that larger strain amplitudes usually result in lower MR effect due to a smaller ratio of applied magnetic to mechanical force, as presented in Table 2. Also, as shown in Figure 13, the

effect of magnetic field on the effective shear stiffness decreases with increasing axial load. This may be due to reduced distance between the iron particles, and thus an increase in the base passive shear stiffness values. At higher frequencies, the bearings exhibit a higher stiffness due to viscoelastic properties of the elastomer matrix (Table 2).

**Table 2.** Effective Stiffness [kip/in.] under Various Loading Conditions with Different Axial Loadings.

| Applied current and MR Effect | 5% Strain | | 10% Strain | | 20% Strain | | 50% Strain |
|---|---|---|---|---|---|---|---|
| | 0.1 (Hz) | 4 (Hz) | 0.1 (Hz) | 4 (Hz) | 0.1 (Hz) | 4 (Hz) | 0.1 (Hz) |
| Axial Force = 0 kip | | | | | | | |
| 0.0 A | 3.91 | 4.72 | 3.46 | 4.20 | 3.35 | 3.96 | 2.90 |
| 19.5 A | 4.61 | 5.36 | 4.03 | 4.72 | 3.76 | 4.40 | 3.05 |
| MR effect (%) | 18 | 14 | 17 | 12 | 12 | 11 | 5 |
| Axial Force = 5 kip | | | | | | | |
| 0.0 A | 5.04 | 6.15 | 4.86 | 5.60 | 4.41 | 5.20 | NA |
| 19.5 A | 6.19 | 7.40 | 5.54 | 6.36 | 4.80 | 5.77 | NA |
| MR effect (%) | 23 | 20 | 14 | 14 | 9 | 11 | NA |
| Axial Force = 10 kip | | | | | | | |
| 0.0 A | 8.06 | 8.41 | 7.42 | 7.96 | 5.90 | 7.00 | 3.59 |
| 19.5 A | 9.58 | 10.27 | 8.00 | 8.69 | 6.13 | 7.51 | 3.93 |
| MR effect (%) | 19 | 22 | 8 | 9 | 4 | 7 | 9 |

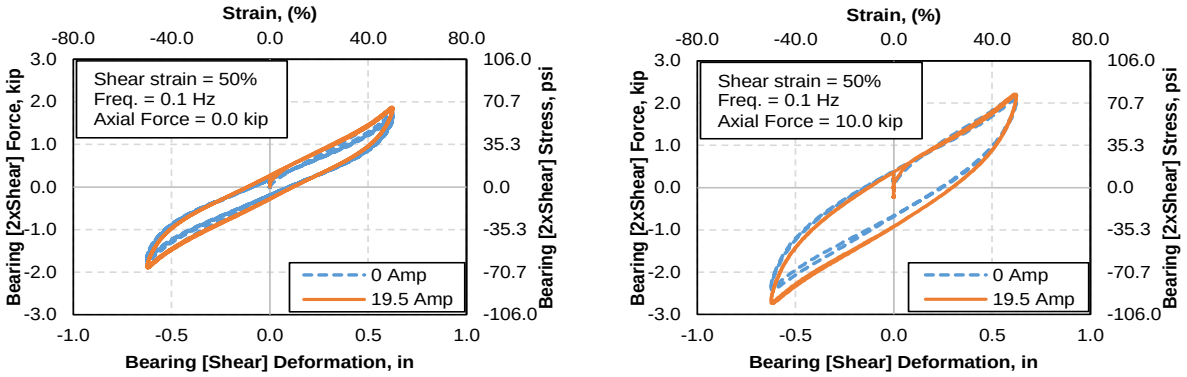


(a) (b)

**Figure 12.** Effect of magnetic field on the effective shear stiffness with (a) P = 0 kips and (b) P = 10 kips.

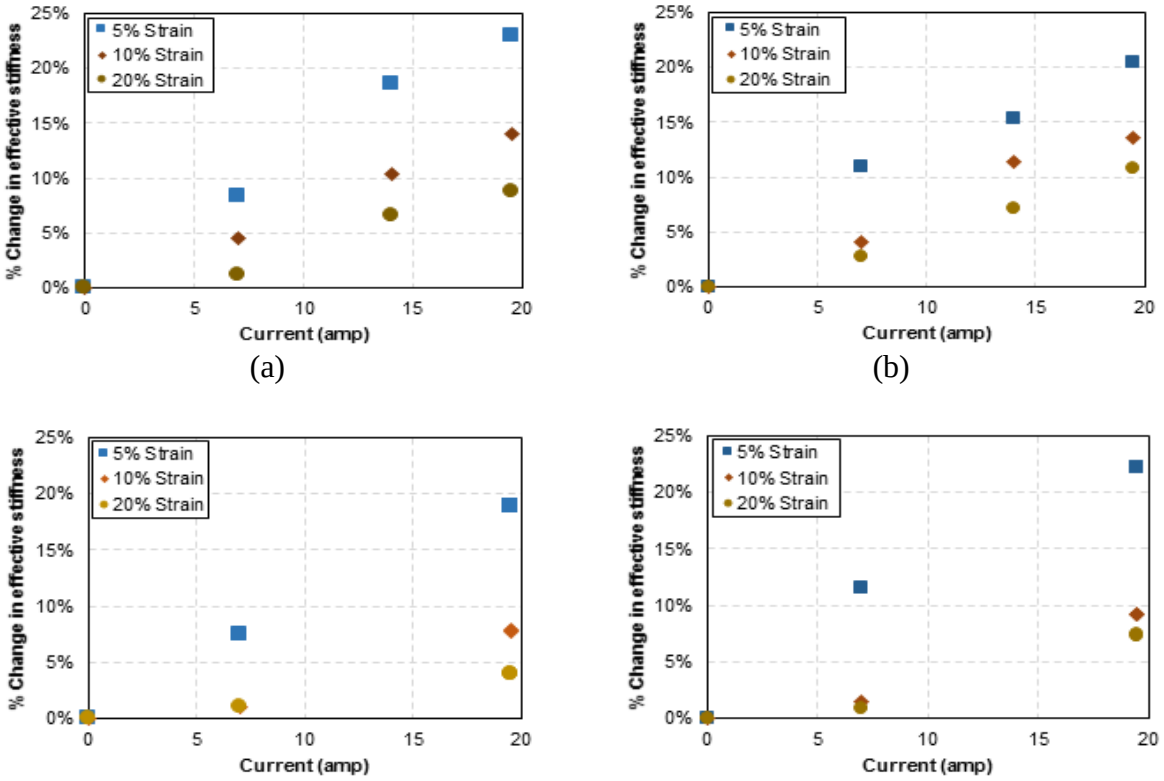


(a) (b)

(c) (d)

**Figure 13.** Effect of magnetic field on the effective shear stiffness with different axial forces and loading frequencies of: (a) 5-kip, 0.1 Hz, (b) 5 kip, 4 Hz, (c) 10 kip, 0.1 Hz, and (d) 10 kip, 4 Hz.

### 3.4.3.3. Compressive loading

As pre-load condition, hydraulic actuator was used to hold bearing system at zero shear strain position and studied magnetic field effect at different axial forces applied using hydraulic cylinder. These experiments were conducted to investigate adaptability of the bearings while supporting large structural loads based on AASHTO axial strain limits. The maximum compression force was determined based on AASHTO [33] as 23 kip, which results in 115psi. Bearings were tested under different axial forces with varying magnetic field and loading frequencies. The axial force-displacement plots shown in Figure 14(a) and (b) demonstrates a smaller increase in axial stiffness compared to shear stiffness due to increasing magnetic field. Table 3 shows axial stiffness increment with increased magnetic field. The stiffness increment is 12% for 10-kip axial force and 4% under 20 kip axial load. Therefore, similar to shear stiffness, the relative effect of magnetic field on the stiffness decreases with increasing axial load.

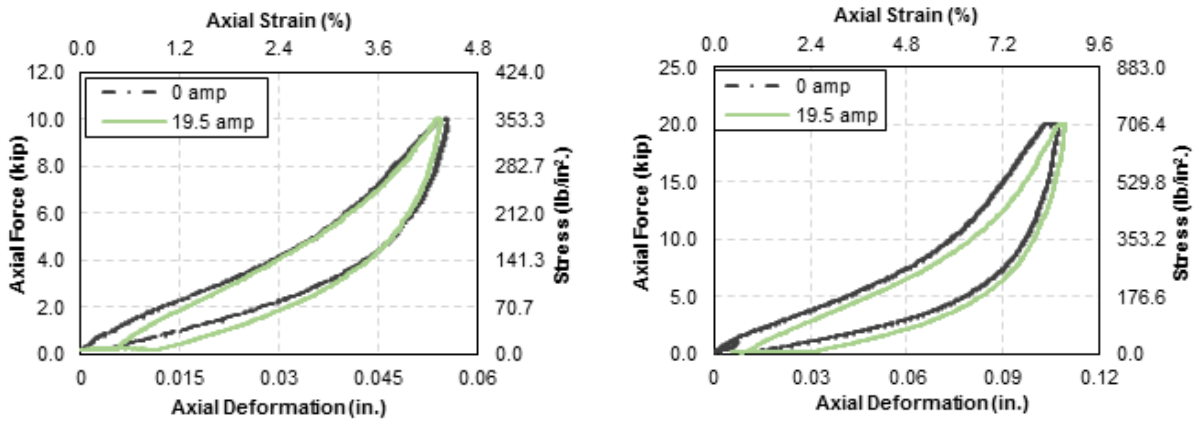


**Figure 14.** Axial force-displacement relationships under (a) P = 10-kip axial load (b) P=20 kip axial load.

Table 3. Pure Compression Test Results.

| Axial Force (kip) | Amp | Load Rating (lb/sec) | Thickness of MRE (in.) | Axial Displacement (in.) | Axial Strain (%) | Axial Stiffness (lb /in.) |
|---|---|---|---|---|---|---|
| 10.00 | 0.00 | 50.00 | 1.25 | 0.056 | 4.48 | 178.57 |
| | 19.50 | 50.00 | 1.25 | 0.050 | 4.00 | 200.00 |
| 20.00 | 0.00 | 200.00 | 1.25 | 0.105 | 8.60 | 190.48 |
| | 19.50 | 200.00 | 1.25 | 0.101 | 8.09 | 198.02 |

#### 3.4.3.4. Temperature

During the experimental testing, bearing electromagnets temperature was measured and it varied from $23^0$ C at 0 amp to $27^0$ C at 19.5 amp.

#### 3.4.3.5. Mode of failure

Finally, the failure of the adaptive bearings was investigated by subjecting the bearings to 100% shear strain cyclic loading. Figure 15 shows the force-displacement response of the adaptive bearing under the constant strain of 100%, frequency of 0.1 Hz with zero magnetic fields. As shown in the Figure 16, failure was observed approximately at 74% strain amplitude. Further investigation of the MRE layers revealed that the failure was due to the bond failure between MRE and steel surfaces, as shown in Figure 16.

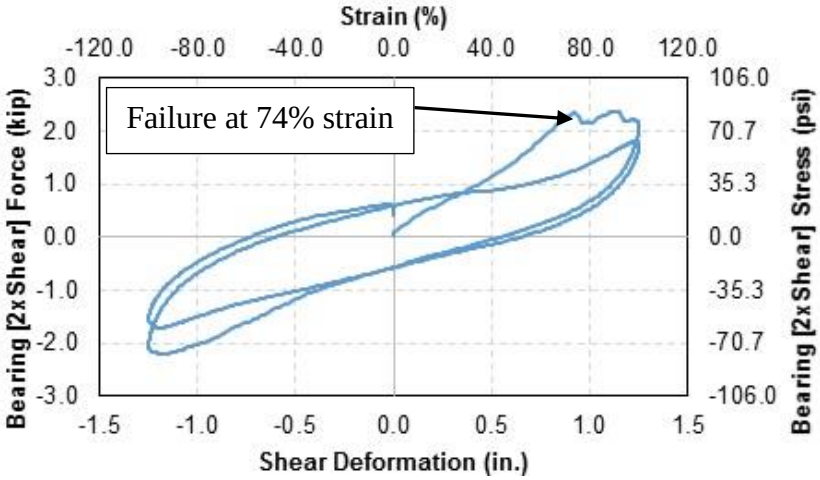


**Figure 15.** Force-displacement response of the bearing under 100% strain, 0 amp, and 0.1 Hz loading frequency.


**Figure 16.** Failure of the MRE stacks of the bearing system.

## 3.5. Conclusions

A large-scale adaptive MRE bridge bearing (vibration isolator) was designed and manufactured to investigate the effect of structural loads on its MR effect. The effects of magnetic field, strain level, and loading frequency on the effective stiffness of the bearing were studied. The observed MR effect under combined shear and compression loading ranged between 23% and 9% at 5-kip axial load and strains 5% and 20%, respectively. However, increasing the compression force

further to 10 kip reduced the MR effect relative to 5 kip. Effective stiffness increased with increasing frequency for a given strain amplitude. In the absence of compressive force, the maximum and minimum change in effective shear stiffness (due to increased frequency) were between 13% and 66% for strains between 5% and 20%, respectively. Under compression only loading, MR effect was reduced from 12% to 4% when the axial load increased from 10 to 20 kip. Larger axial force resulted in larger apparent passive stiffness which increased by 7% when the axial force was increased from 10 kip to 20 kip. The computed damping was insignificant. Adhesive failure was observed between MRE and steel surface at 74% shear strain.

## 3.6. Acknowledgements

This project was funded by the Federal Highway Administration under the contract number DTFH61-13-C-00020. The authors would like to express their gratitude to Dynamic Isolation Systems, Inc., and to Scougal Rubber Corporation. The authors also acknowledge Mr. Tony Berendsen, Development Technician of the Mechanical Engineering Department, Mr. Chad Lyttle, Development Technician of the University of Nevada, Reno Center for Civil Engineering Earthquake Research, and Dr. Patrick Laplace, Research Associate Professor and Manager of the Large-Scale Structures and Earthquake Engineering Laboratory, for their assistance and guidance. The authors also wish to thank Mr. Troy Martin, Structures Division of the Nevada Department of Transportation (NDOT), for his valuable feedback and participation during the component testing of the adaptive bearings. Finally, the authors would like to thank undergraduate assistants D. Mar, N. Pinuelas, and B. Muznich for their assistance.

## 3.7. References

AASHTO (2012) Bridge design specifications, customary US units, with 2012 and 2013 interim revisions.

AASHTO (2015) Bridge Construction Specifications with 2016 interim revisions.

AASHTO (2016) Standard Specifications for Transportation Materials and Methods of Sampling and Testing.

ASCE (2016) Minimum design loads for buildings and other structures. ISBN: 9780784414248.

AmiriHormozaki E (2013) Analytical Fragility Curves for Horizontally Curved Steel Girder Highway Bridges. Doctoral dissertation, University of Nevada-Reno, USA.

ANSYS Maxwell Computer software. Version 11.1. (2016) ANSOFT/Maxwell3D FEA software package Available at: http://www.ansys.com/products/electronics/ansys-maxwell (accessed 25 November 2016).

Behrooz M, Wang X and Gordaninejad F (2013) Modeling of a new magnetorheological elastomer-based isolator. In Proc. SPIE (Vol. 8688, p. 86880Z).

Behrooz M, Wang X, and Gordaninejad F (2013) Seismic control of base isolated structures using novel magnetorheological elastomeric bearings. Proc. ASME, V001T03A027–V001T03A027.

Behrooz M, Sutrisno J, Zhang L, et al. (2015) Behavior of magnetorheological elastomers with coated particles. Smart Materials and Structures, 24(3), p.035026.

Behrooza M, Yarra S, Marc D, et al. (2016) A self-sensing magnetorheological elastomer-based adaptive bridge bearing with a wireless data monitoring system. In Proc. of SPIE Vol (Vol. 9803, pp. 98030D-1).

Chen L, Gong XL and Li WH (2008) Effect of carbon black on the mechanical performances of magnetorheological elastomers. Polymer Testing, 27(3), pp.340-345.

Chen S, Wang X, Zhang Z, et al. (2016) Optimal design of laminated-MRE bearings with multi-scale model. Smart Materials and Structures, 25(10), p.105037.

CSIBRIDGE Computer software Version 15 (2015) Available at: https://www.csiamerica.com/products/csibridge (accessed 25 May 2014).

Davis LC (1999) Model of magnetorheological elastomers. Journal of Applied Physics, 85(6), pp.3348-3351.

Deng HX, Gong XL and Wang LH (2006) Development of an adaptive tuned vibration absorber with magnetorheological elastomer. Smart materials and structures, 15(5), p.N111.

Deng HX and Gong XL (2008) Application of magnetorheological elastomer to vibration absorber. Communications in nonlinear science and numerical simulation, 13(9), pp.1938-1947.

Dong X, Ma N, Qi M, et al. (2012) The pressure-dependent MR effect of magnetorheological elastomers. Smart Materials and Structures, 21(7), p.075014.

Du H, Li W and Zhang N (2011) Semi-active variable stiffness vibration control of vehicle seat suspension using an MR elastomer isolator. Smart materials and structures, 20(10), p.105003.

Fu J, Zheng X, Yu M, Ju, et al. (2013) A new magnetorheological elastomer isolator in shear-Compression mixed mode. In Advanced Intelligent Mechatronics (AIM), 2013 IEEE/ASME International Conference on (pp. 1702-1706).

Ginder JM, Nichols ME, Elie LD, et al. (1999) Magnetorheological elastomers: properties and applications. In Smart Structures and Materials, Vol. 3675, pp. 131-139

Ginder JM, Nichols ME, Elie LD, et al. (2000) Controllable-stiffness components based on magnetorheological elastomers. In Proceedings-SPIE the International Society for Optical Engineering (pp. 418-425).

Gong XL, Chen L, and Li JF (2007) Study of utilizable magnetorheological elastomers. International Journal of Modern Physics B, 21(28n29), pp.4875-4882.

Hoang N, Zhang N and Du H (2010) An adaptive tunable vibration absorber using a new magnetorheological elastomer for vehicular powertrain transient vibration reduction. Smart Materials and Structures, 20(1), p.015019.

Jolly MR, Carlson JD, Muñoz BC, et al. (1996) The magneto viscoelastic response of elastomer composites consisting of ferrous particles embedded in a polymer matrix. Journal of Intelligent Material Systems and Structures, 7(6), pp.613-622.

Jolly MR, Carlson JD and Munoz BC (1996) A model of the behaviour of magnetorheological materials. Smart Materials and Structures, 5(5), p.607-614.

Jung HJ, Lee SJ, Jang DD, et al. (2009) Dynamic characterization of magneto-rheological elastomers in shear mode. IEEE transactions on magnetics, 45(10), pp.3930-3933.

Kashima S, Miyasaka F and Hirata K (2012) Novel soft actuator using magnetorheological elastomer. IEEE Transactions on Magnetics, 48(4), pp.1649-1652.

Liao G, Gong X and Xuan S (2013) Influence of shear deformation on the normal force of magnetorheological elastomer. Materials Letters, 106, pp.270-272.

Li Y, Li J, Li W, et al. (2013) Development and characterization of a magnetorheological elastomer based adaptive seismic isolator. Smart Materials and Structures, 22(3), p.035005.

Li Y and Li J (2014) Base isolator with variable stiffness and damping: design, experimental testing and modelling. In ST Smith (ed.), *23rd Australasian Conference on the Mechanics of Structures and Materials (ACMSM23)*, vol. II, pp. 913-918. ISBN: 9780994152008.

Liu G, Lu K, Zou D, (2017) Development of a semi-active dynamic vibration absorber for longitudinal vibration of propulsion shaft system based on magnetorheological elastomer. *Smart Mater. Struct*, *26*(075009), p.075009.

MATLAB version 8.3 (2014) MATLAB R2014 a. The Mathworks Inc.

Nguyen VQ and Ramanujan RV (2010) Novel Coiling Behavior in Magnet-Polymer Composites. Macromolecular Chemistry and Physics, 211(6), pp.618-626.

Schubert G and Harrison P (2015) Large-strain behaviour of magneto-rheological elastomers tested under uniaxial compression and tension, and pure shear deformations. Polymer Testing, 42, pp.122-134.

Shen Y, Golnaraghi MF and Heppler GR (2004) Experimental research and modeling of magnetorheological elastomers. Journal of Intelligent Material Systems and Structures, 15(1), pp.27-35.

Stepanov GV, Abramchuk SS, Grishin DA, et al. (2007) Effect of a homogeneous magnetic field on the viscoelastic behavior of magnetic elastomers. Polymer, 48(2), pp.488-495.

Tu JW, Tu B, Mei ST, et al. (2014) Research on new type MRE isolator and its mechanical model. Materials Research Innovations, 18(sup2), pp.S2-552.

Wahab NAA., Mazlan SA, Kamaruddin S, et al. (2016) Fabrication and investigation on field-dependent properties of natural rubber-based magneto-rheological elastomer isolator. *Smart Materials and Structures*, *25*(10), p.107002.

Xing ZW, Yu M, Fu J, et al. (2015) A laminated magnetorheological elastomer bearing prototype for seismic mitigation of bridge superstructures. Journal of Intelligent Material Systems and Structures, 26(14), pp.1818-1825.

Yang CY, Fu J, Yu M, et al. (2015) A new magnetorheological elastomer isolator in shear–compression mixed mode. Journal of Intelligent Material Systems and Structures, 26(10), pp.1290-1300.

Yang J, Sun SS, Du H, et al. (2014) A novel magnetorheological elastomer isolator with negative changing stiffness for vibration reduction. Smart materials and structures, 23(10), p.105023.

Yarra S, Behrooz M, Pekcan G, et al. (2017) A large-scale adaptive magnetorheological elastomer-based bridge bearing. In SPIE Smart Structures and Materials+ Nondestructive Evaluation and Health Monitoring, pp. 1016425-1016425.

Yarra S, Pekcan G, Behrooz M, (2017) Characterization of Carbon Black-Filled Natural Rubber and Silicone Magnetorheological Elastomers under pure shear loading. In 8th ECCOMAS Thematic Conference on Smart Structures and Materials 2017 June 6, pg. 860-870.

Zhao L, Yu M, Fu, J, et al. (2017) A miniature MRE isolator for lateral vibration suppression of bridge monitoring equipment: design and verification. *Smart Materials and Structures*, *26*(4), p.047001.

# Chapter 4. Modeling of natural rubber-based isotropic magnetorheological elastomers subjected to combined compressive and shear loading

Note. This chapter is a stand-alone paper will be submitted on December 06, 2018 for review and possible publication by the Journal of sound and vibration - Elsevier.

## ABSTRACT

This study presents a seven-parameter linear viscoelastic model that was developed to capture the behavior of isotropic natural rubber-based magnetorheological elastomers under high shear strains. The model comprised of a dashpot and three Maxwell elements arranged in parallel. The model parameters were identified using a nonlinear multivariable regression approach by minimizing simultaneously the error between experimental and model predicted properties. The comparison between the predicted and experimental storage and loss moduli, and effect of magnetic field thereof, demonstrated the validity of the proposed model. However, since the hysteretic behavior of natural rubber is highly nonlinear and therefore deviates from that of a linear viscoelastic model, particularly at large strain amplitudes. It was demonstrated that magnetic-field may have significant effect on the stiffness of MREs, while damping is not affected, as much.

**Keywords:** Natural rubber, magnetorheological elastomer, viscoelastic model, combined compressive and shear loading.

## 4.1. Introduction

Magnetorheological elastomers (MRE) belong to a class of adaptive materials, which consist of elastomeric matrix material, magnetically permeable iron particles and other additives such as carbon black. The mechanical properties, shear storage, G', and loss moduli, G", of MREs can be controlled in real-time under an applied external magnetic field. MREs exhibit magneto-

viscoelastic response and, upon application of an external magnetic field, the force between the particles increases which results in increased apparent stiffness and damping. Controllability of these key properties renders MREs as possible candidates for use in semi-active control devices. These composites have been considered for different engineering applications where vibration mitigation is needed, such as, vehicle engine mounts, transmission systems, seat suspensions, adaptive tuned vibration absorbers, and civil structural vibration isolation [1-3]. It is noted that all previous investigations have focused mainly on small-scale applications and relatively small-strain regimes, which limit the use of MRE-based vibration isolators for large-scale structural systems, such as buildings and bridges. More recently, Yarra et al. [4] demonstrated that silicon-based elastomers demonstrate inherently limited deformation capacity and investigated natural rubber-based isotropic MREs for applications where large strain deformation capacities are required [5].

The need for reliable analytical models for various MRE material compositions is recognized [6]. Such analytical models can facilitate the design and widespread use of MRE-based devices. Prior work modeling efforts have been focused on to predict performance of MREs and MRE-based devices [7-8]. These models have been categorized based on particle interaction [9-13], magneto-elastic response [14-15], magneto-viscoelastic response [16-22], and models including the effect of environmental conditions and fatigue [23].

Li et al. [19] proposed a four-parameter linear viscoelastic model to predict MRE performance under various loading conditions and demonstrated the model validity for loading frequencies and strain amplitudes less than 10Hz and 10%, respectively. A rheological model considering the effect of material matrix, embedded iron particles and the interaction between iron particles was developed to capture MRE’s response under dynamic loading and external

magnetic fields [17]. The study demonstrated that dynamic response of MRE containing any volume of iron particles and properties of matrix can be simulated, successfully. Ivaneyko et al. [24] proposed a lattice model that can predict the effect of particle distribution and concluded that the Young's modulus (E) decreases for chain-like distributions and increases for plane-like distributions with increasing magnetic field. Norouzi et al. [25] developed an eight-parameter viscoelastic model to predict the response of MRE under combined tensile and compressive loads. Kaleta et al. [26] adopted a four-parameter constitutive model to predict the inelastic properties of MRE composites under cyclic shear conditions and concluded that the model is valid in a frequency range above 5 Hz. Eem et al. [18] developed a dynamic model by arranging Ramberg-Osgood and Maxwell models in parallel and demonstrated that it can predict the response of MREs' under shear deformation. Behrooz et al. [8] employed Bouc-Wen hysteresis element to characterize the force-displacement relationship of a variable stiffness and damping isolator. Yang et al. [21] proposed a new model which incorporates Bouc-Wen component to reproduce hysteresis loops and Voigt element to predict solid material response in parallel and showed that can predict MRE isolator response very well. Phenomenological model that comprised of a variable friction damper and a nonlinear spring was recommended to simulate the dynamic response of the MR fluid-elastomer mount [27]. Zhu et al. [22] proposed a magneto viscoelasticity parametric model to describe the MRE vibration mitigation device and concluded that the model forecast experimental results. Jung et al. [28] calibrated a Bouc-Wen model based on test results of MRE samples and validated with experimental results.

This study introduces an experimentally calibrated viscoelastic model that can simulate dynamic characteristics and response of isotropic natural rubber-based magnetorheological elastomers under combined compressive and shear loadings. The model was calibrated using

data generated following a comprehensive experimental investigation [5, 29] for a wide range of test frequencies and magnetic-field intensities. The results indicate that the seven-parameter viscoelastic model can capture solid and fluid-like behavior, and stress relaxation of MRE material. An empirical relationship is introduced to account for the effect of magnetic field intensity on the model parameters.

## 4.2. Experimental study of natural rubber-based MREs

This section describes material fabrication, experimental setup and testing procedure adopted for the material testing of MREs under pure shear and combined compressive and shear loads. Experimentally observed and recorded response was used to validate the proposed model. Detailed information on the characterization of isotropic natural rubber-based, as well as anisotropic TAP-silicone based MREs with various material compositions can be found in earlier study [4-5, 29-30] and summarized herein.

### 4.2.1. Material fabrication

The natural rubber MRE samples were manufactured by a certified supplier. Natural rubber - TSR 20, Iron powder and N550 Carbon black were mixed in a 1.6 liter tilt body internal mixer with tangential rotors. Rotor speed was set to 40 rpm and temperature was varied between 80$^{o}$C and 110$^{o}$C to achieve uniform dispersion of iron powder and carbon black. Rubber batches were warmed up on a mill and taken off in a thick slab. The slabs were placed in a 254 mm x 254 mm x 12.5 mm picture frame mold and put in a press. The press was set to 138$^{o}$C to help the rubber flow, but to minimize sticking of the rubber to the top and bottom plates. A semi-permanent mold release (Stoner A353 Endurance Mold Release) was used to reduce sticking. The press was crash cooled until temperature was below 3.2$^{o}$C and slab was removed from the mold. For the experimental study, fabricated natural rubber based MRE slabs were cut following ASTM

D5992 [31] to a recommended standard size of 40-mm x 16-mm x 5 -mm for double lap shear testing. Natural rubber-based MRE samples that were fabricated and tested are summarized in Table 1. Carbon black was used to improve base passive stiffness of the material [4-5, 32-34].

**Table 1.** Material Compositions of Natural Rubber-Based MRE Samples (%wt.).

| Test ID | Iron particles | Carbon black | Natural rubber TSR- 20 |
|---|---|---|---|
| NR-S-1 | 80.0 | 0.0 | 20.0 |
| NR-S-4 | 77.6 | 3.0 | 19.4 |
| NR-S-6 | 76.0 | 5.0 | 19.0 |

### 4.2.2. Experimental setup and testing

Natural rubber-based MRE properties were characterized using a uniquely designed test apparatus shown in Figure 1. The test setup was used to apply and control shear and compression forces individually and/or concurrently. Hydraulic actuator was used for the application and control of shear force that was measured with an inbuilt Instron loadcell. Axial force was applied and controlled manually and measured with an external loadcell. Monotonic and limited cyclic tests were performed on all the samples listed in Table 1. Based on the preliminary monotonic testing, [5], it was concluded that NR-S-4 was the most viable candidate for civil engineering applications due to its moduli in passive mode and controllability thereof. Therefore, NR-S-4 sample was subjected to comprehensive sinusoidal cyclic tests at different frequencies (0.1, 0.5, 1, 3, 5, 7 and 10Hz), strain amplitudes, $\gamma$ (10%, 30%, 50%, 75%, 100%, 125% and 150%) and magnetic-fields, B (0, 0.3, 0.5 and 0.6 Tesla) under pure shear and combined loading conditions. Furthermore, a constant compressive force of $P$ = 445 N was applied since it resulted in 0.7 N/mm$^2$ normal stress, which is common for isolation bearings used in civil engineering applications.

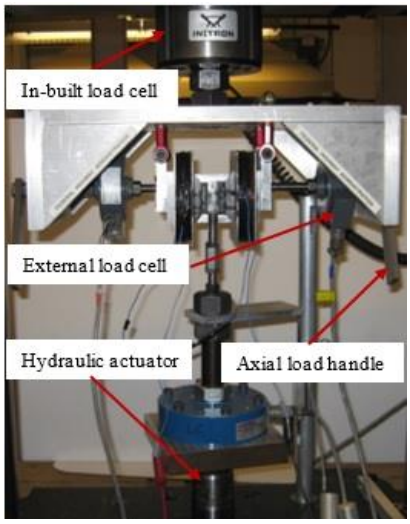


**Figure 1.** Experimental setup for characterization of NR-based MREs

### 4.2.3. Summary of experimental observations

The overall performance of MRE samples subjected to various magnetic field intensities, *B* was quantified in terms of percentage of MR effect as:

$$\%\text{MR effect} = \frac{G_{on} - G_{off}}{G_{off}} * 100 \quad (1)$$

where $G_{off}$ and $G_{on}$ are shear moduli without and with a magnetic field, respectively.

Sinusoidal cyclic tests were performed under pure shear and combined compressive and shear loadings. It was observed that natural rubber-based MRE demonstrated uniform MR effect when subjected to pure shear loading. A uniform MR effect of approximately 30% was observed at all strain amplitudes. This observation was attributed to the random distribution of iron particles that allow formation of alternative magnetic-field paths irrespective of the amount of shear deformation. Under combined loading condition, it was observed that samples showed higher MR effect (92%) under low strain amplitudes (10%). The MR effect reduced asymptotically to 30% at 100% shear strains under combined compressive and shear loading. This observation was

attributed to the fact that compressive force reduces distance between iron particles thus causing increase in MR effect at low strain amplitudes. However, this effect diminishes with increasing strain due to increased distance between iron particles. It was observed that both storage (stiffness) and loss (damping) moduli show increasing trend with increased frequency or magnetic-field for any given strain amplitude under pure shear. However, MR effect reduced with increasing frequencies. Further detailed discussion of experimental observations are presented in [5].

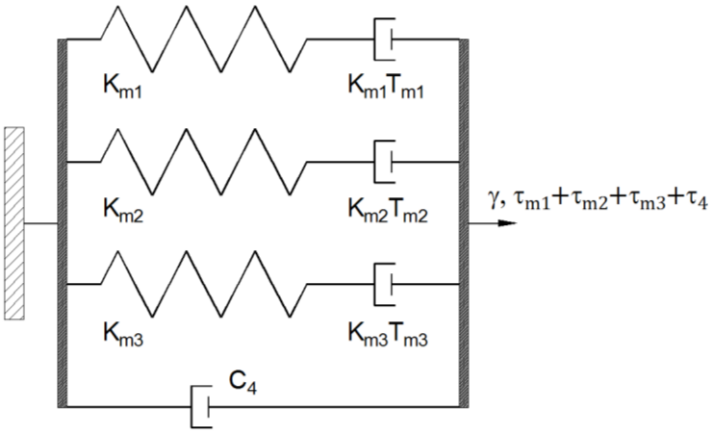


**Figure 2.** Seven-parameter viscoelastic model for natural rubber-based MREs

## 4.3. Material modelling of natural rubber-based MRE

A seven-parameter viscoelastic model, depicted in Figure 2 was developed to simulate the experimentally observed response of natural rubber-based MREs. In this model, a single dashpot and Maxwell models are arranged in parallel branches as shown in the Figure 2. The dashpot element, $C_4$, represents the variation of effective material damping as a function of frequency. The model establishes relationship between shear stress and strain. It is noted that while pure natural rubber is expected to demonstrate essentially pure viscoelastic characteristics, natural rubber compounds with additives (iron particles and carbon black) possess nonlinear hysteretic and damping properties. However, equivalent linear representation of mechanical properties

provides valuable insight towards establishing unified nonlinear viscoelastic models. Accordingly, the general relationship between complex shear strain, $\gamma^*$ and stress, $\tau^*$ is represented through complex modulus, $G^*$ as:

$$\tau^* = G^* \gamma^* = (G' + i\, G'')\, \gamma^* \tag{2}$$

in which $G'$ and $G''$ are storage and loss modulus, respectively. The storage ($G'$) and loss ($G''$) modulus expressions for the proposed seven-parameter model can be derived using integral formulations and the Laplace transform as summarized in Eq. (3) through Eq. (12). Accordingly, the moduli are represented in terms of the seven model parameters as follows:

$$G' = \frac{(-\omega^2 b_2 + \omega^4 b_4)(a_0 - \omega^2 a_2) + (\omega b_1 - \omega^3 b_3)(\omega a_1 - \omega^3 a_3)}{(a_0 - \omega^2 a_2)^2 + (\omega a_1 - \omega^3 a_3)^2} \tag{3}$$

$$G'' = \frac{(\omega b_1 - \omega^3 b_3)(a_0 - \omega^2 a_2) - (-\omega^2 b_2 + \omega^4 b_4)(\omega a_1 - \omega^3 a_3)}{(a_0 - \omega^2 a_2)^2 + (\omega a_1 - \omega^3 a_3)^2} \tag{4}$$

in which $\omega = 2\pi f$ is the circular frequency (r/sec) of the excitation, $f$ = frequency (Hz) and the model parameters are:

$$a_0 = K_{m1} K_{m2} K_{m3} \tag{5}$$

$$a_1 = K_{m1} K_{m2} K_{m3} (T_{m1} + T_{m2} + T_{m3}) \tag{6}$$

$$a_2 = K_{m1} K_{m2} K_{m3} (T_{m1} T_{m2} + T_{m2} T_{m3} + T_{m3} T_{m1}) \tag{7}$$

$$a_3 = K_{m1} K_{m2} K_{m3} T_{m1} T_{m2} T_{m3} \tag{8}$$

$$b_1 = K_{m1} K_{m2} K_{m3} (T_{m1} K_{m1} + T_{m2} K_{m2} + T_{m3} K_{m3} + C_4) \tag{9}$$

$$b_2 = K_{m1}K_{m2}K_{m3}\,(K_{m1}T_{m1}T_{m2} + K_{m1}T_{m3}T_{m1} + K_{m2}T_{m1}T_{m2} + K_{m2}T_{m2}T_{m3} + K_{m3}T_{m1}T_{m3} + K_{m3}T_{m2}T_{m3} + T_{m1}C_4 + T_{m2}C_4 + T_{m3}C_4) \quad (10)$$

$$b_3 = K_{m1}K_{m2}K_{m3}T_{m1}T_{m2}T_{m3}\,(K_{m1} + K_{m2} + K_{m3}) + K_{m1}K_{m2}K_{m3}\,C_4(T_{m1}T_{m2} + T_{m2}T_{m3} + T_{m3}T_{m1}) \quad (11)$$

$$b_4 = K_{m1}K_{m2}K_{m3}T_{m1}T_{m2}T_{m3}C_4 \quad (12)$$

If the applied shear strain, γ(t) is a harmonic excitation (Eq. (13)), the corresponding shear stress and phase angle is given by Eq. (14) and Eq. (15), respectively. It is noted that $\delta$ is the loss factor as a measure of energy dissipation capacity.

$$\gamma(t) = \gamma_0 \sin(\omega t) \quad (13)$$

$$\tau(t) = \gamma_0\sqrt{(G')^2 + (G'')^2}\sin(\omega t + \varphi) \quad (14)$$

$$\delta = \tan(\varphi) = G''/G' \quad (15)$$

### 4.3.1. Identification of viscoelastic model parameters

The storage and loss moduli were calculated from the experimentally recorded cyclic shear stress versus strain response data. The model parameters ($K_{m1}$, $K_{m2}$, $K_{m3}$, $T_{m1}$, $T_{m2}$, $T_{m3}$, and $C_4$) were identified using Nonlinear Generalized Reduced Gradient (GRG) method implemented in MS Excel, by minimizing simultaneously the square-root-of-sum-of-squares (SRSS) error between the experimentally measured and the model-predicted moduli (Eq. (3) through Eq. (12)) for a given strain amplitude as:

$$\epsilon = \left[\sum_{i=1}^{n_\omega} [G'_E(\omega_i) - G'_M(\omega_i)]^2 + \left[G''_E(\omega_i) - \alpha(\gamma, B)G''_M(\omega_i)\right]^2\right]^{1/2} \quad (16)$$

in which $G'_E$ and $G''_E$ are experimentally measured moduli and $G'_M$ and $G''_M$ are corresponding model predicted values, $\alpha(\gamma, B)$ is loss modulus adjustment factor as discussed further below, $B$ = magnetic field intensity in Tesla, and $n_\omega$ is the number of frequency measurements.

The parameters $K_{m1}$, $K_{m2}$, $K_{m3}$, represent the effective stiffness contributions of natural rubber-based MRE material. These parameters decrease with increasing strain amplitude due to strain-softening (Figure 3 (a), 3(b), 3(c)). Initial overall stiffness of the samples at small strain amplitudes was determined as 6.89 N/mm/mm from monotonic shear force-deformation response. This initial stiffness conforms with the model-predicted combined effective stiffness ($K_{m1}+K_{m2}+K_{m3}$) of 5.35 N/mm/mm at zero magnetic field and 10% shear strain.

The dashpot constant $C_4$, represents primarily frequency dependency of loss modulus with respect to storage modulus, hence damping as a function of the frequency of imposed deformations. In essence, dashpot element intends to simulate the fluid-like behavior. This effect can be seen due to consistently reducing $C_4$ values for increasing strain (Figure 3(d)), while it remains nearly constant for all magnetic-field intensities for a given strain amplitude. The proposed model decouples the individual effects of strain versus magnetic field on the measured damping via $\alpha$ parameter in Eq. (16). As can be seen in Figure 3(e), the loss modulus adjustment factor, $\alpha$ increases linearly with respect to the applied magnetic field and demonstrates increasing contributions at larger strain amplitudes. When the material is subjected to increasing strains, and furthermore subjected to increasing magnetic-field intensities, particle surface areas contributing to interparticle friction increases. Therefore, friction induced damping

contributes to the overall effecting damping and may offset the reduction in $C_4$. It is noted that both $C_4$ and $\alpha$ have net effects on the loss modulus only, however, as it is further demonstrated in the following section, the magnetic field does not lead to any significant effect on the overall damping.

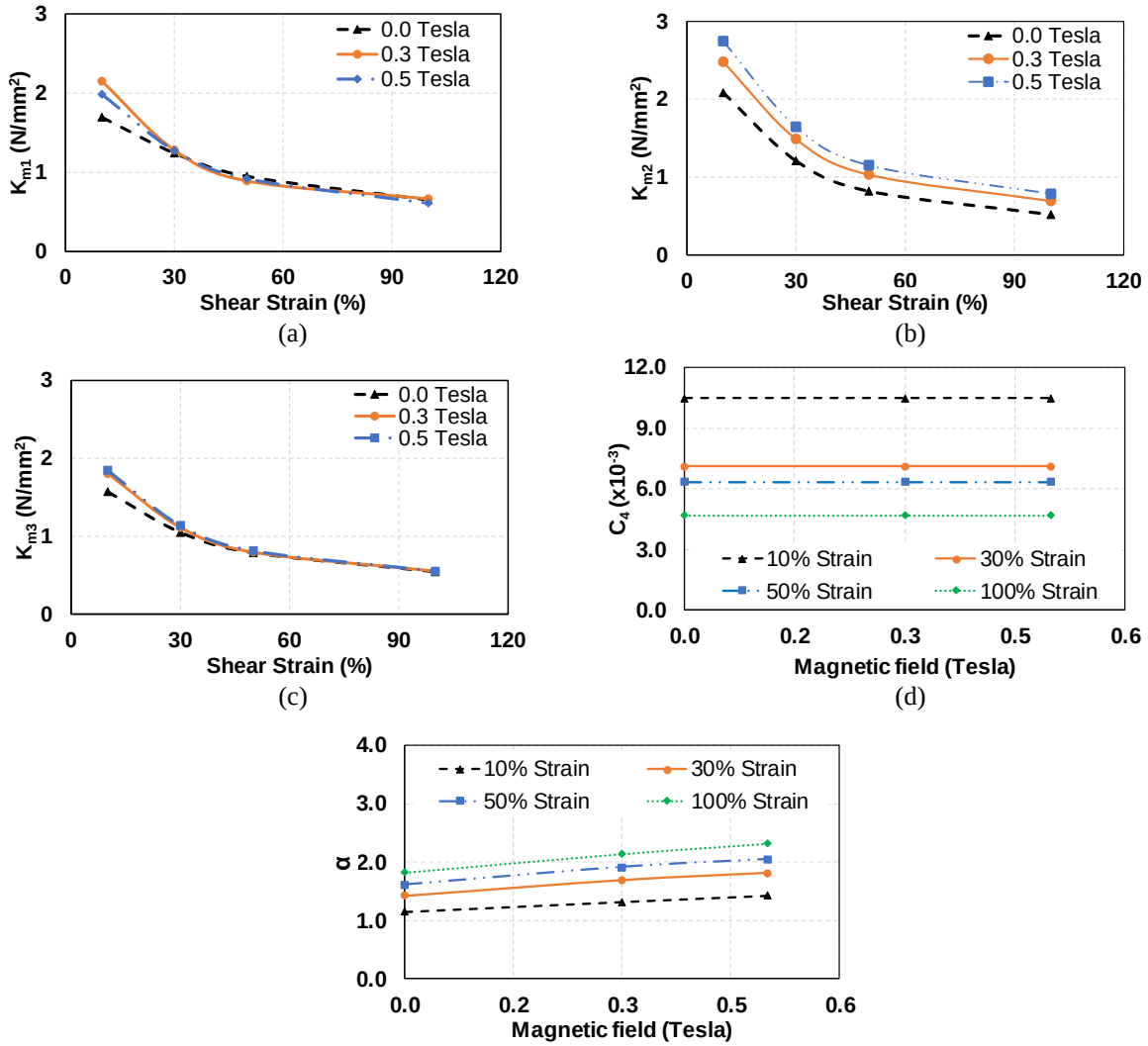


**Figure 3.** Variations of model parameters.

Furthermore, $T_{m1}$, $T_{m2}$, $T_{m3}$ suggest different relaxation times as expected based on average particle sizes of molecules in natural rubber, iron particles (micron) and carbon black (nanometre). Model predicted relaxation time for $T_{m1}$, $T_{m2}$, and $T_{m3}$ are 0.03, 5.60, and 0.24 sec,

respectively. Viscoelastic flow in the material or breakage of the hydrocarbon chains supporting the stress are possible reasons for stress relaxation.

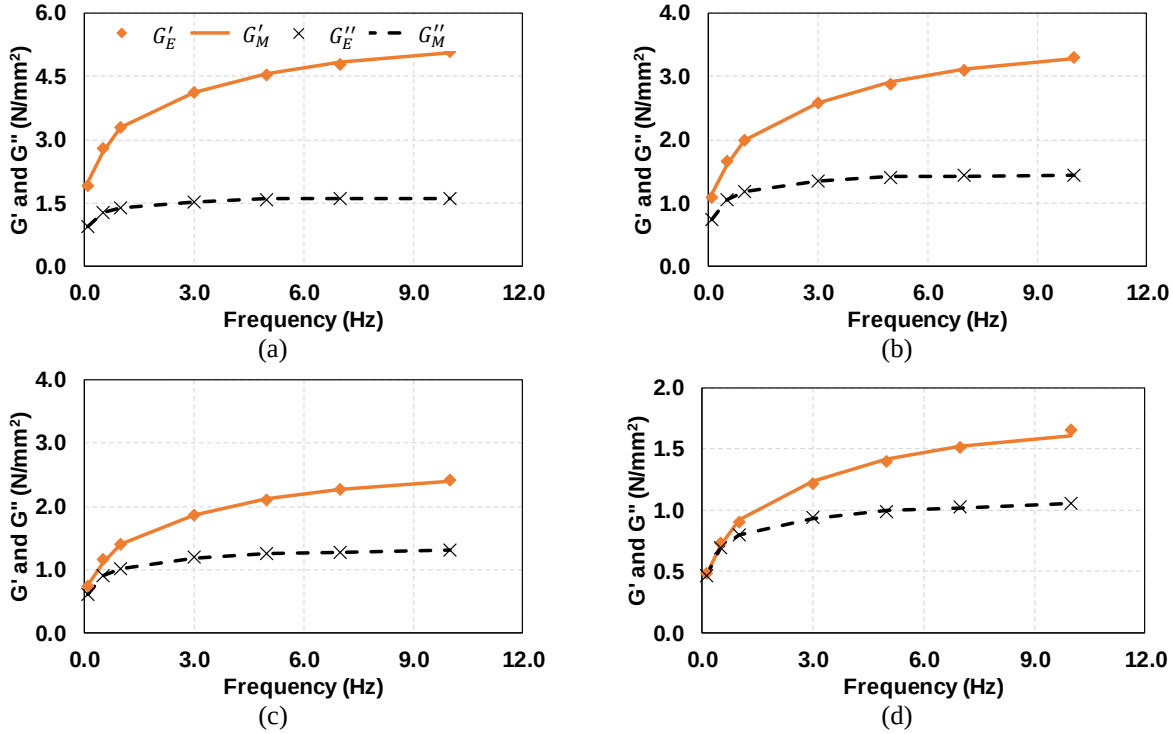


**Figure 4.** Effect of frequency on the moduli, *B*=0 Tesla and shear strain: (a) 10%, (b) 30%, (c) 50% and (d) 100%

## 4.4. Experimental results versus model-predicted response

### 4.4.1. Pure shear loading

The storage and loss moduli predicted by the proposed seven-parameter model are compared to experimentally calculated values in Figure 4 and Table 2. As can be seen in Figure 4, experimental and model predicted storage and loss modulus both increase with increasing frequency for a given strain amplitude. Table 2 summarizes the experimentally calculated and model predicted storage, loss moduli, corresponding regression error, and loss factor ($\delta = G''/G'$). Comparison of model predicted and experimentally determined shear and loss moduli with varying magnetic fields is presented in Figure 5. As can be seen in the

Figure, both storage and loss moduli increase with increased magnetic fields for any given strain amplitude. This trend confirms that natural rubber-based MRE exhibits variable stiffness properties.

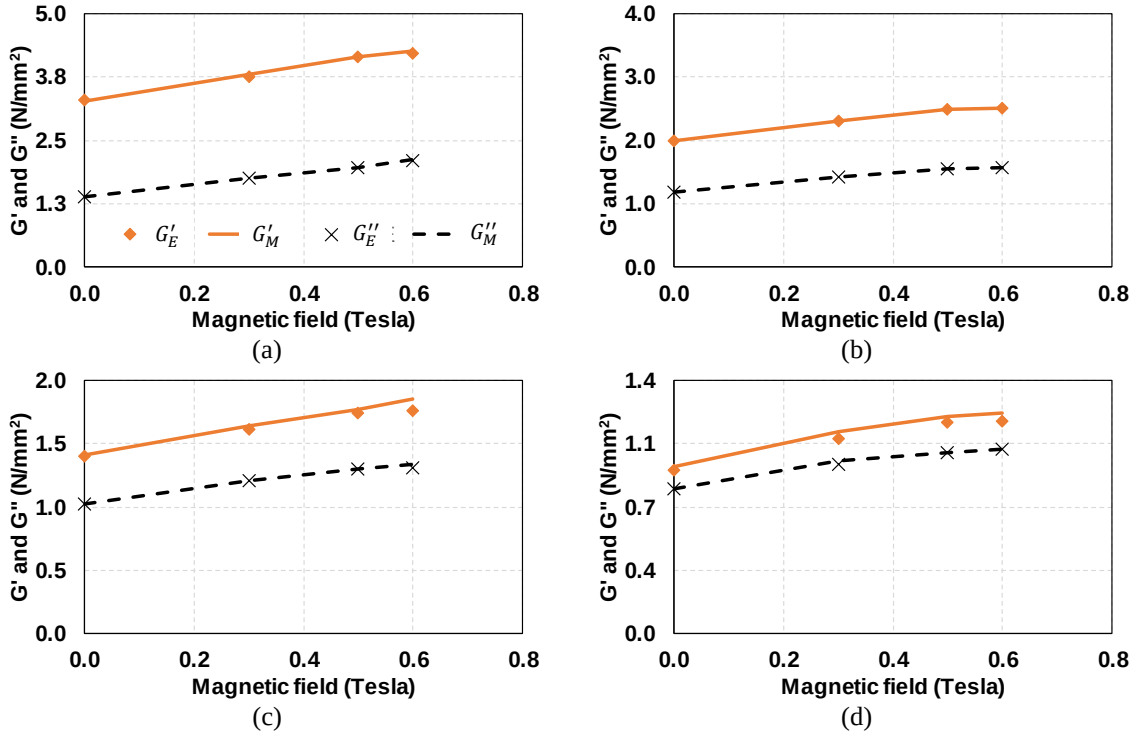


**Figure 5.** Effect of magnetic field on the rheological properties; f=1 Hz, shear strain: (a) 10%, (b) 30%, (c) 50% and (d) 100%

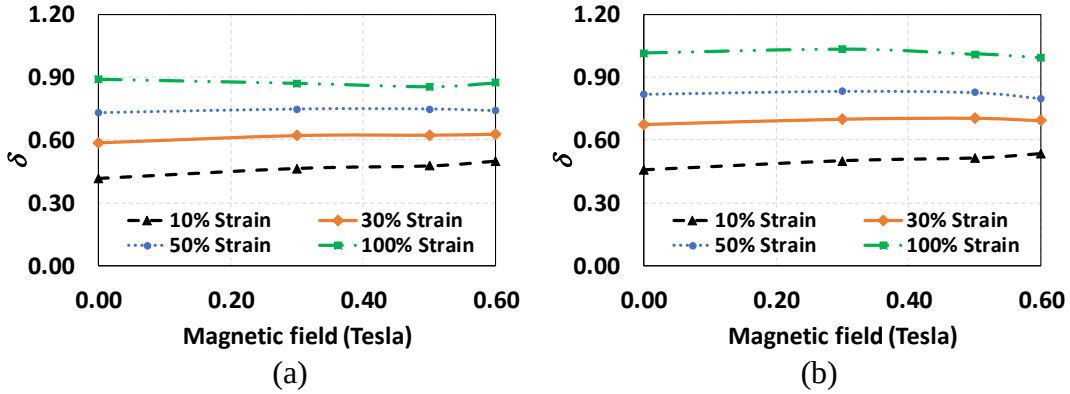


**Figure 6.** Variation of damping with respect to magnetic field; (a) P = 0, (b) P = 445 N

**Table 2.** Experimental Versus Model Predicted Moduli ($N/mm^2$), *B = 0*.

| Frequency (Hz) | $G'_E$ | $G'_M$ | Error (%) | $G''_E$ | $G''_M$ | Error (%) | δ=G"/G' |
|---|---|---|---|---|---|---|---|
| 10% Shear Strain | | | | | | | |
| 1.0 | 3.30 | 3.25 | 1.5 | 1.38 | 1.38 | 0.0 | 0.42 |
| 3.0 | 4.12 | 4.11 | 0.2 | 1.53 | 1.52 | 0.7 | 0.37 |
| 5.0 | 4.55 | 4.57 | 0.4 | 1.58 | 1.59 | 0.6 | 0.35 |
| 7.0 | 4.80 | 4.85 | 1.0 | 1.60 | 1.59 | 0.6 | 0.33 |
| 10.0 | 5.09 | 5.06 | 0.6 | 1.61 | 1.61 | 0.0 | 0.32 |
| 30% Shear Strain | | | | | | | |
| 1.0 | 1.99 | 1.99 | 0.0 | 1.17 | 1.17 | 0.0 | 0.59 |
| 3.0 | 2.58 | 2.58 | 0.0 | 1.34 | 1.34 | 0.0 | 0.52 |
| 5.0 | 2.88 | 2.91 | 1.0 | 1.41 | 1.42 | 0.7 | 0.49 |
| 7.0 | 3.09 | 3.11 | 0.6 | 1.44 | 1.43 | 0.7 | 0.47 |
| 10.0 | 3.31 | 3.28 | 0.9 | 1.44 | 1.44 | 0.0 | 0.44 |
| 50% Shear Strain | | | | | | | |
| 1.0 | 1.40 | 1.41 | 0.7 | 1.02 | 1.02 | 0.0 | 0.73 |
| 3.0 | 1.86 | 1.86 | 0.0 | 1.19 | 1.19 | 0.0 | 0.64 |
| 5.0 | 2.10 | 2.12 | 1.0 | 1.25 | 1.26 | 0.8 | 0.60 |
| 7.0 | 2.26 | 2.27 | 0.4 | 1.28 | 1.27 | 0.8 | 0.57 |
| 10.0 | 2.42 | 2.39 | 1.2 | 1.30 | 1.30 | 0.0 | 0.54 |
| 100% Shear Strain | | | | | | | |
| 1.0 | 0.90 | 0.92 | 2.2 | 0.80 | 0.80 | 0.0 | 0.89 |
| 3.0 | 1.22 | 1.24 | 1.6 | 0.94 | 0.94 | 0.0 | 0.77 |
| 5.0 | 1.39 | 1.42 | 2.2 | 0.99 | 1.00 | 1.0 | 0.71 |
| 7.0 | 1.51 | 1.52 | 0.7 | 1.02 | 1.02 | 0.0 | 0.68 |
| 10.0 | 1.65 | 1.60 | 3.0 | 1.05 | 1.06 | 1.0 | 0.64 |

As it was reported by [4, 5], magnetic field does not have sensible effect on the damping of natural rubber based MREs. This is demonstrated in Figure 6 (a) in terms of the measured $\delta$ corresponding to 1.0 Hz cyclic tests for various shear strain amplitudes. While the damping increases for strain amplitudes that are less than 30%, the increase is not of any practical magnitude. The same observation is valid in the presence of compressive loads on the samples (Figure 6 (b)). It is noted that the apparent damping is larger for higher shear strains, and corresponding values due to compressive loads are higher as expected.

Figure 7 shows the reconstructed shear force versus displacement hysteresis for different strain amplitudes at a frequency of 1 Hz. As can be seen in the Figure, the model is able to simulate the hysteretic MRE's response considerably well particularly for small strain response.

However, the hysteretic response of the MRE deviates - from that of a viscoelastic material at large strain amplitude.

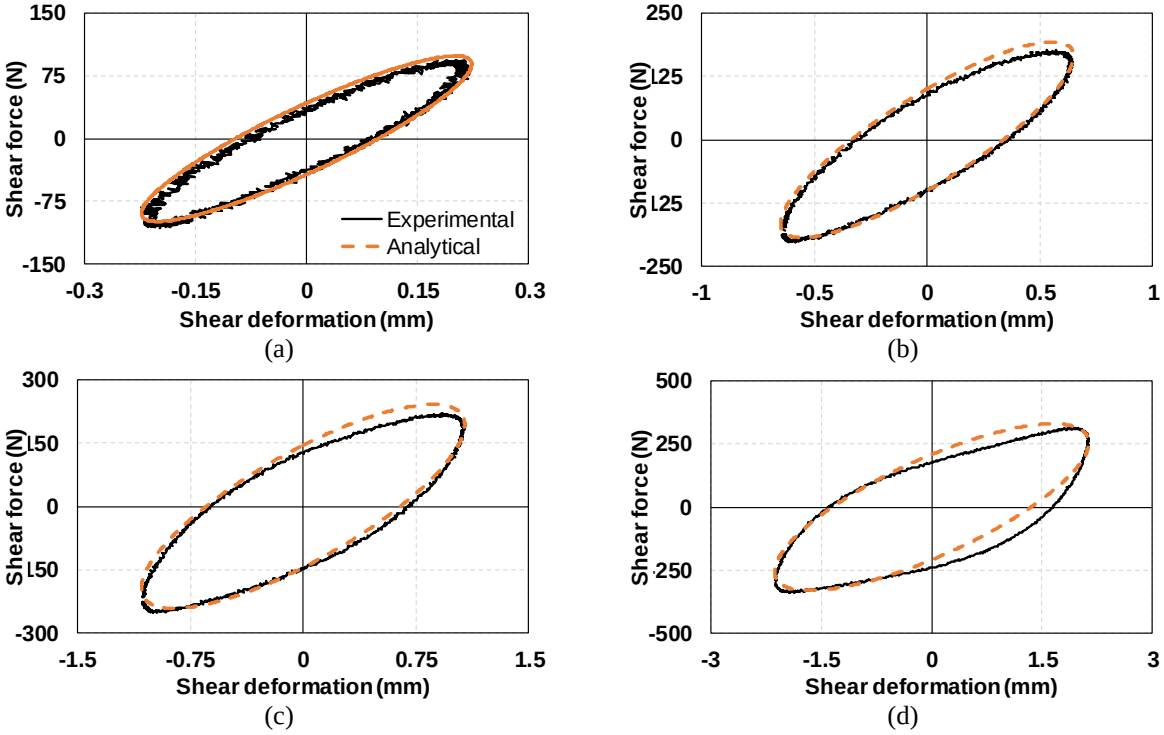


**Figure 7.** Shear force – deformation; *f*=1 Hz, *B*=0 Tesla, and shear strain: (a) 10%, (b) 30%, (c) 50% and (d) 100%

### 4.4.2. Combined compressive and shear load

The NR-S-4 sample was further tested under a constant compressive load of $P$ = 445 N for different shear strains, frequencies, and magnetic field strengths. Compressive load was chosen to result in typical axial stress (0.7 N/mm$^2$) in bridge bearing applications [4]. Figure 8 shows the estimated model parameter variations. Applied compressive load reduces the distance between iron particles thus increase magnetic field effect due to iron particles in comparison to pure shear results (Figure 3). On the other hand, the apparent moduli are slight reduced due to the presence of compressive load.

Figure 9 shows the comparison between experimentally calculated versus model predicted storage and loss moduli over the range of test frequencies and under a constant

compressive load (445 N). Table 3 summarizes the experimentally calculated and model predicted storage, loss moduli, corresponding regression error, and damping. Figure 10 shows the magnetic field effect on storage and loss modulus for varying shear strains. As can be seen in Figure 10, both moduli increase with increasing magnetic field for any given strain amplitude. However, magnetic field effect on storage and loss moduli at higher fields reduces due to near saturation of iron particles. In addition, it can be observed that both moduli decrease with increased strain. These observations indicate that the model predicts MR effect and axial load effect on natural rubber based MRE properties.

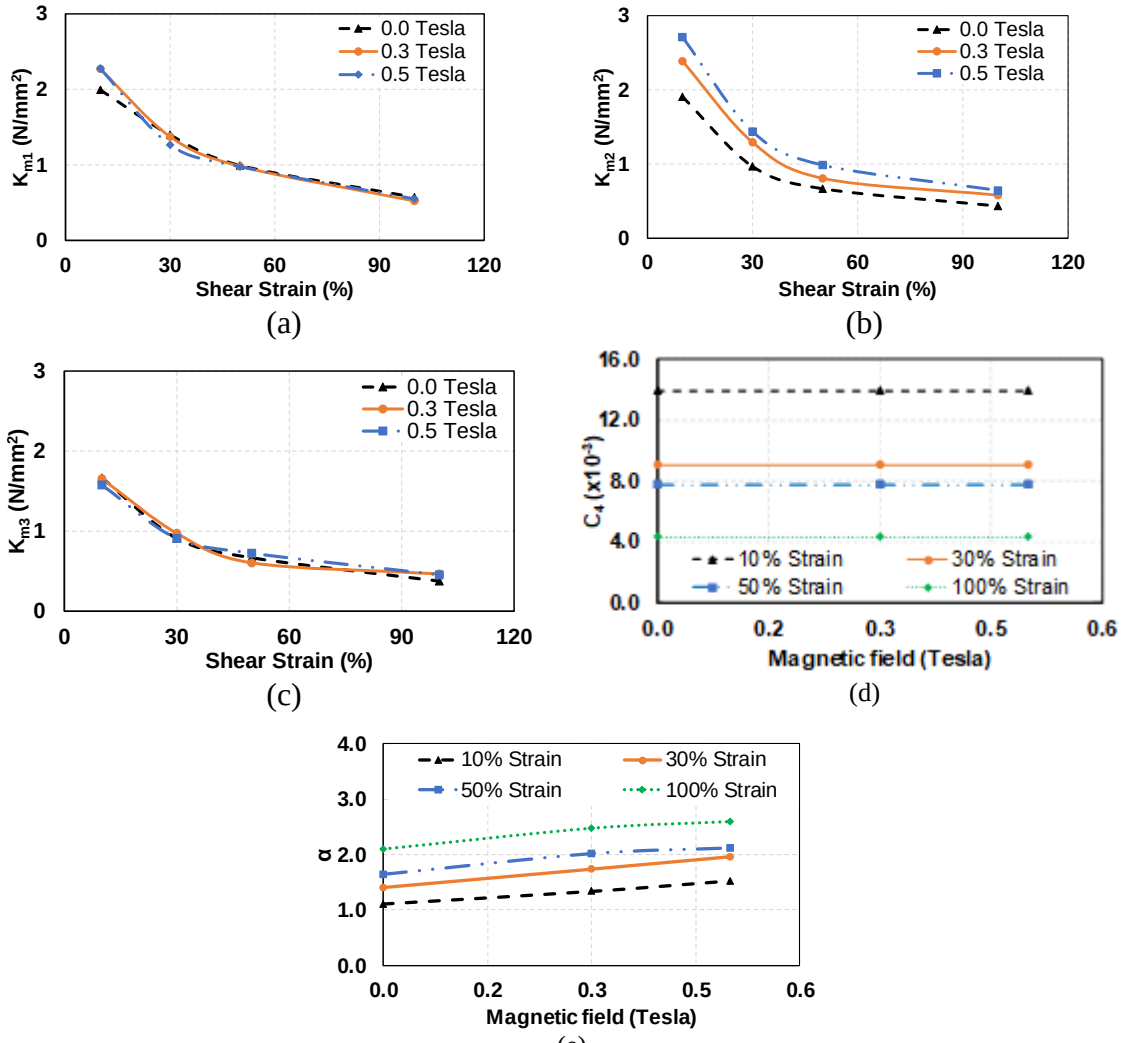


**Figure 8.** Variations in model parameters, P= 445 N

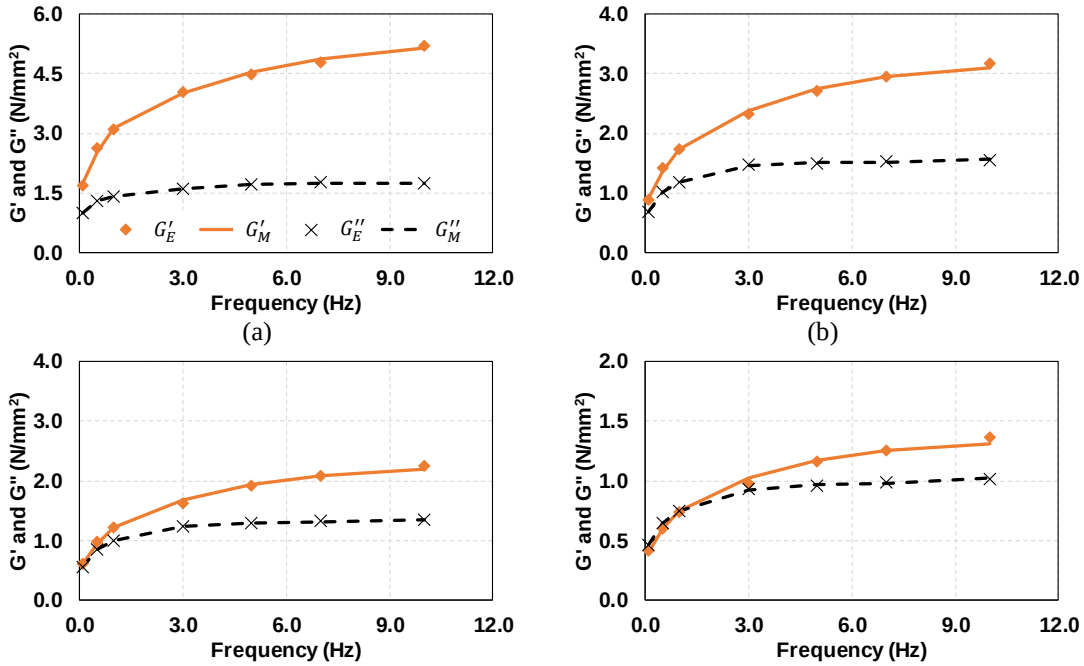


**Figure 9.** Effect of frequency on the rheological properties under combined loading, *B*=0 Tesla, and shear strain: (a) 10%, (b) 30%, (c) 50 and (d) 100%

**Table 3.** Experimental Versus Model Predicted Moduli (N/mm$^2$), *B = 0*, P = 445 N.

| Frequency (Hz) | $G'_E$ | $G'_M$ | Error (%) | $G''_E$ | $G''_M$ | Error (%) | G”/G’ |
|---|---|---|---|---|---|---|---|
| 10% Shear Strain | | | | | | | |
| 1.0 | 3.10 | 3.13 | 1.0 | 1.42 | 1.42 | 0.0 | 0.46 |
| 3.0 | 4.04 | 4.01 | 0.7 | 1.61 | 1.60 | 0.6 | 0.40 |
| 5.0 | 4.49 | 4.52 | 0.7 | 1.70 | 1.72 | 1.2 | 0.38 |
| 7.0 | 4.80 | 4.86 | 1.3 | 1.76 | 1.74 | 1.1 | 0.37 |
| 10.0 | 5.20 | 5.15 | 1.0 | 1.74 | 1.74 | 0.0 | 0.33 |
| 30% Shear Strain | | | | | | | |
| 1.0 | 1.74 | 1.73 | 0.6 | 1.17 | 1.17 | 0.0 | 0.67 |
| 3.0 | 2.32 | 2.38 | 2.6 | 1.47 | 1.46 | 0.7 | 0.63 |
| 5.0 | 2.75 | 2.75 | 0.0 | 1.50 | 1.52 | 1.3 | 0.55 |
| 7.0 | 2.95 | 2.95 | 0.0 | 1.53 | 1.52 | 0.7 | 0.52 |
| 10.0 | 3.10 | 3.10 | 0.0 | 1.55 | 1.56 | 0.6 | 0.50 |
| 50% Shear Strain | | | | | | | |
| 1.0 | 1.21 | 1.21 | 0.0 | 0.99 | 0.99 | 0.0 | 0.82 |
| 3.0 | 1.63 | 1.68 | 3.1 | 1.24 | 1.24 | 0.0 | 0.76 |
| 5.0 | 1.91 | 1.94 | 1.6 | 1.28 | 1.30 | 1.6 | 0.67 |
| 7.0 | 2.09 | 2.09 | 0.0 | 1.32 | 1.31 | 0.8 | 0.63 |
| 10.0 | 2.20 | 2.20 | 0.0 | 1.35 | 1.35 | 0.0 | 0.61 |
| 100% Shear Strain | | | | | | | |
| 1.0 | 0.73 | 0.75 | 2.7 | 0.74 | 0.74 | 0.0 | 1.01 |
| 3.0 | 0.98 | 1.02 | 4.1 | 0.93 | 0.92 | 1.1 | 0.95 |
| 5.0 | 1.16 | 1.18 | 1.7 | 0.95 | 0.96 | 1.1 | 0.82 |
| 7.0 | 1.26 | 1.26 | 0.0 | 0.98 | 0.97 | 1.0 | 0.78 |
| 10.0 | 1.36 | 1.31 | 3.7 | 1.02 | 1.02 | 0.0 | 0.75 |

Figure 11 show the reconstructed hysteretic shear force - deformation relationship for 10% and 100% strain amplitudes and for different axial loads (0 and 445 N) with varying magnetic field (0 and 0.6 Tesla). As can be seen in the Figure, the effective stiffness increases with increased magnetic field for all strain amplitudes. In general, equivalent damping is proportional to the hysteresis area, which represent the energy dissipation of a cycle. However, as it can be inferred from Figure 11 that the magnetic field has a nominal effect on the damping at small strain amplitude, and the effect diminishes for larger strain values. Furthermore, a similar conclusion can be derived in case the MRE is subjected to compressive loads.

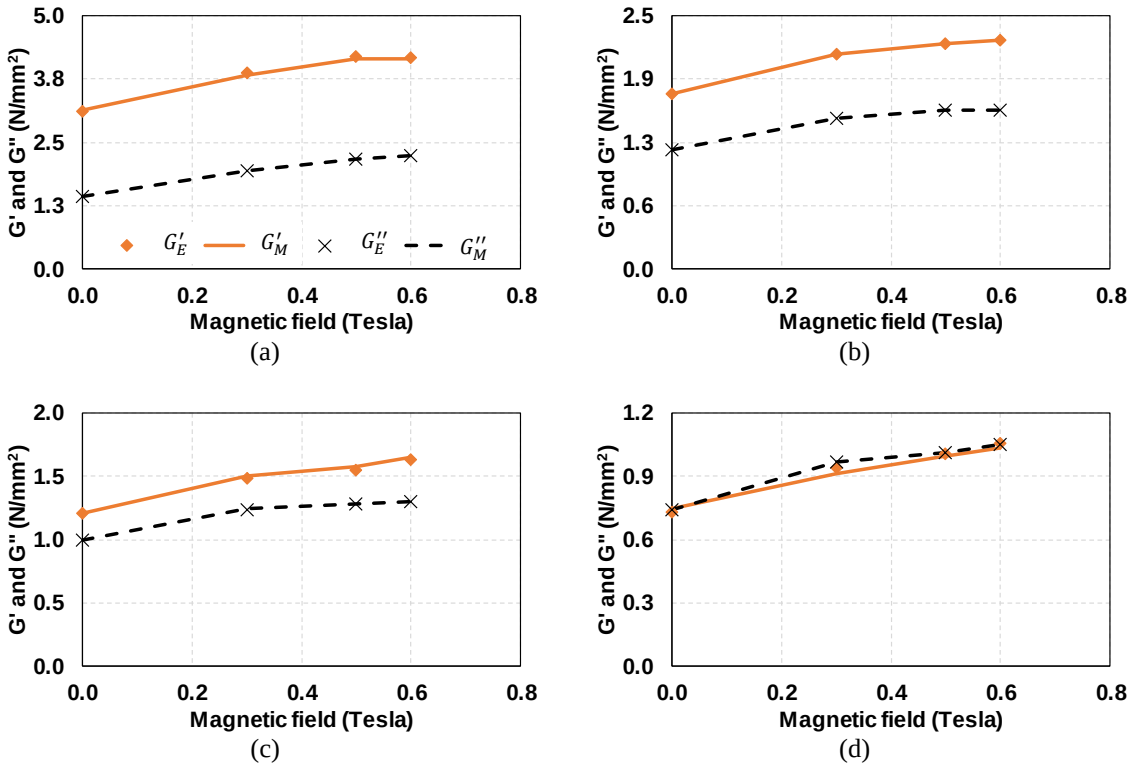


**Figure 10.** Effect of magnetic field on the rheological properties P = 445 N, shear strain - f: (a) 10% - 1 Hz, (b) 30% - 1 Hz (c) 50% - 5 Hz and (d) 100% - 5 Hz

## 4.5. Concluding remarks

A seven-parameter viscoelastic model was developed to predict the static and dynamic behavior of the natural rubber-based isotropic magnetorheological elastomers. The parameters were

identified using nonlinear GRG method implemented in Excel, by simultaneously minimizing SRSS error between experimentally determined and model predicted moduli for different excitation frequencies, strains and magnetic fields. The stiffness contribution increases with increased magnetic field for any given strain amplitude as magnetic field attracts particles towards each other and this effect increases further under axial force. However, strain-softening, the shear stiffness of MRE reduces under large strains.

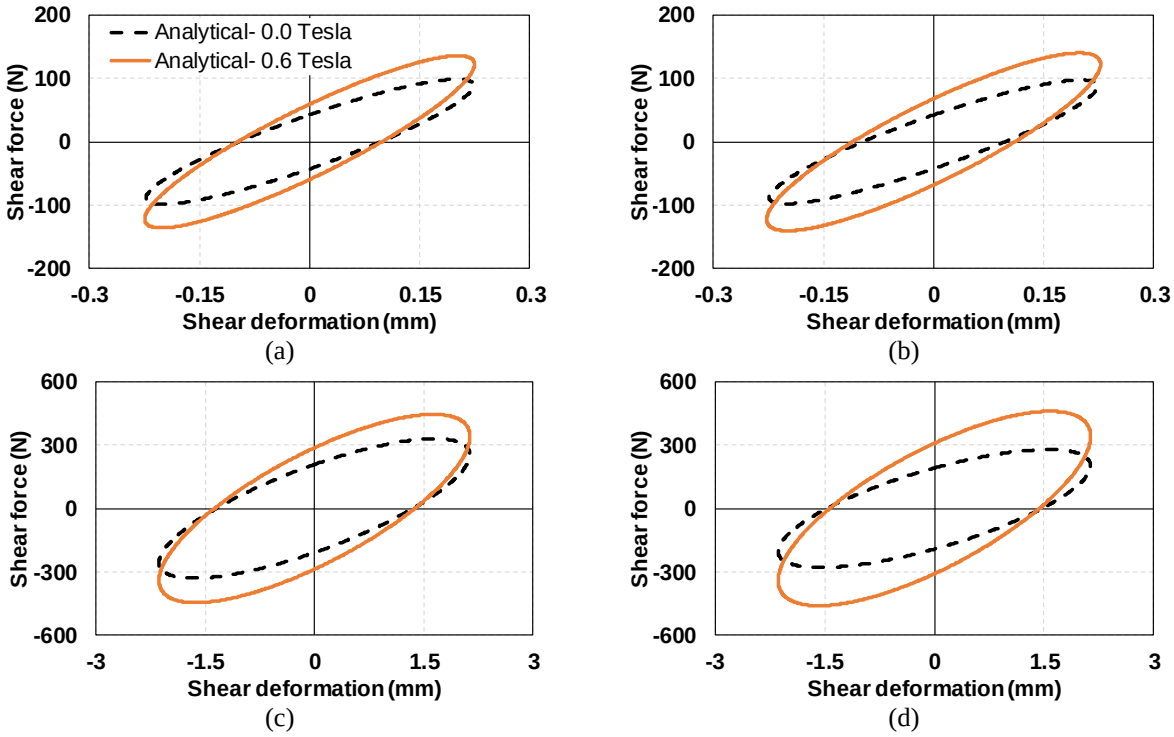


**Figure 11.** Model predicted shear force - deformation hysteresis under two different compressive load conditions and with varying magnetic field, shear strain-P: (a) 10% - 0 N (b) 10% - 445 N (c) 100% - 0 N and (d) 100% - 445 N

The comparison between the predicted and experimental storage and loss moduli, and effect of magnetic field thereof, demonstrated the validity of the proposed model.

Accurate model should be able to predict the response of MRE materials due to changes in stiffness, damping, and hysteresis under varying strains, frequencies, magnetic fields, and

axial loads. The accuracy with linear models when it comes to predicting stiffness and damping seems to be satisfactory. However, the simulation of highly nonlinear hysteretic response of rubber-based materials presents a challenge due to complex particle interactions, cyclic Mullins and Payne effects, and hyper-elasticity. Therefore, there is a need to develop models which can incorporates nonlinearity of material characteristics such as hysteresis shape and strain-hardening of MRE due to large strains. In addition to nonlinear viscoelasticity models, the nonlinear stress-strain response may be described using phenomenological models that can incorporate effect of magnetic field in case of MREs.

## 4.6. Acknowledgements

The author(s) would like to acknowledge the funding of Federal Highway Administration (FHWA) under contract DTFH61-13-C00020.

## 4.7. References

[1] H. Du, W. Li, N. Zhang, Semi-active variable stiffness vibration control of vehicle seat suspension using an MR elastomer isolator, Smart Mater. Struct. 20 (2011). doi:10.1088/0964-1726/20/10/105003.

[2] G. Liu, K. Lu, D. Zou, Z. Xie, Z. Rao, N. Ta, Development of a semi-active dynamic vibration absorber for longitudinal vibration of propulsion shaft system based on magnetorheological elastomer, Smart Mater. Struct. 26 (2017). doi:10.1088/1361-665X/aa73f3.

[3] M. Behrooz, X. Wang, F. Gordaninejad, Seismic Control of Base Isolated Structures Using Novel Magnetorheological Elastomeric Bearings, Vol. 1 Dev. Charact. Multifunct. Mater. Model. Simul. Control Adapt. Syst. Integr. Syst. Des. Implement. (2013) V001T03A027. doi:10.1115/SMASIS2013-3147.

[4] S. Yarra, F. Gordaninejad, M. Behrooz, G. Pekcan, A.M. Itani, N. Publicover, Performance of a large-scale magnetorheological elastomer–based vibration isolator for

highway bridges, J. Intell. Mater. Syst. Struct. (2018) 1045389X1879949. doi:10.1177/1045389X18799493.

[5] S. Yarra, F. Gordaninejad, M. Behrooz, G. Pekcan, Performance of natural rubber and silicone-based magnetorheological elastomers under large-strain combined axial and shear loading, J. Intell. Mater. Syst. Struct. (2018) 1045389X1880839. doi:10.1177/1045389X18808393.

[6] M.A. Cantera, M. Behrooz, R.F. Gibson, F. Gordaninejad, Modeling of magneto-mechanical response of magnetorheological elastomers (MRE) and MRE-based systems: A review, Smart Mater. Struct. 26 (2017). doi:10.1088/1361-665X/aa549c.

[7] R. Greco, G.C. Marano, Identification of parameters of Maxwell and Kelvin-Voigt generalized models for fluid viscous dampers, JVC/Journal Vib. Control. 21 (2015) 260–274. doi:10.1177/1077546313487937.

[8] M. Behrooz, X. Wang, F. Gordaninejad, Modeling of a new semi-active/passive magnetorheological elastomer isolator, Smart Mater. Struct. 23 (2014). doi:10.1088/0964-1726/23/4/045013.

[9] Y. Han, W. Hong, L.E. Faidley, Field-stiffening effect of magneto-rheological elastomers, Int. J. Solids Struct. 50 (2013) 2281–2288. doi:10.1016/j.ijsolstr.2013.03.030.

[10] S. Rudykh, K. Bertoldi, Stability of anisotropic magnetorheological elastomers in finite deformations: A micromechanical approach, J. Mech. Phys. Solids. 61 (2013) 949–967. doi:10.1016/j.jmps.2012.12.008.

[11] G. Schubert, P. Harrison, Magnetic induction measurements and identification of the permeability of Magneto-Rheological Elastomers using finite element simulations, J. Magn. Magn. Mater. 404 (2016) 205–214. doi:10.1016/j.jmmm.2015.12.003.

[12] Y. Shen, M.F. Golnaraghi, G.R. Heppler, Experimental research and modeling of magnetorheological elastomers, J. Intell. Mater. Syst. Struct. 15 (2004) 27–35. doi:10.1177/1045389X04039264.

[13] X. Zhang, W. Li, X.L. Gong, An effective permeability model to predict field-dependent modulus of magnetorheological elastomers, Commun. Nonlinear Sci. Numer. Simul. 13 (2008) 1910–1916. doi:10.1016/j.cnsns.2007.03.029.

[14] K. Danas, S. V. Kankanala, N. Triantafyllidis, Experiments and modeling of iron-particle-filled magnetorheological elastomers, J. Mech. Phys. Solids. 60 (2012) 120–138. doi:10.1016/j.jmps.2011.09.006.

[15] L. Daniel, M. Rekik, O. Hubert, A multiscale model for magneto-elastic behaviour including hysteresis effects, Arch. Appl. Mech. 84 (2014) 1307–1323. doi:10.1007/s00419-014-0863-9.

[16] A. Boczkowska, S.F. Awietjan, S. Pietrzko, K.J. Kurzydłowski, Mechanical properties of magnetorheological elastomers under shear deformation, Compos. Part B Eng. 43 (2012) 636–640. doi:10.1016/j.compositesb.2011.08.026.

[17] L. Chen, S. Jerrams, A rheological model of the dynamic behavior of magnetorheological elastomers, J. Appl. Phys. 110 (2011) 1–7. doi:10.1063/1.3603052.

[18] S.H. Eem, H.J. Jung, J.H. Koo, Modeling of magneto-rheological elastomers for harmonic shear deformation, IEEE Trans. Magn. 48 (2012) 3080–3083. doi:10.1109/TMAG.2012.2205140.

[19] W.H. Li, Y. Zhou, T.F. Tian, Viscoelastic properties of MR elastomers under harmonic loading, Rheol. Acta. 49 (2010) 733–740. doi:10.1007/s00397-010-0446-9.

[20] P. Saxena, M. Hossain, P. Steinmann, A theory of finite deformation magneto-viscoelasticity, Int. J. Solids Struct. 50 (2013) 3886–3897. doi:10.1016/j.ijsolstr.2013.07.024.

[21] J. Yang, H. Du, W. Li, Y. Li, J. Li, S. Sun, H.X. Deng, Experimental study and modeling of a novel magnetorheological elastomer isolator, Smart Mater. Struct. 22 (2013). doi:10.1088/0964-1726/22/11/117001.

[22] J.T. Zhu, Z.D. Xu, Y.Q. Guo, Magnetoviscoelasticity parametric model of an MR elastomer vibration mitigation device, Smart Mater. Struct. 21 (2012). doi:10.1088/0964-1726/21/7/075034.

[23] W. Zhang, X.L. Gong, W.Q. Jiang, Y.C. Fan, Investigation of the durability of anisotropic magnetorheological elastomers based on mixed rubber, Smart Mater. Struct. 19 (2010) 085008. doi:10.1088/0964-1726/19/8/085008.

[24] D. Ivaneyko, V.P. Toshchevikov, M. Saphiannikova, G. Heinrich, Magneto-sensitive elastomers in a homogeneous magnetic field: A regular rectangular lattice model, Macromol. Theory Simulations. 20 (2011) 411–424. doi:10.1002/mats.201100018.

[25] M. Norouzi, M. Gilani, S.M.S. Alehashem, H. Vatandoost, Dynamic Characterization and Modeling of Isotropic Magnetorheological Elastomers under Tensile-Compressive Loadings, IEEE Trans. Magn. 53 (2017). doi:10.1109/TMAG.2017.2698403.

[26] J. Kaleta, D. Lewandowski, G. Zitek, Inelastic properties of magnetorheological composites: II. Model, identification of parameters, Smart Mater. Struct. 16 (2007) 1954–1960. doi:10.1088/0964-1726/16/5/053.

[27] X. Wang, F. Gordaninejad, A new magnetorheological fluid-elastomer mount: Phenomenological modeling and experimental study, Smart Mater. Struct. 18 (2009). doi:10.1088/0964-1726/18/9/095045.

[28] H.J. Jung, S.H. Eem, D.D. Jang, J.H. Koo, Seismic performance analysis of a smart base-isolation system considering dynamics of MR elastomers, J. Intell. Mater. Syst. Struct. 22 (2011) 1439–1450. doi:10.1177/1045389X11414224.

[29] S. Yarra, G. Pekcan, M. Behrooz, F. Gordaninejad, Characterization of Carbon Black-Filled Natural Rubber and Silicone Magnetorheological Elastomers under Pure Shear Loading CHARACTERIZATION OF CARBON BLACK-FILLED NATURAL RUBBER AND SILICONE MAGNETORHEOLOGICAL, in: 8th ECCOMAS Themat. Conf. Smart Struct. Mater., International Center for Numerical Methods in Engineering (CIMNE), Spain, 2017: pp. 860–870. http://congress.cimne.com/smart2017/frontal/doc/Ebook_SMART2017.pdf.

[30] S. Yarra, M. Behrooz, G. Pekcan, A. Itani, F. Gordaninejad, A large-scale adaptive magnetorheological elastomer-based bridge bearing, in: 2017: p. 1016425. doi:10.1117/12.2257775.

[31] Standard Guide for Dynamic Testing of Vulcanized Rubber.pdf, n.d. doi:D5992-11.

[32] B. Nayak, S.K. Dwivedy, K.S.R.K. Murthy, Fabrication and characterization of magnetorheological elastomer with carbon black, J. Intell. Mater. Syst. Struct. 26 (2015) 830–839. doi:10.1177/1045389X14535011.

[33] L. Chen, X.L. Gong, W.H. Li, Effect of carbon black on the mechanical performances of magnetorheological elastomers, Polym. Test. 27 (2008) 340–345. doi:10.1016/j.polymertesting.2007.12.003.

[34] M. Behrooz, S. Yarra, D. Mar, N. Pinuelas, B. Muzinich, N.G. Publicover, G. Pekcan, A. Itani, F. Gordaninejad, A self-sensing magnetorheological elastomer-based adaptive bridge bearing with a wireless data monitoring system, in: SPIE Proc., 2016: p. 98030D. doi:10.1117/12.2218691.

# Chapter 5. Summary, Conclusions and Recommendations for future research

## 5.1. Summary

This research was focused on the understanding, design, development, testing, and evaluation of an adaptive bearing (AB) system featuring magnetorheological elastomers that has the potential to function as an adaptive bridge bearing. Two quarter-scale ABs with variable stiffness capabilities were fabricated and successfully tested. This study had three groundbreaking features: (1) the MRE material development for an AB, (2) the design of a new AB system, and (3) the large structural loads applied to an MRE-based device.

The MRE materials development, which was an extremely challenging task and had single objective: (a) MRE layers had to have adaptive mechanical properties, withstand large structural forces, and satisfy AASHTO requirements. The AB design had to be (i) a fail-safe system, (ii) constrained by geometric dimensions, and (iii) generating a large enough magnetic field to activate MRE layers.

## 5.2. Conclusions

This research has contributed in understanding of MRE materials, and MRE-based systems, particularly as applied to the bridge bearing application. The conclusions of this study can qualitatively be summarized, as follows:

The first part of the study was focused on to characterize the mechanical properties of TAP silicone- based and Natural rubber-based MREs to improve MR effects under large strains. The conclusions of this study are summarized, as follows:

1. The magnetorheological (MR) effect is defined as the percent change in stiffness and damping properties of MREs when subjected to varying levels of magnetic field. It was

observed that the MR effect can be characteristically different for cases when iron particles are distributed isotopically or anisotropically within the elastomeric compound. The MR effect reduces significantly at large strains for silicone-based anisotropic MRE samples due to increasing distance between iron particles, which are initially aligned in chain-like formations. Furthermore, as these chain-like formations are subjected to shear deformations, the apparent magnetic field intensity diminishes. However, TAP silicone MREs are recommended for lower strain application due to high MR effect.

2. It was observed that the MR effect for shear modulus was very stable and uniform for the natural rubber-based isotropic MRE samples. The MR effect for a given test frequency remained nearly constant (approximately 30%) for a given strain amplitude and with no axial force. The uniform MR effect on effective stiffness is attributed to the nominally isotropic material composition. The random distribution of iron particles allows formation of alternative and desirable magnetic field paths irrespective of the deformation field within the material. The only notable reduction in the MR effect was due to higher frequencies.

3. The carbon nanofiber improved the performance of TAP silicone-based anisotropic MRE. This may be due to desirable magnetic permeability of carbon nanofibers, which resulted in higher MR effects.

4. Natural rubber MRE demonstrated better MR effect under axial force, however, reduced with increasing strains. It was observed that at 10% and 100% strain with 100 psi axial stress, the achieved MR effects were 92% and 33% compared to 32% and 32% under no axial stress, respectively. This observation is attributed to the fact that axial force, hence

axial deformation, reduces the spacing between iron particles, thereby enhancing the magnetic field.

5. For any given strain and/or frequency, the effective stiffness and damping showed increasing trend with increased magnetic field intensity.

6. The MR effect on the effective damping for NR-S-4 sample was 63% at 10% shear strain and 10 Hz test frequency. Also, it was observed that the MR effect on the effective damping varied from 2 to 13% for all other shear strains (30%, 50%, 75%, 100%, and 125%) and applied frequencies (0.1 Hz, 3 Hz, 7Hz, and 10 Hz).

The second part of the research includes experimental study of MRE-based adaptive bearing. MRE device have been tested under pure shear, compression and combined loading. The observations derived from experiments are summarized here in:

1. The effects of magnetic field, strain and frequency was studied. It was demonstrated that at lower strains and frequency, the increase in stiffness was higher; and as strains and frequency increase, the MR effect of MRE decreases. The adaptive bearing has the potential to change the dynamic response of a bridge, but since lower than expected change in shear stiffness is achieved with larger compressive forces, the design needs to be modified to accommodate large compression forces while still maintaining the shear stiffness change properties.

2. The observed MR effect under combined shear and compression loading varied between 23% and 9% at 5-kip axial load and strains of 5% and 20% respectively.

Finally, a seven-parameter viscoelastic model was developed and adapted to simulate static and dynamic response of natural rubber based isotropic magnetorheological elastomer (MRE). The comparison between the predicted and experimental storage and loss moduli, and effect of magnetic field thereof, demonstrated the validity of the proposed model. The accuracy with linear models when it comes to predicting stiffness and damping is satisfactory. However, the simulation of highly nonlinear hysteretic response of rubber-based materials presents a challenge due to complex particle interactions, cyclic Mullins and Payne effects, hyperelasticity, etc. Therefore, there is a need to develop models which can incorporates nonlinearity of material characteristics such as hysteresis shape and strain-hardening of MRE due to large strains.

## 5.3. Recommendations for future research

This research was the first investigation of its kind in which MRE layers were subjected to large structural strains and loads. Like all new materials that have been adapted in various fields of engineering and have gone through a wide range of synthesis testing and design iterations, the utilization of MRE for structural applications requires further investigations. This project demonstrated the initial steps in understanding the structural capabilities of MREs, utilized in an adaptive bearing system under large forces and strains. The following recommendations are suggested to improve the current AB system:

1. MRE material development for large loads and strains is needed to improve the MR effect.
2. The design of the AB system could be improved to reduce size and increase the magnetic field by incorporating MRE layers which shows high MR effect.

# Appendix A. Conference papers

## A.1 Characterization of carbon black-filled natural rubber and silicone magnetorheological elastomers under pure shear loading

Note: This part of the appendix is a standalone conference paper published in 2017.

Yarra S, Pekcan G, Behrooz M, and Gordaninejad F. (2017) Characterization of Carbon Black-Filled Natural Rubber and Silicone Magnetorheological Elastomers under pure shear loading. In 8th ECCOMAS Thematic Conference on Smart Structures and Materials 2017 June 6, pg. 860-870. A publication of International Centre for Numerical Methods in Engineering (CIMNE), ISBN: 978-84-946909-3-8

### ABSTRACT

This study presents a mechanical characterization of carbon black-filled natural rubber and silicone magnetorheological elastomers (MREs). ASTM standard MRE samples with silicone matrix and carbon black fillers are fabricated and their properties are compared with those of carbon black-filled natural rubber-based isotropic MREs. The mechanical properties of the MREs are investigated with a double-lap shear experimental setup. The effect of loading parameters such as shear strain, loading frequency, and magnetic field on the shear moduli of MRE are presented. Experimental results show that adding carbon black improves not only the passive modulus of MRE, but also the MR effect.

**KEYWORDS:** magnetorheological elastomers, natural rubber, platinum silicone.

### A.1.1 Introduction

Magnetorheological elastomers are a class of materials whose properties can be regulated with an applied external magnetic field. MREs are fabricated by adding micron-sized iron particles to a polymeric matrix. If a magnetic field is not used during the curing process, MRE material maintains an isotropic structure. Isotropic MREs with large and irregular shaped iron particles

are known to show a higher MR effect (percentage change in moduli due to magnetic field) due to smaller distance between particles compared to isotropic MREs with regular carbonyl iron [1]. Pre-compressed isotropic MREs show higher elastic modulus when compared to isotropic MREs without pre-compression [2]. The MR effect of an isotropic MRE increases due to an increased magnetic field and loading frequency [3]. Gong et al. [4] showed that shear modulus of isotropic MREs can be increased up to 60% when subjected to 1.0 T magnetic field intensity. Furthermore, MREs with carbon black show higher tensile strength (56.8% increase) compared to MREs with no carbon black [5]. It was also demonstrated by [5] that MREs with carbon black can operate at higher temperatures due to their higher thermal stability. Isotropic MREs show a linear shear stress-strain behavior when the applied strain is less than 10% [6].

When a MRE is cured under a magnetic field, particles form chain-like structures that will result in an anisotropic MRE. Shear modulus and hysteresis damping of an anisotropic silicone MRE increases with an increased magnetic field [7-9]. Anisotropic MREs made of polyurethane shows 20% higher MR effect than anisotropic natural rubber MRE under a varying magnetic field of 0 to 0.395T [8]. Non-magnetic fillers in MRE mixtures can be used to modify the properties to achieve desired passive stiffness and damping levels. Chen et al. [10] concluded that adding carbon black to MRE improves the microstructure bonding, MR effect, and tensile strength. Thickness and length of iron particle chains increase with an increased magnetic field; therefore, anisotropic MREs fabricated in a higher magnetic field show higher MR effect [11]. MRE has a short response time, in the order of milliseconds, with a reversible behavior under a magnetic field. Therefore, static and dynamic properties of MRE can be controlled in real time. Both isotropic and anisotropic MREs were studied experimentally as well as analytically and used in different vibration absorption applications such as adaptive tunable energy absorbers,

isolators, and tunable stiffness engine mounts. MRE layers have been proposed in vibration absorbers for structural applications that can reduce the vibration transmissibility [12]. Also, using MRE isolators with an appropriate control strategy results in a reduction of acceleration and displacement in a scaled model of a building structure [13]. Lateral stiffness of a MRE base isolator can be increased up to 1,630% from quasi-static tests with increased electric current from 0 to 3 amp [14]. An isolator made with anisotropic MRE performs better under combined shear-compression than shear or compression only [15]. The natural frequency, stiffness, and damping of an anisotropic MRE isolator can be controlled by an applied current to electromagnets that supply magnetic field through MRE material. When the current increases from 0 amp to 1.5 amp, the natural frequency increases 103%, stiffness increases 330%, and damping increases 180%, respectively [15]. In the present study, two different MREs with different curing conditions, additives, and matrices are fabricated. The mechanical properties of MREs are experimentally evaluated under quasi-static monotonic and cyclic loadings. Experimental results demonstrate that adding carbon black improves the MR effect and the shear modulus of MREs.

### A.1.2 Fabrication of natural rubber and silicone MREs

Elastomeric matrix was created by mixing TAP platinum silicone side A base and side B catalyst with a weight ratio of 1:1. Carbonyl iron particles (Grade-R-2410; High purity micro powder iron) of average sizes ranging from 5 to 8 microns were used for magnetic permeability, SR303 carbon black (provided by Sid Richardson) was used as an additive. Silicone-based anisotropic MREs are fabricated by mixing 80.5g of iron particles, 0.5g of carbon black and 18g of platinum silicone side A and side B in a beaker. After thoroughly mixing, the mixture was placed into a mold designed to produce ASTM standard size [16] MRE samples with the geometrical

dimensions presented in Table 1. To remove air bubbles, the mold with mixture went through a two-step vacuum process. First, the mold was placed into a vacuum chamber without the top until the pressure reaches -70 kPA, and then with top the vacuum process was repeated. Finally, the mold was placed into the electromagnet and cured under 1.2 T magnetic field. Figure 1 (a) shows a sample of the aligned silicone MRE sample.

Isotropic MREs slabs with natural rubber (254 mm x 254 mm x 12.7 mm) were fabricated using milling technique with different carbon black percentages (0, 1, 2, 3, 4 and 5) at Akron Rubber Development Laboratory (Akron, OH, USA). The samples were cut to the ASTM standard size by Scougal Rubber Corp. (McCarran, NV, USA). Figure 1 (b) shows an isotropic rubber MRE sample. Recipe of different MRE samples is summarized in Table 2.

**Figure 1.** MRE samples using different polymeric material with: (a) silicone rubber and (b) Natural rubber.

**Table 1:** ASTM Standard Size of Specimens' Dimensions [16]

| Units | Length | Width | Thickness |
|---|---|---|---|
| mm | 40 | 16 | 5 |
| Inches | 1.6 | 0.625 | 0.2 |

**Table 2:** Chemical Composition of MRE Samples

| Test ID | IP% (w/w) | CB% (w/w) | A% (w/w) | B% (w/w) | NR-TSR20 (w/w) |
|---|---|---|---|---|---|
| MRE-S-1 | 80.5 | 0.5 | 9.5 | 9.5 | N/A |
| NR-S-2 | 76.0 | 5.0 | N/A | N/A | 19 |

### A.1.3 MRE microstructure analysis

Scanning Electron Microscope was used to observe the microstructure of silicone and rubber MREs. The samples were dipped in liquid nitrogen to achieve smooth sectional surface for imaging purposes. Then, the surface was coated with a thin layer of platinum and finally placed in the SEM machine. Accelerating voltage of 20 kV was used while taking pictures. Figure 2(a) demonstrates the iron particle chains in a 40%wt. iron particles and 15%wt. carbon black. SEM picture of isotropic rubber MRE sample with 80%wt. natural rubber and 5% carbon black is shown in Figure 2 (b). The anisotropic silicone MRE has the particle chains while in the rubber MRE particles are randomly dispersed that results in an isotropic MRE.

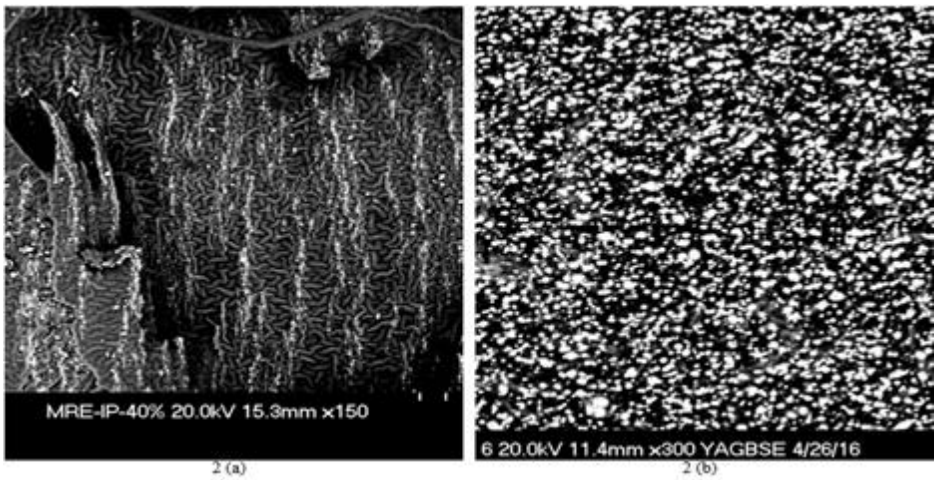


**Figure 2.** SEM image of the MREs fabricated at different curing conditions: (a) with a magnetic field; (b) without a magnetic field.

### A.1.4 Experimental setup

To characterize the mechanical properties of MREs with different matrices, a special test setup was designed and fabricated as shown in Figure 2. This test setup was used for the application and control of shear strains with different loading frequencies and magnetic field intensities. As shown in Figure 2, electromagnets were used to apply the magnetic field.

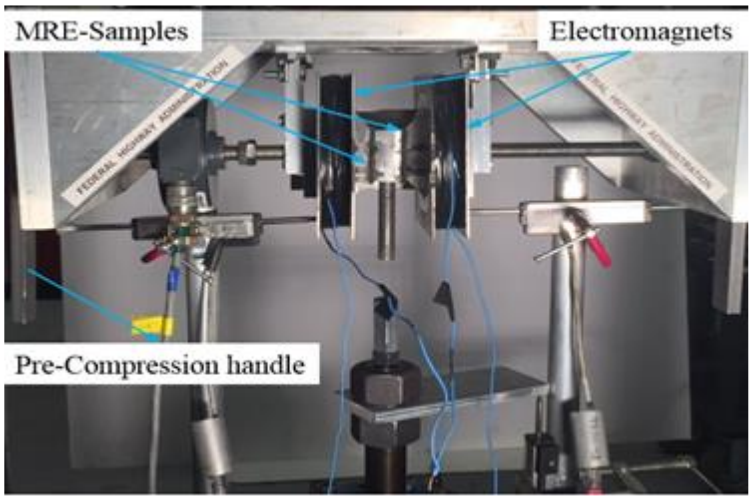


**Figure 3.** Double-lap shear test setup.

Experiments are performed with monotonic and cyclic tests under pure shear loading, different magnetic field intensities, and loading frequencies. Results are used to compute shear moduli of ASTM standard size samples. Table 3 shows test protocol of experiments.

**Table 3:** Test Protocol for Monotonic and Cyclic Tests

| Strain (%) | Frequency (Hz) | Magnetic field intensities (Tesla) (Amp) |
|---|---|---|
| 10, 20, 30, 40 and 50 | 0.1 | 0.0 (0) |
| | 0.5 | 0.3 (1) |
| | 1.0 | 0.5 (2) |
| | 3.0 | 0.6 (3) |
| | 5.0 | 0.7 (4) |
| | 10.0 | 0.8 (5) |

Magnetorheological effect (MR effect) was calculated as the ratio of absolute relative magnetic field to the modulus measured with zero magnetic field. The absolute relative magnetic field was calculated as difference between modulus measured at certain magnetic field and the modulus measured under no magnetic field.

$$MR\ effect = \frac{G_m - G_0}{G_0} \quad (1)$$

### A.1.4.1 Monotonic experiments

Monotonic tests were conducted to characterize mechanical properties such as shear modulus of both isotropic and anisotropic MRE's. The effect of magnetic field on shear modulus of MRE-S-1 and NR-S-2 is shown in Figure 4. As can be seen, the anisotropic silicone MRE (MRE-S-1) sample shows 11%, 11%, and 6% MR effect at 10%, 30%, and 50% strain amplitudes, respectively. The isotropic natural rubber MRE (NR-S-2) sample achieved 11%, 51%, and 38% MR effect at 10%, 30%, and 50% strain amplitudes, respectively. The effective shear modulus values are summarized in Table 4.

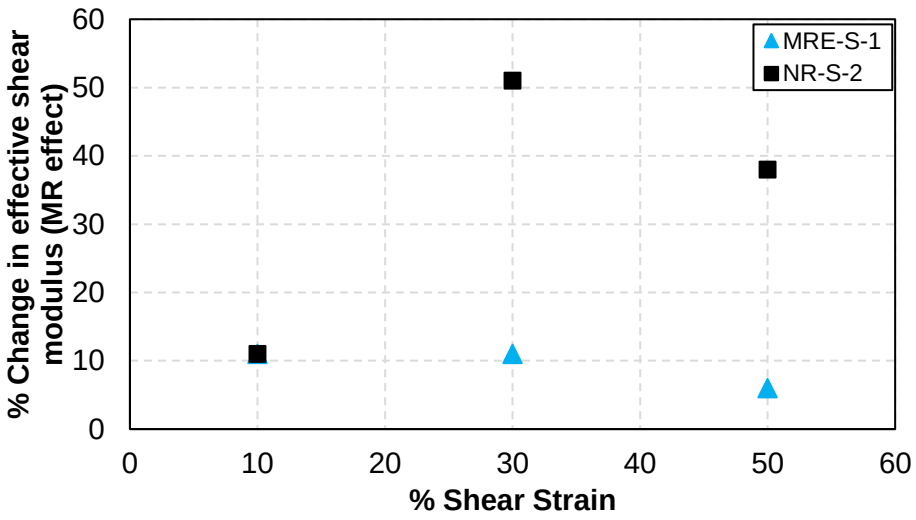


**Figure 4.** Experimentally determined MR effect.

**Table 4:** Effective Shear Modulus Values

| Effective shear modulus (psi) | MRE-S-1 | | | NR-S-2 | | |
|---|---|---|---|---|---|---|
| | 10% Shear strain | 30% Shear strain | 50% Shear strain | 10% Shear strain | 30% Shear strain | 50% Shear strain |
| $G_0$ | 160.0 | 137.0 | 129.0 | 78.0 | 33.3 | 29.0 |
| $G_4$ | 178.0 | 152.0 | 137.0 | 86.5 | 50.2 | 40.0 |
| % Change in effective shear modulus | 11 | 11 | 6 | 11 | 51 | 38 |

$G_0$ - Shear modulus under no magnetic field, and $G_4$ - Shear modulus under 0.7 Tesla magnetic field

### A.1.4.2 Cyclic experiments

MRE samples were subjected to six cycles of strain-controlled sinusoidal motions to study viscoelastic properties under varying shear loading frequencies and magnetic field intensities. The storage and loss moduli were calculated by using Eqs. (2) and (3), respectively, as follows:

$$G' = \tau/\gamma \cos\delta \quad (2)$$

$$G'' = \tau/\gamma \sin\delta \quad (3)$$

where δ is the phase lag measured from the reordered the shear stress and shear strain responses.

The effect of frequency on storage and loss moduli of MRE-S-1 is shown in Figure 5. Both moduli increase with increasing test frequency. As can be seen in the Figure 6, the MRE-S-1 sample show various levels of MR effect due to the applied magnetic field. In general, an increase in magnetic field results in larger storage and loss moduli for any given strain amplitude. However, while the MR effect associated with the storage modulus decreases with increasing strain amplitudes, MR effect for loss modulus increases with increasing strain amplitudes. Table 5 summarizes the measured MRE effects. Accordingly, the storage modulus of MRE-S-1 sample achieved approximately 68%, 42% and 24% MR effect at 10%, 30% and 50% strain amplitudes, respectively. The loss modulus of MRE-S-1 show 40%, 111%, and 119% MR effect at 10%, 30%, and 50% strain amplitudes, respectively, which implies a higher damping capacity at larger strain amplitudes. Figure 7 shows a sample of cyclic force-displacement response of silicone MRE under different strains and magnetic field intensities.

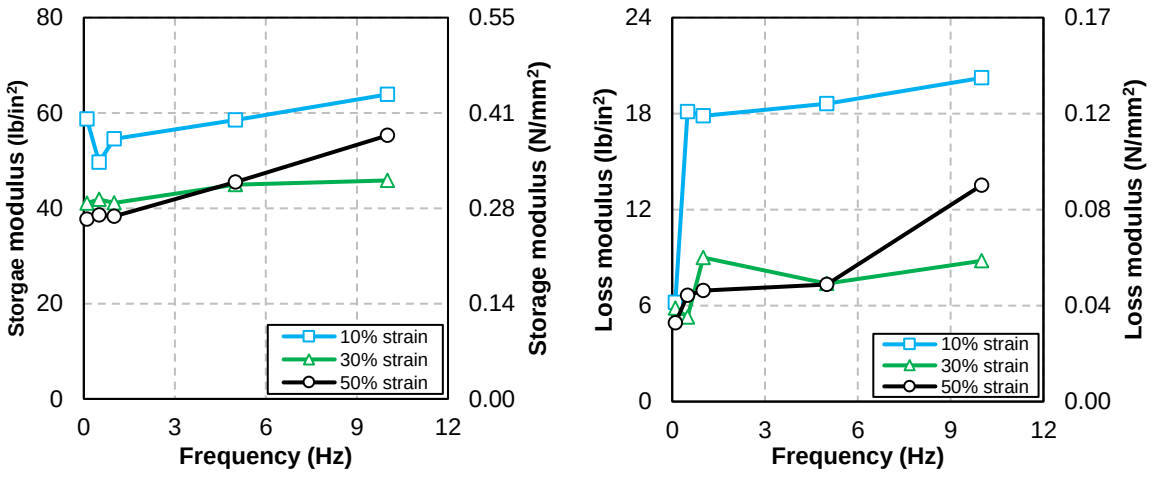


**Figure 5.** Effect of frequency on the rheological properties of MRE-S-1 at zero magnetic field: (a) Storage modulus (b) Loss modulus.

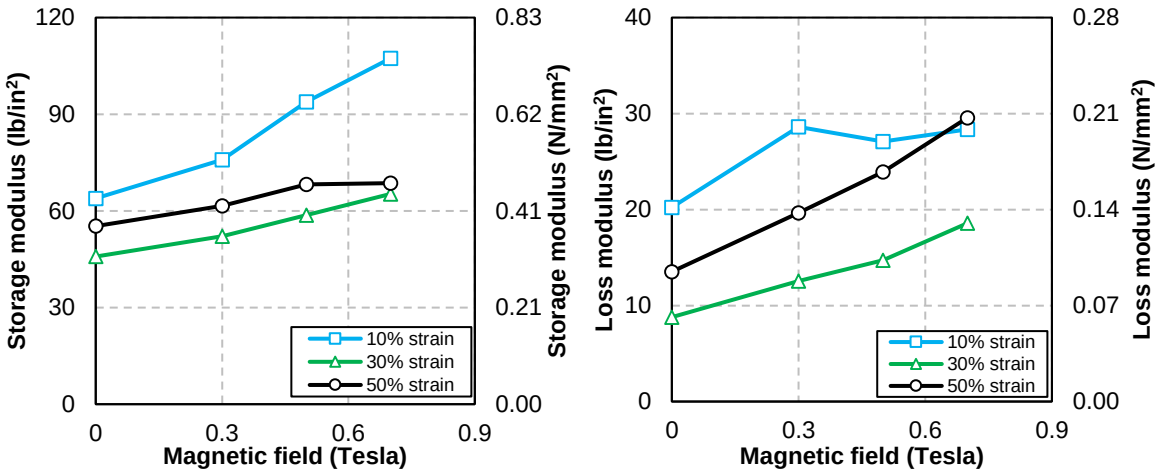


**Figure 6.** Effect of magnetic field on the rheological properties of MRE-S-1 at frequency of 10Hz: (a) Storage modulus (b) Loss modulus.

**Table 5:** Storage and loss modulus values of MRE-S-1

| Magnetic field (Tesla) | Shear strain | | | | | |
|---|---|---|---|---|---|---|
| | 10% | 30% | 50% | 10% | 30% | 50% |
| | Storage modulus | | | Loss modulus | | |
| | G' | G' | G' | G" | G" | G" |
| 0 | 63.9 | 45.8 | 55.3 | 20.2 | 8.8 | 13.5 |
| 0.3 | 75.9 | 52.1 | 61.6 | 28.6 | 12.6 | 19.7 |
| 0.5 | 93.8 | 58.6 | 68.2 | 27.1 | 14.7 | 23.9 |
| 0.7 | 107.4 | 65.3 | 68.6 | 28.3 | 18.6 | 29.6 |
| MR effect | 68% | 42% | 24% | 40% | 111% | 119% |

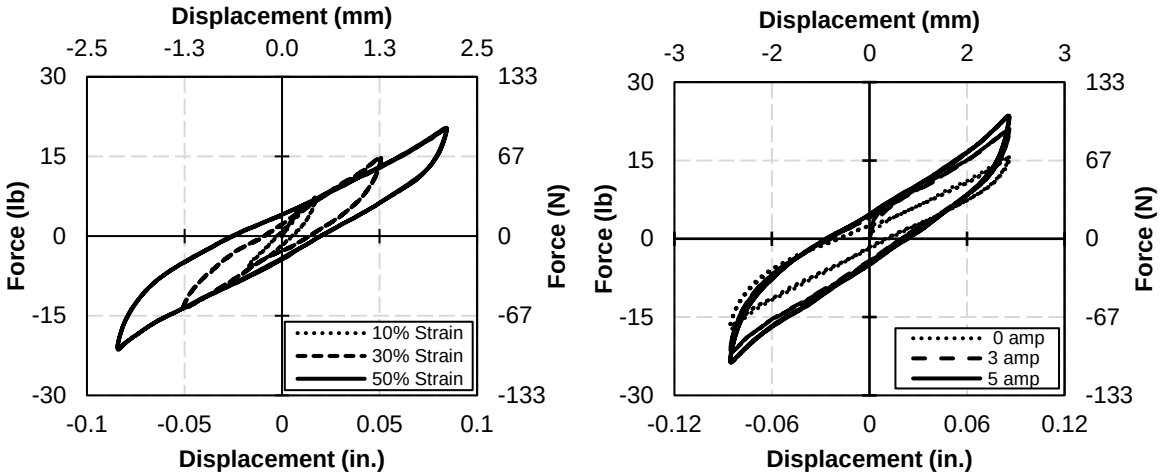


(a) (b)

**Figure 7.** Platinum silicone MRE force-displacement results under varying: (a) Strains and (b) Magnetic field.

As shown in Figure 8, storage loss moduli of the isotropic natural rubber-based MRE (NR-S-2) show an increasing trend with increasing frequency for any given strain amplitude. Also, from Figure 8, it can be seen that both storage modulus and loss modulus show a decreasing trend with increasing strain amplitudes. Figure 9 shows magnetic field effect on storage and loss modulus of NR-S-2. As can be seen in the Figure, both storage modulus and loss modulus increase with increasing magnetic field. The storage modulus of NR-S-2 exhibits 35%, 24%, and 24% MR effect at 10%, 30%, and 50% strain amplitudes, respectively. The loss modulus of NR-S-2 show 45%, 19%, and 26% MR effect at 10%, 30%, and 50% strain amplitudes. Table 6 summarizes the measured storage and loss modulus values and corresponding MR effects. Figure 10 shows the shear force–displacements hysteresis of natural rubber-based isotropic MRE under different loading conditions.

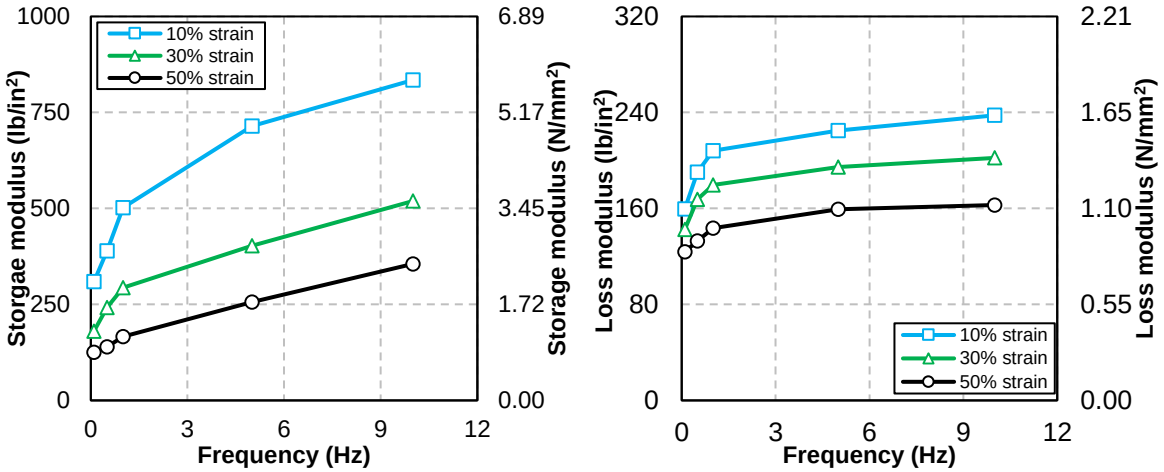


(a) (b)

**Figure 8.** Effect of frequency on the rheological properties of NR-S-2 at zero magnetic field: (a) Storage modulus (b) Loss modulus.

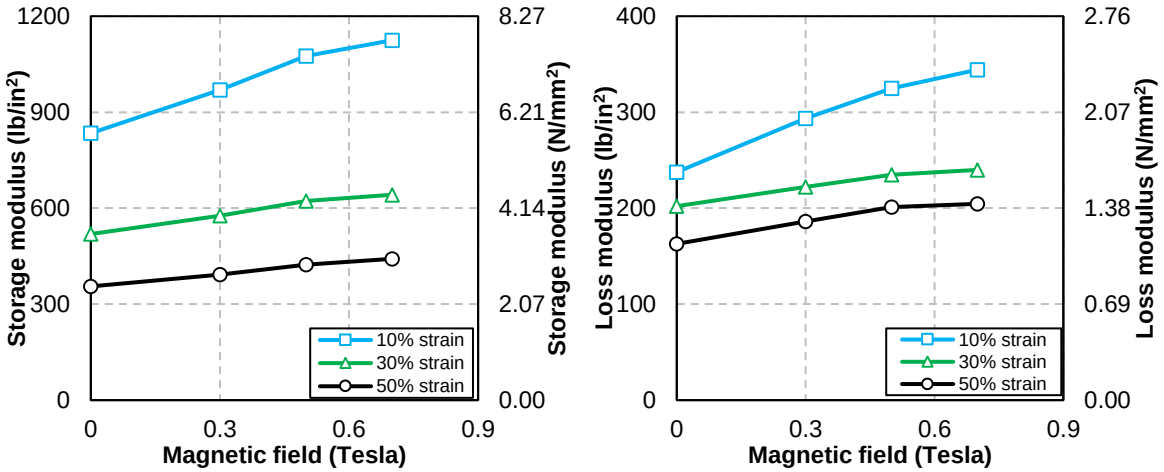


(a) (b)

**Figure 9.** Effect of magnetic field on the rheological properties of NR-S-2 at frequency of 10Hz: (a) Storage modulus (b) Loss modulus

**Table 6:** Storage and loss modulus values of NR-S-2

| Magnetic field (Tesla) | Shear strain 10% | 30% | 50% | 10% | 30% | 50% |
|---|---|---|---|---|---|---|
| | Storage modulus | | | Loss modulus | | |
| | G' | G' | G' | G" | G" | G" |
| 0 | 834.3 | 519.2 | 355.5 | 237.6 | 202.1 | 162.8 |
| 0.3 | 969.7 | 576.3 | 392.3 | 293.5 | 222.1 | 186.0 |
| 0.5 | 1076.0 | 623.0 | 423.7 | 324.8 | 234.9 | 201.3 |
| 0.7 | 1124.9 | 642.0 | 441.7 | 344.2 | 239.9 | 204.5 |
| MR effect | 35% | 24% | 24% | 45% | 19% | 26% |

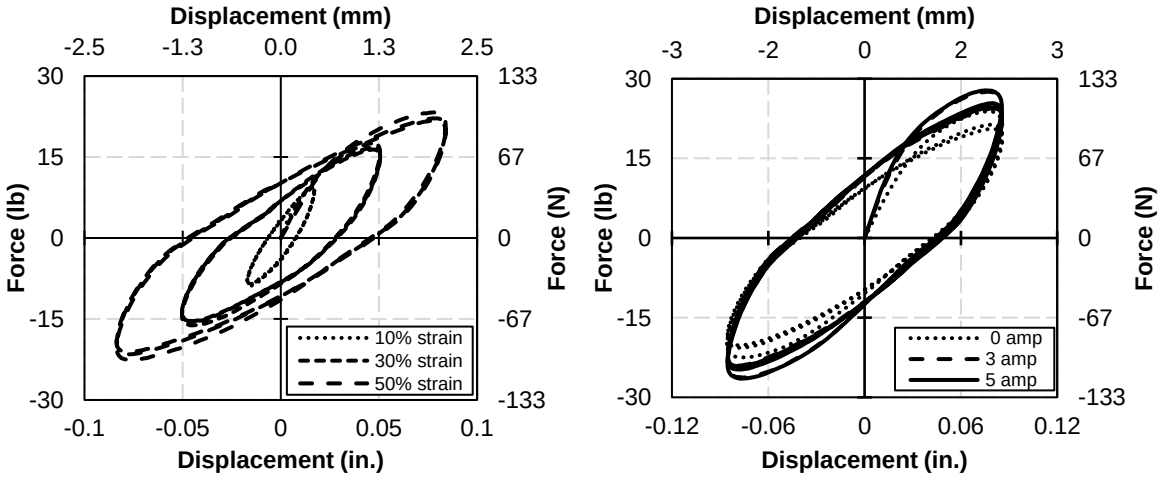


**Figure 10.** Natural rubber MRE force-displacement results under varying: (a) Strains and (b) Magnetic field.

## A.1.5 Conclusions

In this study, different MRE samples are characterized using a double-lap shear test setup that is designed for combined shear and compression experiments. Experiments were carried out for anisotropic and isotropic MRE samples. The silicone MRE (MRE-S-1) sample were characterized as anisotropic (cured under magnetic field) and Natural rubber-based MRE (NR-S-2) samples were characterized as isotropic (cured without magnetic field). Both samples demonstrated varying levels of MR effect ranging between 11%-6% for MRE-S-1 and 11%-38%

for NR-S-2 at 0.7 Tesla (4amp). It is important to note that NR-S-2 sample achieved a higher MR effect which tends to increase with larger strains. Additional material tests are planned for further investigation under various loading conditions and larger strain amplitudes.

### A.1.6 Acknowledgments

The authors would like to express their gratitude to the U.S. Federal Highway Administration for their support under contract # DTFH61-13-C-00020 under the exploratory Advanced Research Program. Also, the authors would like to thank undergraduate assistant Nathan Pinuelas for his assistance.

### A.1.7 References

[35] Lokander, M. and Stenberg, B. Performance of isotropic magnetorheological rubber materials. *Polymer Testing* (2003) **22**: 245–251.

[36] Jung, H. J., Lee, S. J., Jang, D. D., Kim, I. H., Koo, J. H. and Khan, F. Dynamic characterization of magneto-rheological elastomers in shear mode. IEEE *Trans Magn*, (2009), 40:39303933.

[37] Koo, J. H., Khan, F., Jang, D. D. and Jung, H. J., Dynamic characterization and modeling of magneto-rheological elastomers under compressive loading, *Smart Mater. Struct.*, (2010) **19**, pp. 1–6, 2010.

[38] Gong, X. L., Zhang, X. Z. and Zhang, P. Q., Fabrication and characterization of isotropic magnetorheological elastomers. *Polymer Testing*, (2005) **24**, 669-676.

[39] Nayak, B., Dwivedy, S. K. and Murthy, K. S., Fabrication and characterization of magnetorheological elastomer with carbon black. *J. Intll. Matl. Sys. Struct* (2014) **26** 830–9.

[40] Li. W. H., Zhou. Y. and Tian. T. F., Viscoelastic properties of MR elastomers under harmonic loading, *Rheologica Acta*, (2010) **49**, 733-740.

[41] Behrooz, M., Yarra, S., Mar, D., Pinuelas, N., Muzinich, B., Publicover, N. G., Pekcan, G., Itani, A. and Gordaninejad, F. A self-sensing magnetorheological elastomer-based

adaptive bridge bearing with a wireless data monitoring system. *Proc. SPIE 9803, Sensors and Smart Structures Technologies for Civil, Mechanical, and Aerospace Systems* (2016), 98030D; doi:10.1117/12.2218691.

[42] Shen Y., Golnaraghi, M. F. and Heppler, G. R., Experimental research and modeling of magnetorheological elastomers. *J. Intell. Matl Sys. and Structures* (2004) **15**: 27–35.

[43] Zhou, G. Y., Complex shear modulus of a magnetorheological elastomer, *Smart Materials and Structures*, (2004) **13**, 1203-1210, 2004.

[44] Chen, L., Gong X. L. and Li, W. H., Effect of carbon black on the mechanical performances of magnetorheological elastomers, *Polymer Testing*, (2008) **27**, 340-345.

[45] Chen, L., Gong X. L. and Li W. H., Microstructures and viscoelastic properties of anisotropic magnetorheological elastomers, *Smart Materials and Structures*, (2007)**16**, 2645-2650.

[46] Behrooz, M., Wang, X., and Gordaninejad, F., A new semi-active/passive isolator," *Proceedings 5th World Conf. on Structural Control and Monitoring*, (2010), 10308, Tokyo, Japan.

[47] Behrooz, M., Wang, X. and Gordaninejad, F., Seismic control of base isolated structures using novel magnetorheological elastomeric bearings. *Proceedings of ASME Conference on Smart Materials, Adaptive Structures and Intelligent Systems, SMASIS 2013*, Snowbird, UT, (2013) 16–18 September. New York: American Society of Mechanical Engineers.

[48] Li, Y., Li. J., Tian, T. and Li, W., A highly adjustable magnetorheological elastomer base isolator for applications of real-time adaptive control. *Smart Mater Struct.* (2013) **22**:095020

[49] Yang, C., Fu, J., Yu, M., Zheng, X. and Ju, B., A new magnetorheological elastomer isolator in shear–compression mixed mode. *J. Intell. Mater. Syst. Struct.* (2014) doi:10.1177/ 1045389X14541492

[50] ASTM D5992-96 Standard Guide for Dynamic Testing of Vulcanized Rubber and Rubber-Like Materials Using Vibratory Methods, ASTM International, West Conshohocken, PA, (2011),http://dx.doi.org/10.1520/D5992-96R11.

## A.2 A large-scale adaptive magnetorheological elastomer-based bridge bearing

Note: This part of the appendix is a standalone conference paper published in SPIE -Smart Structures + Nondestructive Evaluation in 2017.

Yarra, S., Behrooz, M., Pekcan, G., Itani, A. and Gordaninejad, F., 2017, April. A large-scale adaptive magnetorheological elastomer-based bridge bearing. In Active and Passive Smart Structures and Integrated Systems 2017 (Vol. 10164, p. 1016425). International Society for Optics and Photonics.

ABSTRACT

This study presents the design, development, testing, and performance evaluation of a scaled bridge bearing utilizing magnetorheological elastomer (MRE) layers as adaptive elements, which allow for a varying stiffness under a magnetic field. The adaptive bridge bearing system incorporates a closed-loop magnetic circuit that results in an enhanced magnetic field in the MRE layers. A new design is introduced and optimized using structural and magnetic finite element analyses. Two bearings and a test setup for applying simultaneous variable shear, constant compression, and a variable magnetic field on the bearing are fabricated. The adaptive bridge bearing results demonstrate the stiffness change of the bearing under different strain levels and loading frequencies, as well as the ability of the bearing to change its stiffness under different applied electric currents, which can be correlated to the applied magnetic field.

**Keywords:** Magnetorheological elastomers, Adaptive bearing, Base isolation, Bridge Bearings

### A.2.1 Introduction

Conventional bearings are passive systems that have been installed widely in civil infrastructure to accommodate translational and rotational movement in order to protect them from seismic, wind, and traffic loads. However, conventional bearings are designed and limited to a specific stiffness and damping, therefore conventional bearings may not be suitable for all operating

conditions. On the other hand, a controllable vibration absorber can control the stiffness, and its performance may accommodate a wider frequency range and type of loading conditions.

Magnetorheological elastomers (MREs) are materials whose instantaneous mechanical properties can be controlled in real-time. These materials are capable of changing their mechanical properties continuously, reversibly, and rapidly under an applied external magnetic field. A MRE is isotropic if it is cured with no magnetic field[1], and is anisotropic if cured under a magnetic field[2]. In recent years, researchers have investigated the capabilities of MREs to design controllable bearings for various structural systems. Using numerical simulations, Colette et. al.[3] showed that a dynamic vibration absorber incorporating MRE can reduce displacements in a structure by 10 percent. Also, a scaled MRE-base isolator showed a 30% increase in stiffness[4]. By controlling the input current, MRE vibration absorption systems utilized different excitations and outperformed passive system[5]. Li et al.[6] proposed an adaptive MRE-base isolator with 47 alternating anisotropic MRE and steel shims, sizes of 2mm thickness and 1 mm thickness with a diameter of 140mm, respectively. Based on experiments conducted on this small-scale device, it was shown that MR effect (change in apparent stiffness with respect to passive mode stiffness) was 45% at a frequency of 0.5 Hz and 5% strain. Natural rubber-based laminated MRE isolator showed a maximum of 14.56% change in effective stiffness under static compression test for 30% strain[7]. Furthermore, it was demonstrated by Yang et al.[8] that both negative and positive stiffness change could be achieved by incorporating permanent magnets and changing the direction of the electrical current. The corresponding range of MR effect was reported as ±90%. Another study showed that effective stiffness of an adaptive MRE base isolator subjected to 16% strain and 0.1 Hz loading frequency could increase over eleven folds[9]. In other recent studies, 120% MR effect for a laminated MRE vibration isolator[10] and 175%

increase in equivalent stiffness of a MRE isolator[11] are reported. Various semi-active control strategies, such as Lyapunov control[12], Optimal Control[13], Fuzzy-logic[14], and NARX neural network[14] have been used to control seismic response of scaled-model structural systems. In a previous work by the authors, preliminary results of investigations on MRE material properties and design of a bridge bearing using MRE was demonstrated[15].

In this paper, for the first time, the experimental performance of a MRE-based bearing subjected to large structural loads is investigated. In the following, the design of the adaptive bearing is presented, which consists of four MRE and steel shim stacks that are magnetized using eight electromagnets. The magnetic field of the adaptive bridge bearing is investigated and optimized using finite element analyses. The adaptive bearing is fabricated with anisotropic MREs which are cured under a magnetic field of 1.2 Tesla. A double lap shear test setup was designed and fabricated to conduct component tests of two adaptive bearings under different loading conditions. Experimental results of the change in the effective stiffness of the adaptive bearings based on the applied strain level and loading frequency are presented

### A.2.2 MRE – based bearing design and fabrication

For the system considered in this study, a quarter-scale adaptive bridge bearing was found appropriate based on the limitations of the experimental facility. The prototype bearings were designed such that they resemble traditional passive isolation bearings commonly used in highway bridges. Overall dimensions, rubber area, shear stiffness and deformation demand were determined from an extensive analytical study of different bridges around the United States. For the analytical study, AASHTO M251[16] which is referenced in Section 14 of AASHTO LRFD Bridge Design Specs[17] and Section 18 of AASHTO LRFD Bridge Construction Specs[18], was considered as the basis for the laminated bridge bearing design and properties. The analytical

study considered different highway bridges across the United States with multiple span length, bridge width, girder spacing, and shear modulus[19]. Accordingly, the quarter-scale bearings were designed for a compression load of 41 kip and combined shear and compression loads of 5 kip and 23 kip, respectively. A schematic of the adaptive bearing is shown in Figure 1.

The adaptive bearing consists of four stacks of alternating MRE and steel shim layers, eight electromagnets, one sole plate, and one masonry plate. Magnetorheological elastomers with size of 3in diameter and 1/8in thickness were fabricated using carbonyl iron particles (Grade-R-2410; High purity micro-fine iron powder), SR303 carbon black and TAP® Platinum Silicone A and B mixed together with a weight ratio of 1:1.

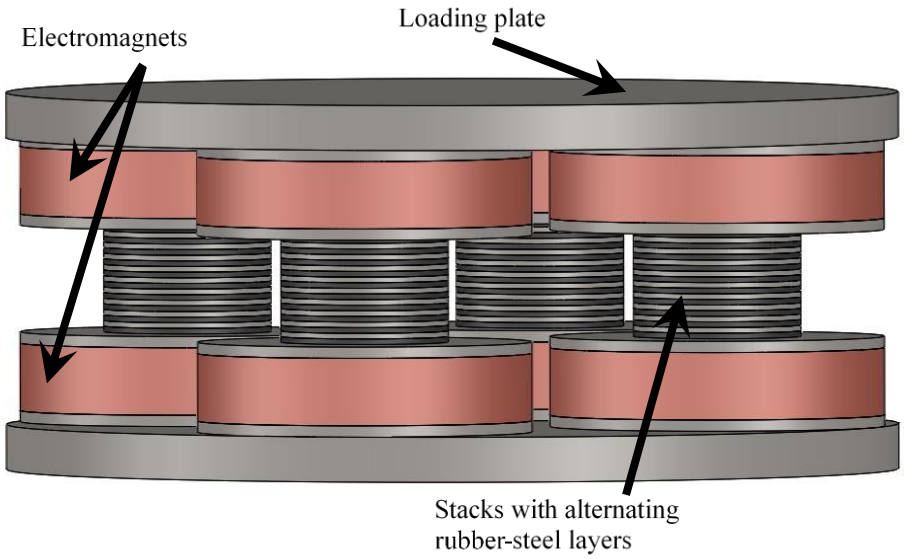


**Figure 1.** Adaptive bridge bearing design.

To achieve high magnetic permeability, the steel shims, electromagnet core, shim layers, electromagnets, sole plate, and masonry plate were fabricated from steel 1018. A total of 10 MRE layers and 9 steel shims were used for each stack. Electromagnets with 15-gauge wire and

10,000 amp-turn per coil, were designed that are powered by two power supplies to induce a magnetic field in MRE layers. Magnetic field analyses were performed on a finite element model of the bearing using ANSOFT. The average magnetic field across the middle surface of MRE layers was determined as 1.3 Tesla, as shown in Figure 2.

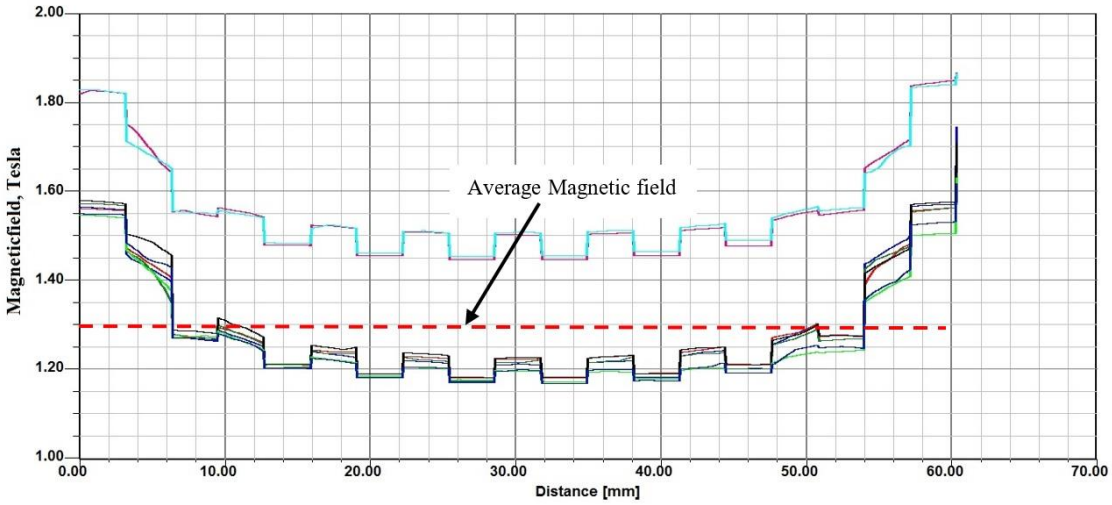


**Figure 2.** Magnetic field density distribution across the middle surface of a MRE layer with an average of 1.3 T.

### A.2.3 Experimental study

A double-*lap* shear and compression test setup was developed to test the performance of the two identical adaptive bearings under different loading conditions. The component tests were performed to characterize the mechanical properties of the bearings such as vertical and lateral stiffness as well as energy dissipation characteristics under various magnetic field intensities. Figure 3 demonstrates the assembled double-lap shear and compression test setup for quarter-scale bearings. The setup was used for the application and control of horizontal shear and axial force on the bearing system. The horizontal shear force was applied and controlled using a hydraulic actuator, and axial force was applied and controlled using a hydraulic jack. The instrumentation of the test setup consisted of eight position transducers (four per each bearing),

four electrodes (two per each bearing), and three string pots. Position transducers were used to monitor axial deformations due to applied axial loads and rotations due to combined loading. String pots were installed to measure potential out-of-plane movements due to imperfections in the test setup.

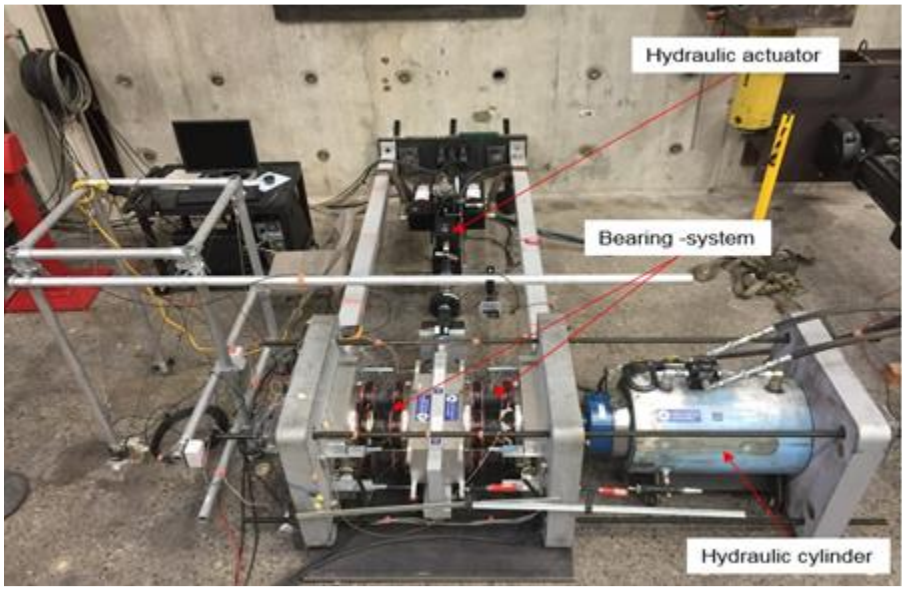


**Figure 3.** Experimental test setup for the MRE adaptive bearing system.

A pseudo-dynamic testing program was developed for the component tests at the Large-Scale Structures Laboratory at the University of Nevada, Reno. Two identical MRE based adaptive bearings were tested under varying strains, frequencies, and magnetic fields. Each test consisted of 6 sinusoidal loading and unloading.

### A.2.4 Results and discussion

The component tests were used to evaluate the effect of various frequencies, strains, and magnetic field intensities on the effective stiffness of MRE based adaptive bearings calculated from force-deformation hysteresis. Effective stiffness was obtained using Eq. (1)[20].

$$k_{eff} = \frac{|F^+|+|F^-|}{|\Delta^+|+|\Delta^-|} \quad (1)$$

where $F^+$ and $F^-$ are the positive and negative shear forces, at $\Delta^+$ and $\Delta^-$ shear displacements of the bearing, respectively.

The effective stiffness of MRE-based adaptive bearings in the off-state (no magnetic field) increases with increasing frequency as shown in Figure 4. The effective stiffness is not sensitive to loading frequency at smaller frequencies of up to 1Hz but increases up to 66% for higher frequency of 4 Hz. For the next set of experiments, the strain level was increased from 5% to 20% to observe the strain-dependent changes of the effective stiffness. At 0.1 Hz loading frequency, the effective stiffness decreases by approximately 16% at larger strains as shown in Figure 5. The effective stiffness for 5% and 20% strains are 4.10 kip/in and 3.47 kip/in, respectively. Table 1 summarizes effective stiffness values for a constant frequency of 0.1Hz with varying strains.

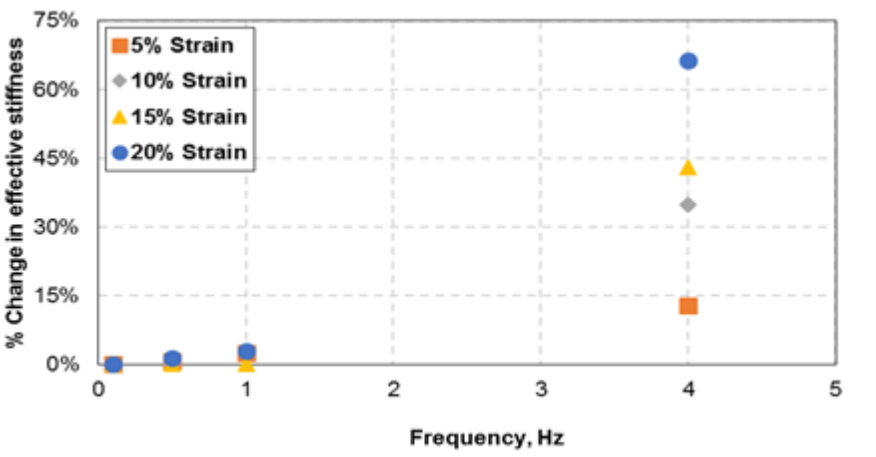


**Figure 4.** Frequency effect on effective stiffness of MRE based adaptive bearing.

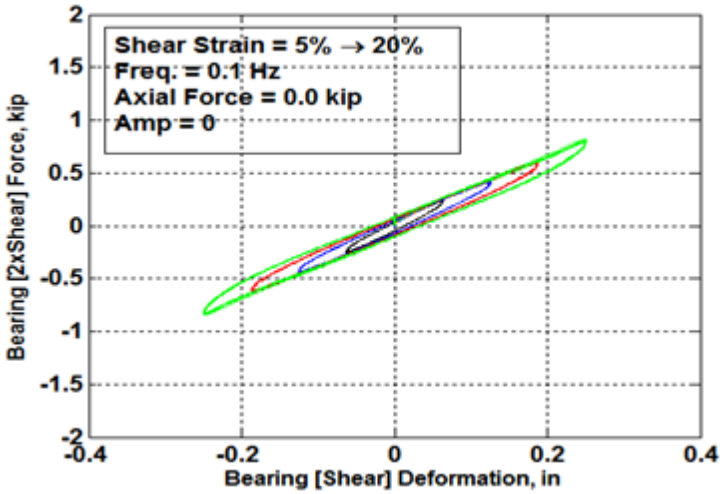


**Figure 5.** Strain effect on effective stiffness of MRE based adaptive bearing.

**Table 1.** Effective Stiffness Values for a Constant Frequency and Varying Strains.

| Effective stiffness (kip/in) | Strain (%) | | | | Reduction (5 % Strain - 20% Strain) |
|---|---|---|---|---|---|
| | 5 | 10 | 15 | 20 | |
| 0.1 Hz | 4.10 | 3.70 | 3.53 | 3.47 | 18% |

Magnetorheological (MR) effect is defined as change in the properties of MRE under the magnetic field as presented in Eq. (2) and defined as the ratio of absolute magnetorheological effect to zero field effective stiffness.

$$MR\ effect = \frac{k(I)-k(0)}{k(0)} * 100 \quad (2)$$

where $k(I)$ is the current-dependent stiffness and where $k(0)$ is the off-state stiffness.

Figure 6 shows shear force-deformation hysteresis for a constant frequency of 0.1 Hz with varying strains (20%, 50%) and varying magnetic fields (0 Tesla, 1.2 Tesla). As can be seen in Figure 6, the effective stiffness of MRE-based adaptive bearing increases with increased

magnetic field. The percentage increase in effective stiffness were 12% and 5% for 20%, 50% strains, respectively. Table 2 shows effective stiffness values for a given constant frequency with varying strains and magnetic fields.

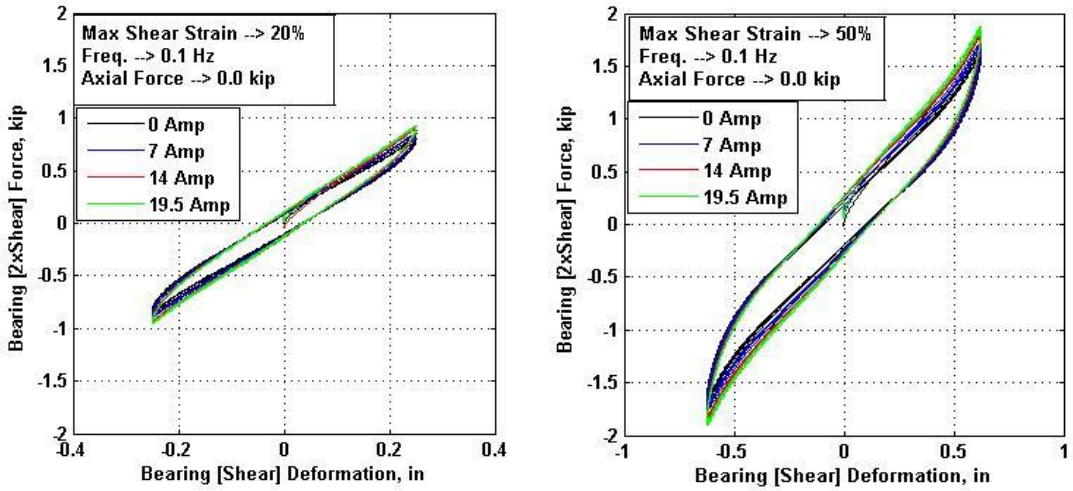


(a) (b)

**Figure 6.** Magnetic field effect on effective stiffness of MRE-based adaptive bearing with: (a) maximum 20% strain (b) maximum 50% strain.

**Table 2.** Effective Stiffness Values under Different Strains for Varying Magnetic Field.

| Effective stiffness (kip/in.) | 20% Strain | 50% Strain |
|---|---|---|
| | 0.1 Hz | 0.1 Hz |
| 0.0 A | 3.35 | 2.9 |
| 7.0 A | 3.49 | 2.82 |
| 14.0 A | 3.69 | 2.98 |
| 19.5 A | 3.76 | 3.05 |
| Increase (0 - 19.5 A) | 12% | 5% |

## A.2.5 Conclusions

This study presents a new large-scale MRE-based adaptive bridge bearing that was designed and fabricated strictly following realistic demands imposed on conventional bridge isolation

bearings. A double-lap shear and compression test setup was fabricated and assembled to evaluate adaptive bearings under various loading conditions. The force-displacement characteristics for different loading conditions and magnetic fields were obtained through an experimental investigation. The effective stiffness of the adaptive bearing increases at higher frequencies and magnetic fields; however, the increase in effective stiffness can be significantly lower at larger strain amplitudes. It was observed that the MR effect was 12% and 5% at 20% and 50% strains levels, respectively.

### A.2.6 Acknowledgements

Funding for the study was provided by the Federal Highway Administration under the contract number DTFH61-13-C-00020. The authors would like to express their gratitude to Dynamic Isolation Systems, Inc. for allowing modification and use their bearing test setup, and to Scougal Rubber Corporation for their assistance with the fabrication of the adaptive bearings. The authors also acknowledge Mr. Tony Berendsen, Development Technician of the Mechanical Engineering Department, for his assistance with the fabrication; Mr. Chad Lyttle, Development Technician and Dr. Patrick Laplace, Research Associate Professor and Manager of the Civil and Environmental Engineering's Large-Scale Structures Engineering Laboratory, for their assistance with instrumentation of the adaptive bearing experiments. The authors also wish to thank Mr. Troy Martin, Structures Division of the Nevada Department of Transportation (NDOT), for his valuable feedback and participation during the component testing of the adaptive bearings. Finally, the authors would like to thank undergraduate assistants Nathan Pinuelas, David Mar, and Blake Muzinich for their assistance.

### A.2.7 References

[51] Lokander, M., and Stenberg, B., “Performance of isotropic magnetorheological rubber materials,” Polymer Testing 22(3), 245–251 (2003).

[52] Yu, M., Qi, S., Fu, J., and Zhu, M., “A high-damping magnetorheological elastomer with bi-directional magnetic-control modulus for potential application in seismology,” Applied Physics Letters 107(11), 111901 (2015).

[53] Collette, C., Kroll, G., Saive, G., Guillemier, V., and Avraam, M., “On Magnetorheologic Elastomers for Vibration Isolation, Damping, and Stress Reduction in Mass-varying Structures,” Journal of Intelligent Material Systems and Structures 21(15), 1463–1469 (2010).

[54] Behrooz, M., Wang, X., and Gordaninejad, F., “A new semi-active/Passive Isolator,” The 5th World Conference on Structural Control and Monitoring, Shinjuku, Tokyo, paper No. 049, July (2010).

[55] Eem, S.H., Jung, H.J., and Koo, J.H., “Seismic performance evaluation of an MR elastomer-based smart base isolation system using real-time hybrid simulation,” Smart Materials and Structures 22(5), 55003 (2013).

[56] Li, Y., Li, J., and Li, W., “Design and experimental testing of an adaptive magneto-rheological elastomer base isolator,” in 2013 IEEEASME Int. Conf. Adv. Intell. Mechatron. AIM, 381–386 (2013).

[57] Wahab, N.A.A., Mazlan, S.A., Ubaidillah, Sharif, A.H.R., and Kamaruddin, S., “Steady compression characteristics of laminated MRE isolator,” Journal of Physics: Conference Series 776(1), 12036 (2016).

[58] Yang, J., Sun, S.S., Du, H., Li, W.H., Alici, G., and Deng, H.X., “A novel magnetorheological elastomer isolator with negative changing stiffness for vibration reduction,” Smart Materials and Structures 23(10), 105023 (2014).

[59] Gu, X., Li, J., Li, Y., and Askari, M., “Frequency control of smart base isolation system employing a novel adaptive magneto-rheological elastomer base isolator,” Journal of Intelligent Material Systems and Structures1045389X15595291 (2015).

[60] Wahab, N.A.A., Mazlan, S.A., Ubaidillah, Kamaruddin, S., Ismail, N.I.N., Seung-Bok Choi, and Sharif, A.H.R., "Fabrication and investigation on field-dependent properties of natural rubber-based magneto-rheological elastomer isolator," Smart Materials and Structures 25(10), 107002 (2016).

[61] Fu, J., Li, P., Liao, G., Lai, J., and Yu, M., "Development and Dynamic Characterization of a Mixed Mode Magnetorheological Elastomer Isolator," IEEE Transactions on Magnetics 53(1), 1–4 (2017).

[62] Behrooz, M., Wang, X., and Gordaninejad, F., "Control of structures featuring a new MRE isolator system," in Proc SPIE, 83411I–83411I–9 (2012).

[63] Bai, X.-X., Xin, F.-L., Qian, L.-J., and Kan, P., "Design and Control of a Magnetorheological Elastomer Dynamic Vibration Absorber for Powertrain Mount Systems of Automobiles," V001T03A014 (2015).

[64] Fu, J., Liao, G., Yu, M., Li, P., and Lai, J., "NARX neural network modeling and robustness analysis of magnetorheological elastomer isolator," Smart Materials and Structures 25(12), 125019 (2016).

[65] Behrooz, M., Yarra, S., Mar, D., Pinuelas, N., Muzinich, B., Publicover, N.G., Pekcan, G., Itani, A., and Gordaninejad, F., "A self-sensing magnetorheological elastomer-based adaptive bridge bearing with a wireless data monitoring system," 2016, 98030D–98030D–11.

[66] American Association of State Highway and Transportation Officials (AASHTO). (2016). Standard Specifications for Transportation Materials and Methods of Sampling and Testing and AASHTO Provisional Standards (2016 Edition). American Association of State Highway and Transportation Officials (AASHTO).

[67] AASHTO. (2014; 2015). AASHTO LRFD Bridge Design Specifications, U.S. Customary Units with 2015 and 2016 Interim Revisions (7th Edition). American Association of State Highway and Transportation Officials (AASHTO).

[68] AASHTO. (2010; 2011; 2012; 2013; 2014; 2016). AASHTO LRFD Bridge Construction Specifications (3rd Edition) with 2010, 2011, 2012, 2014, 2015 and 2016 Interim

Revisions. American Association of State Highway and Transportation Officials (AASHTO).

[69] AmiriHormozaki, E., Pekcan, G., and Itani, A., “Analytical Fragility Functions for Horizontally Curved Steel I-Girder Highway Bridges,” Earthquake Spectra 31(4), 2235–2254 (2014).

[70] ASCE (2010) Minimum Design Loads for Buildings and Other Structures, ASCE 7-10 ed. American Society of Civil Engineers.

## A.3 A self-sensing magnetorheological elastomer-based adaptive bridge bearing with a wireless data monitoring system

Note: This part of the appendix is a standalone conference paper published in SPIE -Smart Structures + Nondestructive Evaluation in 2016.

Behrooz, M., Yarra, S., Mar, D., Pinuelas, N., Muzinich, B., Publicover, N.G., Pekcan, G., Itani, A. and Gordaninejad, F., 2016, April. A self-sensing magnetorheological elastomer-based adaptive bridge bearing with a wireless data monitoring system. In Sensors and Smart Structures Technologies for Civil, Mechanical, and Aerospace Systems 2016 (Vol. 9803, p. 98030D). International Society for Optics and Photonics.

### ABSTRACT

This study presents an adaptive bridge bearing that can sense structural loads and tune its properties to mitigate structural vibrations. The bearing utilizes magnetorheological elastomer (MRE) layers which allow for an increased stiffness induced with a magnetic field. The system also features a MRE-based sensing system for sensing the structural wind and traffic load. The sensing system is capable of transmitting data wirelessly to a central logging computer for monitoring bridge performance and sending alerts in the case of a major event. The capability of the MRE-based sensing system for sensing structural loads and wireless transmission of data were investigated. The adaptive bridge bearing incorporates a closed-loop magnetic circuit that results in an enhanced magnetic field in the MRE layers. Results show the sensitivity of the MRE-based sensors and the performance of the wireless system, as well as the design and analysis of the tunable bridge bearing.

**Keywords:** Magnetorheological elastomer isolator, magnetorheological elastomer sensor, adaptive bridge bearing, wireless sensing

### A.3.1 INTRODUCTION

Magnetorheological elastomers (MREs) are multi-functional composite materials whose mechanical properties can be regulated in real-time to achieve variable effective stiffness and damping when subjected to varying magnetic field strengths. The change in the effective

stiffness (storage and loss moduli) can be achieved within milliseconds under a magnetic field[1,2]. The controllability of these properties deems MREs as plausible candidates for use in vibration control and isolation applications. Various types of semi-active and active variable stiffness devices have been proposed and studied. These devices achieve the desired variable stiffness features via either conventional materials coupled with intricate mechanical details, or so-called smart materials[3-9]. Two recent studies demonstrated that MRE-based isolation systems show a promising solution for isolation systems due to their tunable stiffness under a magnetic field[9,10]. Stiffness and damping of a MRE isolator can be adjusted by increasing the applied magnetic field to a MRE isolator[4]. MRE-based isolators for building structures with 80%wt. iron particles demonstrate increased stiffness by approximately 34%[11]. A prototype laminated MRE-based bearing showed over 300% stiffness increase[12]. If the layers of a MRE-based isolator are soft enough, lateral stiffness can be increased up to sixteen fold[13]. Models are presented to capture the dynamic and magnetic field-dependent behavior of MRE isolators[14].

Application of load on a MRE layer leads to a change in electrical resistance measured across the thickness of the MRE layers[15]. A phenomenological model was proposed that can capture this behavior[16]. It was proposed that such properties could be used for load sensing applications. In this study, it is demonstrated that carbon black can be used to increase the stiffness of MRE layers and also lower its electrical resistance. Chen et al.[17] added 0, 4, and 7% carbon black to MRE's elastomer compound and found that the MR effect and tensile strength of MREs improved significantly with the addition of carbon black. Carbon black increases thermal stability, Young's modulus, and the shear storage modulus of an isotropic magnetorheological elastomer[18]. A MRE vibration absorber, with an embedded silicone based conductive elastomer as sensor, was investigated by Komatsuzaki et al.[19] that can sense the vibration and accordingly

tune its natural frequency. Moreover, by combining the electronics required for data acquisition and generating the control signal with a self-sensing absorber, a standalone and pre-programmed system can be achieved that reduces vibration transferred to a system, and only requires the connection to a power supply.

By combining adaptive stiffness and load sensing capabilities of MRE, design, development, and performance testing of an integrated wireless sensor and adaptive bridge bearing, using magnetorheological elastomers, are presented in this work. The wireless sensor is composed of a MRE layer that produces variations in resistance due to applied external forces. The proposed self-sensing adaptive bearing (SSAB) encompasses a sensing system that can measure the applied force and transmit data wirelessly. The bridge bearing consists of MRE layers whose stiffness can be adjusted to a desired level with an external magnetic field. Such a system can be used for effective vibration mitigation strategies and furthermore it can be incorporated readily in wireless structural load monitoring applications.

### A.3.2 WIRELESS SENSING SYSTEM DESIGN

The wireless sensing system consists of a microcontroller platform with wireless capabilities. It is programmed to perform on-board data processing and analysis to interpret load values from the measured resistances. The sensing system can also transfer data wirelessly to a remote computer for monitoring and storing purposes. The microcontroller used for the sensing system is the Raspberry Pi Model A+ which is shown in Figure 1. It runs a Linux operating system and can store data on a microSD card.

The wireless sensing system based on the Raspberry Pi microcontroller includes two shields: Real Time Clock (RTC) and 20 bit Analog-to-Digital Converter (ADC). The RTC shield is used to timestamp the acquired data. The ADC shield is used to obtain analog data

which consists of force, shear, and strain readings. The housing box was printed out of high-density plastic on a 3D printer. As shown in Figure 1, a 9V battery (on the right) powers the wireless sensing system (on the left) using a micro USB connector. The sensing system can sense input data from up to six channels that can be dedicated to recording compressive load, shear load, displacement, etc. and to perform various types of signal processing (e.g. DFT). The system also allows enabling/disabling of a channel and setting different thresholds for each channel to trigger wireless text or web-based alerts to users.

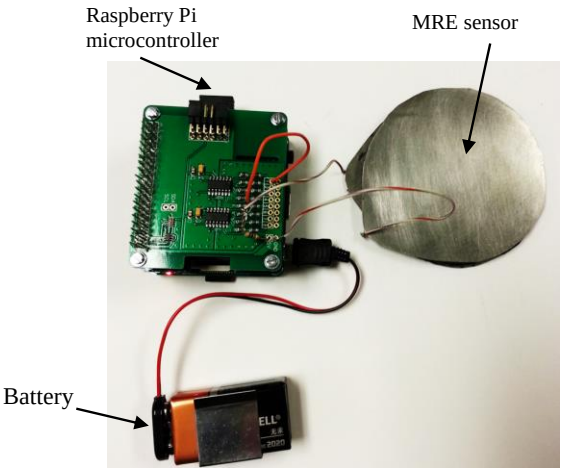


Figure 1. A voltage divider circuit used to measure the voltage drop across the MRE.

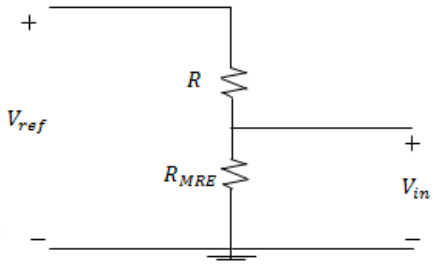


Figure 2. MRE wireless sensor electronics.

Addition of carbon black to MRE leads to a decrease in the measured resistance from GΩ to MΩ range and thus, allows the use of a simple voltage divider circuit to measure the resistance of MRE under an applied load. In Figure 2, $V_{ref}$ represents a reference voltage supplied by the circuit, and $R$ represents a known resistance. MRE resistance is represented as $R_{MRE}$, and $V_{in}$ is the voltage drop across the MRE which is recorded by the microcontroller. A calibration was performed using Eq. (1) to compute the relation between $V_{in}$ and the MRE resistance.

$$R_{MRE} = R * \frac{V_{ref}}{V_{in} - V_{ref}} \quad (1)$$

The data from selected channels is stored in a CSV file. A flexible graphing tool is utilized to allow users to easily view and compare data as shown in Figure 3. The CSV file contains the date and time the data were sampled, shown in the title header of the graph. An USB Wi-Fi adapter was attached to allow interactions with remote computers and have Internet access when available. This adapter also allows the Raspberry Pi to be programmed and/or updated wirelessly. Apache web server software was installed to allow access to the sensor database and graph the data. Exim mail transfer agent was installed to send emails whenever an extreme event occurred as established by predefined thresholds. The sensing system can also send text notifications to users through the TextMagic text message server. This functionality allows text and/or email functions to alert the user in case of an event.

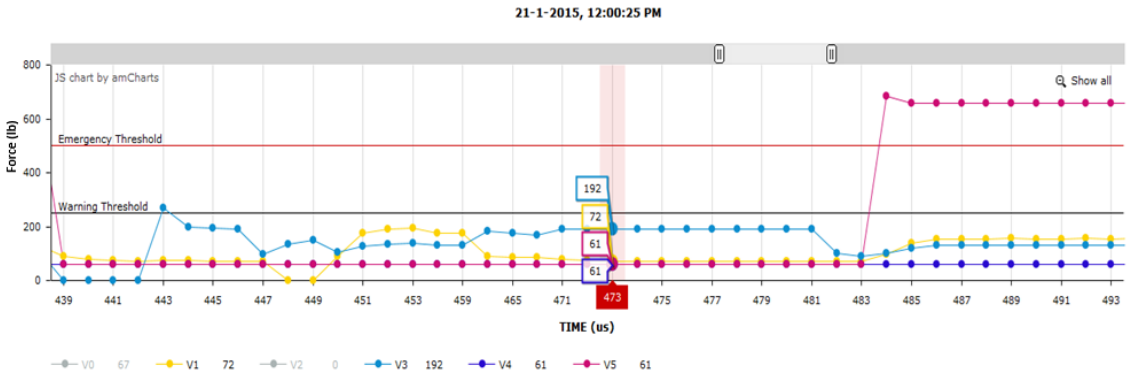


**Figure 3.** Graph of selected data points.

The sensing system is capable of sampling up to 70 samples per second. Moreover, it can be programmed to sample at variable rates as a function of the intensity of the recorded response. Furthermore, the recorded data can be processed in real-time to generate Fourier Amplitude Spectrum as shown in Figure 4 and results are stored in a CSV file.

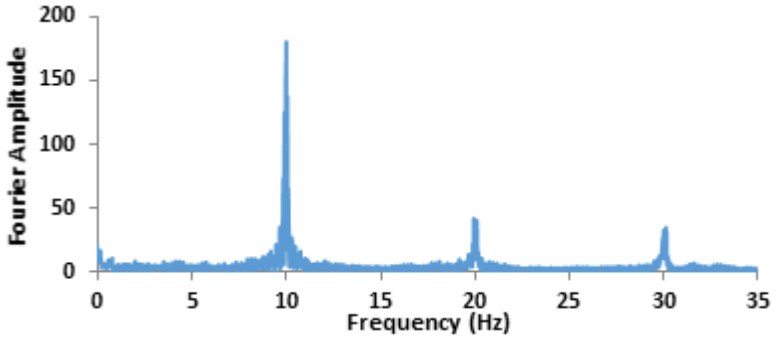


**Figure 4.** Calculated Discrete Fourier Transform (DFT) in real-time.

Figure 5 demonstrates the tree diagram of the graphical user interface (GUI). The GUI is designed to allow easy and intuitive access to the current state of a bearing and to data archived within an SD memory module.

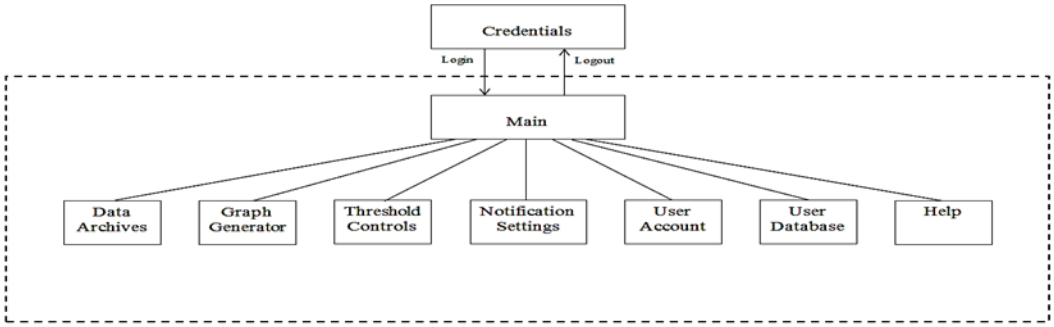


**Figure 5.** Tree diagram structure of the GUI for the wireless sensing system controls.

### A.3.3 MRE Characterization

MREs are fabricated using carbonyl iron particles (Grade-R-2410; High purity micro-fine iron powder), SR303 and SR511 carbon black and TAP® Platinum Silicone A and B mixed together with a weight ratio of 1:1. For the systematic characterization of mechanical and electrical properties of the MRE samples, samples are fabricated in ASTM standard sizes of 0.63x1.57x0.20 in (16 x 40 x 5 mm), as shown in Figure 6.

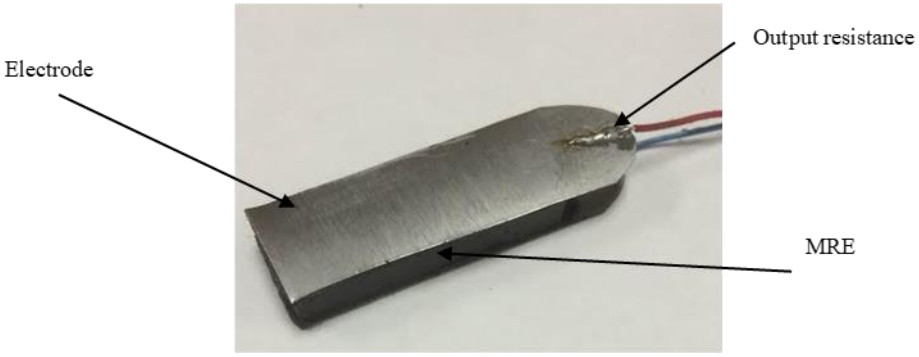


**Figure 6.** A typical MRE specimen for combined shear, compression and electrical resistance testing.

The objectives of the ongoing material testing program are to quantify the effect of various mixture components and their relative compositions on the compressive and shear moduli and electrical resistivity. A series of round-shape MRE samples (shown in Figure 1) were fabricated with different percentages of carbon black (0, 1.5 and 3%wt) content and 80%wt iron particles. The experimental setup used for the compression-only tests is shown in Figure 7. The monotonically increasing compression load was applied using an Instron testing machine. Young's modulus of the material shows an increasing trend with increasing carbon black percentages. Table 1 lists measured values for compression tests where, *D* is diameter, *h* is thickness, *E* is Young's modulus, *G* is shear modulus, IP% is iron particle percentage, and CB% is carbon black percentage of MRE specimens.

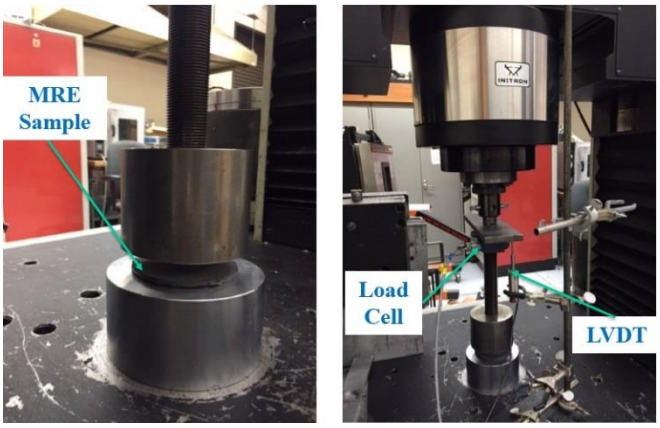


**Figure 7.** MRE compression test setup.

**Table 1.** MRE Compression Test Results.

| Sample Number | D (in.) | h (in) | IP % | CB % | A % | B % | E, (psi) | G, (psi) |
|---|---|---|---|---|---|---|---|---|
| Elastomer only | 3.12 | 0.11 | | | | | 1,179.00 | 398.00 |
| MRE-S-1 | 3.12 | 0.16 | 80.00 | 0.00 | 10.00 | 10.00 | 1,528.00 | 516.00 |
| MRE-S-2 | 3.12 | 0.12 | 80.00 | 1.50 | 9.25 | 9.25 | 2,257.00 | 762.00 |
| MRE-S-3 | 3.12 | 0.16 | 80.00 | 3.00 | 8.50 | 8.50 | 4,519.00 | 1,526.00 |
| MRE-S-4 | 3.12 | 0.15 | 40.00 | 10.00 | 25.00 | 25.00 | 1,181.00 | 399.00 |
| MRE-S-5 | 3.12 | 0.16 | 40.00 | 15.00 | 22.50 | 22.50 | 1,113.00 | 375.00 |

A test apparatus was design and developed to perform shear and compression experiments as well as to measure electric resistivity under an applied magnetic field. The MRE specimens were based on ASTM standard size (D5992-96). Figure 9 shows the experimental test setup. The aluminum housing was mounted to the fixed section of the Instron machine, while the central plunger was mounted to the actuator. The setup allowed the application and control of shear, axial forces, and magnetic field on MRE samples. Shear force was applied and controlled using a hydraulic actuator, and axial force was applied and controlled by a handle and measured by a load cell. The Instron provided up to 1 in of displacement. The magnetic field was measured as 0.8 Tesla within the samples near the saturation point of the MRE's.

Figure 10 shows the results of a pure shear test for carbon black field MREs subjected to 0.1 loading frequency with 10 and 50% strains. The effect of the magnetic field on the stiffness of MRE can be seen in the Figure. Furthermore, the area of the force-displacement loops also increase, corresponding to an increase in hysteresis damping. At 0.1Hz and 10% strain MRE shows 291 lb/in, while increasing the strain to 50% at the same frequency results in a lower 161.69 lb/in stiffness. These results suggest that MREs show lower stiffness at larger strains. Also, the stiffness increases for 10% strain is 52.7% while there is a 38.7% increase for 50% strain. This confirms lower MRE effect at larger applied strains. Figure 11 shows similar results for 30% applied strain with different frequencies. The passive stiffness increases from 215 (lb/in) to 244 lb/in which shows an increase in the stiffness of MRE with increasing frequency. However, the on-state stiffness also increases with higher frequencies. The MR effect is 31.6% for 0.1Hz frequency while it is 38.5% for 5 Hz frequency, therefore, the MR effect does not change significantly with increasing frequency.

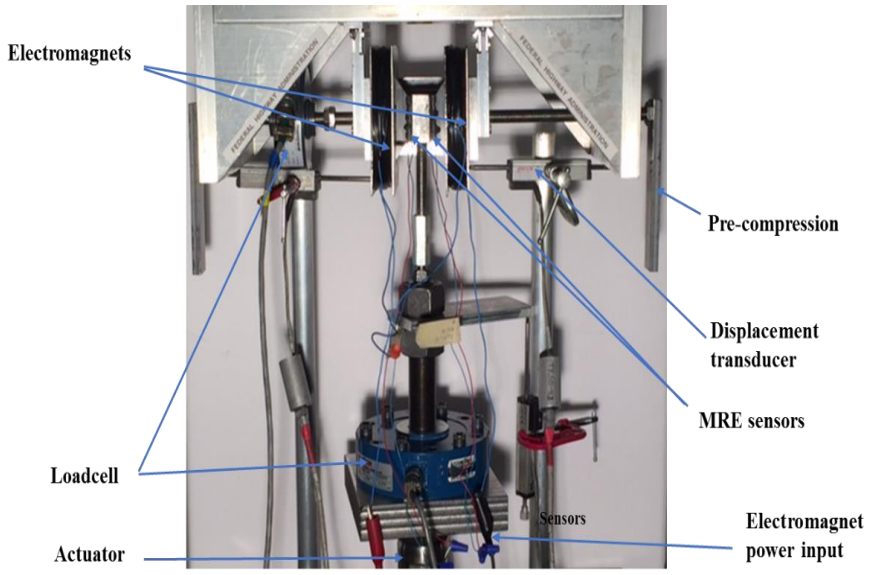


**Figure 8.** Experimental setup for combined shear, compression, and resistance testing.

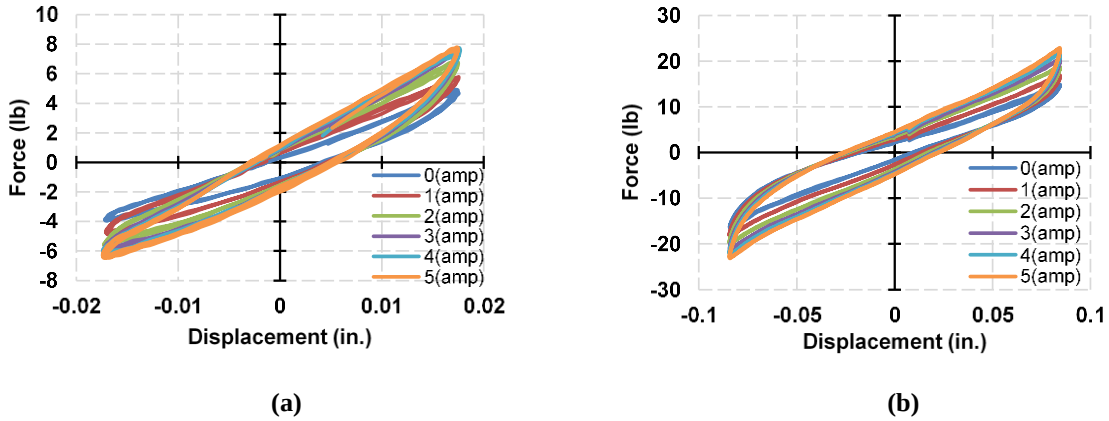


**Figure 9.** Shear force displacement behavior of 80% wt. MRE with 0.5% wt. carbon black under 0.1 Hz loading frequency at: (a) 10% and (b) 50% strain.

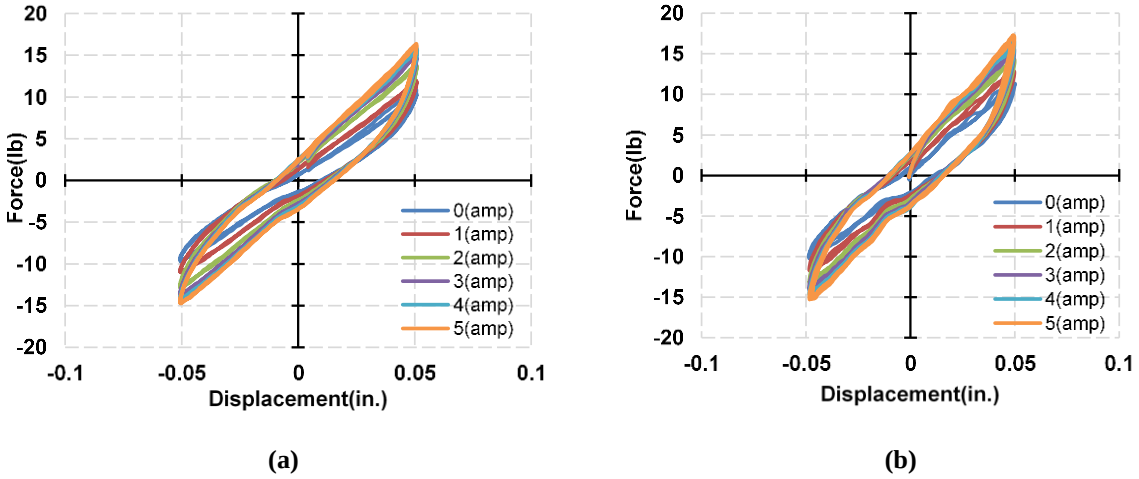


**Figure 10.** Shear force displacement behavior of 80% wt. MRE with 0.5% wt. carbon black under 30% strain at: (a) 0.1Hz and b) 5 Hz loading frequency.

### A.3.4 ADAPTIVE BRIDGE BEARING DESIGN

Bearings are key components in bridge structures that govern the overall static and dynamic responses. While they serve as essential support elements subjected to various vertical loads, the vibration induced structural response of highway bridges is related in part to the compressive as well as shear stiffness of the bearings. Support reactions (bearing forces) are distributed relatively uniformly in regular bridges, however, uneven distribution of such forces are expected

in geometrically irregular bridges even under service loading conditions. On the other hand, significant deviations from expected levels of bearing forces may be a sign of redistribution of forces due to different factors such as support settlement, yielding/failure of other components elsewhere in the structural system. Therefore, load on the bearings as well as associated deformations may be correlated with the condition and longevity of the structure. In general, it is difficult to detect such conditions in bridges with conventional bearings until a leading cause is visible. The present study introduces a SSAB bearing system that addresses some of these issues. While the self-sensing feature allows real-time measurements and monitoring of individual bearing forces and deformations, adaptive features allow real-time control of stiffness characteristics of the bearings as a function of the instantaneous response due to existing loading conditions. Implementation of these features results in a more desired distribution of forces in the structural system, thereby reducing the risk of failure, and provides means for the early detection of adverse conditions.

The prototype SSAB bearing (Figure 11) was designed in conformance with load carrying capacity and stiffness characteristics of a conventional circular bridge bearing. The design is based on a technology that provides a closed loop magnetic field[20]. The average bearing dimensions were determined based on an extensive analytical study of typical highway bridges across the United States. The SSAB bearing consists of two main components; 1) alternating MRE and steel layers, and 2) electromagnets. It is noted that stiffness of MRE layers can be controlled with the application of a magnetic field. Therefore, a closed-loop electromagnet was designed and incorporated in the SSAB which induces a relatively uniform magnetic field in the MRE layers. The bearing features 12 electromagnets each capable of producing 10,000 amp-turns. The magnetic coils induce the magnetic field within the MRE

layers. Efforts were made to increase the size of the coils to compensate for any potential loss of magnetic field. Steel 1018 was used for the bearing coils and steel rings located at the top and bottom of the bearing assembly. Magnetic field analyses were performed on the computational model of the bearing using ANSOFT Maxwell finite element package. The achieved magnetic field distribution is at the middle MRE layers in the radial direction, as shown in Figure 12. As can be seen in Figure 11, the average magnetic field across MRE layers was approximately 1.1 T.

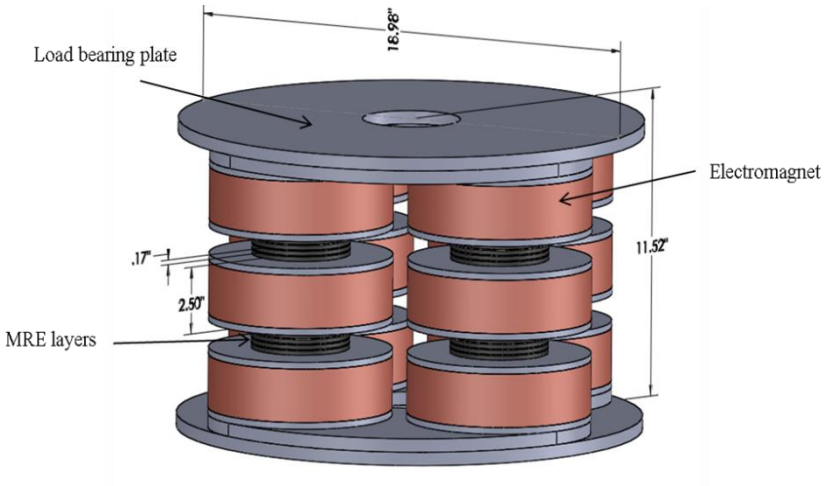


**Figure 11.** Design of the adaptive MRE bearing.

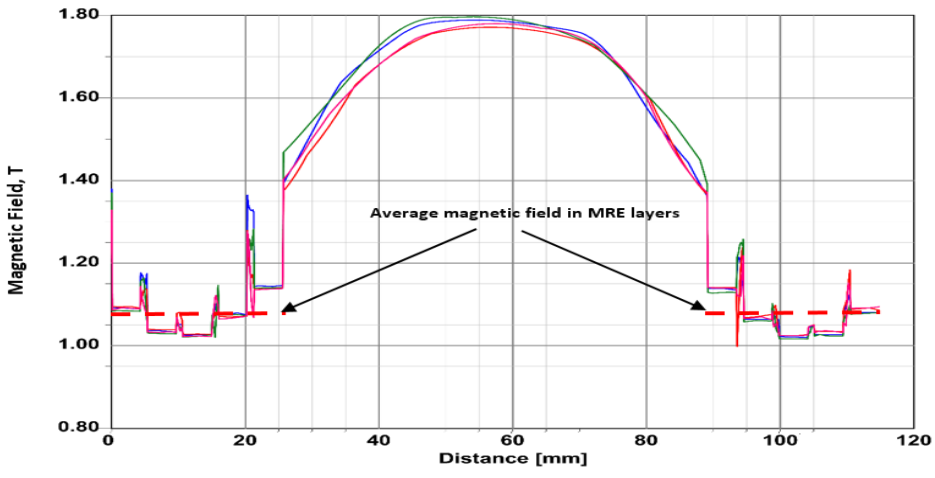


**Figure 12.** Magnetic field distribution across the middle surface of a MRE layer.

## A.3.5 SUMMARY AND CONCLUSIONS

This paper is a report on a work in progress on the design of a self-sensing adaptive bridge bearing (SSAB) system that utilizes magnetorheological elastomers (MREs) both as a load sensing element and also as an adaptive element for vibration control. A microcontroller-based wireless data transmission system was utilized to collect and process the data acquired from MRE sensors and to send an alert in case of an extreme event. MRE sensors using carbon black-filled MREs were manufactured and their load measuring properties were investigated. ASTM-standard MRE samples were manufactured for material testing and characterization of electrical properties. A combined shear and compression test setup was fabricated to characterize the sensors under simultaneous shear and compression loading to simulate structural loading/sensing conditions. A bearing design was achieved that ensures the desired magnetic field strength to control the stiffness of MRE layers. Results of this ongoing study show promising capabilities for the MRE-based SSABs.

## A.3.6 ACKNOWLEDGEMENT

Funding for this study was provided by the Federal Highway Administration contract #DTFH61-13-C-00020 under the Exploratory Advanced Research Program. The authors are thankful for this support.

## A.3.7 REFERENCES

[71] Boczkowska, A., and Awietj, S., [Microstructure and Properties of Magnetorheological Elastomers], in Advanced Elastomers - Technology, Properties and Applications, A. Boczkowska, Ed., InTech (2012).

[72] Stepanov, G.V., Abramchuk, S.S., Grishin, D.A., Nikitin, L.V., Kramarenko, E.Y., and Khokhlov, A.R., “Effect of a homogeneous magnetic field on the viscoelastic behavior of magnetic elastomers,” Polymer 48(2), 488–495 (2007).

[73] Kobori, T., Takahashi, M., Nasu, T., Niwa, N., and Ogasawara, K., "Seismic response-controlled structure with Active Variable Stiffness system," Earthquake Engineering & Structural Dynamics 22(11), 925–941 (1993).

[74] Yang, J.N., Kim, J.-H., and Agrawal, A.K., "Resetting Semiactive Stiffness Damper for Seismic Response Control," Journal of Structural Engineering 126(12), 1427–1433 (2000).

[75] Nasu, T., Kobori, T., Takahashi, M., Niwa, N., and Ogasawara, K., "Active variable stiffness system with non-resonant control," Earthquake Engrg & Structural Dynamics 30(11), 1597–1614 (2001).

[76] Agrawal, A.K., Yang, J.N., and He, W.L., "Applications of some semiactive control systems to benchmark cable-stayed bridge," Journal of Structural Engineering 129(7), 884–894 (2003).

[77] Nagarajaiah, S., and Mate, D., "Semi-active control of continuously variable stiffness system," in Second World Conference on Structural Control, 397–406 (1998).

[78] Nagarajaiah, S., and Sahasrabudhe, S., "Seismic response control of smart sliding isolated buildings using variable stiffness systems: an experimental and numerical study," Earthquake Engineering & Structural Dynamics 35(2), 177–197 (2006).

[79] Koo, J.H., Jang, D.D., Usman, M., and Jung, H.J., "A feasibility study on smart base isolation systems using magneto-rheological elastomers," Structural Engineering and Mechanics 32(6), 755–770 (2009).

[80] Eem, S.H., Jung, H.J., and Koo, J.H., "Seismic performance evaluation of an MR elastomer-based smart base isolation system using real-time hybrid simulation," Smart Materials and Structures 22(5), 055003 (2013).

[81] Behrooz, M., Wang, X., and Gordaninejad, F., "Seismic control of base isolated structures using novel magnetorheological elastomeric bearings," in Proc. ASME, V001T03A027–V001T03A027 (2013).

[82] Xing, Z.-W., Yu, M., Fu, J., Wang, Y., and Zhao, L.-J., "A laminated magnetorheological elastomer bearing prototype for seismic mitigation of bridge superstructures," Journal of Intelligent Material Systems and Structures1045389X15577654 (2015).

[83] Li, Y., Li, J., Tian, T., and Li, W., “A highly adjustable magnetorheological elastomer base isolator for applications of real-time adaptive control,” Smart Materials and Structures 22(9), 095020 (2013).

[84] Behrooz, M., “A Controllable Flexible Micropump and a Semi-Active Vibration Absorber Using Magnetorheological Elastomers,” UNIVERSITY OF NEVADA, RENO (2015).

[85] Li, W., Kostidis, K., Zhang, X., and Zhou, Y., “Development of a force sensor working with MR elastomers,” in IEEE/ASME International Conference on Advanced Intelligent Mechatronics, 2009. AIM 2009, 233–238 (2009).

*[86]* Ghafoorianfar, N., Wang, X., and Gordaninejad, F., “Magnetic and Mechanical Sensing of Magnetorheological Elastomers through Electrical Resistivity Behavior,” Smart Materials and Structures, No. 23, (2014).

[87] Chen, L., Gong, X.L., and Li, W.H., “Effect of carbon black on the mechanical performances of magnetorheological elastomers,” Polymer Testing 27(3), 340–345 (2008).

[88] Nayak, B., Dwivedy, S.K., and Murthy, K.S., “Fabrication and characterization of magnetorheological elastomer with carbon black,” Journal of Intelligent Material Systems and Structures1045389X14535011 (2014).

[89] Komatsuzaki, T., Inoue, T., and Iwata, Y., “Experimental Investigation of an Adaptively Tuned Dynamic Absorber Incorporating Magnetorheological Elastomer with Self-Sensing Property,” Experimental Mechanics1–10 (2016).

[90] Kavlicoglu, B., Liu, Y., Sahin, H., and Wallis, B., “Soft magnetorheological Mounts for Shock and Vibration Isolations,” US patent 8,820,492 (2014).

# Appendix B. Experiments documentation

## B.1 Quasi –Static (Monotonic) Test Results of Silicone-based MRE Samples

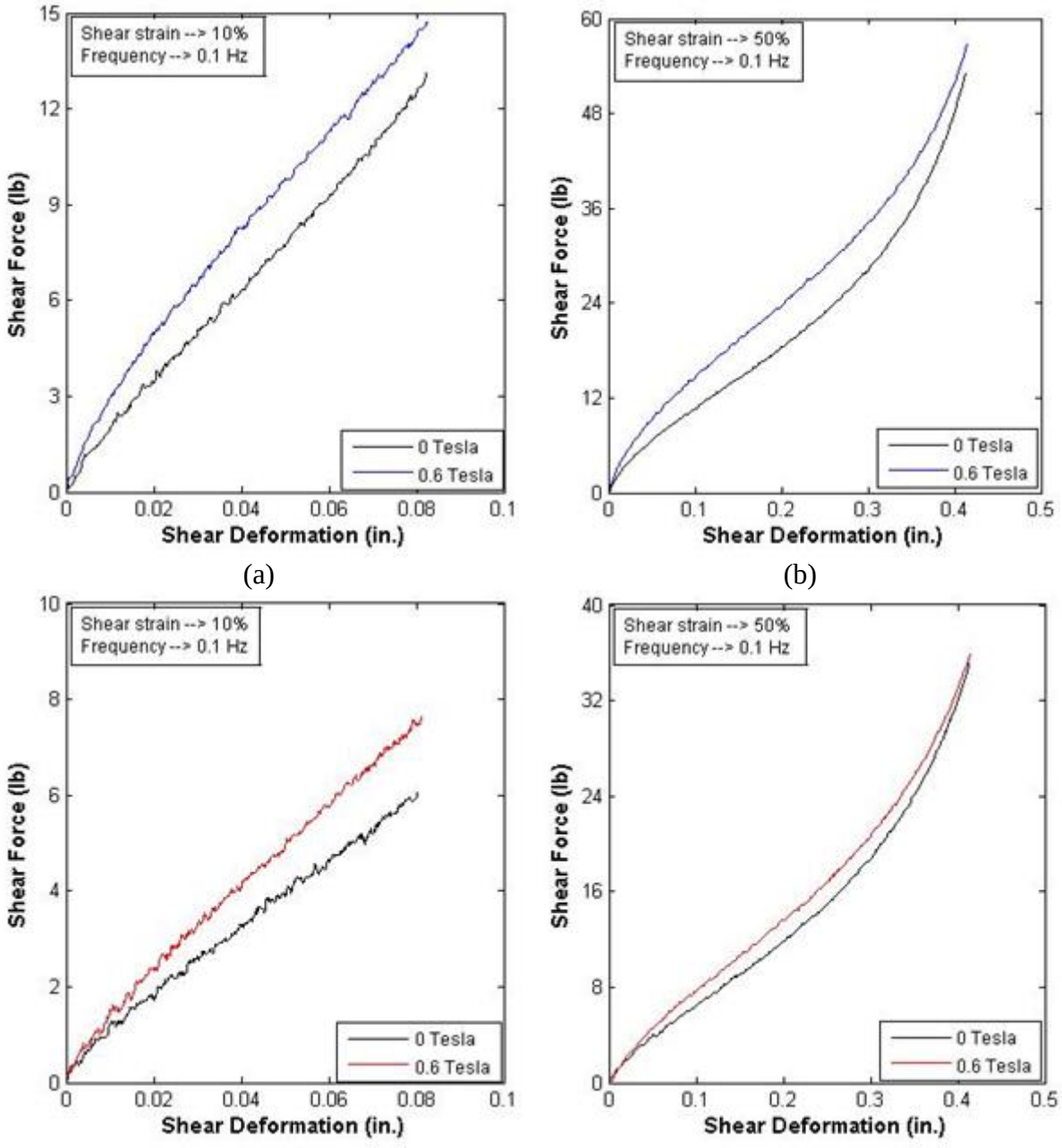


Figure B.1.1. Force – Displacement curves under pure shear: (a) MRE-S-1 (b) MRE-S-1 (c) MRE-S-3 (d) MRE-S-3.

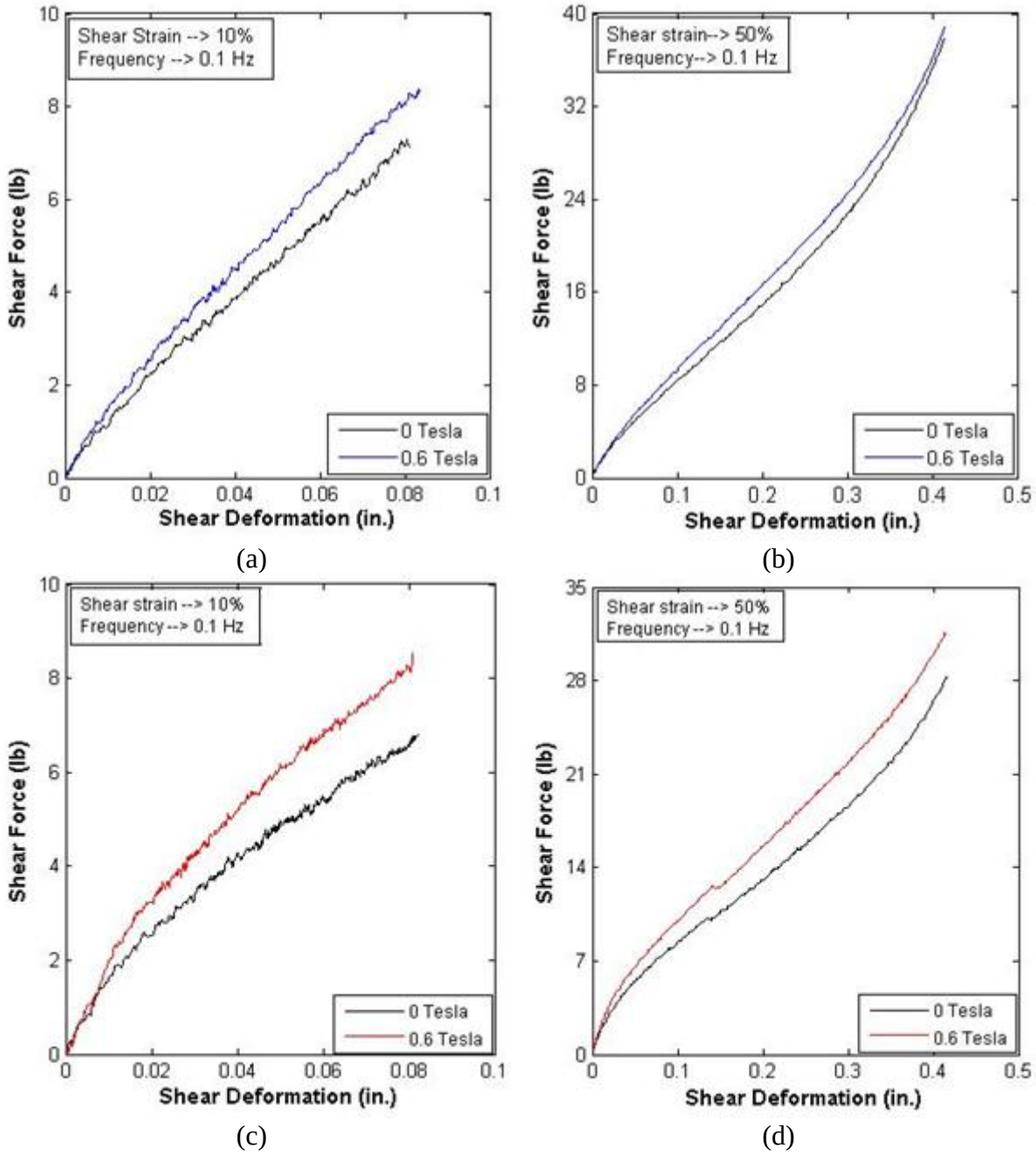


Figure B.1.2. Force – Displacement curves under pure shear: (a) MRE-S-4 (b) MRE-S-4 (c) MRE-S-5 (d) MRE-S-5.

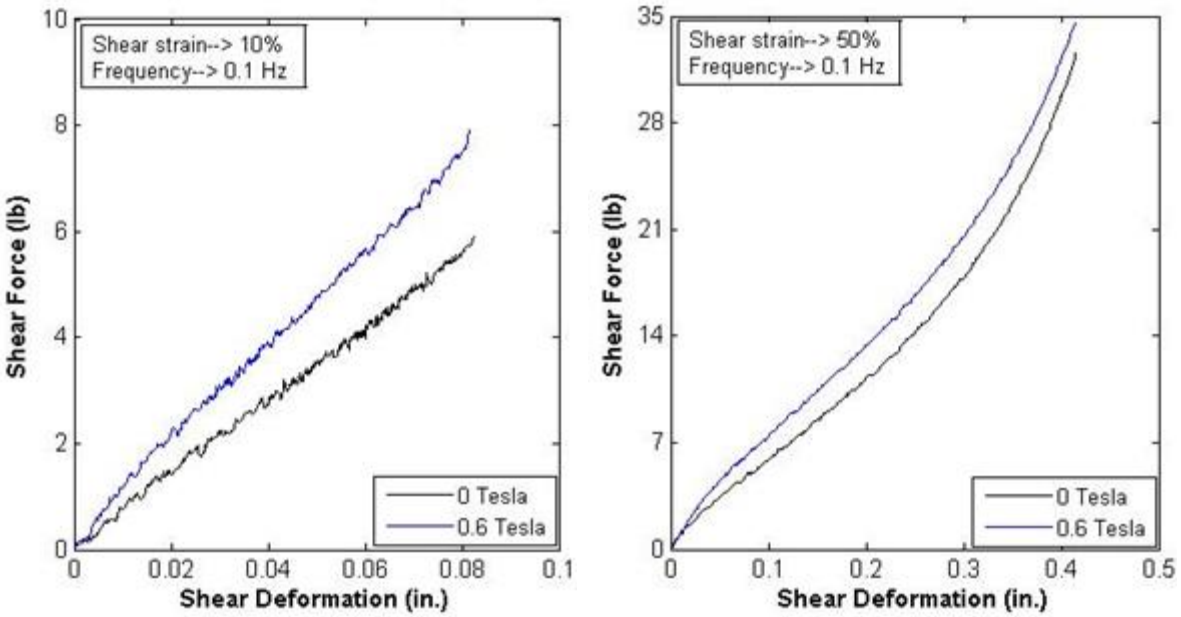


(a) (b)

Figure B.1.3. Force – Displacement curves for MR-S-6 under pure shear.

## B.2 Quasi –Static Test Results of Natural rubber-based MRE Samples

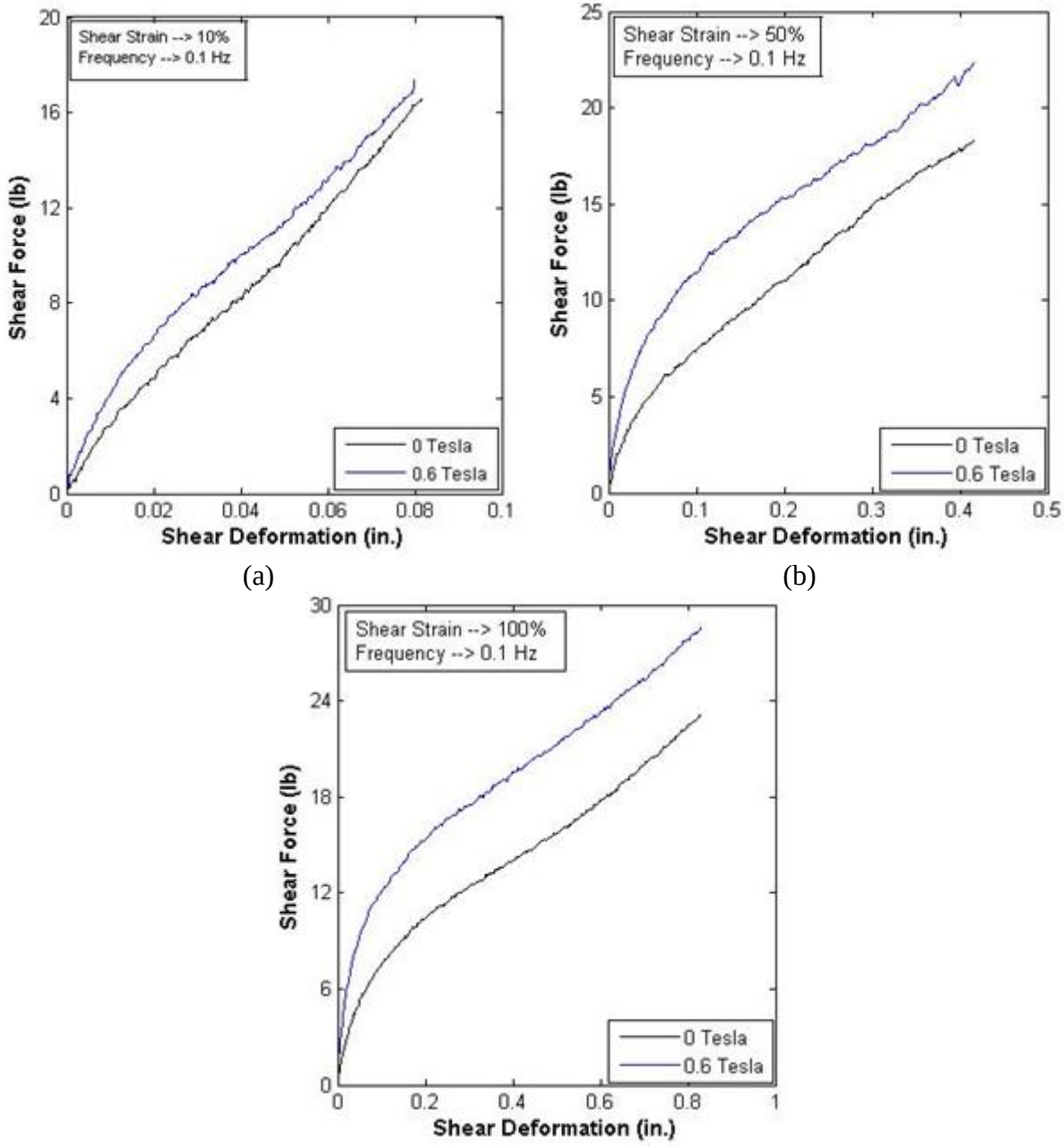


(a) (b)

(c)

Figure B.2.1. Force – Displacement curves for NR-S-1under pure shear.

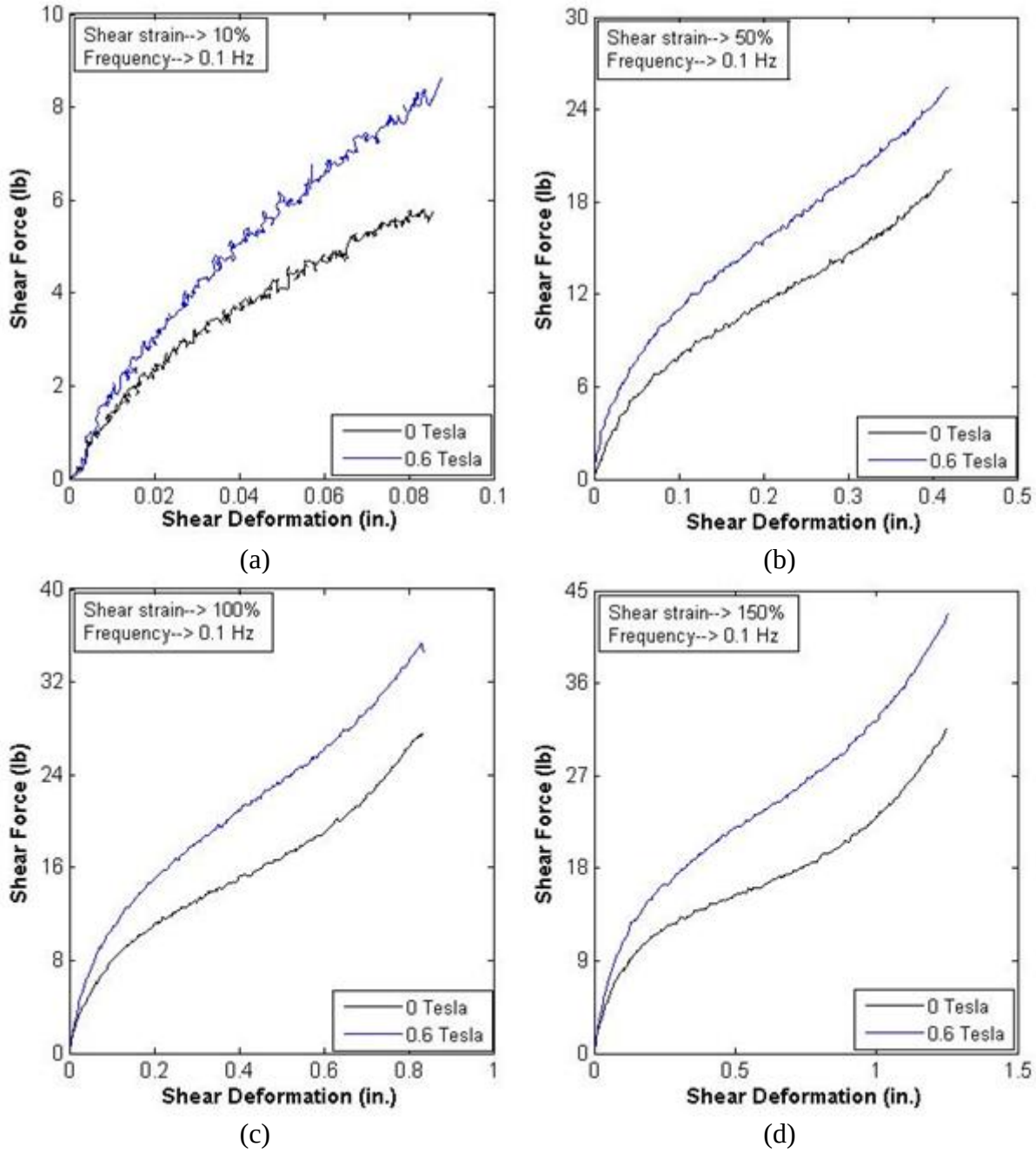


Figure B.2.2. Force – Displacement curves for NR-S-6 under pure shear.

## B.3 Cyclic Tests Results Summary for Natural rubber-based MRE Sample

Table B.3.1. Storage modulus ($G'$) and Loss modulus ($G^{"}$) of NR-S-4 Sample under Pure Shear ($lb/in^2$).

| Frequency/ Magnetic field | | Shear Strain | | | | | | | | | | | |
|---|---|---|---|---|---|---|---|---|---|---|---|---|---|
| | | 10% | | 30% | | 50% | | 75% | | 100% | | 125% | |
| | | G' | G" | G' | G" | G' | G" | G' | G" | G' | G" | G' | G" |
| 0.1 Hz | 0.0 | 276.2 | 135.3 | 158.6 | 106.5 | 106.6 | 88.9 | 126.1 | 96.8 | 69.7 | 68.0 | 65.3 | 63.7 |
| | 0.3 | 327.7 | 176.8 | 198.4 | 139.7 | 140.0 | 117.7 | 131.2 | 107.1 | 95.7 | 92.0 | 82.9 | 82.8 |
| | 0.5 | 369.9 | 203.3 | 223.1 | 157.3 | 157.1 | 130.0 | 136.3 | 113.0 | 109.6 | 101.5 | 94.9 | 91.8 |
| | 0.7 | 388.8 | 215.9 | 233.3 | 162.1 | 166.4 | 133.7 | 146.5 | 115.7 | 121.1 | 106.9 | 101.1 | 95.7 |
| **%MR-Effect** | | **41** | **60** | **47** | **52** | **56** | **50** | **16** | **19** | **74** | **57** | **55** | **50** |
| 0.5 Hz | 0.0 | 405.8 | 183.2 | 241.6 | 150.9 | 167.2 | 129.7 | 170.9 | 127.0 | 106.5 | 101.2 | 94.7 | 92.9 |
| | 0.3 | 476.1 | 232.9 | 285.7 | 187.2 | 200.7 | 158.3 | 180.5 | 140.9 | 134.6 | 123.0 | 114.8 | 110.8 |
| | 0.5 | 523.7 | 265.2 | 311.7 | 205.5 | 218.9 | 171.1 | 181.4 | 145.9 | 147.6 | 132.1 | 126.0 | 119.7 |
| | 0.7 | 538.4 | 279.3 | 315.2 | 205.7 | 225.0 | 174.3 | 168.9 | 142.4 | 153.7 | 135.8 | 128.6 | 122.1 |
| **%MR-Effect** | | **33** | **52** | **30** | **36** | **35** | **34** | **7** | **15** | **44** | **34** | **36** | **31** |
| 1 Hz | 0.0 | 478.0 | 200.0 | 288.4 | 169.7 | 203.5 | 147.9 | 196.9 | 139.6 | 131.2 | 115.7 | 114.5 | 105.4 |
| | 0.3 | 546.6 | 253.7 | 333.0 | 206.7 | 234.3 | 174.9 | 206.5 | 154.0 | 156.7 | 135.8 | 133.3 | 122.2 |
| | 0.5 | 600.6 | 285.3 | 357.9 | 223.3 | 252.4 | 188.3 | 208.4 | 155.2 | 169.5 | 145.3 | 144.0 | 131.6 |
| | 0.7 | 611.7 | 304.4 | 362.2 | 228.3 | 255.3 | 190.6 | 185.3 | 154.6 | 170.3 | 147.6 | 143.0 | 133.0 |
| **%MR-Effect** | | **28** | **52** | **26** | **35** | **25** | **29** | **12** | **11** | **30** | **28** | **26** | **26** |
| 3 Hz | 0.0 | 597.1 | 221.7 | 373.7 | 194.8 | 269.3 | 172.4 | 249.0 | 158.1 | 176.9 | 136.1 | 153.7 | 124.2 |
| | 0.3 | 681.4 | 281.1 | 419.2 | 231.6 | 299.3 | 199.4 | 259.5 | 173.3 | 202.6 | 155.4 | 173.9 | 140.9 |
| | 0.5 | 743.4 | 315.6 | 442.3 | 247.3 | 318.1 | 213.4 | 258.2 | 172.7 | 214.8 | 164.9 | 185.0 | 151.0 |
| | 0.7 | 745.1 | 337.3 | 442.6 | 259.6 | 318.1 | 217.4 | 224.1 | 175.1 | 209.4 | 166.8 | 179.3 | 152.0 |
| **%MR-Effect** | | **25** | **52** | **18** | **33** | **18** | **26** | **16** | **11** | **21** | **23** | **20** | **22** |

## B.4 Test Protocol

Table B.4.1. Quasi – Static test protocol.

| Strain (%) | Frequency (Hz) | Period (Sec) | Magnetic field (Tesla) | | | |
|---|---|---|---|---|---|---|
| 5.0 | 0.1 | 10.0 | 0.0 | 0.3 | 0.5 | 0.7 |
| 10.0 | 0.1 | 10.0 | 0.0 | 0.3 | 0.5 | 0.7 |
| 30.0 | 0.1 | 10.0 | 0.0 | 0.3 | 0.5 | 0.7 |
| 50.0 | 0.1 | 10.0 | 0.0 | 0.3 | 0.5 | 0.7 |
| 75.0 | 0.1 | 10.0 | 0.0 | 0.3 | 0.5 | 0.7 |
| 100.0 | 0.1 | 10.0 | 0.0 | 0.3 | 0.5 | 0.7 |
| 125.0 | 0.1 | 10.0 | 0.0 | 0.3 | 0.5 | 0.7 |
| 150.0 | 0.1 | 10.0 | 0.0 | 0.3 | 0.5 | 0.7 |

Table B.4.2. Cyclic test protocol.

| Strain (%) | Frequency (Hz) | Period (Sec) | Magnetic field (Tesla) | | | |
|---|---|---|---|---|---|---|
| 10, 30, 50, 75, 100, 125, 150 | 0.1 | 10.0 | 0.0 | 0.3 | 0.5 | 0.7 |
| | 0.5 | 2.0 | 0.0 | 0.3 | 0.5 | 0.7 |
| | 1.0 | 1.0 | 0.0 | 0.3 | 0.5 | 0.7 |
| | 3.0 | 0.3 | 0.0 | 0.3 | 0.5 | 0.7 |
| | 5.0 | 0.2 | 0.0 | 0.3 | 0.5 | 0.7 |
| | 7.0 | 0.1 | 0.0 | 0.3 | 0.5 | 0.7 |
| | 10.0 | 0.1 | 0.0 | 0.3 | 0.5 | 0.7 |

## B.5 Test setup Assembly

(a)

(b)

(c)

(d)

Figure 5.1. (a) Outer plates installation, (b) Actuator and knife plate installation, (c) Complete test setup without bearings, (d) Bringing half glued bearing to install.

(e)

(f)

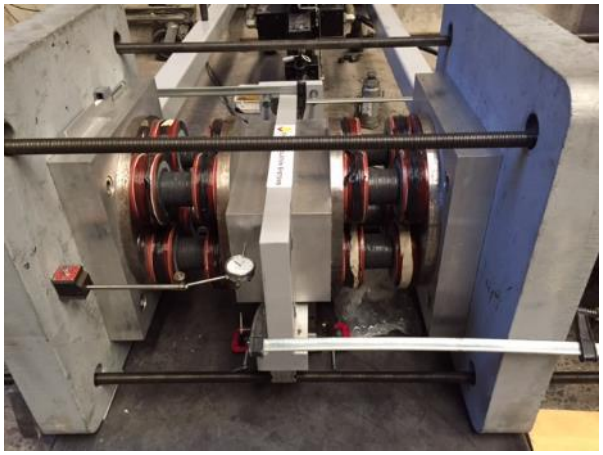

(g)

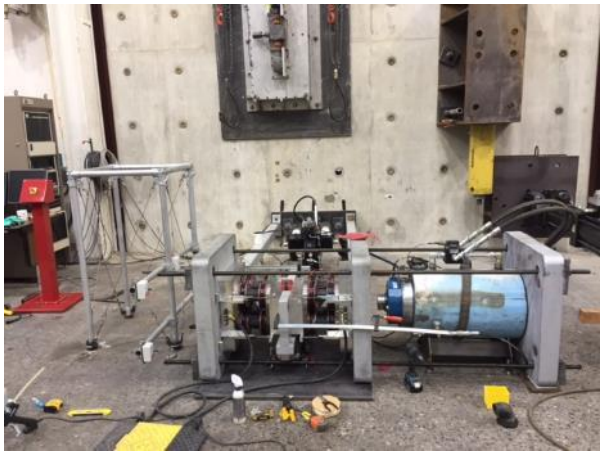

(h)

Figure 5.1. (e) Half bearing installed, (f) Gluing to finish bearing installation, (g) Complete bearings installation, and (h) Complete test setup.

## B.6 Test Protocol

Table B.6. Test protocol

| Test ID | Shear | | Number of Cycles | Axial Load | Ampere | Frequency | Rate (2πAf) |
|---|---|---|---|---|---|---|---|
| | Strain (%) | Amplitude (in.) | | (lb) | (amp) | (Hz) | (in./Sec) |
| PB-001 | 2.5 | 0.03 | 6 | 0 | 0 | 0.1 | 0.02 |
| PB-005 | 5 | 0.06 | 6 | 0 | 0 | 0.1 | 0.04 |
| PB-009 | 10 | 0.13 | 6 | 0 | 0 | 0.1 | 0.08 |
| PB-013 | 15 | 0.19 | 6 | 0 | 0 | 0.1 | 0.12 |
| PB-017 | 20 | 0.25 | 6 | 0 | 0 | 0.1 | 0.16 |
| PB-021 | 2.5 | 0.03 | 6 | 0 | 0 | 0.5 | 0.10 |
| PB-025 | 5 | 0.06 | 6 | 0 | 0 | 0.5 | 0.20 |
| PB-029 | 10 | 0.13 | 6 | 0 | 0 | 0.5 | 0.39 |
| PB-033 | 15 | 0.19 | 6 | 0 | 0 | 0.5 | 0.59 |
| PB-037 | 20 | 0.25 | 6 | 0 | 0 | 0.5 | 0.79 |
| PB-041 | 2.5 | 0.03 | 6 | 0 | 0 | 1 | 0.20 |
| PB-045 | 5 | 0.06 | 6 | 0 | 0 | 1 | 0.39 |
| PB-049 | 10 | 0.13 | 6 | 0 | 0 | 1 | 0.79 |
| PB-053 | 15 | 0.19 | 6 | 0 | 0 | 1 | 1.18 |
| PB-057 | 20 | 0.25 | 6 | 0 | 0 | 1 | 1.57 |
| PB-061 | 2.5 | 0.03 | 6 | 0 | 0 | 4 | 0.79 |
| PB-065 | 5 | 0.06 | 6 | 0 | 0 | 4 | 1.57 |
| PB-069 | 10 | 0.13 | 6 | 0 | 0 | 4 | 3.14 |
| PB-073 | 15 | 0.19 | 6 | 0 | 0 | 4 | 4.71 |
| PB-077 | 20 | 0.25 | 6 | 0 | 0 | 4 | 6.28 |

| Test ID | Shear | | Number of Cycles | Axial Load | Ampere | Frequency | Rate (2πAf) |
|---|---|---|---|---|---|---|---|
| | Strain (%) | Amplitude (in.) | | (lb) | (amp) | (Hz) | (in./Sec) |
| 001 | 2.5 | 0.03125 | 6 | 0 | 0 | 0.1 | 0.02 |
| 002 | 2.5 | 0.03125 | 6 | 0 | 7 | 0.1 | 0.02 |
| 003 | 2.5 | 0.03125 | 6 | 0 | 14 | 0.1 | 0.02 |
| 004 | 2.5 | 0.03125 | 6 | 0 | 19.5 | 0.1 | 0.02 |
| 005 | 5 | 0.0625 | 6 | 0 | 0 | 0.1 | 0.04 |
| 006 | 5 | 0.0625 | 6 | 0 | 7 | 0.1 | 0.04 |
| 007 | 5 | 0.0625 | 6 | 0 | 14 | 0.1 | 0.04 |
| 008 | 5 | 0.0625 | 6 | 0 | 19.5 | 0.1 | 0.04 |
| 009 | 10 | 0.125 | 6 | 0 | 0 | 0.1 | 0.08 |
| 010 | 10 | 0.125 | 6 | 0 | 7 | 0.1 | 0.08 |
| 011 | 10 | 0.125 | 6 | 0 | 14 | 0.1 | 0.08 |
| 012 | 10 | 0.125 | 6 | 0 | 19.5 | 0.1 | 0.08 |
| 013 | 15 | 0.1875 | 6 | 0 | 0 | 0.1 | 0.12 |
| 014 | 15 | 0.1875 | 6 | 0 | 7 | 0.1 | 0.12 |
| 015 | 15 | 0.1875 | 6 | 0 | 14 | 0.1 | 0.12 |
| 016 | 15 | 0.1875 | 6 | 0 | 19.5 | 0.1 | 0.12 |
| 017 | 20 | 0.25 | 6 | 0 | 0 | 0.1 | 0.16 |
| 018 | 20 | 0.25 | 6 | 0 | 7 | 0.1 | 0.16 |
| 019 | 20 | 0.25 | 6 | 0 | 14 | 0.1 | 0.16 |
| 020 | 20 | 0.25 | 6 | 0 | 19.5 | 0.1 | 0.16 |

| Test ID | Shear | | Number of Cycles | Axial Load | Ampere | Frequency | Rate (2πAf) |
|---|---|---|---|---|---|---|---|
| | Strain (%) | Amplitude (in.) | | (lb) | (amp) | (Hz) | (in./Sec) |
| 021 | 2.5 | 0.03125 | 6 | 0 | 0 | 0.5 | 0.10 |
| 022 | 2.5 | 0.03125 | 6 | 0 | 7 | 0.5 | 0.10 |
| 023 | 2.5 | 0.03125 | 6 | 0 | 14 | 0.5 | 0.10 |
| 024 | 2.5 | 0.03125 | 6 | 0 | 19.5 | 0.5 | 0.10 |
| 025 | 5 | 0.0625 | 6 | 0 | 0 | 0.5 | 0.20 |
| 026 | 5 | 0.0625 | 6 | 0 | 7 | 0.5 | 0.20 |
| 027 | 5 | 0.0625 | 6 | 0 | 14 | 0.5 | 0.20 |
| 028 | 5 | 0.0625 | 6 | 0 | 19.5 | 0.5 | 0.20 |
| 029 | 10 | 0.125 | 6 | 0 | 0 | 0.5 | 0.39 |
| 030 | 10 | 0.125 | 6 | 0 | 7 | 0.5 | 0.39 |
| 031 | 10 | 0.125 | 6 | 0 | 14 | 0.5 | 0.39 |
| 032 | 10 | 0.125 | 6 | 0 | 19.5 | 0.5 | 0.39 |
| 033 | 15 | 0.1875 | 6 | 0 | 0 | 0.5 | 0.59 |
| 034 | 15 | 0.1875 | 6 | 0 | 7 | 0.5 | 0.59 |
| 035 | 15 | 0.1875 | 6 | 0 | 14 | 0.5 | 0.59 |
| 036 | 15 | 0.1875 | 6 | 0 | 19.5 | 0.5 | 0.59 |
| 037 | 20 | 0.25 | 6 | 0 | 0 | 0.5 | 0.79 |
| 038 | 20 | 0.25 | 6 | 0 | 7 | 0.5 | 0.79 |
| 039 | 20 | 0.25 | 6 | 0 | 14 | 0.5 | 0.79 |
| 040 | 20 | 0.25 | 6 | 0 | 19.5 | 0.5 | 0.79 |

| Test ID | Shear | | Number of Cycles | Axial Load | Ampere | Frequency | Rate (2πAf) |
|---|---|---|---|---|---|---|---|
| | Strain (%) | Amplitude (in.) | | (lb) | (amp) | (Hz) | (in./Sec) |
| 041 | 2.5 | 0.03125 | 6 | 0 | 0 | 1 | 0.20 |
| 042 | 2.5 | 0.03125 | 6 | 0 | 7 | 1 | 0.20 |
| 043 | 2.5 | 0.03125 | 6 | 0 | 14 | 1 | 0.20 |
| 044 | 2.5 | 0.03125 | 6 | 0 | 19.5 | 1 | 0.20 |
| 045 | 5 | 0.0625 | 6 | 0 | 0 | 1 | 0.39 |
| 046 | 5 | 0.0625 | 6 | 0 | 7 | 1 | 0.39 |
| 047 | 5 | 0.0625 | 6 | 0 | 14 | 1 | 0.39 |
| 048 | 5 | 0.0625 | 6 | 0 | 19.5 | 1 | 0.39 |
| 049 | 10 | 0.125 | 6 | 0 | 0 | 1 | 0.79 |
| 050 | 10 | 0.125 | 6 | 0 | 7 | 1 | 0.79 |
| 051 | 10 | 0.125 | 6 | 0 | 14 | 1 | 0.79 |
| 052 | 10 | 0.125 | 6 | 0 | 19.5 | 1 | 0.79 |
| 053 | 15 | 0.1875 | 6 | 0 | 0 | 1 | 1.18 |
| 054 | 15 | 0.1875 | 6 | 0 | 7 | 1 | 1.18 |
| 055 | 15 | 0.1875 | 6 | 0 | 14 | 1 | 1.18 |
| 056 | 15 | 0.1875 | 6 | 0 | 19.5 | 1 | 1.18 |
| 057 | 20 | 0.25 | 6 | 0 | 0 | 1 | 1.57 |
| 058 | 20 | 0.25 | 6 | 0 | 7 | 1 | 1.57 |
| 059 | 20 | 0.25 | 6 | 0 | 14 | 1 | 1.57 |
| 060 | 20 | 0.25 | 6 | 0 | 19.5 | 1 | 1.57 |

| Test ID | Shear | | Number of Cycles | Axial Load | Ampere | Frequency | Rate (2πAf) |
|---|---|---|---|---|---|---|---|
| | Strain (%) | Amplitude (in.) | | (lb) | (amp) | (Hz) | (in./Sec) |
| 061 | 2.5 | 0.03125 | 6 | 0 | 0 | 4 | 0.79 |
| 062 | 2.5 | 0.03125 | 6 | 0 | 7 | 4 | 0.79 |
| 063 | 2.5 | 0.03125 | 6 | 0 | 14 | 4 | 0.79 |
| 064 | 2.5 | 0.03125 | 6 | 0 | 19.5 | 4 | 0.79 |
| 065 | 5 | 0.0625 | 6 | 0 | 0 | 4 | 1.57 |
| 066 | 5 | 0.0625 | 6 | 0 | 7 | 4 | 1.57 |
| 067 | 5 | 0.0625 | 6 | 0 | 14 | 4 | 1.57 |
| 068 | 5 | 0.0625 | 6 | 0 | 19.5 | 4 | 1.57 |
| 069 | 10 | 0.125 | 6 | 0 | 0 | 4 | 3.14 |
| 070 | 10 | 0.125 | 6 | 0 | 7 | 4 | 3.14 |
| 071 | 10 | 0.125 | 6 | 0 | 14 | 4 | 3.14 |
| 072 | 10 | 0.125 | 6 | 0 | 19.5 | 4 | 3.14 |
| 073 | 15 | 0.1875 | 6 | 0 | 0 | 4 | 4.71 |
| 074 | 15 | 0.1875 | 6 | 0 | 7 | 4 | 4.71 |
| 075 | 15 | 0.1875 | 6 | 0 | 14 | 4 | 4.71 |
| 076 | 15 | 0.1875 | 6 | 0 | 19.5 | 4 | 4.71 |
| 077 | 20 | 0.25 | 6 | 0 | 0 | 4 | 6.28 |
| 078 | 20 | 0.25 | 6 | 0 | 7 | 4 | 6.28 |
| 079 | 20 | 0.25 | 6 | 0 | 14 | 4 | 6.28 |
| 080 | 20 | 0.25 | 6 | 0 | 19.5 | 4 | 6.28 |

| Test ID | Shear | | Number of Cycles | Axial Load | Ampere | Frequency | Rate (2πAf) |
|---|---|---|---|---|---|---|---|
| | Strain (%) | Amplitude (in.) | | (lb) | (amp) | (Hz) | (in./Sec) |
| 081 | 5 | 0.0625 | 6 | 2,500 | 0 | 0.1 | 0.04 |
| 082 | 5 | 0.0625 | 6 | 2,500 | 7 | 0.1 | 0.04 |
| 083 | 5 | 0.0625 | 6 | 2,500 | 14 | 0.1 | 0.04 |
| 084 | 5 | 0.0625 | 6 | 2,500 | 19.5 | 0.1 | 0.04 |
| 085 | 10 | 0.125 | 6 | 2,500 | 0 | 0.1 | 0.08 |
| 086 | 10 | 0.125 | 6 | 2,500 | 7 | 0.1 | 0.08 |
| 087 | 10 | 0.125 | 6 | 2,500 | 14 | 0.1 | 0.08 |
| 088 | 10 | 0.125 | 6 | 2,500 | 19.5 | 0.1 | 0.08 |
| 089 | 15 | 0.1875 | 6 | 2,500 | 0 | 0.1 | 0.12 |
| 090 | 15 | 0.1875 | 6 | 2,500 | 7 | 0.1 | 0.12 |
| 091 | 15 | 0.1875 | 6 | 2,500 | 14 | 0.1 | 0.12 |
| 092 | 15 | 0.1875 | 6 | 2,500 | 19.5 | 0.1 | 0.12 |
| 093 | 20 | 0.25 | 6 | 2,500 | 0 | 0.1 | 0.16 |
| 094 | 20 | 0.25 | 6 | 2,500 | 7 | 0.1 | 0.16 |
| 095 | 20 | 0.25 | 6 | 2,500 | 14 | 0.1 | 0.16 |
| 096 | 20 | 0.25 | 6 | 2,500 | 19.5 | 0.1 | 0.16 |

| Test ID | Shear | | Number of Cycles | Axial Load | Ampere | Frequency | Rate (2πAf) |
|---|---|---|---|---|---|---|---|
| | Strain (%) | Amplitude (in.) | | (lb) | (amp) | (Hz) | (in./Sec) |
| 097 | 5 | 0.0625 | 6 | 2,500 | 0 | 0.5 | 0.20 |
| 098 | 5 | 0.0625 | 6 | 2,500 | 7 | 0.5 | 0.20 |
| 099 | 5 | 0.0625 | 6 | 2,500 | 14 | 0.5 | 0.20 |
| 100 | 5 | 0.0625 | 6 | 2,500 | 19.5 | 0.5 | 0.20 |
| 101 | 10 | 0.125 | 6 | 2,500 | 0 | 0.5 | 0.39 |
| 102 | 10 | 0.125 | 6 | 2,500 | 7 | 0.5 | 0.39 |
| 103 | 10 | 0.125 | 6 | 2,500 | 14 | 0.5 | 0.39 |
| 104 | 10 | 0.125 | 6 | 2,500 | 19.5 | 0.5 | 0.39 |
| 105 | 15 | 0.1875 | 6 | 2,500 | 0 | 0.5 | 0.59 |
| 106 | 15 | 0.1875 | 6 | 2,500 | 7 | 0.5 | 0.59 |
| 107 | 15 | 0.1875 | 6 | 2,500 | 14 | 0.5 | 0.59 |
| 108 | 15 | 0.1875 | 6 | 2,500 | 19.5 | 0.5 | 0.59 |
| 109 | 20 | 0.25 | 6 | 2,500 | 0 | 0.5 | 0.79 |
| 110 | 20 | 0.25 | 6 | 2,500 | 7 | 0.5 | 0.79 |
| 111 | 20 | 0.25 | 6 | 2,500 | 14 | 0.5 | 0.79 |
| 112 | 20 | 0.25 | 6 | 2,500 | 19.5 | 0.5 | 0.79 |

| Test ID | Shear | | Number of Cycles | Axial Load | Ampere | Frequency | Rate (2πAf) |
|---|---|---|---|---|---|---|---|
| | Strain (%) | Amplitude (in.) | | (lb) | (amp) | (Hz) | (in./Sec) |
| 113 | 5 | 0.0625 | 6 | 2,500 | 0 | 1 | 0.39 |
| 114 | 5 | 0.0625 | 6 | 2,500 | 7 | 1 | 0.39 |
| 115 | 5 | 0.0625 | 6 | 2,500 | 14 | 1 | 0.39 |
| 116 | 5 | 0.0625 | 6 | 2,500 | 19.5 | 1 | 0.39 |
| 117 | 10 | 0.125 | 6 | 2,500 | 0 | 1 | 0.79 |
| 118 | 10 | 0.125 | 6 | 2,500 | 7 | 1 | 0.79 |
| 119 | 10 | 0.125 | 6 | 2,500 | 14 | 1 | 0.79 |
| 120 | 10 | 0.125 | 6 | 2,500 | 19.5 | 1 | 0.79 |
| 121 | 15 | 0.1875 | 6 | 2,500 | 0 | 1 | 1.18 |
| 122 | 15 | 0.1875 | 6 | 2,500 | 7 | 1 | 1.18 |
| 123 | 15 | 0.1875 | 6 | 2,500 | 14 | 1 | 1.18 |
| 124 | 15 | 0.1875 | 6 | 2,500 | 19.5 | 1 | 1.18 |
| 125 | 20 | 0.25 | 6 | 2,500 | 0 | 1 | 1.57 |
| 126 | 20 | 0.25 | 6 | 2,500 | 7 | 1 | 1.57 |
| 127 | 20 | 0.25 | 6 | 2,500 | 14 | 1 | 1.57 |
| 128 | 20 | 0.25 | 6 | 2,500 | 19.5 | 1 | 1.57 |

| Test ID | Shear | | Number of Cycles | Axial Load | Ampere | Frequency | Rate (2πAf) |
|---|---|---|---|---|---|---|---|
| | Strain (%) | Amplitude (in.) | | (lb) | (amp) | (Hz) | (in./Sec) |
| 129 | 5 | 0.0625 | 6 | 2,500 | 0 | 4 | 1.57 |
| 130 | 5 | 0.0625 | 6 | 2,500 | 7 | 4 | 1.57 |
| 131 | 5 | 0.0625 | 6 | 2,500 | 14 | 4 | 1.57 |
| 132 | 5 | 0.0625 | 6 | 2,500 | 19.5 | 4 | 1.57 |
| 133 | 10 | 0.125 | 6 | 2,500 | 0 | 4 | 3.14 |
| 134 | 10 | 0.125 | 6 | 2,500 | 7 | 4 | 3.14 |
| 135 | 10 | 0.125 | 6 | 2,500 | 14 | 4 | 3.14 |
| 136 | 10 | 0.125 | 6 | 2,500 | 19.5 | 4 | 3.14 |
| 137 | 15 | 0.1875 | 6 | 2,500 | 0 | 4 | 4.71 |
| 138 | 15 | 0.1875 | 6 | 2,500 | 7 | 4 | 4.71 |
| 139 | 15 | 0.1875 | 6 | 2,500 | 14 | 4 | 4.71 |
| 140 | 15 | 0.1875 | 6 | 2,500 | 19.5 | 4 | 4.71 |
| 141 | 20 | 0.25 | 6 | 2,500 | 0 | 4 | 6.28 |
| 142 | 20 | 0.25 | 6 | 2,500 | 7 | 4 | 6.28 |
| 143 | 20 | 0.25 | 6 | 2,500 | 14 | 4 | 6.28 |
| 144 | 20 | 0.25 | 6 | 2,500 | 19.5 | 4 | 6.28 |

| Test ID | Shear | | Number of Cycles | Axial Load | Ampere | Frequency | Rate (2πAf) |
|---|---|---|---|---|---|---|---|
| | Strain (%) | Amplitude (in.) | | (lb) | (amp) | (Hz) | (in./Sec) |
| 145 | 5 | 0.0625 | 6 | 5,000 | 0 | 0.1 | 0.04 |
| 146 | 5 | 0.0625 | 6 | 5,000 | 7 | 0.1 | 0.04 |
| 147 | 5 | 0.0625 | 6 | 5,000 | 14 | 0.1 | 0.04 |
| 148 | 5 | 0.0625 | 6 | 5,000 | 19.5 | 0.1 | 0.04 |
| 149 | 10 | 0.125 | 6 | 5,000 | 0 | 0.1 | 0.08 |
| 150 | 10 | 0.125 | 6 | 5,000 | 7 | 0.1 | 0.08 |
| 151 | 10 | 0.125 | 6 | 5,000 | 14 | 0.1 | 0.08 |
| 152 | 10 | 0.125 | 6 | 5,000 | 19.5 | 0.1 | 0.08 |
| 153 | 15 | 0.1875 | 6 | 5,000 | 0 | 0.1 | 0.12 |
| 154 | 15 | 0.1875 | 6 | 5,000 | 7 | 0.1 | 0.12 |
| 155 | 15 | 0.1875 | 6 | 5,000 | 14 | 0.1 | 0.12 |
| 156 | 15 | 0.1875 | 6 | 5,000 | 19.5 | 0.1 | 0.12 |
| 157 | 20 | 0.25 | 6 | 5,000 | 0 | 0.1 | 0.16 |
| 158 | 20 | 0.25 | 6 | 5,000 | 7 | 0.1 | 0.16 |
| 159 | 20 | 0.25 | 6 | 5,000 | 14 | 0.1 | 0.16 |
| 160 | 20 | 0.25 | 6 | 5,000 | 19.5 | 0.1 | 0.16 |

| Test ID | Shear | | Number of Cycles | Axial Load | Ampere | Frequency | Rate (2πAf) |
|---|---|---|---|---|---|---|---|
| | Strain (%) | Amplitude (in.) | | (lb) | (amp) | (Hz) | (in./Sec) |
| 161 | 5 | 0.0625 | 6 | 5,000 | 0 | 0.5 | 0.20 |
| 162 | 5 | 0.0625 | 6 | 5,000 | 7 | 0.5 | 0.20 |
| 163 | 5 | 0.0625 | 6 | 5,000 | 14 | 0.5 | 0.20 |
| 164 | 5 | 0.0625 | 6 | 5,000 | 19.5 | 0.5 | 0.20 |
| 165 | 10 | 0.125 | 6 | 5,000 | 0 | 0.5 | 0.39 |
| 166 | 10 | 0.125 | 6 | 5,000 | 7 | 0.5 | 0.39 |
| 167 | 10 | 0.125 | 6 | 5,000 | 14 | 0.5 | 0.39 |
| 168 | 10 | 0.125 | 6 | 5,000 | 19.5 | 0.5 | 0.39 |
| 169 | 15 | 0.1875 | 6 | 5,000 | 0 | 0.5 | 0.59 |
| 170 | 15 | 0.1875 | 6 | 5,000 | 7 | 0.5 | 0.59 |
| 171 | 15 | 0.1875 | 6 | 5,000 | 14 | 0.5 | 0.59 |
| 172 | 15 | 0.1875 | 6 | 5,000 | 19.5 | 0.5 | 0.59 |
| 173 | 20 | 0.25 | 6 | 5,000 | 0 | 0.5 | 0.79 |
| 174 | 20 | 0.25 | 6 | 5,000 | 7 | 0.5 | 0.79 |
| 175 | 20 | 0.25 | 6 | 5,000 | 14 | 0.5 | 0.79 |
| 176 | 20 | 0.25 | 6 | 5,000 | 19.5 | 0.5 | 0.79 |

| Test ID | Shear | | Number of Cycles | Axial Load | Ampere | Frequency | Rate (2πAf) |
|---|---|---|---|---|---|---|---|
| | Strain (%) | Amplitude (in.) | | (lb) | (amp) | (Hz) | (in./Sec) |
| 177 | 5 | 0.0625 | 6 | 5,000 | 0 | 1 | 0.39 |
| 178 | 5 | 0.0625 | 6 | 5,000 | 7 | 1 | 0.39 |
| 179 | 5 | 0.0625 | 6 | 5,000 | 14 | 1 | 0.39 |
| 180 | 5 | 0.0625 | 6 | 5,000 | 19.5 | 1 | 0.39 |
| 181 | 10 | 0.125 | 6 | 5,000 | 0 | 1 | 0.79 |
| 182 | 10 | 0.125 | 6 | 5,000 | 7 | 1 | 0.79 |
| 183 | 10 | 0.125 | 6 | 5,000 | 14 | 1 | 0.79 |
| 184 | 10 | 0.125 | 6 | 5,000 | 19.5 | 1 | 0.79 |
| 185 | 15 | 0.1875 | 6 | 5,000 | 0 | 1 | 1.18 |
| 186 | 15 | 0.1875 | 6 | 5,000 | 7 | 1 | 1.18 |
| 187 | 15 | 0.1875 | 6 | 5,000 | 14 | 1 | 1.18 |
| 188 | 15 | 0.1875 | 6 | 5,000 | 19.5 | 1 | 1.18 |
| 189 | 20 | 0.25 | 6 | 5,000 | 0 | 1 | 1.57 |
| 190 | 20 | 0.25 | 6 | 5,000 | 7 | 1 | 1.57 |
| 191 | 20 | 0.25 | 6 | 5,000 | 14 | 1 | 1.57 |
| 192 | 20 | 0.25 | 6 | 5,000 | 19.5 | 1 | 1.57 |

| Test ID | Shear | | Number of Cycles | Axial Load | Ampere | Frequency | Rate (2πAf) |
|---|---|---|---|---|---|---|---|
| | Strain (%) | Amplitude (in.) | | (lb) | (amp) | (Hz) | (in./Sec) |
| 193 | 5 | 0.0625 | 6 | 5,000 | 0 | 4 | 1.57 |
| 194 | 5 | 0.0625 | 6 | 5,000 | 7 | 4 | 1.57 |
| 195 | 5 | 0.0625 | 6 | 5,000 | 14 | 4 | 1.57 |
| 196 | 5 | 0.0625 | 6 | 5,000 | 19.5 | 4 | 1.57 |
| 197 | 10 | 0.125 | 6 | 5,000 | 0 | 4 | 3.14 |
| 198 | 10 | 0.125 | 6 | 5,000 | 7 | 4 | 3.14 |
| 199 | 10 | 0.125 | 6 | 5,000 | 14 | 4 | 3.14 |
| 200 | 10 | 0.125 | 6 | 5,000 | 19.5 | 4 | 3.14 |
| 201 | 15 | 0.1875 | 6 | 5,000 | 0 | 4 | 4.71 |
| 202 | 15 | 0.1875 | 6 | 5,000 | 7 | 4 | 4.71 |
| 203 | 15 | 0.1875 | 6 | 5,000 | 14 | 4 | 4.71 |
| 204 | 15 | 0.1875 | 6 | 5,000 | 19.5 | 4 | 4.71 |
| 205 | 20 | 0.25 | 6 | 5,000 | 0 | 4 | 6.28 |
| 206 | 20 | 0.25 | 6 | 5,000 | 7 | 4 | 6.28 |
| 207 | 20 | 0.25 | 6 | 5,000 | 14 | 4 | 6.28 |
| 208 | 20 | 0.25 | 6 | 5,000 | 19.5 | 4 | 6.28 |

| Test ID | Shear | | Number of Cycles | Axial Load | Ampere | Frequency | Rate (2πAf) |
|---|---|---|---|---|---|---|---|
| | Strain (%) | Amplitude (in.) | | (lb) | (amp) | (Hz) | (in./Sec) |
| 209 | 5 | 0.0625 | 6 | 10,000 | 0 | 0.1 | 0.04 |
| 210 | 5 | 0.0625 | 6 | 10,000 | 7 | 0.1 | 0.04 |
| 212 | 5 | 0.0625 | 6 | 10,000 | 19.5 | 0.1 | 0.04 |
| 213 | 10 | 0.125 | 6 | 10,000 | 0 | 0.1 | 0.08 |
| 214 | 10 | 0.125 | 6 | 10,000 | 7 | 0.1 | 0.08 |
| 216 | 10 | 0.125 | 6 | 10,000 | 19.5 | 0.1 | 0.08 |
| 217 | 15 | 0.1875 | 6 | 10,000 | 0 | 0.1 | 0.12 |
| 218 | 15 | 0.1875 | 6 | 10,000 | 7 | 0.1 | 0.12 |
| 220 | 15 | 0.1875 | 6 | 10,000 | 19.5 | 0.1 | 0.12 |
| 221 | 20 | 0.25 | 6 | 10,000 | 0 | 0.1 | 0.16 |
| 222 | 20 | 0.25 | 6 | 10,000 | 7 | 0.1 | 0.16 |
| 224 | 20 | 0.25 | 6 | 10,000 | 19.5 | 0.1 | 0.16 |

| Test ID | Shear | | Number of Cycles | Axial Load | Ampere | Frequency | Rate (2πAf) |
|---|---|---|---|---|---|---|---|
| | Strain (%) | Amplitude (in.) | | (lb) | (amp) | (Hz) | (in./Sec) |
| 225 | 5 | 0.0625 | 6 | 10,000 | 0 | 0.5 | 0.20 |
| 256 | 5 | 0.0625 | 6 | 10,000 | 7 | 0.5 | 0.20 |
| 228 | 5 | 0.0625 | 6 | 10,000 | 19.5 | 0.5 | 0.20 |
| 229 | 10 | 0.125 | 6 | 10,000 | 0 | 0.5 | 0.39 |
| 230 | 10 | 0.125 | 6 | 10,000 | 7 | 0.5 | 0.39 |
| 232 | 10 | 0.125 | 6 | 10,000 | 19.5 | 0.5 | 0.39 |
| 233 | 15 | 0.1875 | 6 | 10,000 | 0 | 0.5 | 0.59 |
| 234 | 15 | 0.1875 | 6 | 10,000 | 7 | 0.5 | 0.59 |
| 236 | 15 | 0.1875 | 6 | 10,000 | 19.5 | 0.5 | 0.59 |
| 237 | 20 | 0.25 | 6 | 10,000 | 0 | 0.5 | 0.79 |
| 238 | 20 | 0.25 | 6 | 10,000 | 7 | 0.5 | 0.79 |
| 240 | 20 | 0.25 | 6 | 10,000 | 19.5 | 0.5 | 0.79 |

| Test ID | Shear | | Number of Cycles | Axial Load | Ampere | Frequency | Rate (2πAf) |
|---|---|---|---|---|---|---|---|
| | Strain (%) | Amplitude (in.) | | (lb) | (amp) | (Hz) | (in./Sec) |
| 241 | 5 | 0.0625 | 6 | 10,000 | 0 | 1 | 0.39 |
| 242 | 5 | 0.0625 | 6 | 10,000 | 7 | 1 | 0.39 |
| 244 | 5 | 0.0625 | 6 | 10,000 | 19.5 | 1 | 0.39 |
| 245 | 10 | 0.125 | 6 | 10,000 | 0 | 1 | 0.79 |
| 246 | 10 | 0.125 | 6 | 10,000 | 7 | 1 | 0.79 |
| 248 | 10 | 0.125 | 6 | 10,000 | 19.5 | 1 | 0.79 |
| 249 | 15 | 0.1875 | 6 | 10,000 | 0 | 1 | 1.18 |
| 250 | 15 | 0.1875 | 6 | 10,000 | 7 | 1 | 1.18 |
| 252 | 15 | 0.1875 | 6 | 10,000 | 19.5 | 1 | 1.18 |
| 253 | 20 | 0.25 | 6 | 10,000 | 0 | 1 | 1.57 |
| 254 | 20 | 0.25 | 6 | 10,000 | 7 | 1 | 1.57 |
| 256 | 20 | 0.25 | 6 | 10,000 | 19.5 | 1 | 1.57 |

| Test ID | Shear | | Number of Cycles | Axial Load | Ampere | Frequency | Rate (2πAf) |
|---|---|---|---|---|---|---|---|
| | Strain (%) | Amplitude (in.) | | (lb) | (amp) | (Hz) | (in./Sec) |
| 257 | 5 | 0.0625 | 6 | 10,000 | 0 | 4 | 1.57 |
| 258 | 5 | 0.0625 | 6 | 10,000 | 7 | 4 | 1.57 |
| 260 | 5 | 0.0625 | 6 | 10,000 | 19.5 | 4 | 1.57 |
| 261 | 10 | 0.125 | 6 | 10,000 | 0 | 4 | 3.14 |
| 262 | 10 | 0.125 | 6 | 10,000 | 7 | 4 | 3.14 |
| 264 | 10 | 0.125 | 6 | 10,000 | 19.5 | 4 | 3.14 |
| 265 | 15 | 0.1875 | 6 | 10,000 | 0 | 4 | 4.71 |
| 266 | 15 | 0.1875 | 6 | 10,000 | 7 | 4 | 4.71 |
| 268 | 15 | 0.1875 | 6 | 10,000 | 19.5 | 4 | 4.71 |
| 269 | 20 | 0.25 | 6 | 10,000 | 0 | 4 | 6.28 |
| 270 | 20 | 0.25 | 6 | 10,000 | 7 | 4 | 6.28 |
| 272 | 20 | 0.25 | 6 | 10,000 | 19.5 | 4 | 6.28 |

| Test ID | Shear | | Number of Cycles | Axial Load | Ampere | Frequency | Rate (2πAf) |
|---|---|---|---|---|---|---|---|
| | Strain (%) | Amplitude (in.) | | (lb) | (amp) | (Hz) | (in./Sec) |
| 289 | 50 | 0.625 | 2 | 10,000 | 0 | 0.1 | 0.39 |
| 290 | 50 | 0.625 | 2 | 10,000 | 19.5 | 0.1 | 0.39 |
| 293 | 50 | 0.625 | 2 | 10,000 | 0 | 1 | 3.93 |
| 294 | 50 | 0.625 | 2 | 10,000 | 19.5 | 1 | 3.93 |
| 295 | 100 | 1.25 | 2 | 0 | 0 | 0.1 | 0.79 |

## B.7 Test Results

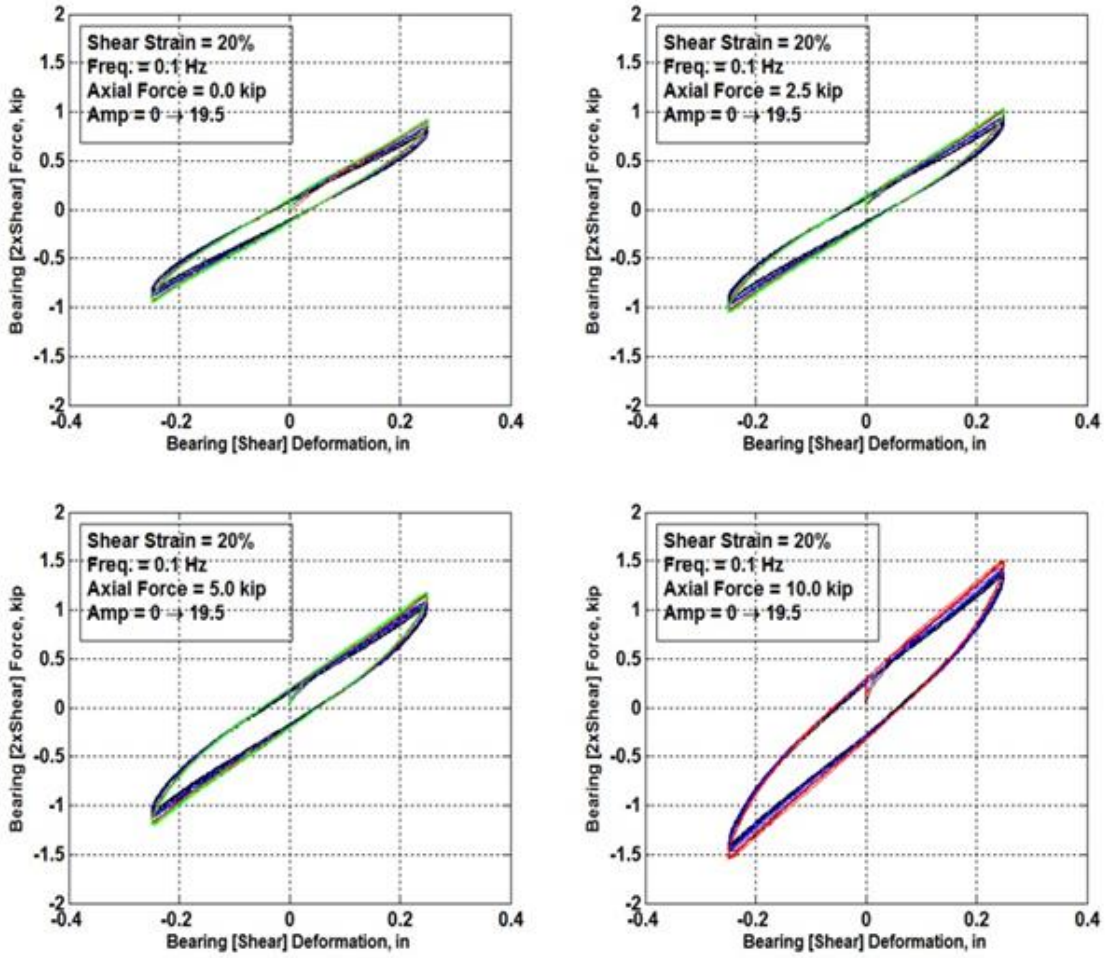


**Figure B.7.1.** Force versus displacement hysteresis of adaptive bearing system at a frequency of 0.1 Hz with varying electric current.

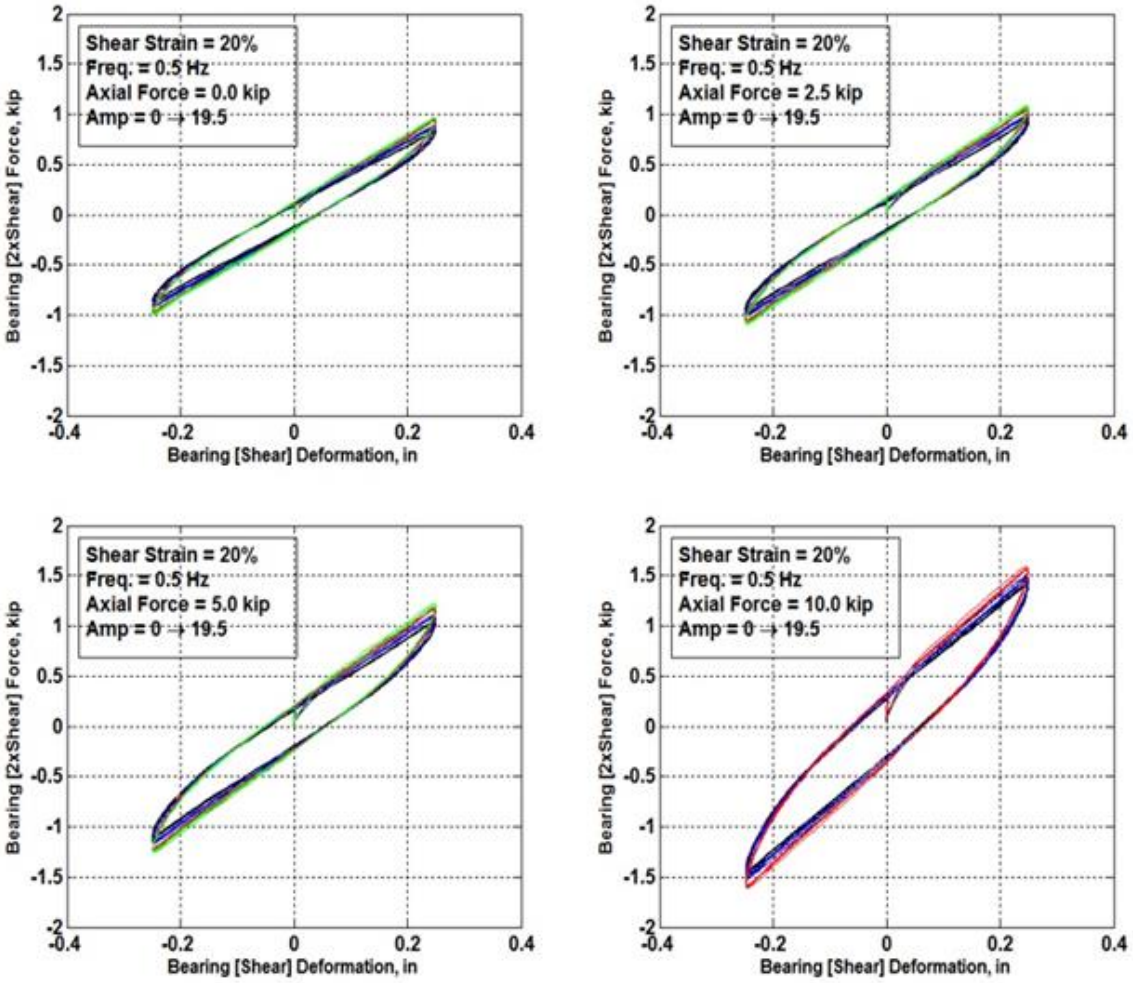


**Figure B.7.2.** Force versus displacement hysteresis of adaptive bearing system at a frequency of 0.5 Hz with varying electric current.

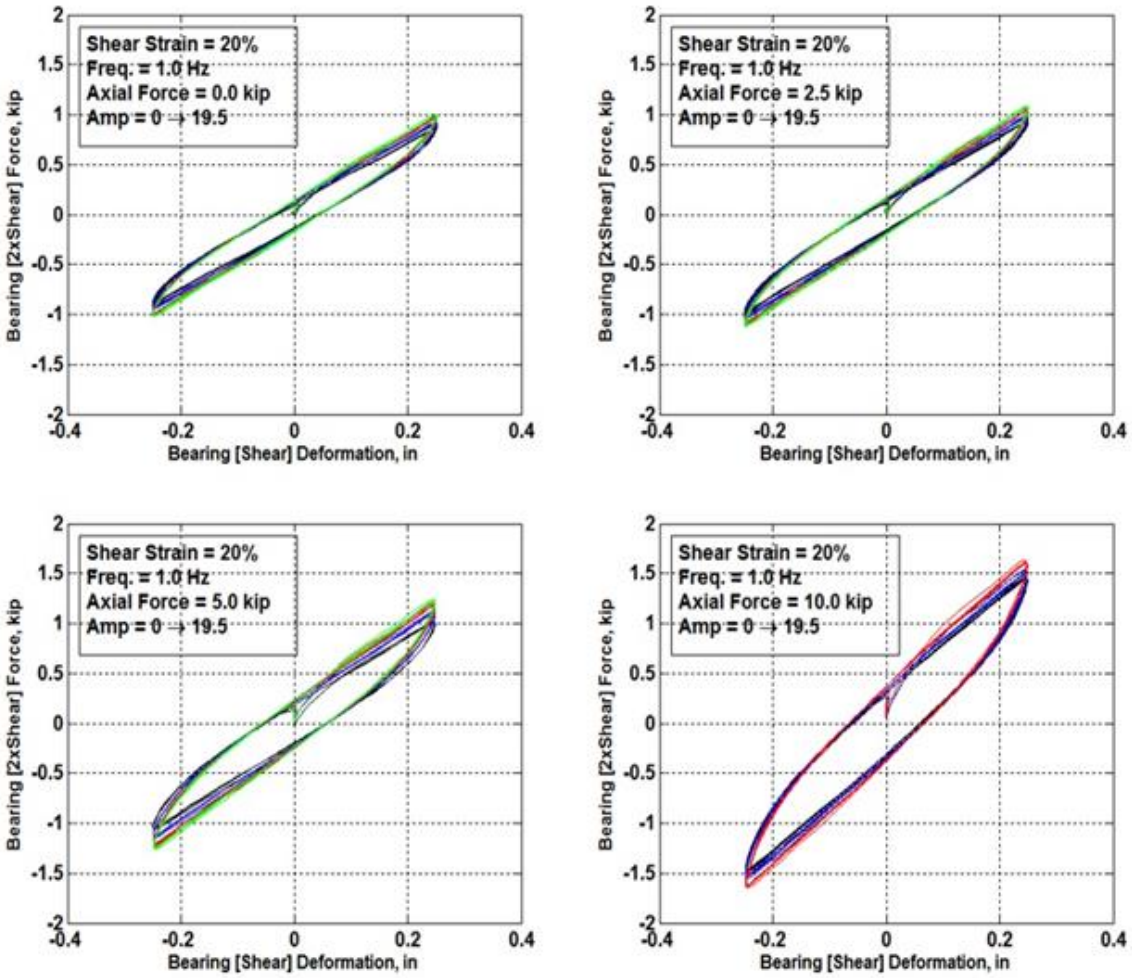


**Figure B.7.3.** Force versus displacement hysteresis of adaptive bearing system at a frequency of 1 Hz with varying electric current.

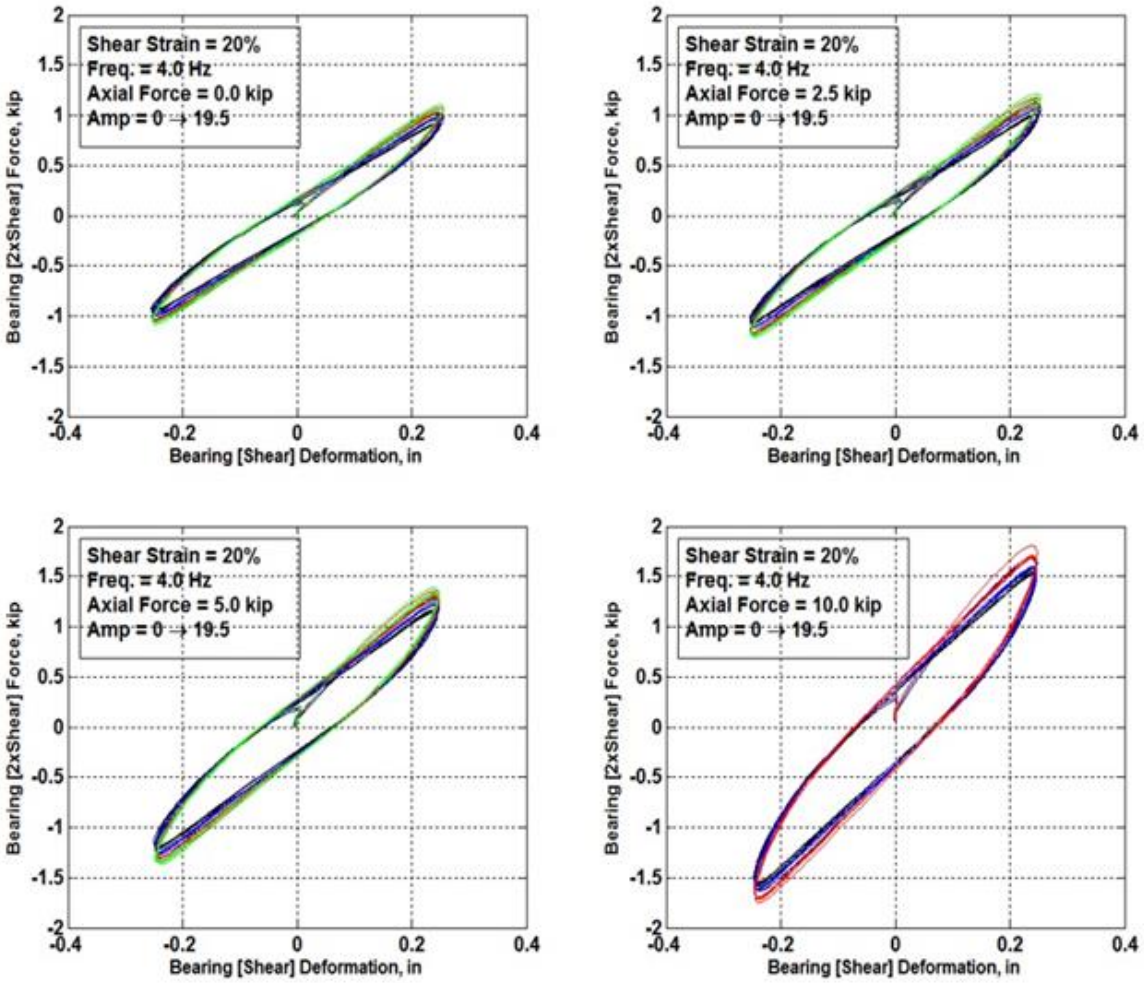


**Figure B.7.4.** Force versus displacement hysteresis of adaptive bearing system at a frequency of 4 Hz with varying electric current.

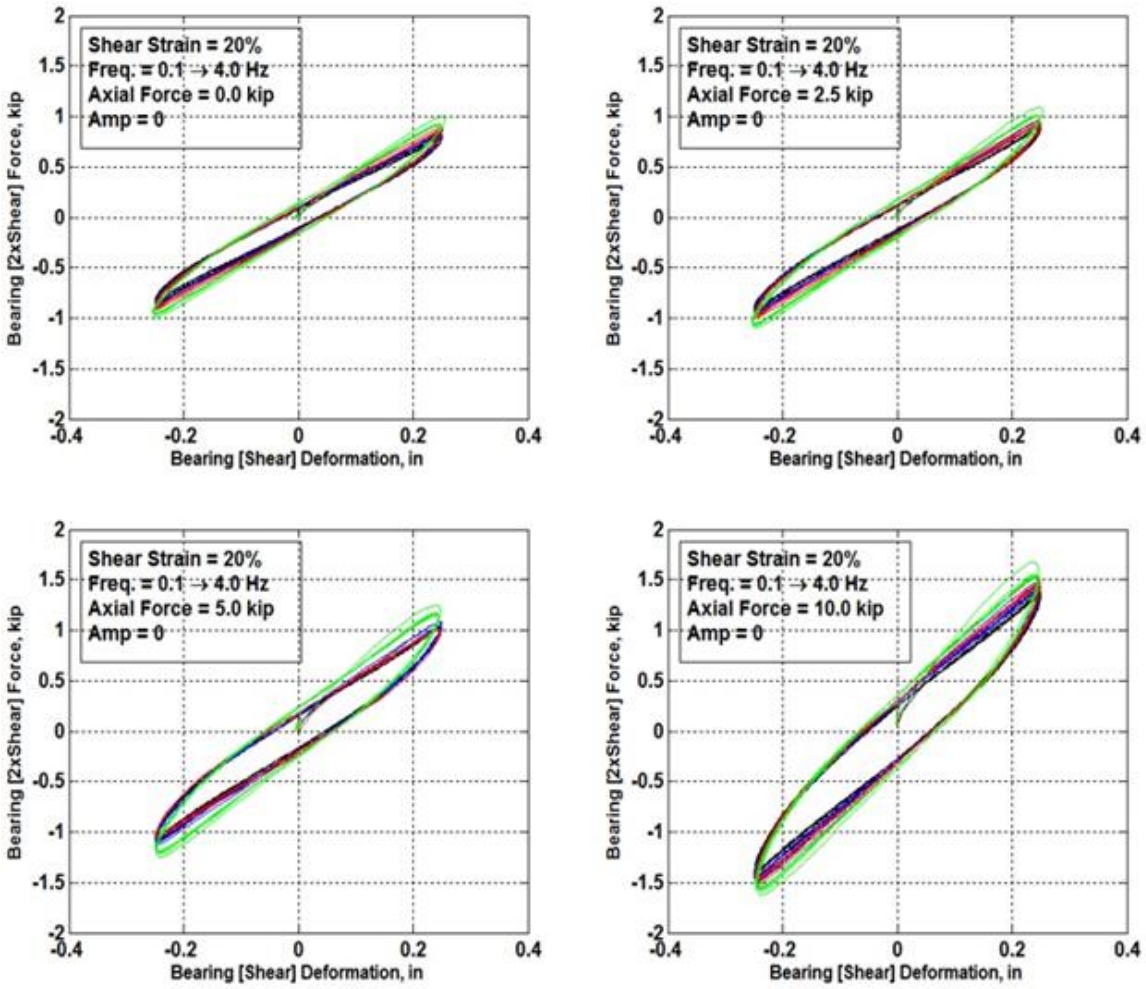


**Figure B.7.5.** Force versus displacement hysteresis of adaptive bearing system in passive state with varying frequencies.

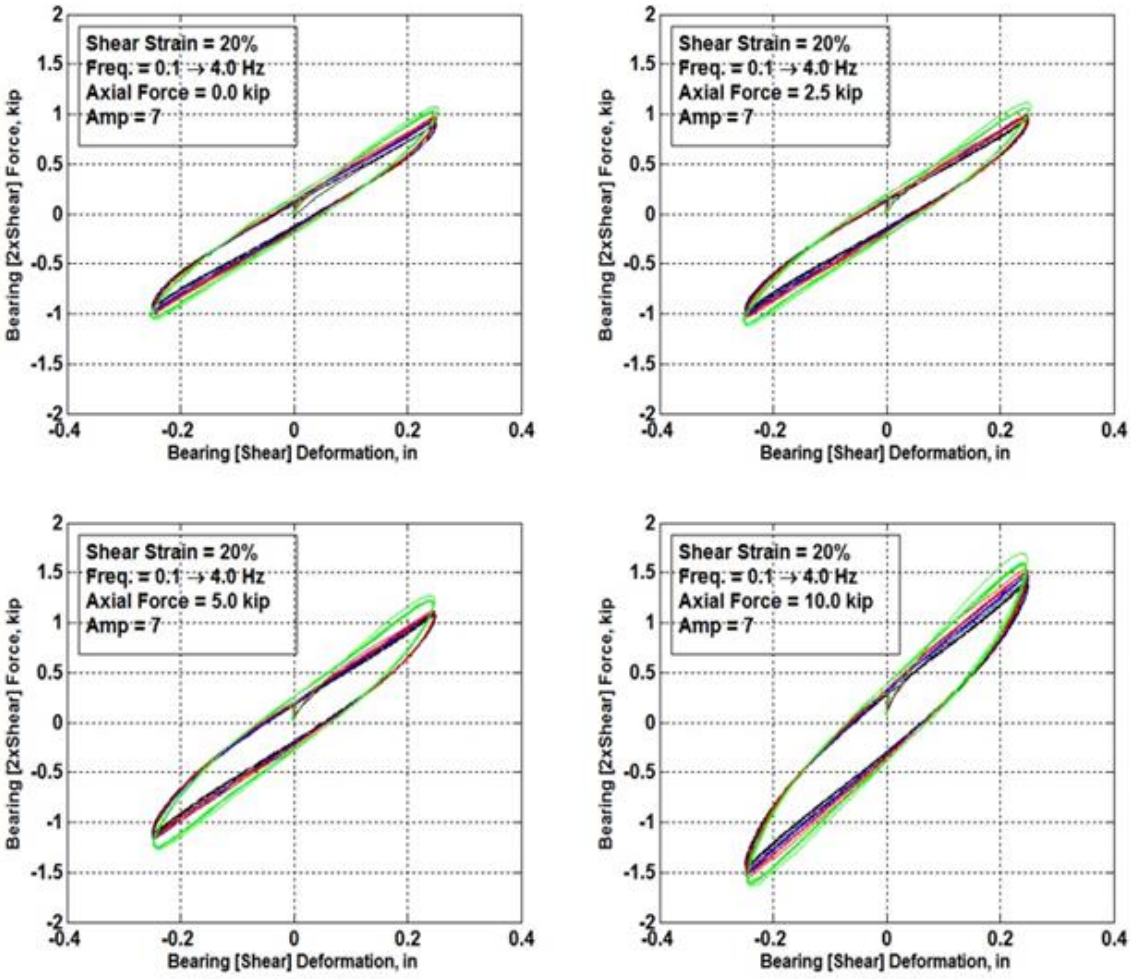


**Figure B.7.6.** Force versus displacement hysteresis of adaptive bearing system at 7-amp electric current with varying frequencies.

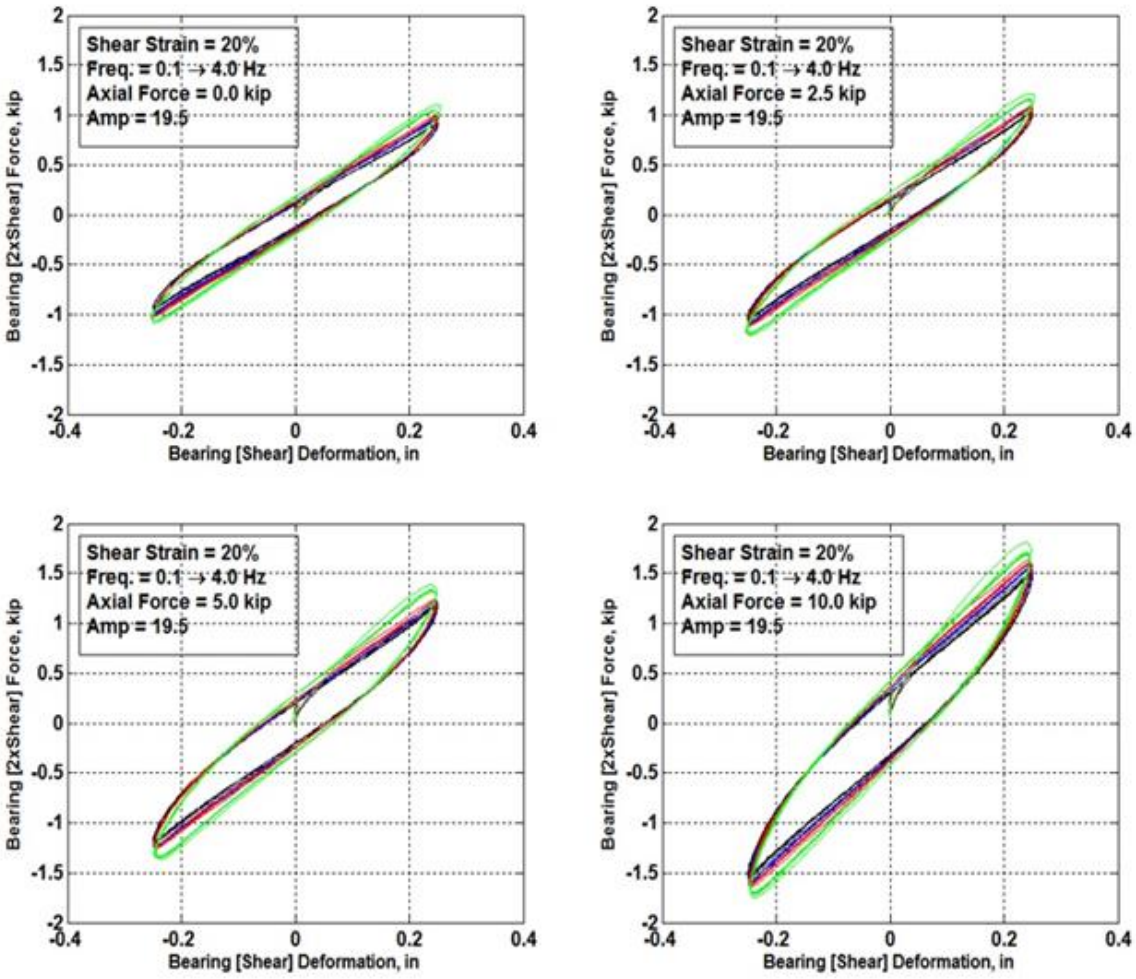


**Figure B.7.7.** Force versus displacement hysteresis of adaptive bearing system at 19.5-amp electric current with varying frequencies.

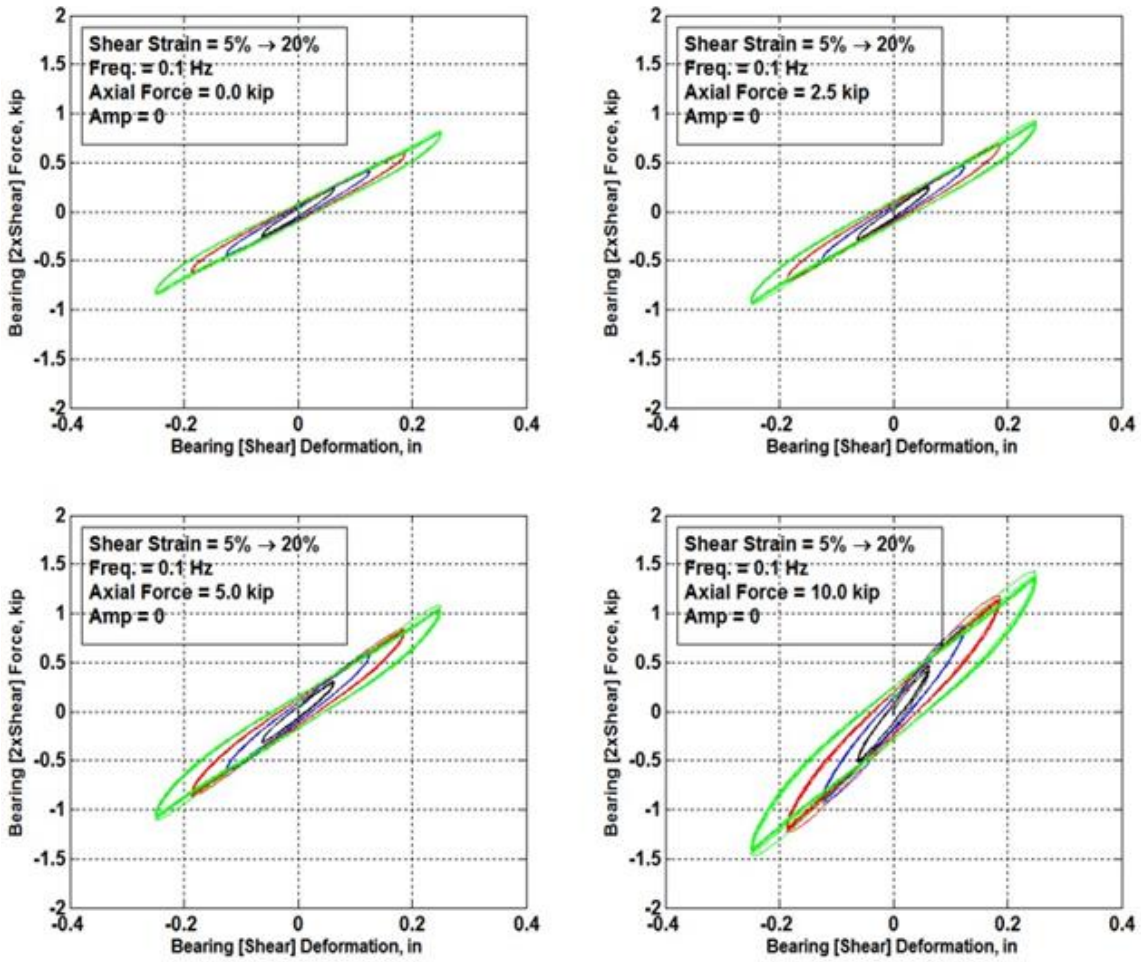


**Figure B.7.8.** Force versus displacement hysteresis of adaptive bearing system at a frequency of 0.1 Hz with varying strains in passive state.

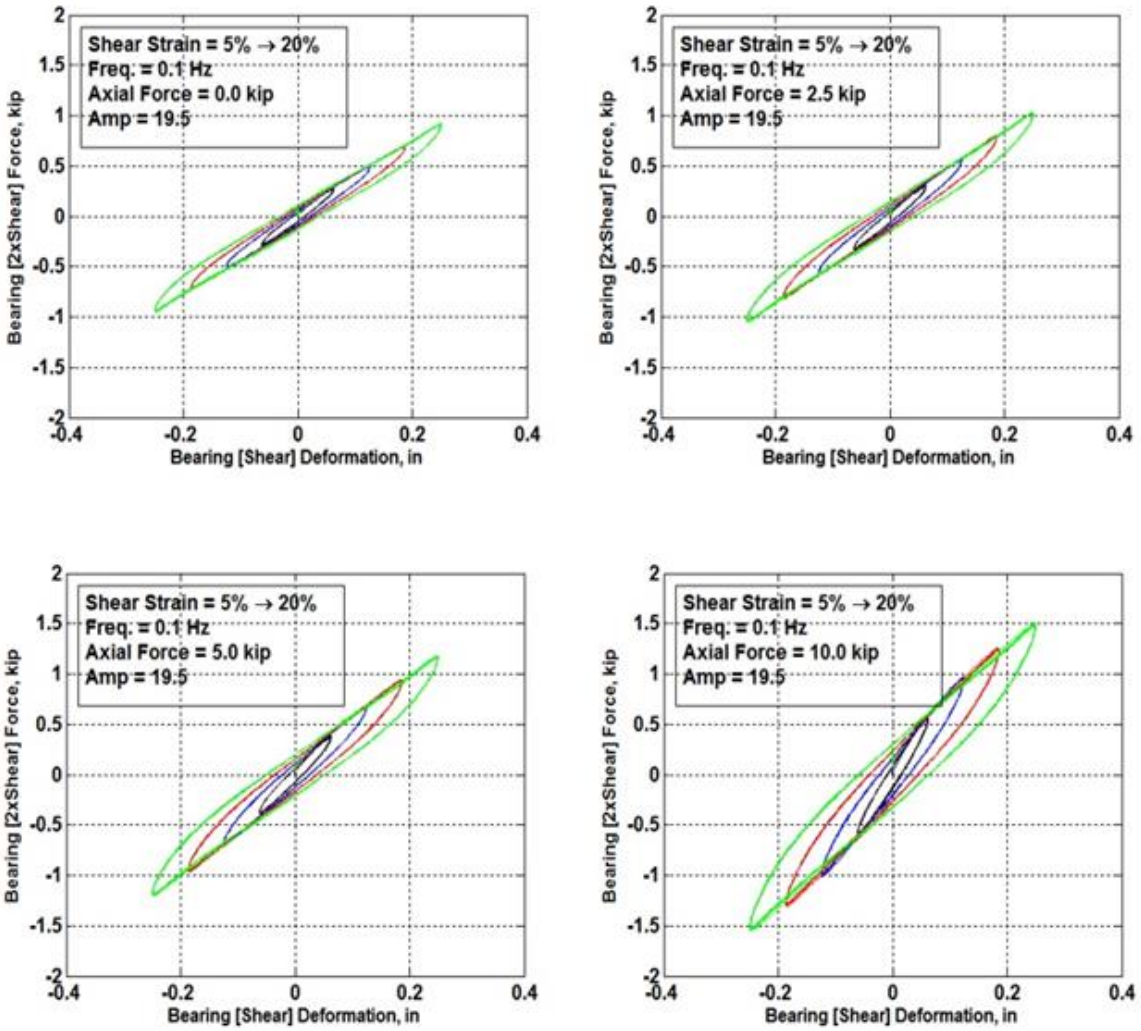


**Figure B.7.9.** Force versus displacement hysteresis of adaptive bearing system at a frequency of 0.1 Hz with varying strains and 19.5-amp electric current.

# Appendix C. Viscoelastic Material Modeling

**Definitions:**

Viscoelastic materials exhibit viscous (fluid) and elastic (solid) characteristics when undergoing deformation. In generally, solid components are modeled with springs and fluids are modeled with dashpots.

For an elastic material, the relationship between stress and strain can be stated as the following equation (1):

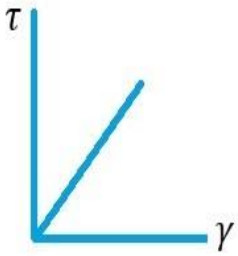


$$\tau = k\gamma \quad (1)$$

where k ($N/m^2$) is linear elastic spring (Spring with stiffness)

For a linearly viscous fluid, the relationship between stress and strain can be expressed as the following general form (Eq. 2):

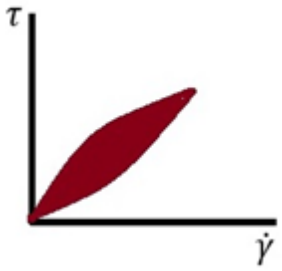


$$\tau = \eta\dot{\gamma} \quad (2)$$

where η ($N\text{-}s/m^2$) is the viscosity (dashpot containing a viscous fluid)

For a viscoelastic material, stress is a function of strain and strain rate can be described as the following (Eq. 3):

$$\tau = \tau(\gamma, \dot{\gamma}) \tag{3}$$

**Maxwell model:**

As shown in Figure 1. Spring and dashpot are arranged in series

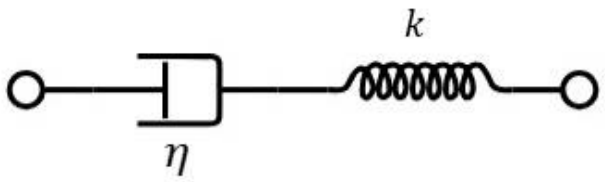


**Figure 1.** Maxwell element

**Stress condition:**

Each element has the same stress and that is equal to the total stress of the system

$$\tau_t = \tau_s = \tau_d \tag{4}$$

**Strain condition:**

Total strain is the sum of the strains in each element

$$\gamma_t = \gamma_s + \gamma_d \tag{5}$$

The relation between stress and strain can be derived

$$\frac{d\gamma_t}{dt} = \frac{d\gamma_s}{dt} + \frac{d\gamma_d}{dt} \tag{6}$$

where, $\gamma_s = \frac{\tau_s}{k}$ ➔$\frac{d\gamma_s}{dt} = \left(\frac{1}{k}\right)\frac{d\tau_s}{dt}$ and

$$\frac{d\gamma_d}{dt} = \left(\frac{1}{\eta}\right)\tau_d$$

plug in Eq. (6).

$$\frac{d\gamma_t}{dt} = \left(\frac{1}{k}\right)\frac{d\tau_s}{dt} + \left(\frac{1}{\eta}\right)\tau_d \quad (7)$$

we can rewrite as the following

$$\dot{\gamma}_t = \frac{1}{k}(\dot{\tau})_s + \left(\frac{1}{\eta}\right)\tau_d \quad (8)$$

**Advantages:**

1. Predicts fluid like a behavior

2. Stress relaxation can be modeled well

**Stress relaxation:**

Stress relaxation can be defined as the time that takes for a material to come to equilibrium due to stress decline when stretched to a fixed length and can be expressed as the following

$$T = \frac{\eta}{k} \quad [(\text{N-s/m}^2)/(\text{N-m}^2) = \text{Sec}]$$

**Kelvin – Voigt model:**

As shown in Figure 2. Spring and dashpot are arranged in parallel

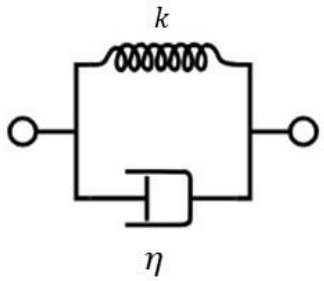


**Figure 2.** Kelvin-Voigt element

**Stress condition:**

Total stress is the sum of the stresses in each element

$$\tau_t = \tau_s + \tau_d \tag{9}$$

**Strain condition:**

Each element has the same strain and that is equal to the total strain of the system

$$\gamma_t = \gamma_s = \gamma_d \tag{10}$$

where, $\tau_s = k\gamma_s$

$$\tau_d = \eta \frac{d\gamma_d}{dt}$$

$$\tau_t = k\gamma_s + \eta \frac{d\gamma_d}{dt} \tag{11}$$

$$\tau_t = k\gamma_s + \eta\dot{\gamma}_d \tag{12}$$

**Advantages:**

1. Predicts solid like a behavior

2. Creep can be modeled well

**Complex modulus of viscoelastic materials can be derived from generalized Hooks law:**

The generalized stress-strain relationship (Hooks law) can be written as follows:

$$a_0\tau + a_1\dot{\tau} + a_2\ddot{\tau} + a_3\dddot{\tau} + \cdots = b_0\gamma + b_1\dot{\gamma} + b_2\ddot{\gamma} + b_2\dddot{\gamma} \ldots \tag{13}$$

For harmonic excitation at steady state applying

$$\tau = \tau_0 e^{i\omega t} \text{ and } \gamma = \gamma_0 e^{i\omega t}$$

we get

$$\begin{aligned} a_0\tau_0 e^{i\omega t} + a_1 (i\omega)\tau_0 e^{i\omega t} + a_2(i\omega)^2\tau_0 e^{i\omega t} + a_3(i\omega)^3\tau_0 e^{i\omega t} + \cdots \\ = b_0\gamma_0 e^{i\omega t} + b_1(i\omega)\gamma_0 e^{i\omega t} + b_2(i\omega)^2\gamma_0 e^{i\omega t} + b_2\gamma_0(i\omega)^3 e^{i\omega t} \\ + \cdots \end{aligned} \tag{14}$$

$$\frac{\tau_0}{\gamma_0} = \frac{b_0 + b_1(i\omega) + b_2(i\omega)^2 + b_2(i\omega)^3 + \cdots}{a_0 + a_1(i\omega) + a_2(i\omega)^2 + a_3(i\omega)^3 + \cdots} \quad (15)$$

the ratio could be denoted as complex shear modulus such that

$$G^* = \frac{(b_0 - b_2(\omega)^2 + \cdots) + i(b_1\omega - b_2(\omega)^3 + \cdots)}{(a_0 - a_2(\omega)^2 + \cdots) + i(a_1\omega - a_2(\omega)^3 + \cdots)} \quad (16)$$

multiply with conjugate of denominator to convert into

$$G^* = G' + iG'' \quad (17)$$

where $G'$ is storage modulus and $G''$ is loss modulus

loss factor $\tan\delta = \frac{G''}{G'}$ (18)

**Useful Laplace Transformation formulas:**

$$L\{F(t)\} = \bar{F}(S) \quad (19)$$

$$L\{\dot{F}(t)\} = S\bar{F}(S) - \bar{F}(0) \quad (20)$$

$\bar{F}(0) = 0$ (assume initial condition zero)

**Applying Laplace transforms to Maxwell model**

$$\dot{\gamma}_t = \frac{1}{k}(\dot{\tau})_s + \left(\frac{1}{\eta}\right)\tau_d \quad (21)$$

$$L(\dot{\gamma}_t) = \frac{1}{k}L((\dot{\tau})_s) + \left(\frac{1}{\eta}\right)L(\tau_d) \quad (22)$$

$$S\bar{\gamma} = \left(\frac{S}{k} + \frac{1}{\eta}\right)\bar{\tau} \quad (23)$$

$$\bar{\tau} = \left(\frac{k\eta s}{\eta s + k}\right)\bar{\gamma} \quad (24)$$

In Laplace transform, power of S will determine the derivative of stress and strain.

$$\bar{\sigma}S^3 = \dddot{\sigma} \qquad \bar{\varepsilon}S^3 = \dddot{\varepsilon}$$
$$\bar{\sigma}S^2 = \ddot{\sigma} \qquad \bar{\varepsilon}S^2 = \ddot{\varepsilon}$$
$$\bar{\sigma}S = \dot{\sigma} \qquad \bar{\varepsilon}S = \dot{\varepsilon}$$
$$\bar{\sigma} = \sigma \qquad \bar{\varepsilon} = \varepsilon$$

**Seven-parameter viscoelastic model**

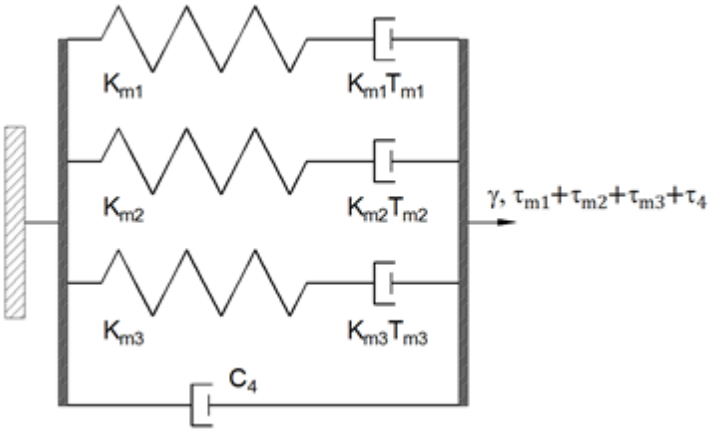


**Figure 3.** Seven parameter viscoelastic model

It is assumed that all elements in the model experience same strain and the total stress is equal to the sum of the stresses in each element and can be expressed as follows.

$$\bar{\sigma} = \left[\left(\frac{K_{m1}\eta_{m1}S}{\eta_{m1}S + K_{m1}}\right) + \left(\frac{K_{m2}\eta_{m2}S}{\eta_{m2}S + K_{m2}}\right) + \left(\frac{K_{m3}\eta_{m3}S}{\eta_{m3}S + K_{m3}}\right) + C_4S\right]\bar{\varepsilon} \tag{25}$$

$$\begin{aligned}\bar{\sigma}[(\eta_{m1}S + K_{m1})(\eta_{m2}S + K_{m2})(\eta_{m3}S + K_{m3})] \\ = [(K_{m1}\eta_{m1}S)(\eta_{m2}S + K_{m2})(\eta_{m3}S + K_{m3}) \\ + (K_{m2}\eta_{m2}S)(\eta_{m1}S + K_{m1})(\eta_{m3}S + K_{m3}) \\ + (K_{m3}\eta_{m3}S)(\eta_{m1}S + K_{m1})(\eta_{m2}S + K_{m2}) \\ + C_4S(\eta_{m1}S + K_{m1})(\eta_{m2}S + K_{m2})(\eta_{m3}S + K_{m3})]\bar{\varepsilon}\end{aligned} \tag{26}$$

From equation 26, we can find all the constants shown in Eq. 14. To calculate storage and loss moduli using Eq. 35 and Eq. 36.

$$a_0 = K_{m1}K_{m2}K_{m3} \tag{27}$$

$$a_1 = K_{m1}K_{m2}K_{m3}\,(T_{m1} + T_{m2} + T_{m3}) \tag{28}$$

$$a_2 = K_{m1}K_{m2}K_{m3}\,(T_{m1}T_{m2} + T_{m2}T_{m3} + T_{m3}T_{m1}) \tag{29}$$

$$a_3 = K_{m1}K_{m2}K_{m3}T_{m1}T_{m2}T_{m3} \tag{30}$$

$$b_1 = K_{m1}K_{m2}K_{m3}\,(T_{m1}K_{m1} + T_{m2}K_{m2} + T_{m3}K_{m3} + C_4) \tag{31}$$

$$b_2 = K_{m1}K_{m2}K_{m3}\,(K_{m1}T_{m1}T_{m2} + K_{m1}T_{m3}T_{m1} + K_{m2}T_{m1}T_{m2} + K_{m2}T_{m2}T_{m3} + K_{m3}T_{m1}T_{m3} + K_{m3}T_{m2}T_{m3} + T_{m1}C_4 + T_{m2}C_4 + T_{m3}C_4) \tag{32}$$

$$b_3 = K_{m1}K_{m2}K_{m3}T_{m1}T_{m2}T_{m3}\,(K_{m1} + K_{m2} + K_{m3}) + K_{m1}K_{m2}K_{m3}\,C_4(T_{m1}T_{m2} + T_{m2}T_{m3} + T_{m3}T_{m1}) \tag{33}$$

$$b_4 = K_{m1}K_{m2}K_{m3}T_{m1}T_{m2}T_{m3}C_4 \tag{34}$$

$$G' = \frac{(-\omega^2 b_2 + \omega^4 b_4)(a_0 - \omega^2 a_2) + (\omega b_1 - \omega^3 b_3)(\omega a_1 - \omega^3 a_3)}{(a_0 - \omega^2 a_2)^2 + (\omega a_1 - \omega^3 a_3)^2} \tag{35}$$

$$G'' = \frac{(\omega b_1 - \omega^3 b_3)(a_0 - \omega^2 a_2) - (-\omega^2 b_2 + \omega^4 b_4)(\omega a_1 - \omega^3 a_3)}{(a_0 - \omega^2 a_2)^2 + (\omega a_1 - \omega^3 a_3)^2} \tag{36}$$

in which $\omega = 2\pi f$ is the circular frequency (r/sec) of the excitation, $f$ = frequency (Hz) and the model parameters are:

# Appendix D. MRE-Based Sensor and Wireless Sensing System

## D.1 MRE-Based Sensor

The electrical resistance (or resistance) of MRE changes due to applied compression or shear loads. To measure the change in resistance as a function of the applied load, two stainless steel electrodes were connected to each side of a MRE layer and one wire is soldered to each shim to measure the output resistance. Originally, the resistance of MRE samples made were in the range of GΩ which was difficult to measure, since it needed a high resistance meter to measure the resistance. Thus, carbon black (SR303, Sid Richardson) was added to MRE specimens' mixture to lower the resistance. In Phase II a suitable carbon black type (i.e. SR303, Sid Richardson) was used in the MRE sensors. Carbon Black was mixed into the MRE at 0.25, 1, 1.5, 2, 2.5, 3, and 6% (wt.). Figure 1 displays disk-shape MRE samples with different iron particle and carbon black contents. Figure 2 shows the low load resistance measurement test setup at lower loads. The compressive load was applied by adding 10 lb weights and change in the resistance was measured with a multimeter.


Figure 1. MRE-based sensors with carbon black filled MREs.

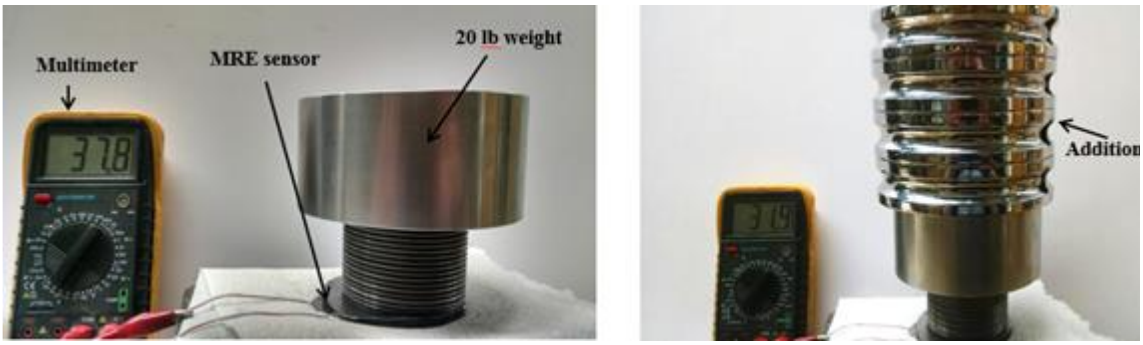


Figure 2. Measuring resistance change with an applied load

Figure 3 shows the reduction in the resistance with increasing the axial stress. The axial stress is normalized with respect to maximum stress of 10.51 psi. Such a decrease in the load can be correlated with applied load and the resulting relationship was used in the data acquisition system. At a low load regime, it was shown that polynomial function can predict the reduction in resistance with respect to applied load. Experiments were conducted for larger compression forces using Instron testing machine on another sensor with higher zero-load resistance. The normalized axial stress vs. resistance relationship was developed as shown in Figure 4 for a maximum stress of 0.73 ksi.

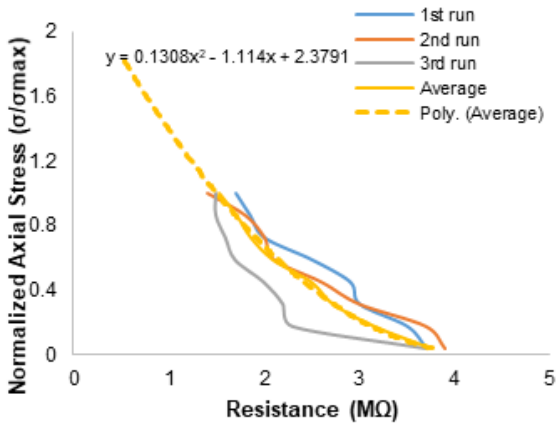


Figure 3. Low compressive load vs. resistance for a 2% carbon black 80% iron particle MRE sensor.

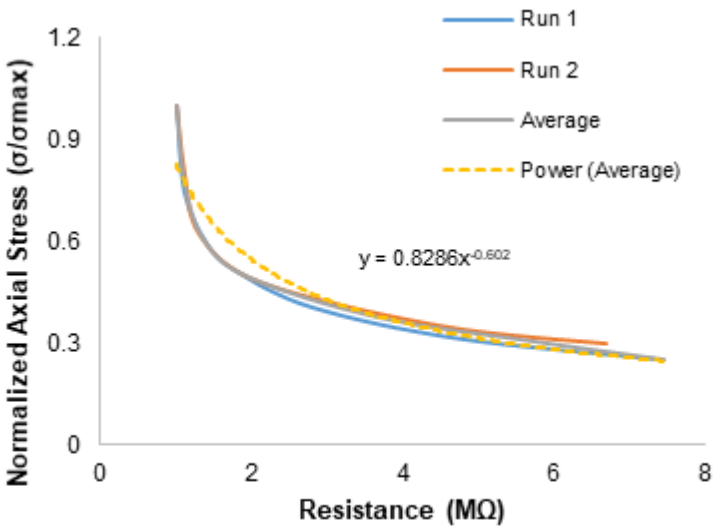


Figure 4. High compressive load vs. resistance for a 2% carbon black 80% iron particle MRE sensor

Tests were also performed using one MRE layer of the adaptive bearing during combined shear and compression experiments. The resistance is measured by connecting wires to the shims attached to both sides of the fifth layer of MRE. Upon increasing the compressive force, the resistance significantly drops as shown in the semi-logarithmic plot of Figure 5. Also, since MRE layers of the bearing will be subjected to a magnetic field during operation, the change in resistance of MRE with increasing the magnetic field was studied. Figure 6 shows a sample result of 0.5 Hz sinusoidal shear loading with 2.5% strain and different applied currents.

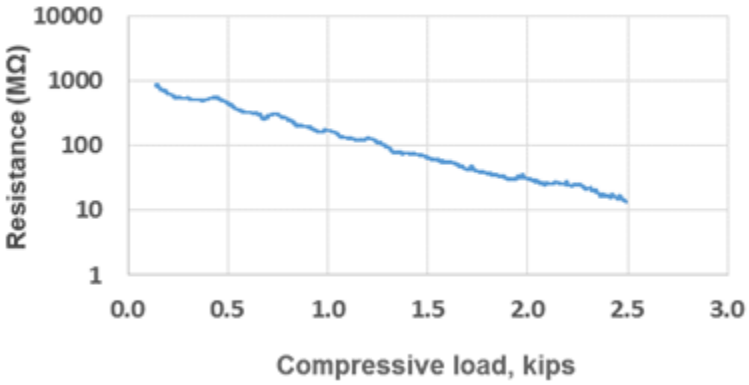


Figure 5. Compressive load vs. resistance for a layer of MRE within the bearing stacks.

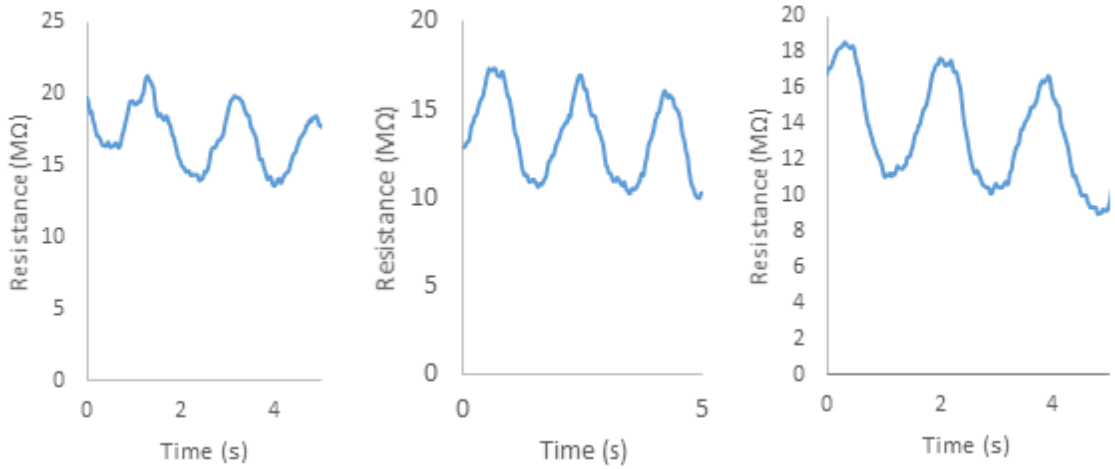


(a) (b) (c)

Figure 6. Shear load vs. resistance for a layer of MRE within the bearing stacks under applied current of (a) 7, (b) 14, and (c) 19.5 amperes.

## D.2 Wireless Sensing System

The wireless sensing system was developed based on three foundations. The first foundation is to collect multi-channel data from the MRE sensor which can then be transmitted to a remote computer. The computer may be anywhere in the world, and it can receive data in near real time. The second foundation is to send notifications through e-mail or text messaging should a specific (i.e., pre-defined) event occur. The user will be

able to set any conditions that may be reached for the system to send such notifications. Instead of a need to continually monitor bearing operations, this allows a "set and forget" mode of operation. Finally, the wireless sensing system serves as a survivable "black box". In an extreme or unusual event, such as a bridge collapse, an external memory card from the sensing system can be retrieved to analyze the stored data up to the time of the event.

The basic layout of the wireless sensing system is shown in Figure 7. The sensor consists of a MRE sandwiched between two metal electrodes. Any force applied to this sensor changes its resistance. The electrodes are connected to a circuit that produces voltages that may be used to compute MRE resistance. Data are transferred to a microcontroller that also acts as a web server. Thus, the microcontroller acts as both a data acquisition system and as an interface to the outside world. After collecting the raw data, the microcontroller processes the data and performs any necessary actions such as storing data and transmitting the data to one or more remote computers.

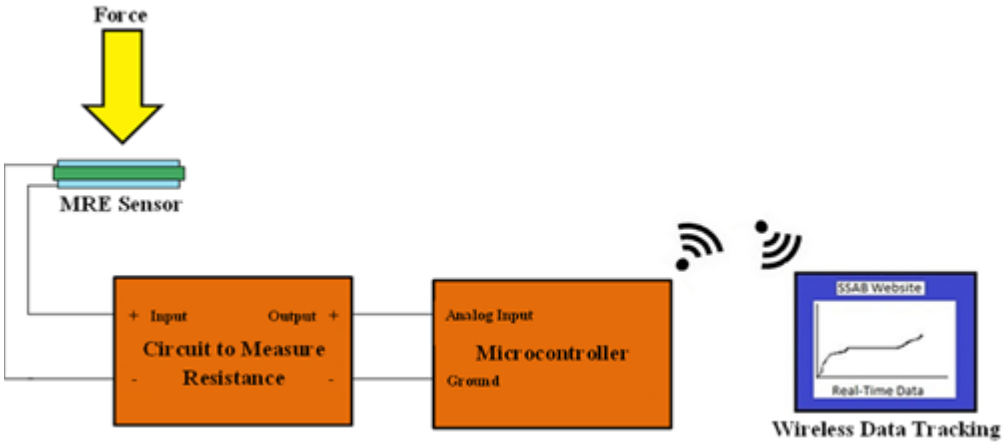


Figure 7. Wireless sensing system design concept

**Wireless System Electronics:** The microcontroller used for the wireless sensing system is an ATSAMD21J18, shown in Figure 8. This is a portion of an Atmel SMART SAM D ARM-based microcontroller that uses a low-power cortex-M0+ processor, commonly used in cell phones. This microcontroller can collect and graph data from up to 16 channels, simultaneously. Two extension boards are attached to the microcontroller. One board, an I/O1 Xplained Pro, is used to store data onto a microSD card. This serves the "black box" function of the wireless sensing system. At any time, this card may be retrieved from the system and inserted into any computer to view the data acquired up to the point of any catastrophic event. The other board is a WINC1500 Xplained Pro board, which serves two purposes: (1) to synchronize the time clock with the current time. The time clock is used to time stamp all data, and (2) to wirelessly transmit data to a remote data site.

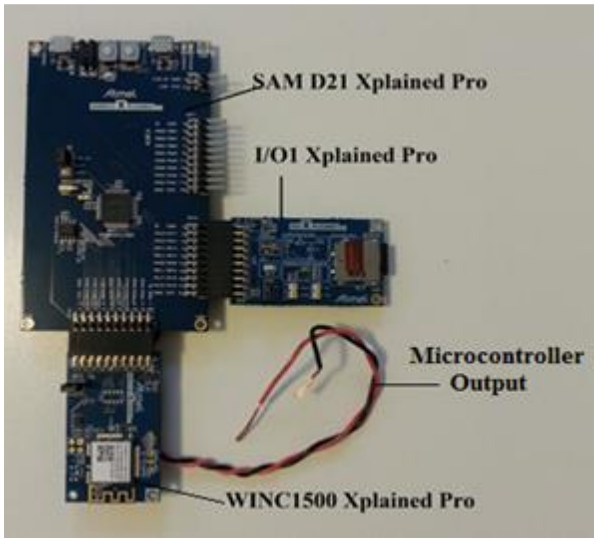


Figure 8. Atmel microcontroller at the heart of the wireless sensing system.

Like other mobile devices such as a cell phone, the Atmel microcontroller consumes a relatively small amount of power. The amount of power consumed is dependent on the clock frequency running the system. The clock can be adjusted to run slower and consume even less power at the cost of performance. Figure 9 shows the general relation between the base clock frequency and power consumption. The graph demonstrates a roughly linear relation with a maximum possible main clock frequency of 48 MHz. During normal operation of the software, if the clock frequency falls below 2 MHz, the system will break. Based on the desired specifications (e.g., sample rate, rates of wireless transmission) and other requirements for the system, the clock frequency may be optimized so that the microcontroller consumes as little power as possible while maintaining a selected performance.

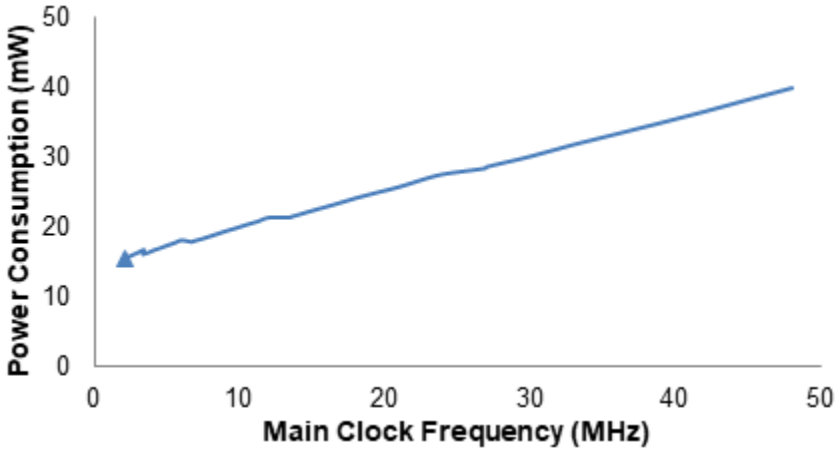


Figure 9. The general relation between power consumption and the main clock frequency.

**System Interaction with MRE:** Foundationally, the sensing system measures the resistance from each MRE sensor. By knowing such resistances, other values such as

force and strain can be determined and monitored. To be able to measure the resistance of MRE, a voltage divider circuit is used as shown schematically in Figure 10.

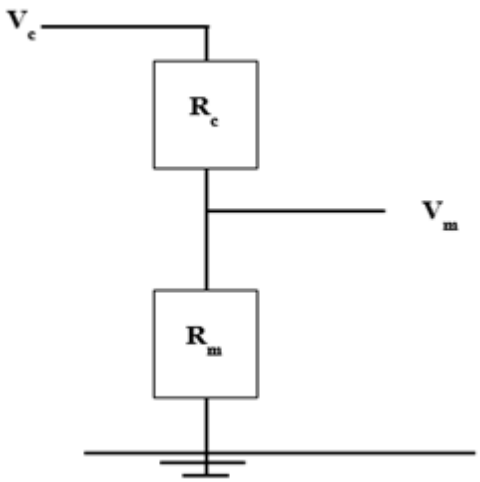


Figure 10. Basic voltage divider circuit.

The equation to obtain the MRE resistance is, as follows:

$$R_m = \frac{R_c V_m}{V_c - V_m} \quad (1)$$

Where $R_m$ is the resistance of the MRE sensor, $R_c$ is a constant resistor, $V_m$ is the measured voltage, and $V_c$ is a constant reference voltage. The reference voltage and the resistance of the constant resistor are known values, while the measured voltage is read by the sensing system. The three variables are then used to obtain the resistance of the MRE. This resistance can be used to compute other measures where the relation between applied load and resistance is described in more detail below.

If measurements surpass a given threshold, the sensing system is set to send a notification via e-mail or text, alerting a user to the occurrence of the event. Furthermore, the system may automatically adjust its sampling rate based on a pre-determined

“urgency” of the situation. In order to measure the amplitudes of oscillations at specific frequencies, data are also transformed into the frequency domain using Fourier analysis (Figure 11). The system can be configured to analyze frequencies at within pre-defined ranges.

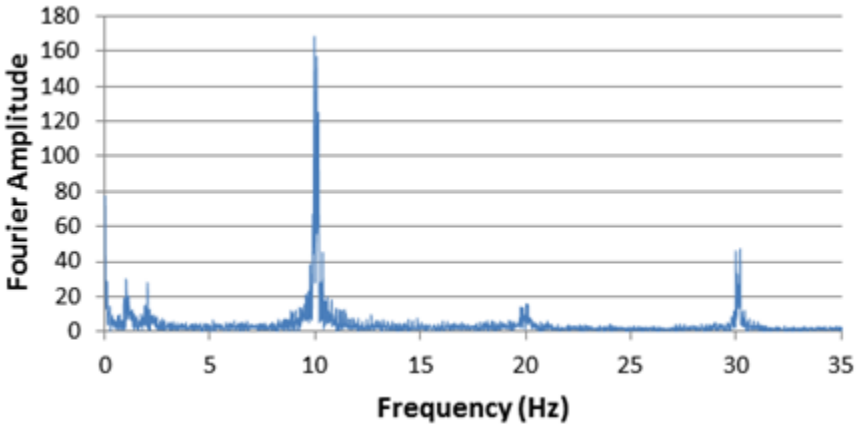


Figure 11. Fourier analysis of an applied load.

In real time, the sensing system may also output voltages for feedback control of the bearing. Using a Digit-to-Analog Channel (DAC), the system can directly output voltages between 0V and 1V as shown in Figure 12. Using an operational amplifier, the voltage range can be scaled to any range needed to control the circuitry used to drive current through the coils that control magnetic fields applied to then MREs. The relation between measured load and the feedback MRE control is profiled using a simple look-up table. This facilitates a real-time and automated feedback control of bridge stiffness.

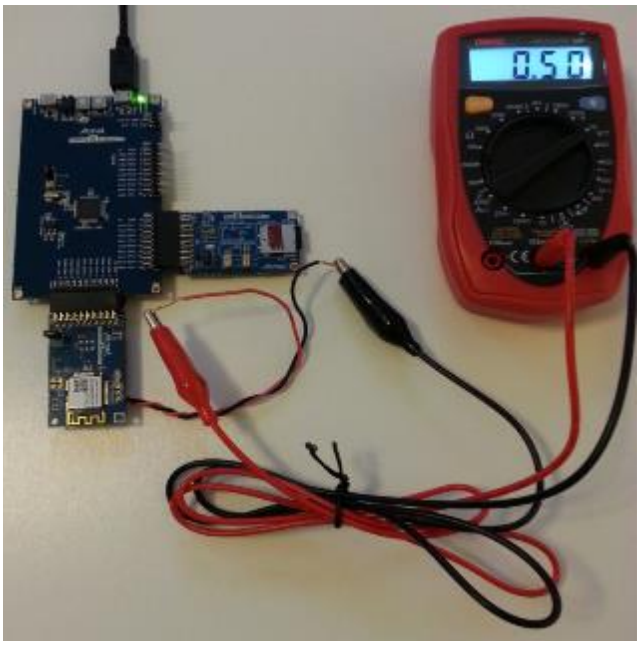


Figure 12. Atmel microcontroller outputting 0.5 volts to multi-meter.

**Controls and Documentation:** A website has been created to view and adjust graphs for the sensing system. Figure 13 demonstrates the structure of the systems server. Upon request, the system transmits data from a selected period for a user to view in graphical form. A graph from any sensor (or combination of sensors) and any period can be plotted as shown in Figure 14.

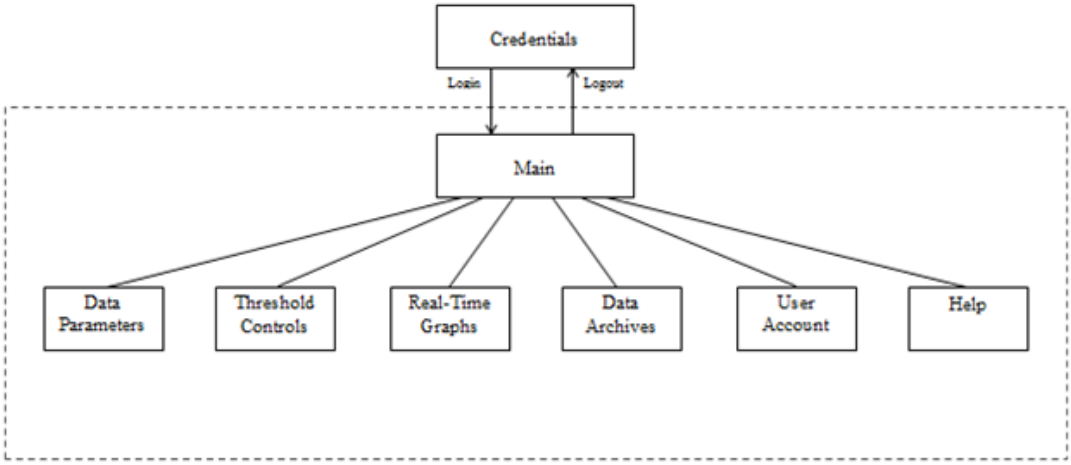


Figure 13. Layout for system server.

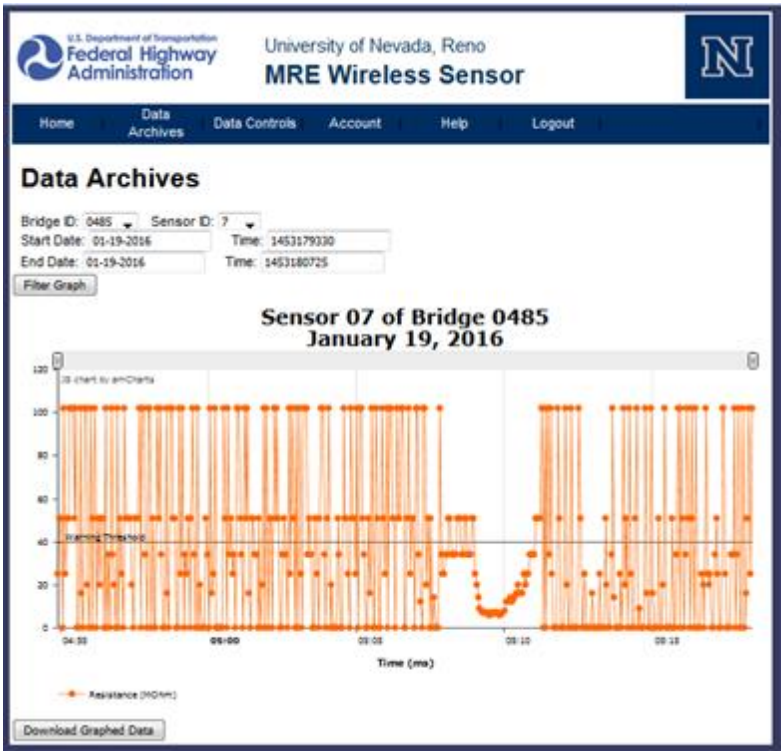


Figure 14. The website for viewing graphical data from the sensing system.

**Experimental measurements for the SSAB:** The wireless sensing system was tested on a bearing shear and compression test setup to collect, and archive the data to an external memory card, and wirelessly transfer data to a remote computer. As shown in Figure 15, the system is attached to a metal plate placed on the side of the test bearing.

Batteries shown on the top left corner are used to power the system. Once the sensing system is turned on and initialized, data acquisition begins automatically. For initial testing, the system is shown collecting three resistances values from MRE stacks, the temperature of the bearing, and the displacement produced by an actuator. These data are time-stamped and then transmitted to a remote computer. An example of data collected and transmitted to a remote computer can be seen in Figure 16.

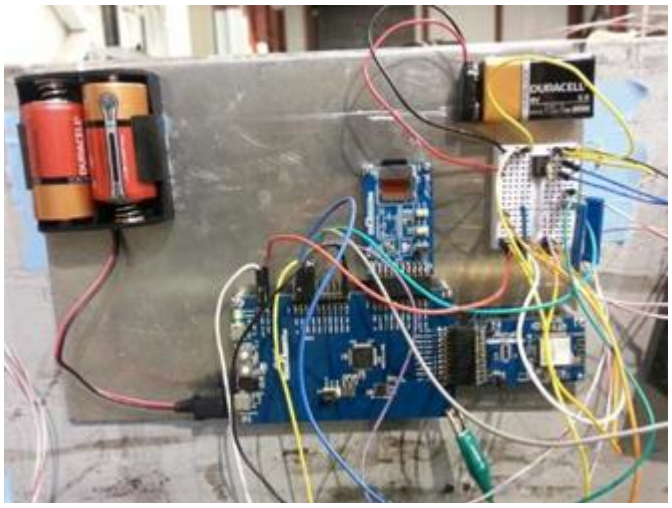

Figure 15. Wireless sensing system attached to the test bearing.

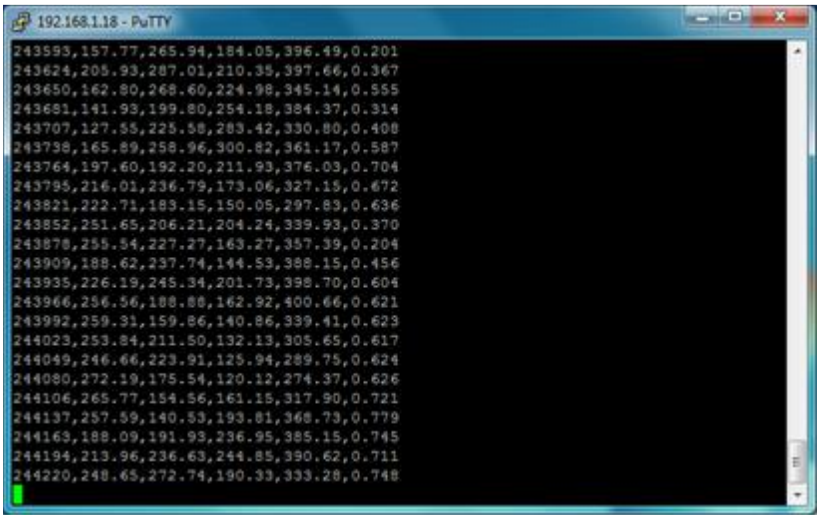


Figure 16. Acquired data displayed on a remote computer using PuTTY.

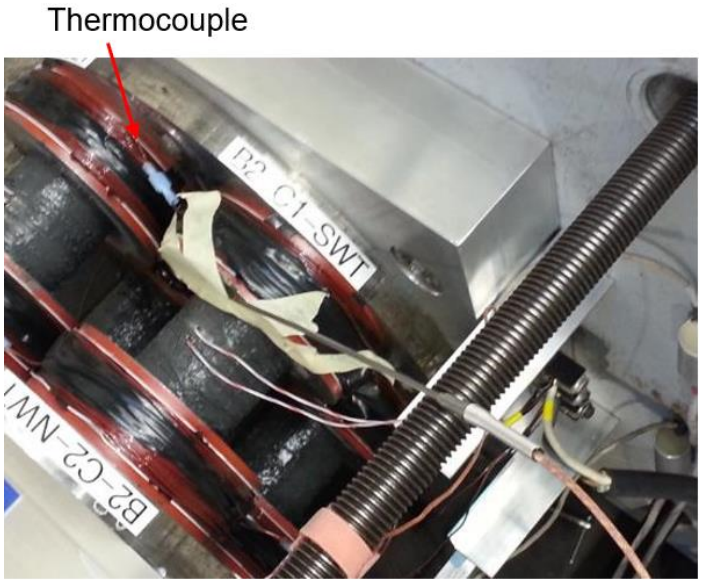


Figure 17. A thermocouple attached to the bearing.

Figure 17 shows a thermocouple that is attached to the surface of the coils. The relation relating temperature to the voltage produced by the thermocouple was determined by performing an experiment in which voltages were recorded at various temperatures. The results show a linear relation between temperature and voltage. Figure 18 shows a comparison between the temperature obtained by the sensing system and that measured by a National Instruments-based thermocouple.

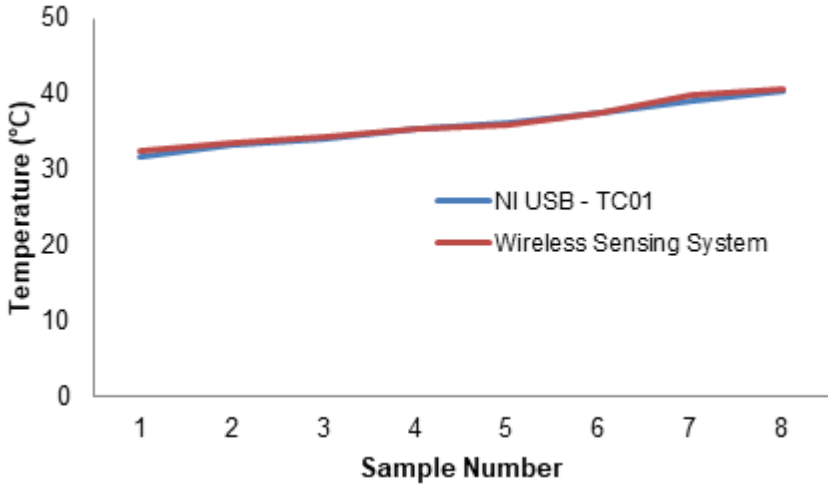


Figure 18. Calibration of temperature measurements.